Personalized pulmonary mechanics : modeling, estimation and application to pulmonary fibrosis

Cécile Patte

To cite this version:

Cécile Patte. Personalized pulmonary mechanics : modeling, estimation and application to pulmonary fibrosis. Biomechanics [physics.med-ph]. Institut Polytechnique de Paris, 2020. English. NNT : 2020IPPAX076 . tel-03144413

HAL Id: tel-03144413
https://theses.hal.science/tel-03144413

Submitted on 17 Feb 2021

NNT : 2020IPPAX076

Thèse de doctorat

Personalized pulmonary mechanics: modeling, estimation and application to pulmonary fibrosis

Thèse de doctorat de l'Institut Polytechnique de Paris
préparée à École Polytechnique

École doctorale n°626 de l'Institut Polytechnique de Paris (ED IP Paris)
Spécialité de doctorat : Mécanique

Thèse présentée et soutenue à Palaiseau, le 18 décembre 2020, par

Cécile Patte

Après avis des rapporteurs :

Stéphane Avril
Professeur, Mines de Saint-Étienne

Merryn Tawhai
Professeur, University of Auckland

Composition du Jury :

Wolfgang A. Wall Professeur, Technical University of Munich	Président
Stéphane Avril Professeur, Mines de Saint-Étienne	Rapporteur
Pauline Assemat Chargée de recherche CNRS, IMFT	Examinateur
Aline Bel-Brunon Maître de conférences, INSA Lyon	Examinateur
Jean-François Bernaudin Professeur émérite, Sorbonne Université	Examinateur
Nicolas Triantafyllidis Directeur de recherche CNRS, École polytechnique	Examinateur
Dominique Chapelle Directeur de recherche Inria	Directeur de thèse
Martin Genet Maître de conférences, École polytechnique	Co-directeur de thèse

Remerciements

Cette thèse a été une aventure de trois ans au cours desquels j'ai été entourée de personnes formidables sans qui ce travail n'aurait pu avoir lieu et que j'aimerais remercier chaleureusement.

Je tiens tout d'abord à remercier mes deux directeurs de thèse, Dominique Chapelle et Martin Genet. Merci à vous deux pour votre confiance, puisque vous m'avez proposé ce sujet de thèse sans me connaître au préalable. Merci Martin pour ta disponibilité et pour ton aide au quotidien. Je ne compte plus le nombre de fois où j'ai débarqué à l'improviste dans ton bureau et tu as toujours pris le temps de résoudre mes problèmes. Ton enthousiasme et tes nombreuses idées m'ont été bien utiles pour avancer. Je crois que je suis devenue un peu geek avec toutes les astuces que tu m'as transmises. Et tu m'as appris à relativiser les différentes embûches que l'on peut rencontrer avec ta formule « C'est la vie ! ». Merci Dominique pour ta rigueur scientifique et ton exigence qui m'ont poussée à donner le meilleur de moi, pour ton calme face à toute situation, pour ta présence et tes encouragements aux moments clefs. Tes grandes connaissances scientifiques et ton recul sont précieux. Merci pour m'avoir guidée pendant ces trois années et pour l'autonomie que vous m'avez laissée. J'ai appris énormément à vos côtés. Sans vous, jamais je n'aurais pu atteindre un tel résultat.

Je souhaite aussi remercier Jean-François Bernaudin, Hilario Nunes, Pierre-Yves Brillet et Thomas Gille, cliniciens de l'hôpital APHP Avicenne de Bobigny. Cette thèse n'aurait pas vu le jour sans eux et leur volonté d'approfondir les recherches sur la fibrose pulmonaire idiopathique, maladie à laquelle ils sont confrontés au quotidien et qui reste mal connue. Nos différentes rencontres au cours de ces trois années m'ont permis de mieux comprendre les enjeux cliniques de mon travail et nos discussions ont été stimulantes et très enrichissantes. Les aider à mieux appréhender les concepts de la mécanique et m'enrichir en retour de leur expertise a été un réel plaisir. Leur intérêt pour ce travail m'a apporté une motivation supplémentaire. Merci aussi pour leur patience, car la recherche va toujours moins vite que ce qu'on aimerait, surtout quand il s'agit d'améliorer le diagnostic et le pronostic des malades. Je remercie également Catalin Fetita, partie intégrante de la collaboration, pour les aspects de traitement d'image. Il a gentiment pris le temps notamment de segmenter les poumons sur les images médicales des patients grâce à son algorithme spécialement développé pour les images de poumons fibrosés.

J'aimerais remercier vivement les deux rapporteurs de ce présent manuscrit, Stéphane Avril et Merryn Tawhai, pour avoir accepté de consacrer du temps à lire mon travail et pour leurs commentaires constructifs. Je remercie également Wolfgang A. Wall d'avoir accepté de présider le jury ainsi que les autres membres du jury, Pauline Assemat, Aline Bel-Brunon, Jean-François Bernaudin et Nicolas Triantafyllidis, qui ont gentiment accepté d'assister à ma soutenance malgré les conditions particulières dues aux conditions sanitaires et pour leur intérêt dans mon travail.

Tout au long de ces trois ans, j'ai rencontré de nombreuses personnes dans des domaines divers, avec qui les discussions ont été très riches et ont permis d'apporter à chaque fois de nouvelles idées pour avancer ce travail. Merci à Jean-Noël Foulquier et Milovan Sanovic de l'hôpital Tenon, pour m'avoir fait découvrir leurs problématiques autour de la radiothérapie des poumons. Merci à Aline Bel-Brunon et Ana-Maria Sfarghiu du LAMCOS de l'INSA Lyon, pour les échanges sur l'acquisition de données expérimentales et le rôle du surfactant. Merci à Xavier Maître et Tanguy Boucneau de l'IR4M, pour les discussions à propos de l'IRM du poumon. Merci à Gilles Mangiapan de m'avoir accueillie au CHI de Créteil pour parler de pression pleurale. Merci à Marianne Kambouchner de l'hôpital Avicenne pour m'avoir montré ses coupes d'histologie de poumons fibrosés.

Je souhaite aussi remercier Sylvie Boldo pour m'avoir fait confiance et m'avoir encadrée pour une mission de médiation scientifique. Il me paraissait intéressant d'essayer de partager ma passion des sciences avec les jeunes pour leur donner envie d'en faire à leur tour. J'ai fortement apprécié cette expérience de construire un atelier pour la fête des sciences, malgré les obstacles rencontrés. Je retiendrai en particulier l'épisode de gonflage de ballons qui nous a bien fait rire.

Une thèse, c'est un travail scientifique, mais c'est aussi des gens qui nous entourent au quotidien. Un grand merci à l'ensemble de l'équipe MΞDISIM pour son accueil, son ambiance et tous les échanges que j'ai pu avoir chacun d'entre vous. Sa multidisciplinarité ainsi que ses fortes interactions avec le monde clinique sont une grande richesse de l'équipe et rendent ses projets d'autant plus passionnants. Merci à Philippe Moireau pour l'attention qu'il porte à maintenir la dynamique de l'équipe et pour les très bonnes conditions de travail qu'il assure aux doctorants. Les traditionnelles réunions chouquettes du lundi matin vont me manquer. Je souhaite en particulier remercier François Kimmig, pour sa patience à répondre à mes innombrables questions et pour toutes les discussions non scientifiques que l'on a eues, notamment à propos de tennis ou de ski. Grâce à ta persévérance, tu as même fini par me convaincre de venir travailler en vélo. Je remercie aussi grandement Chloé Giraudet et Frédérique Robin. Merci pour votre écoute, votre soutien et vos encouragements à toute épreuve. J'ai beaucoup apprécié de discuter avec vous de tout et n'importe quoi autour d'une tasse de thé. Merci à Jérôme Diaz de s'être toujours penché sur mes problèmes et de m'avoir fait découvrir les 25 bosses de Fontainebleau. Merci à Radek Chabiniok pour sa générosité et son enthousiasme. J'attends toujours l'initiation au hockey que tu m'as promise. Merci à Frédérique Clément, initiatrice des fameux tours du lac post-déjeuner, qui ont été propices à de sympathiques conversations. Merci à Maria Gusseva, Hajer Methenni, Jessica Manganotti et Guillaume Balif, mes partenaires d'open space, toujours prêts à discuter un instant. Merci à Arthur Le Gall pour sa curiosité et sa volonté de percer les secrets de la mécanique. Merci à Federica Caforio pour sa bonne humeur. Merci à Jean-Marc Allain, Sébastien Impériale, Patrick Le Tallec et Fabrice Vallée pour leur intérêt dans mon travail. Merci à tous les doctorants et stagiaires que j'ai croisés : Nicole Tueni, Florent Wijanto, Jona Joachim, Francesco Regazzoni, Felipe Alvarez, Mahdi Manoochehrtayebi, Mathieu Barre, Tiphaine Delaunay. Je ne veux pas non plus oublier l'ensemble des collègues du LMS, en particulier Abdelfattah Halim qui a toujours fait de son mieux pour résoudre les problèmes liés au cluster.

Finalement, je souhaite remercier l'ensemble de mes amis et de ma famille pour avoir toujours été présents à mes côtés et pour m'avoir toujours soutenue.

Contents

Introduction (English)

General context

Clinical context

In silico medicine

In silico medicine, also called digital medicine, is the use of numerical tools in medicine, in particular mathematical models and associated computer simulations, for diagnosis, prognosis, surgical procedures, treatments or also clinical trials. Although statistical approaches are also largely used for medical applications, this work mainly focuses on biophysical models, to which the terms "*in silico* models" or "numerical models" will refer throughout.

Largely used in the aeronautics and automotive fields, numerical tools like *in silico* models start to be used in medicine, giving rise to new opportunities in healthcare [Naseer et al., 2008; Lim et al., 2020] and making *in silico* medicine an emergent and promising area. As proof, the worldwide market of digital health has been estimated to be $234.5 billion by 2023, *i.e.,* an 160 %-increase compared with 2019 market[1]. This fast development is motivated by some social issues (*e.g.,* ageing of the population, need of health cost containment, desire for better care) and is supported by new effective mathematical models, combined with an increase in computing capacity. These last technical issues have been developed in the last decades and are now able to meet the needs of *in silico* medicine.

In silico medicine can be applied to a large variety of medical fields, with the development of specific numerical tools, which aim to reproduce real biological phenomena in a virtual environment. These technologies require the development of *in silico* models, which describe the biological functions of various organs or even the whole body, in considering interactions between the different physics involved. An *in silico* model becomes a digital twin of a real physical system, being updated in real time by data, on which tests can be performed, hypotheses can be tried, parameters can be changed to assess consequences, etc. Some of these models can be patient-specific. They can bring personalized information about the patient, difficult or even impossible to measure. Predictive information can also be provided, like prediction of future behavior. Both types of information are helpful for further clinical decisions and the use of such tools brings new opportunities.

We introduce here some examples of applications of *in silico* medicine.

- The development of new drugs is improved by numerical models [Bharath et al., 2011]. First, *in silico* models allow to reduce experimental testing during clinical trials, on both animals and people, satisfying the new legislation governing these tests[2]. Thus, performance, toxicity and side effects of new molecules can be tested upstream on models, leading to removal of some of them before any *in vivo* test, reducing the number of animals tested and decreasing the risk for patients volunteers in these clinical trials [Claude et al., 2009; Gleeson et al., 2012]. Moreover, *in silico* tests speed up pharmacological research by testing many more molecules or molecules combinations than with *in vivo* tests and then boost the discovery of new promising molecules [Ekins et al., 2007; Kazmi et al., 2019]. Whereas clinical trials are highly risky and last about a decade before launching in case of good outcome [Dickson and Gagnon, 2004], the use of *in silico* models results in a reduction of their duration, and, consequently, in a decrease of research costs and products prices [Michelson et al., 2006].

---

[1] Data from the Frost & Sullivan's analysis *Global Digital Health Outlook, 2020.* Website: https://ww2.frost.com/

[2] European Directive 2010/63/EU on the protection of animals used for scientific purposes, adopted on 22 September 2010

- The performance of surgical procedures starts to be tested by *in silico* models, following the process described in Figure 4. Surgical interventions can be simulated on patient-virtual specific models that take into account the physiological characteristics of the patients [Vy et al., 2016]. For instance, the impact on arterial deformation of a guidewire insertion during an endovascular repair can be computed using personalized geometries of arteries, in order to prepare and guide the intervention [Gindre et al., 2017]. From such models, several surgical strategies can be tested *in silico* to choose the most appropriate one for the patient and to evaluate the success of the intervention virtually, before carrying it out for real [Carniel et al., 2017, 2020]. As for cardiac resynchronization therapy, patient-specific models of the heart are able to predict the impact of pacing under different spatial conditions and then help choosing between them the best one for the patient [Sermesant et al., 2012]. Another application, very challenging as it requires real-time simulation, is the use of such models to assist the surgery during the intervention, in order to follow the patient state and assist clinicians to make decision [Marescaux et al., 1998; Khor et al., 2016]. Medical schools also make use of numerical models to avoid the use of cadavers to teach the anatomy or to train medicine students in difficult surgical procedures [Courtecuisse et al., 2014].

- Medical devices benefit from *in silico* medicine, from design and positioning to the prediction of *in vivo* behavior and durability. They become more and more personalized to the patient, making them more adapted, more efficient and less risky for the patient. Many medical devices are concerned. In the cardiovascular field, stents can be developed with a patient-specific geometry, adapted to the shape of the patient blood vessels, which is often impacted by the targeted disease like aneurysm [Perrin et al., 2016]. Different procedures for the deployment of transcatheter aortic valves can be simulated to investigate possible complications and to help clinicians in the valve selection [Bianchi et al., 2019]. Concerning other fields, the resistance to the fatigue of hip implants can be improved by the use of numerical models [Colic et al., 2016], the bone stress distribution caused by dental implants can be computed to determine indicators of bone overloading [Baggi et al., 2008] and a finite element model of stent-grafts allows to investigate the relationship between their design and their flexibility to prevent any complications [Demanget et al., 2012].

- Diagnosis is improved by numerical tools since algorithms run faster than human, reduce errors and can bring more information than available in the data. Artificial intelligence is the one of the main numerical tools when diagnosis is performed from images. Machine learning algorithms should often be first trained from truth data given by clinicians, then they can be used to detect diseases. These tools can be very helpful for clinicians as manual diagnosis from images is often tricky, biased as well as tedious. It can also bring quantitative information (*e.g.,* accurate morphological characteristics) in addition to the qualitative observations of clinicians [Topol, 2019; Tarando, 2018]. *In silico* models not only explore the direct measurement of biological quantities, but also compute other quantities of interest impossible to measure, like myocardium contractility to assess cardiac pathologies [Chabiniok et al., 2012] or material parameters of aneurismal aortic tissues to evaluate the probability of aneurysm rupture [Kim et al., 2012], which are not measurable *in vivo*. Estimation of these additional quantities can be performed through inverse problems, which minimize the difference between the data and the model with respect to these unknown quantities, weighed by the confidence in the model [Moireau et al., 2008; Avril et al., 2008]. The interaction between model and data is illustrated in Fig 5. Model-aided monitoring is also a new challenge, especially for cardiovascular monitoring of patients during critical cares. For instance, Le Gall et al. [2020] derive from patient-specific heart models the pressure-volume cardiac loop with the restricted available data. It brings additional information on the physiological state of the patient, useful for therapeutic strategies.

- Patient prognosis is regularly anticipated using predictive numerical models. Predicting the patient outcome can lead to better clinical decisions. Numerical models are developed, requiring a good understanding of the disease and the consideration of multiple factors which could have an impact on the prognosis (*e.g.,* physiological factors, environmental factors, etc). Then, determining these factors about the patient, the probability of experiencing a state (*e.g.,* curing of a disease, dying, ...) within a given time can be calculated. As an example, the prognosis of patients with a head injury can be estimated knowing the age of the patient, her/his country, the reaction of pupils to light, the severity of extra-cranial injury and a coma score [MRC CRASH Trial Collaborators, 2008]. Data assimilation is a collection of methods which allow to predict the future outcome of a system from real data, also called observations, and a dynamical model of the system. The model prediction is continuously corrected with new observations in time (with sequential approach), and leads to a better determination of the previous states of the system (mostly variational approach). In particular, this last approach makes it possible to find the initial conditions of the system, which are often not fully known when considering systems as complex as biological systems. Such methods have already proved their worth in meteorology [Ghil and Malanotte-Rizzoli, 1991] and tend to be applied in biomechanics, both for diagnosis and prognosis issues [Moireau, 2008].

This list of examples is non-exhaustive but gives a good view of what can be performed with such numerical tools. However, most of the mentioned works are still at the research stage and only proofs of concept have been shown. Many initiatives are being set up to connect these worldwide research works, like the Virtual Physiological Human (VPH). This European project aims to bring together all these fragmentary knowledges to build a predictive and personalized model of the whole body, ensuring a collaboration between research and clinic [Viceconti and Hunter, 2016]. Closer to industrial applications, the Living Heart Project (LHP), led by the Dassault Systems company, gathers researchers, clinicians and medical devices manufacturers to develop a patient-specific high-precision numerical model of the heart [Baillargeon et al., 2014]. The main goal is to achieve a fast translation from the innovative tools to an increasing quality of healthcare. Finally, in addition to large companies in the health sector, like General Electric Healthcare, Air Liquide Healthcare, Siemens Healthcare or Philips Healthcare, many startups have been created to tackle health issues. For instance, Predisurge develops numerical models to better design and implant cardiovascular medical devices, like stent-grafts, and Ebenbuild creates a digital twin of patient lung for precision therapy of patients suffering from Acute Respiratory Distress Syndrome (ARDS). In France, the Healthtech is the first sector represented among the program *French Tech 2020*, a selection of the most promising French startups, concerning about 20 % of them.

In silico technologies still need to be improved, to consider the whole complexity of the biological environment and to be employed in a day-to-day protocol by clinicians. Some limitations to their use should also be removed. Numerical models need to be validated in order to bring a sufficient accuracy in predictions. Thus, models are often based on noisy data and the related uncertainty is propagated to the results. An uncertainty propagation analysis should be performed to ensure model quality [Lin et al., 2015]. *In silico* medicine

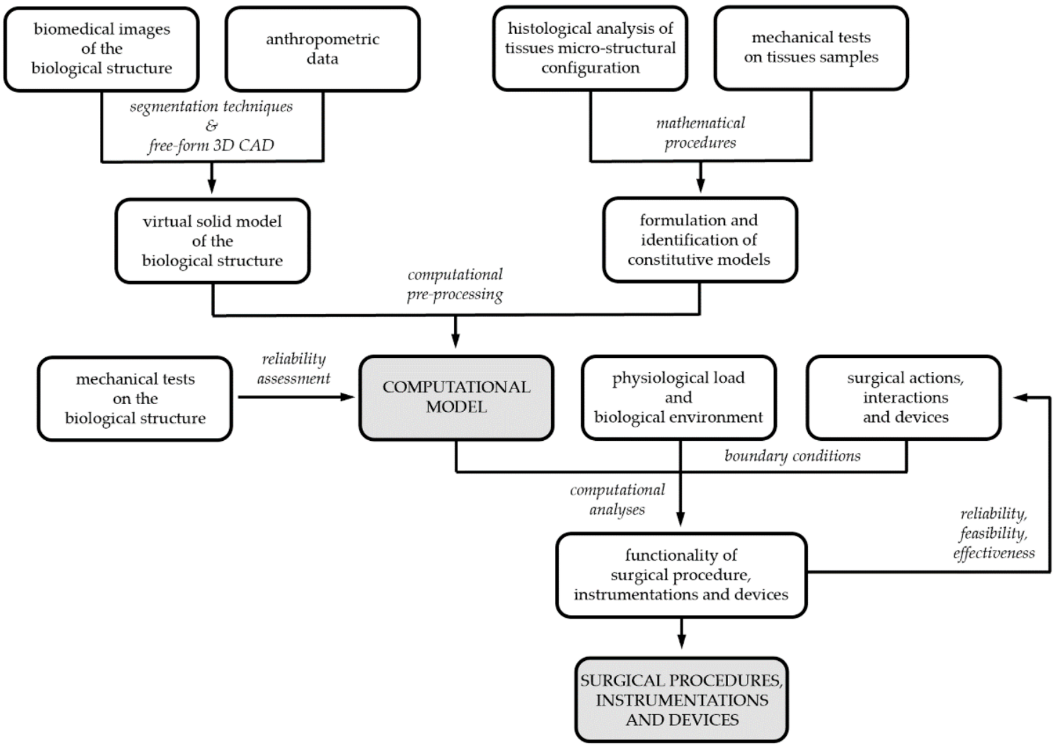

Figure 1 – Development of models to design, optimize and certify surgical procedures, instrumentations and devices. Figure taken from Carniel et al. [2020].

Figure 2 – Interaction between model and clinical data to address clinical questions. Figure taken from Chabiniok et al. [2016].

raises also privacy and security concerns. Patient data, as essential elements of patient-specific models, should be manipulated with a great care according to current laws, like the General Data Protection Regulation (GDPR) in the European Union. Moreover, the question of acceptance of these technologies by both clinicians and patients is key, as the former can be afraid to be replaced by computers whereas the latter can have difficulties to trust these "black boxes". *In silico* trials start to be taken into account by regulatory agencies, which shows that the situation is evolving.

Specific questions in pulmonology

All medical disciplines can benefit from these technical advances, as shown in the previous examples, and pulmonology is not an exception. A lot of questions can be answered with the use of numerical technologies: a better understanding of the pathophysiology and of the pulmonary function, as well as a better diagnosis and a better prognosis of pathologies, leading to treatment improvements. In pulmonology for example, oncology, drugs delivery and mechanical ventilation are some areas which could benefit from *in silico* models.

Lung cancer is treated by radiotherapy, which involves sending radiation to kill the cancer cells and stop them from multiplying. Preserving the healthy cells around the targeted cancer cells is crucial and delicate due to lung motion during breathing. Indeed, such motion induces cancer nodules displacements, making the radiation targeting difficult: each session of radiation lasts some minutes whereas an inhalation - exhalation cycle lasts some seconds. The beam direction should then be changed in order to follow the cancerous zone, as it would reach healthy zones in remaining in the same position. Finally, the main issue is to be able to predict nodule displacements during radiation session, even though the breathing depth is unstable and then nodule displacements uneven, in order to synchronize the radiation beam with the tumor motion [Seppenwoolde et al., 2002; Sonke et al., 2019]. Internal and external surrogates for tumor motion are investigated [Savanovic et al., 2020]. The radiation dose is also impacted by the uncertainty about reaching correctly the cancer zone: it is reduced to decrease the risks for the healthy zone, whereas it could be increased if the cancer zone is well reached for sure.

Concerning air flow inside lungs, drug delivery is a subject of interest for pulmonologists, to improve treatments of diseases like asthma or chronic obstructive pulmonary disease (COPD). They both need the inhalation of a bronchodilator to expand airways and improve the supply of oxygen. But this kind of treatment raises issues about particle transport in a complex, non-homogeneous pulmonary airway tree, about particle deposition on the targeted zone and about inhaler devices. Indeed, the respiratory tract has intrinsic defense properties to protect inner lung from foreign particles, like the cilia present on the airways surface to clear out such particles. Diseases can also make particle flow difficult, when airways are narrowed for example. Only 20 % of the dose delivered by the inhaler reaches the lungs [Borgström et al., 2006]. The interaction of particles with the targeted surface during the deposition should be also considered, since chemical interactions with surface layers, as mucus, surfactant or enzymes, can lead to degradation of particles as a consequence of immunological barriers. All these challenges should be considered during drug formulation and inhaler design to optimize the treatments [Newman, 2017; Ehrmann et al., 2020].

Whereas lung radiotherapy was concerning lung motion and drug delivery pulmonary airflows, the microstructure behavior is a major concern in anesthesia and critical care when using a ventilator for a patient. The mechanical ventilation with a ventilator is used for patients with an acute respiratory distress, under general anesthesia or in intensive care units. Air is provided to patient lungs with a certain amount of pressure, frequency and flux. Many parameters can be set on a ventilator and are very important for an adequate ventilation. A positive pressure is required to recruit alveoli, inflate lungs and then provide oxygen to the body. However, an excessive pressure can damage the microstructure of lungs, especially alveoli, and leads to what is called ventilator-induced lung injury (VILI). Mechanical ventilation is a compromise between a good oxygenation of the patient while protecting the pulmonary organ from injury. It could be helped by patient-specific models that would consider patient parameters, like the pathology but also the current physiological state, and that could optimize the mechanical ventilation during the process using the live response of the patient [Goligher et al., 2016]. The same principle for cardiovascular monitoring could be performed using heart biomechanical model as a perioperative tool to estimate new information, not measurable, but useful for clinicians [Le Gall et al., 2020].

COVID-19 Mechanical ventilation challenges have been echoed in the current events about COVID-19, since the new coronavirus can affect the lungs. Patients in a serious condition are placed under mechanical ventilation as they are under-oxygenated and are suffering from acute respiratory failure.

COVID-19 leads in some severe cases to pulmonary edema [Kuebler et al., 2020; Archer et al., 2020], characterized by the accumulation of fluid inside lungs, which restricts gas exchange in the alveoli and seems to impact lung compliance. The more fluid is present inside the lungs, the fewer alveoli are available for gas exchange, and the less oxygen is provided to the body, leading to a lack of oxygen. To improve lung compliance and then gas exchange, anesthetists have the possibility to change the patient position (supine or prone) and tune the pressures at both end-exhalation and end-inhalation. However, they do not know in advance the amount of compliance improvement for a specific setting or the best settings to apply. Consequently, they need to try several settings until finding the best one. Patient-specific models could help them to improve the ventilation process.

Another aspect of the disease concerns the long-term evolution of pulmonary lesions. A hypothesis of an evolution towards a fibrosing interstitial lung disease, which could affect 20 % to 30 % of severe cases, has been formulated [George et al., 2020; Spagnolo et al., 2020]. The data are still of the very early phase, however a fibroblastic multiplication with extracellular matrix deposition in clusters has been reported in some autopsies [Tian et al., 2020] and supports the hypothesis. The assumed evolution should be investigated since it could lead in the future to a public health problem due to a secondary respiratory disability.

Idiopathic Pulmonary Fibrosis Idiopathic Pulmonary Fibrosis (IPF) is a pulmonary pathology which is the trigger of this thesis subject and also its main application.

Description Idiopathic Pulmonary Fibrosis belongs to a group of about 200 pulmonary diseases called Interstitial Lung Diseases (ILD), which affect the lung interstitium, *i.e.,* the connective tissue around the alveoli extending around airways or blood vessels and in the visceral pleura. IPF is a chronic disease characterized by tissue scarring, caused by inflammation and leading to tissue thickening, as shown in Figure 6. As a consequence, gas exchanges in alveoli are less efficient and lungs are less compliant [Plantier et al., 2018]. The disease affects men older than 50 years old in a higher proportion [Lederer and Martinez, 2018]. The incidence is about 10 new patients per 100 000 people each year [Nalysnyk et al., 2012], which makes IPF a rare disease even though it is the most common one among the ILD.

Patients suffering from IPF present two main symptoms. The first one is a dyspnea, or breathlessness, which affects everyday life [Swigris, 2005] and becomes worse and worse with the disease evolution. The second one is a chronic cough.

The causes of IPF are unknown, as meant by “idiopathic”. However, some risks factors were identified like genetic or environmental factors. Smoking has also been shown to increase the risk [Sauleda et al., 2018]. Sex and age can also be considered as risk factors, as the incidence of the disease is higher for males above 50.

IPF diagnosis is difficult, since it requires to exclude the known causes of other ILD. It usually involves a combination of techniques [Poletti et al., 2013]. Pulmonary function tests allow to measure the rate of absorption of oxygen as well as the volume of inhaled air during breathing, which are both reduced in case of IPF. Another main tool is X-rays CT-scan, a medical imaging modality, used to visualize lung texture. Some patterns are typical of ILD like honeycombing or ground-glass opacities and play an important part in the diagnosis (see Fig 6). However, this technique cannot be used alone as it may not discriminate IPF against other ILD. Lung biopsy, consisting in sampling a small piece of lung tissue throughout a surgical operation, can also be performed [Hübner et al., 2008; Cavazza et al., 2010]. The histologic tissue is then observed under the microscope to highlight specific features of ILD, but again not exclusive to IPF. Finally, although difficult, an early diagnosis is necessary for an improved long-term outcome.

Whereas the diagnosis is difficult and may take a long time, the prognosis is ill-fated since the average life expectancy after diagnosis is within three-to-five years [Poletti et al., 2013]. The progression of the disease is characterized by a progressive decline of lung functions associated with the expansion of the affected fibrotic part of lungs. Some exacerbations, where the progression is faster, are observed, but remain unpredictable [King et al., 2011].

No treatment to cure the disease exists [Rogliani et al., 2016]. The drugs that are given to IPF patients, pirfenidone and nintedanib, only slow down the decline and prevent exacerbations, which consequently improves life expectancy [King et al., 2011]. Other drugs can also reduce symptoms, like cough. However, these two main drugs have important side effects and patient quality of life is reduced. Finally, the only solution is lung transplantation but it is not available for everyone since several criteria should be met and there is a waiting list for lung transplant.

Challenges IPF is poorly understood, poorly diagnosed and poorly treated. Thus, a better understanding, a better diagnosis and a better prognosis are the three main challenges for pulmonologists concerned with IPF.

However, some improvements are being made. Recently, a hypothesis was formulated about the mechanism of the disease evolution [Liu et al., 2010; Hinz and Suki, 2016; Haak et al., 2018; Wu et al., 2019]. It is supposed that a vicious circle is in place in IPF, where the fibrosis leads to more fibrosis. Indeed, pulmonary fibrosis induces a stiffer scarring tissue by the formation of collagen fibers. During breathing, this stiffer tissue undergoes higher stresses, stimulating fibroblasts, which then produce more collagen fibers and more fibrosis, and so on. This vicious circle, where mechanics plays a major role, should be further studied and validated, but could significantly improve disease understanding.

All these questions could be tackled by models, especially *in silico* models. They could be used to study the hypothesis of the mechanical vicious circle and to improve diagnosis by bringing new information in combining existing tools. Prognosis would also be improved by a better knowledge of the disease and the impact of drugs could be studied through models.

These questions are also those that raised this PhD subject. Having identified them, clinicians and radiologists from the Avicenne APHP Hospital, Bobigny, France, experts in

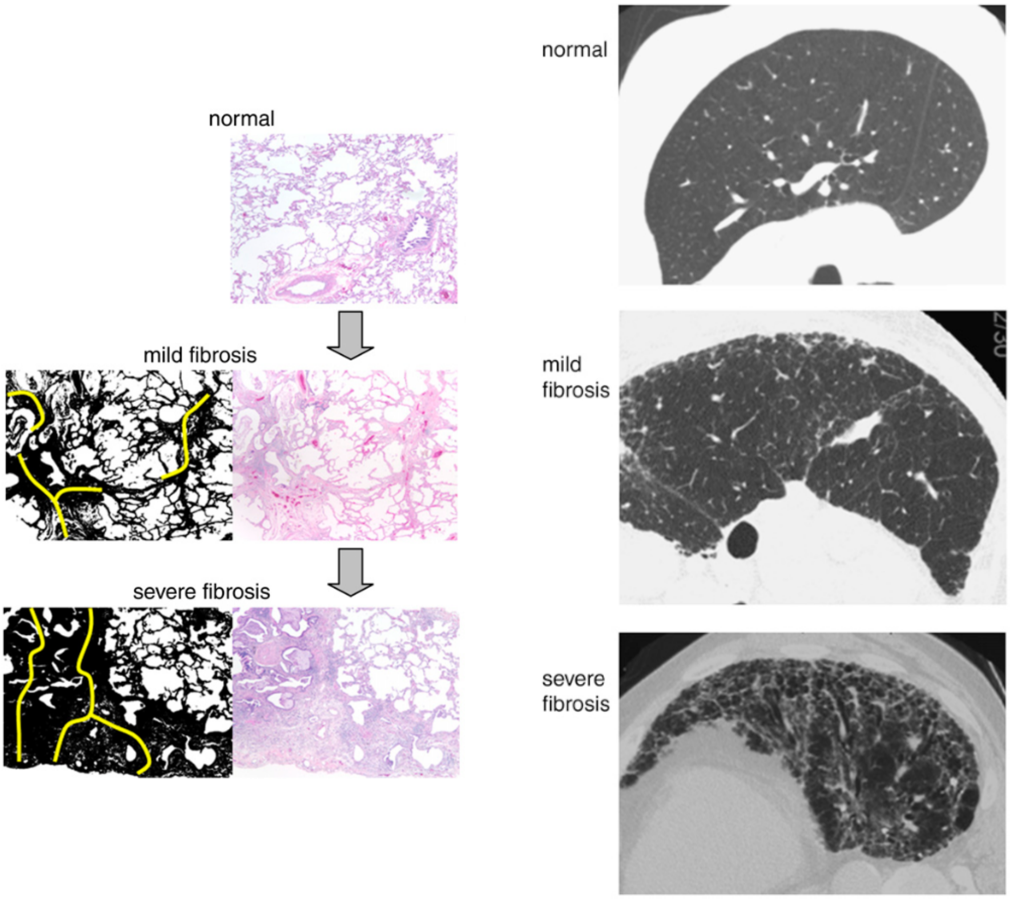

Figure 3 – Illustrations of the IPF impact on lung microstructure. (Left) Lung biopsy sections. (Right) High-resolution computed tomography scan images. Figure taken from Bates et al. [2007].

ILD, contacted the MΞDISIM team to ask for help to understand the role of mechanics in the development of IPF. That is how the collaboration, and especially this PhD, about the use of computational mechanics for IPF applications, started.

Lung modeling

Lung modeling aims to address the previously mentioned pulmonary clinical applications. We focus here on physical models, without considering all the numerical tools relative to data and statistical analysis like Artificial Intelligence.

Lungs are complex organs, by their composition of three phases (air, blood and solid tissue), which can interact with each other, by their microstructure, evolving during breathing, and their environment. Lung modeling is also challenging as it can involve a large diversity of physical phenomena. Moreover, several scales – time scale or space scale – can be considered, depending on the type of phenomena studied and at which scale it occurs. Breathing is a short time scale compared to the long time scale of pathological remodeling, and the alveolar space scale is a microscale which is linked to the pulmonary microstructure in contrast to the organ macroscale. Finally, multiscale, multiphysics and multiphase aspects should be taken into account for lung modeling [Burrowes et al., 2008]. Lungs can be described by various fields, like fluid mechanics, fluid-structure interactions, solid mechanics, poromechanics, chemistry, etc. A model cannot take into account every field and modeling choices should be made according to the targeted goal. Indeed, the more complex the model is, the longer the computation time is and the most difficult the calibration is.

We focus here on mechanics, more specifically fluid mechanics and solid mechanics, which can be described independently, but also coupled [Cazeaux and Grandmont, 2015; Berger et al., 2016], increasing models complexity and computation time.

Pulmonary fluid mechanics Fluid mechanics allows to study airflow inside the lungs. Models are built either in one dimension or can consider the complexity of airways geometry and of airflow characteristics (velocity, turbulence [Lin et al., 2007], compressibility, etc) using Computational Fluid Dynamics (CFD) simulations in three dimensions [Lin et al., 2013]. Airways geometries can be generic [Mauroy et al., 2003], but medical imaging techniques improvements make it possible to get patient-specific geometry for the respiratory tract [Tawhai et al., 2004; Fetita et al., 2004]. Statistical models are also developed to take into a account the geometry variability between people [Koblinger and Hofmann, 1990].

These 3D models allow to describe airflow in diseased lungs as those suffering from asthma, by taking into account the diameter change of inflamed airways which impacts their resistance, as well as the type of airflow, laminar or turbulent [Martonen et al., 2003; Tgavalekos et al., 2005]. Once the airflow is modeled, the study of particles transport with airflow and their deposition into the 3D section of airways [Hofmann and Koblinger, 1990; Annapragada and Mishchiy, 2007; Lambert et al., 2011; Boudin et al., 2015] could also be modeled, with particles defined either in a discrete [Oakes et al., 2014] or a continuous description [Chen et al., 2006]. Local information about drugs deposition, not available with global 1D models, are given with such 3D models [Longest and Holbrook, 2012].

While the first airways are the place of convection phenomena, the peripheral airways are the location of diffusion. Gas exchange occurs then at a smaller scale, the alveolar scale, at the end of peripheral airways. This is why alveoli geometry with the last peripheral airways geometry is used to describe O_2 diffusion across the barrier between air and blood [Weibel et al., 2005]. The key parameter in such a modeling is the partial pressure in O_2 in airways and in blood vessels.

Pulmonary solid mechanics When it comes studying lung deformation during breathing, another type of physics is used. Solid mechanics gives information about kinematics, which describes how the lungs deform throughout the breathing cycle and quantifies displacements and deformations. Kinematics can be computed from images with image registration tools [Hurtado et al., 2016; Vishnevskiy et al., 2017]. Radiotherapy applications use such information, however additional mechanical information like dynamics, the study of forces and stresses, are really important in other applications, like mechanical ventilation or IPF study. Interactions between the lungs and their surroundings are modeled by forces, which provides insight into lungs behavior. Stresses are linked to deformation with the constitutive behavior of the material, which is one of the crucial ingredients in lung mechanical modeling. The constitutive behavior can be considered homogeneous or heterogeneous to model lung pathologies impacting mechanics and can include several parameters characterizing the pulmonary tissue, like elasticity, viscosity, isotropy, etc.

Solid mechanical models can use mathematical [West and Matthews, 1972; Denny and Schroter, 2006], generic [Gefen et al., 1999] or patient-specific geometry [Tawhai et al., 2009] at any spatial scale. Patient-specific geometries are more complex and require a more powerful computing capability. However, they allow to build patient-specific predictive models.

From their complex microstructure, lungs have multiscale properties, which is important in lung mechanical modeling. As well as fluid dynamics models, solid mechanics models can consider various scales to describe the microstructure, from the organ scale to the alveolar scale [Rausch et al., 2011; Concha et al., 2018]. The alveolar scale is more appropriate to describe the impact of ventilation on alveolar structures, as it allows to quantify stresses and strains in the alveolar wall. New elements, like surfactant or collagen fibers, can be included in such models. Both scales can be linked with homogenization procedures [Wiechert and Wall, 2010] to study the impact at the organ scale of parameters describing the microscale or to describe some organ parameters by microscale models [Lauzon et al., 2012].

The lung material is also multiphase, since lungs are composed of several phases, solid tissue, air and blood mainly. Poromechanics, which is the mechanics of porous media, is then relevant to describe porous pulmonary tissue by considering its porosity. Poromechanical theories have already been largely used in geosciences for rocks and soils studies [Biot and Temple, 1972; Coussy, 2004; Dormieux et al., 2006] and was then introduced in biomechanics [Mow et al., 1980; Simon et al., 1985; Chapelle and Moireau, 2014]. The mixture theory considers the superposition of each phase at any point of the porous media, with specific physics and coupling between them. Compared to homogenization approaches, poromechanics has several advantages. No complex microstructure is assumed, using the porosity as the result of the homogenized microstructure instead, which saves computation time. A microstructure can also be assumed afterwards to zoom back to the microscale. Moreover, the effective mechanical behavior can be derived from experimental tests, which is more difficult for the behavior of the solid part required in multiscale approaches.

Among all these kinds of models which can be built to describe lungs, we chose to work in this PhD with poromechanical tools. Indeed, poromechanics is a main competence of MΞDISIM team, which previously developed a poromechanical theory for biomechanics [Chapelle and Moireau, 2014] and already applied it in cardiac perfusion models [Burtschell, 2016].

Objectives: from theory to clinical applications

The goal of this work is to develop a lung model in order to address clinical challenges raised by the pulmonary disease defined as Idiopathic Pulmonary Fibrosis. As mechanics seems to be critical in this disease, both by its impact on the physiology of the diseased lungs and by its role in the disease evolution, the developed model is a mechanical model, and more precisely, a poromechanical model, to consider lungs porosity. In order to use the model for personalized diagnosis and prognosis, the model should be patient-specific and patient data are needed to do so. Thus, biomedical images, acquired by the Avicenne APHP hospital, Bobigny, are used to personalize the different elements of the model.

The three main objectives of this thesis are the following:

Objective 1 - Build a pulmonary model in a poromechanical framework.
The starting point to build the pulmonary model is the general poromechanical formulation of Chapelle and Moireau [2014]. The goal is to adapt it to the pulmonary configuration by proposing specific assumptions. In addition, all the elements of a mechanical model should be defined, mainly the geometry, the constitutive behavior and boundary conditions, in order to describe the breathing process. It requires a good understanding of the breathing physiology.

Objective 2 - Personalize the model to patient with data.

Once the general pulmonary model is built, a personalization pipeline using patient data needs to be designed to make the model patient-specific. Ideally, all the elements of the model should be personalized to get the most physiological digital twin. A first goal is to determine which type of data are required to personalize the model and which type of data clinicians have the possibility to acquire on patients. This step requires a close interaction with clinicians. Then, knowing the available data, they should be exploited to get the needed information: specific geometries require image processing tools or a specific constitutive law involves mathematical optimization procedures.

Objective 3 - Build mechanical biomarkers to answer clinical questions about fibrosis.

Finally, the personalized model should be fully exploited to answer the clinical questions raised by clinicians about IPF. The mechanical model can investigate mechanical effects of the disease on lungs and bring local information about compliance to supplement the global information already acquired by clinicians, which could help the diagnosis of the disease. The hypothesis of a mechanical vicious circle can also be explored by examining the impact of IPF on stresses and strains in lungs.

Structure and contributions

This thesis is organized into three chapters. Their contents and their main contributions are presented here.

Chapter 1 - From pulmonary physiology to lung mechanical modeling

In the first chapter, we present the main elements of pulmonary physiology required for a good understanding of lung mechanical modeling. Lung function and anatomy are described, as well as breathing mechanisms. Various ways to evaluate lung function are also mentioned. Then, we refer to these elements of physiology to relate them to lung modeling. Various types of mechanical models are reviewed: organ scale models, with discussions about the choice of boundary conditions and constitutive behavior, and multiscale models. Finally, poromechanics is introduced, especially the general model on which this work, mainly the following chapters, is based.

Chapter 2 - A poromechanical model of the lungs

In the second chapter, we address the first objective of this thesis in building a pulmonary poromechanical model at the organ scale and at the breathing scale. Based on the poromechanical framework of Chapelle and Moireau [2014], pulmonary-specific hypotheses are formulated. Then, all the elements of a mechanical model are incorporated. A constitutive behavior is designed to consider the non-linearity of the volume behavior of lungs with pressure. Boundary conditions using contact and taking into account the breathing type (spontaneous or mechanical) are defined. A specific problem in biomechanics is solved to estimate the unloaded configuration of the lungs. Finally, a specific problem to poromechanics in large deformation, which is to constrain the porosity to be positive, is addressed and two solutions are proposed. At the end, several illustrations of the model are proposed by studying the impact of different choices made in the model, like the constitutive behavior (compliance, porosity energy) and boundary conditions (contact properties, gravity, pressure).

This chapter takes the form of a pre-print article co-authored by Cécile Patte, Martin Genet and Dominique Chapelle, entitled *A poromechanical model of the lungs.*

Chapter 3 - Estimation of regional pulmonary compliance in IPF based on lung poromechanical modeling

In the third chapter, we first present the personalization pipeline developed for the model, which corresponds to the second objective. Data used are 3D CT-scans of patients; pressure data would have also been needed to complete a more advanced personalization, but there was no way to acquire such data on the considered patients. Images are then used to personalize geometries with segmentation tools and porosity, as well as to differentiate the healthy and diseased regions and to estimate the compliance. This last step is formulated as an optimization problem to minimize the difference in breathing motion between model and data. Two cost-functions, exploiting images in two different ways, are investigated.

Results are then obtained from patients suffering from IPF. On the one hand, the performance of the personalization pipeline is investigated by comparing both cost-functions, the use of two regions and the use of absolute versus effective compliances. On the other hand, relevant quantities are determined and analyzed, handling with the third objective. Regional compliances are estimated in both healthy and diseased regions, allowing to quantify the IPF-induced tissue stiffening. Correlations between compliance ratio and disease-induced decline are also explored and the impact of IPF on stresses is investigated.

This chapter takes the form of a pre-print article co-authored by Cécile Patte, Pierre-Yves Brillet, Catalin Fetita, Thomas Gille, Jean-Francois Bernaudin, Hilario Nunes, Dominique Chapelle and Martin Genet, entitled *Estimation of regional pulmonary compliance in IPF based on lung poromechanical modeling.*

Communications

This work was presented in several conferences in the form of oral presentations and led to two pre-print articles. These different contributions are listed in chronological order.

Oral presentations

- **Oral presentation at "14ème Colloque National en Calcul des Structures" (CSMA 2019).**
  Giens, France - May 13-17, 2019.

- **Oral presentation at the Symposium Jean Mandel 2020.**
  Ecole Polytechnique, Palaiseau, France - June 18-19, 2020.

- **Oral presentation at the VPH 2020 conference.**
  France (online) - August 25-28, 2020.

Publications

Conference papers

- **Mécanique pulmonaire personnalisée : modélisation et estimation – Application à la fibrose pulmonaire [Patte et al., 2019].**
  C. Patte, M. Genet, C. Fetita, P.-Y. Brillet and D. Chapelle.
  14ème Colloque National en Calcul des Structures, May 2019, Giens, France.

- **Personalized Pulmonary Poromechanics [Genet et al., 2020a].**
  M. Genet, C. Patte and D. Chapelle.
  14th World Congress on Computational Mechanics (WCCM), 2020, Paris, France.

- **Estimation of patient-specific mechanical parameters in pulmonary diseases [Patte et al., 2020].**
  C. Patte, P.-Y. Brillet, C. Fetita, T. Gille, J.-F. Bernaudin, H. Nunes, D. Chapelle and M. Genet.
  VPH2020 conference, Aug 2020, Paris, France.

- **Personalized Pulmonary Poromechanics [Genet et al., 2020b].**
  M. Genet, C. Patte, C. Fetita, P.-Y. Brillet and D. Chapelle.
  45ème Congrès de la Société de Biomécanique (SB), Oct 2020, Metz, France.

Journal articles

- **A poromechanical model of the lungs.**
  C. Patte, M. Genet and D. Chapelle.
  Pre-print, to be submitted in October 2020 in *Annals of Biomedical Engineering.*

- **Estimation of regional pulmonary compliance in IPF based on lung poromechanical modeling.**
  C. Patte, P.-Y. Brillet, C. Fetita, T. Gille, J.-F. Bernaudin, H. Nunes, D. Chapelle and M. Genet.
  Pre-print.

Bibliography

Annapragada, A. and Mishchiy, N. (2007). In silico modeling of aerosol deposition in lungs. *Drug Discovery Today: Disease Models*, 4(3):155–161.

Archer, S. L., Sharp, W. W., and Weir, E. K. (2020). Differentiating COVID-19 Pneumonia From Acute Respiratory Distress Syndrome and High Altitude Pulmonary Edema: Therapeutic Implications. *Circulation*, 142(2):101–104.

Avril, S., Bonnet, M., Bretelle, A.-S., Grédiac, M., Hild, F., Ienny, P., Latourte, F., Lemosse, D., Pagano, S., Pagnacco, E., and Pierron, F. (2008). Overview of Identification Methods of Mechanical Parameters Based on Full-field Measurements. *Experimental Mechanics*, 48(4):381–402.

Baggi, L., Cappelloni, I., Maceri, F., and Vairo, G. (2008). Stress-based performance evaluation of osseointegrated dental implants by finite-element simulation. *Simulation Modelling Practice and Theory*, 16(8):971–987.

Baillargeon, B., Rebelo, N., Fox, D. D., Taylor, R. L., and Kuhl, E. (2014). The Living Heart Project: A robust and integrative simulator for human heart function. *European Journal of Mechanics - A/Solids*, 48:38–47.

Bates, J. H. T., Davis, G. S., Majumdar, A., Butnor, K. J., and Suki, B. (2007). Linking Parenchymal Disease Progression to Changes in Lung Mechanical Function by Percolation. *American Journal of Respiratory and Critical Care Medicine*, 176(6):617–623.

Berger, L., Bordas, R., Burrowes, K., Grau, V., Tavener, S., and Kay, D. (2016). A poroelastic model coupled to a fluid network with applications in lung modelling: A poroelastic model coupled to a fluid network with applications in lung modelling. *International Journal for Numerical Methods in Biomedical Engineering*, 32(1).

Bharath, E. N., Manjula, S. N., and Vijaychand, A. (2011). In silico drug design-tool for overcoming the innovation deficit in the drug discovery process. 3(2).

Bianchi, M., Marom, G., Ghosh, R. P., Rotman, O. M., Parikh, P., Gruberg, L., and Bluestein, D. (2019). Patient-specific simulation of transcatheter aortic valve replacement: Impact of deployment options on paravalvular leakage. *Biomechanics and Modeling in Mechanobiology*, 18(2):435–451.

Biot, M. A. and Temple, G. (1972). Theory of Finite Deformations of Porous Solids. *Indiana University Mathematics Journal*, 21(7):597–620.

Borgström, L., Olsson, B., and Thorsson, L. (2006). Degree of Throat Deposition Can Explain the Variability in Lung Deposition of Inhaled Drugs. *Journal of Aerosol Medicine*, 19(4):473–483.

Boudin, L., Grandmont, C., Lorz, A., and Moussa, A. (2015). Modelling and Numerics for Respiratory Aerosols. *Communications in Computational Physics*, 18(3):723–756.

Burrowes, K., Swan, A., Warren, N., and Tawhai, M. (2008). Towards a virtual lung: Multiscale, multi-physics modelling of the pulmonary system. *Philosophical Transactions of the Royal Society A: Mathematical, Physical and Engineering Sciences*, 366(1879):3247–3263.

Burtschell, B. (2016). *Mechanical Modeling and Numerical Methods for Poromechanics: Application to Myocardium Perfusion.* PhD thesis.

Carniel, E. L., Frigo, A., Fontanella, C. G., De Benedictis, G. M., Rubini, A., Barp, L., Pluchino, G., Sabbadini, B., and Polese, L. (2017). A biomechanical approach to the analysis of methods and procedures of bariatric surgery. *Journal of Biomechanics*, 56:32–41.

Carniel, E. L., Toniolo, I., and Fontanella, C. G. (2020). Computational Biomechanics: In-Silico Tools for the Investigation of Surgical Procedures and Devices. *Bioengineering*, 7(2):48.

Cavazza, A., Rossi, G., Carbonelli, C., Spaggiari, L., Paci, M., and Roggeri, A. (2010). The role of histology in idiopathic pulmonary fibrosis: An update. *Respiratory Medicine*, 104:S11–S22.

Cazeaux, P. and Grandmont, C. (2015). Homogenization of a multiscale viscoelastic model with nonlocal damping, application to the human lungs. *Mathematical Models and Methods in Applied Sciences*, 25(06):1125–1177.

Chabiniok, R., Moireau, P., Lesault, P.-F., Rahmouni, A., Deux, J.-F., and Chapelle, D. (2012). Estimation of tissue contractility from cardiac cine-MRI using a biomechanical heart model. *Biomechanics and Modeling in Mechanobiology*, 11(5):609–630.

Chabiniok, R., Wang, V. Y., Hadjicharalambous, M., Asner, L., Lee, J., Sermesant, M., Kuhl, E., Young, A. A., Moireau, P., Nash, M. P., Chapelle, D., and Nordsletten,

D. A. (2016). Multiphysics and multiscale modelling, data–model fusion and integration of organ physiology in the clinic: Ventricular cardiac mechanics. *Interface Focus*, 6(2):20150083.

Chapelle, D. and Moireau, P. (2014). General coupling of porous flows and hyperelastic formulations—From thermodynamics principles to energy balance and compatible time schemes. *European Journal of Mechanics - B/Fluids*, 46:82–96.

Chen, F., Yu, S. C., and Lai, A. C. (2006). Modeling particle distribution and deposition in indoor environments with a new drift–flux model. *Atmospheric Environment*, 40(2):357–367.

Claude, N., Goldfain-Blanc, F., and Guillouzo, A. (2009). La place des méthodes *in silico, in vitro, in omic* dans l'évaluation de la sécurité des médicaments. *médecine/sciences*, 25(1):105–110.

Colic, K., Sedmak, A., Grbovic, A., Burzić, M., Hloch, S., and Sedmak, S. (2016). Numerical Simulation of Fatigue Crack Growth in Hip Implants. *Procedia Engineering*, 149:229–235.

Concha, F., Sarabia-Vallejos, M., and Hurtado, D. E. (2018). Micromechanical model of lung parenchyma hyperelasticity. *Journal of the Mechanics and Physics of Solids*, 112:126–144.

Courtecuisse, H., Allard, J., Kerfriden, P., Bordas, S. P., Cotin, S., and Duriez, C. (2014). Real-time simulation of contact and cutting of heterogeneous soft-tissues. *Medical Image Analysis*, 18(2):394–410.

Coussy, O. (2004). *Poromechanics*. Wiley, Chichester.

Demanget, N., Avril, S., Badel, P., Orgéas, L., Geindreau, C., Albertini, J.-N., and Favre, J.-P. (2012). Computational comparison of the bending behavior of aortic stent-grafts. *Journal of the Mechanical Behavior of Biomedical Materials*, 5(1):272–282.

Denny, E. and Schroter, R. (2006). A model of non-uniform lung parenchyma distortion. *Journal of Biomechanics*, 39(4):652–663.

Dickson, M. and Gagnon, J.-P. (2004). The cost of new drug discovery and development. *Discovery Medicine*, 4(22):172–179.

Dormieux, L., Kondo, D., and Ulm, F.-J. (2006). *Microporomechanics*. John Wiley & Sons, Chichester, West Sussex, England ; Hoboken, NJ.

Ehrmann, S., Schmid, O., Darquenne, C., Rothen-Rutishauser, B., Sznitman, J., Yang, L., Barosova, H., Vecellio, L., Mitchell, J., and Heuze-Vourc'h, N. (2020). Innovative preclinical models for pulmonary drug delivery research. *Expert Opinion on Drug Delivery*, 17(4):463–478.

Ekins, S., Mestres, J., and Testa, B. (2007). *In Silico* pharmacology for drug discovery: Applications to targets and beyond. *British Journal of Pharmacology*, 152(1):21–37.

Fetita, C., Preteux, F., Beigelman-Aubry, C., and Grenier, P. (2004). Pulmonary Airways: 3-D Reconstruction From Multislice CT and Clinical Investigation. *IEEE Transactions on Medical Imaging*, 23(11):1353–1364.

Gefen, A., Elad, D., and Shiner, R. (1999). Analysis of stress distribution in the alveolar septa of normal and simulated emphysematic lungs. *Journal of Biomechanics*, 32(9):891–897.

Genet, M., Patte, C., and Chapelle, D. (2020a). Personalized Pulmonary Poromechanics. *14th World Congress on Computational Mechanics (WCCM)*.

Genet, M., Patte, C., and Fetita, C. (2020b). Personalized Pulmonary Poromechanics. *45ème Congrès de la Société de Biomécanique*.

George, P. M., Wells, A. U., and Jenkins, R. G. (2020). Pulmonary fibrosis and COVID-19: The potential role for antifibrotic therapy. *The Lancet Respiratory Medicine*, 8(8):807–815.

Ghil, M. and Malanotte-Rizzoli, P. (1991). Data Assimilation in Meteorology and Oceanography. In *Advances in Geophysics*, volume 33, pages 141–266. Elsevier.

Gindre, J., Bel-Brunon, A., Rochette, M., Lucas, A., Kaladji, A., Haigron, P., and Combescure, A. (2017). Patient-Specific Finite-Element Simulation of the Insertion of Guidewire During an EVAR Procedure: Guidewire Position Prediction Validation on 28 Cases. *IEEE Transactions on Biomedical Engineering*, 64(5):1057–1066.

Gleeson, M. P., Modi, S., Bender, A., L. Marchese Robinson, R., Kirchmair, J., Promkatkaew, M., Hannongbua, S., and C. Glen, R. (2012). The Challenges Involved in Modeling Toxicity Data In Silico: A Review. *Current Drug Metabolism*, 18(9):1266–1291.

Goligher, E. C., Ferguson, N. D., and Brochard, L. J. (2016). Clinical challenges in mechanical ventilation. *The Lancet*, 387(10030):1856–1866.

Haak, A. J., Tan, Q., and Tschumperlin, D. J. (2018). Matrix biomechanics and dynamics in pulmonary fibrosis. *Matrix Biology*, 73:64–76.

Hinz, B. and Suki, B. (2016). Does Breathing Amplify Fibrosis? *American Journal of Respiratory and Critical Care Medicine*, 194(1):9–11.

Hofmann, W. and Koblinger, L. (1990). Monte Carlo modeling of aerosol deposition in human lungs. Part II: Deposition fractions and their sensitivity to parameter variations. *Journal of Aerosol Science*, 21(5):675–688.

Hübner, R.-H., Gitter, W., Eddine El Mokhtari, N., Mathiak, M., Both, M., Bolte, H., Freitag-Wolf, S., and Bewig, B. (2008). Standardized quantification of pulmonary fibrosis in histological samples. *BioTechniques*, 44(4):507–517.

Hurtado, D. E., Villarroel, N., Retamal, J., Bugedo, G., and Bruhn, A. (2016). Improving the Accuracy of Registration-Based Biomechanical Analysis: A Finite Element Approach to Lung Regional Strain Quantification. *IEEE Transactions on Medical Imaging*, 35(2):580–588.

Kazmi, S. R., Jun, R., Yu, M.-S., Jung, C., and Na, D. (2019). In silico approaches and tools for the prediction of drug metabolism and fate: A review. *Computers in Biology and Medicine*, 106:54–64.

Khor, W. S., Baker, B., Amin, K., Chan, A., Patel, K., and Wong, J. (2016). Augmented and virtual reality in surgery—the digital surgical environment: Applications, limitations and legal pitfalls. *Annals of Translational Medicine*, 4(23):454–454.

Kim, J.-H., Avril, S., Duprey, A., and Favre, J.-P. (2012). Experimental characterization of rupture in human aortic aneurysms using a full-field measurement technique. *Biomechanics and Modeling in Mechanobiology*, 11(6):841–853.

King, T. E., Pardo, A., and Selman, M. (2011). Idiopathic pulmonary fibrosis. *The Lancet*, 378(9807):1949–1961.

Koblinger, L. and Hofmann, W. (1990). Monte Carlo modeling of aerosol deposition in human lungs. Part I: Simulation of particle transport in a stochastic lung structure. *Journal of Aerosol Science*, 21(5):661–674.

Kuebler, W. M., Jordt, S.-E., and Liedtke, W. B. (2020). Urgent reconsideration of lung edema as a preventable outcome in COVID-19: Inhibition of TRPV4 represents a promising and feasible approach. *American Journal of Physiology-Lung Cellular and Molecular Physiology*, 318(6):L1239–L1243.

Lambert, A. R., O'shaughnessy, P. T., Tawhai, M. H., Hoffman, E. A., and Lin, C.-L. (2011). Regional Deposition of Particles in an Image-Based Airway Model: Large-Eddy Simulation and Left-Right Lung Ventilation Asymmetry. *Aerosol Science and Technology*, 45(1):11–25.

Lauzon, A.-M., Bates, J. H. T., Donovan, G., Tawhai, M., Sneyd, J., and Sanderson, M. J. (2012). A Multi-Scale Approach to Airway Hyperresponsiveness: From Molecule to Organ. *Frontiers in Physiology*, 3.

Le Gall, A., Vallée, F., Pushparajah, K., Hussain, T., Mebazaa, A., Chapelle, D., Gayat, É., and Chabiniok, R. (2020). Monitoring of cardiovascular physiology augmented by a patient-specific biomechanical model during general anesthesia. A proof of concept study. *PLOS ONE*, 15(5).

Lederer, D. J. and Martinez, F. J. (2018). Idiopathic Pulmonary Fibrosis. *New England Journal of Medicine*, 378(19):1811–1823.

Lim, K. Y. H., Zheng, P., and Chen, C.-H. (2020). A state-of-the-art survey of Digital Twin: Techniques, engineering product lifecycle management and business innovation perspectives. *Journal of Intelligent Manufacturing*, 31(6):1313–1337.

Lin, C.-L., Tawhai, M. H., and Hoffman, E. A. (2013). Multiscale image-based modeling and simulation of gas flow and particle transport in the human lungs: Gas flow and particle transport in the human lungs. *Wiley Interdisciplinary Reviews: Systems Biology and Medicine*, 5(5):643–655.

Lin, C.-L., Tawhai, M. H., McLennan, G., and Hoffman, E. A. (2007). Characteristics of the turbulent laryngeal jet and its effect on airflow in the human intra-thoracic airways. *Respiratory Physiology & Neurobiology*, 157(2-3):295–309.

Lin, X., Zong, Z., and Niu, J. (2015). Finite element model validation of bridge based on structural health monitoring—Part II: Uncertainty propagation and model validation. *Journal of Traffic and Transportation Engineering (English Edition)*, 2(4):279–289.

Liu, F., Mih, J. D., Shea, B. S., Kho, A. T., Sharif, A. S., Tager, A. M., and Tschumperlin, D. J. (2010). Feedback amplification of fibrosis through matrix stiffening and COX-2 suppression. *The Journal of Cell Biology*, 190(4):693–706.

Longest, P. W. and Holbrook, L. T. (2012). In silico models of aerosol delivery to the respiratory tract — Development and applications. *Advanced Drug Delivery Reviews*, 64(4):296–311.

Marescaux, J., Clément, J.-M., Tassetti, V., Koehl, C., Cotin, S., Russier, Y., Mutter, D., Delingette, H., and Ayache, N. (1998). Virtual Reality Applied to Hepatic Surgery Simulation: The Next Revolution:. *Annals of Surgery*, 228(5):627–634.

Martonen, T., Fleming, J., Schroeter, J., Conway, J., and Hwang, D. (2003). In silico modeling of asthmaq. *Advanced Drug Delivery Reviews*, 55(7):829–849.

Mauroy, B., Filoche, M., Andrade, J. S., and Sapoval, B. (2003). Interplay between Geometry and Flow Distribution in an Airway Tree. *Physical Review Letters*, 90(14):148101.

Michelson, S., Sehgal, A., and Friedrich, C. (2006). In silico prediction of clinical efficacy. *Current Opinion in Biotechnology*, 17(6):666–670.

Moireau, P. (2008). *Assimilation de Données Par Filtrage Pour Les Systèmes Hyperboliques Du Second Ordre - Applications à La Mécanique Cardiaque*. PhD thesis.

Moireau, P., Chapelle, D., and Tallec, P. L. (2008). Joint state and parameter estimation for distributed mechanical systems. *Computer Methods in Applied Mechanics and Engineering*, 197(6-8):659–677.

Mow, V. C., Kuei, S. C., Lai, W. M., and Armstrong, C. G. (1980). Biphasic Creep and Stress Relaxation of Articular Cartilage in Compression: Theory and Experiments. *Journal of Biomechanical Engineering*, 102(1):73–84.

MRC CRASH Trial Collaborators (2008). Predicting outcome after traumatic brain injury: Practical prognostic models based on large cohort of international patients. *BMJ*, 336(7641):425–429.

Nalysnyk, L., Cid-Ruzafa, J., Rotella, P., and Esser, D. (2012). Incidence and prevalence of idiopathic pulmonary fibrosis: Review of the literature. *European Respiratory Review*, 21(126):355–361.

Naseer, A., Jahangirian, M., and Stergioulas, L. (2008). Potential applications of simulation modelling techniques in healthcare: Lessons learned from aerospace & military. page 13.

Newman, S. P. (2017). Drug delivery to the lungs: Challenges and opportunities. *Therapeutic Delivery*, 8(8):647–661.

Oakes, J. M., Marsden, A. L., Grandmont, C., Shadden, S. C., Darquenne, C., and Vignon-Clementel, I. E. (2014). Airflow and Particle Deposition Simulations in Health and Emphysema: From In Vivo to In Silico Animal Experiments. *Annals of Biomedical Engineering*, 42(4):899–914.

Patte, C., Brillet, P.-Y., Fetita, C., Gille, T., Bernaudin, J.-F., Nunes, H., Chapelle, D., and Genet, M. (2020). Estimation of patient-specific mechanical parameters in pulmonary diseases. *VPH2020 conference.*

Patte, C., Genet, M., Fetita, C., Brillet, P.-Y., and Chapelle, D. (2019). Mécanique pulmonaire personnalisée: modélisation et estimation - Application à la fibrose pulmonaire. *14ème Colloque National en Calcul des Structures (CSMA2019).*

Perrin, D., Badel, P., Orgeas, L., Geindreau, C., rolland du Roscoat, S., Albertini, J.-N., and Avril, S. (2016). Patient-specific simulation of endovascular repair surgery with tortuous aneurysms requiring flexible stent-grafts. *Journal of the Mechanical Behavior of Biomedical Materials*, 63:86–99.

Plantier, L., Cazes, A., Dinh-Xuan, A.-T., Bancal, C., Marchand-Adam, S., and Crestani, B. (2018). Physiology of the lung in idiopathic pulmonary fibrosis. *European Respiratory Review*, 27(147):170062.

Poletti, V., Ravaglia, C., Buccioli, M., Tantalocco, P., Piciucchi, S., Dubini, A., Carloni, A., Chilosi, M., and Tomassetti, S. (2013). Idiopathic Pulmonary Fibrosis: Diagnosis and Prognostic Evaluation. *Respiration*, 86(1):5–12.

Rausch, S. M. K., Haberthür, D., Stampanoni, M., Schittny, J. C., and Wall, W. A. (2011). Local Strain Distribution in Real Three-Dimensional Alveolar Geometries. *Annals of Biomedical Engineering*, 39(11):2835–2843.

Rogliani, P., Calzetta, L., Cavalli, F., Matera, M. G., and Cazzola, M. (2016). Pirfenidone, nintedanib and N-acetylcysteine for the treatment of idiopathic pulmonary fibrosis: A systematic review and meta-analysis. *Pulmonary Pharmacology & Therapeutics*, 40:95–103.

Sauleda, J., Núñez, B., Sala, E., and Soriano, J. (2018). Idiopathic Pulmonary Fibrosis: Epidemiology, Natural History, Phenotypes. *Medical Sciences*, 6(4):110.

Savanovic, M., Strbac, B., Jaros, D., Cazic, D., Kolarevic, G., and Foulquier, J.-N. (2020). Assessment of Internal and External Surrogates for Lung Stereotactic Body Radiation Therapy. *Iranian Journal of Medical Physics*.

Seppenwoolde, Y., Shirato, H., Kitamura, K., Shimizu, S., van Herk, M., Lebesque, J. V., and Miyasaka, K. (2002). Precise and real-time measurement of 3D tumor motion in lung due to breathing and heartbeat, measured during radiotherapy. *International Journal of Radiation Oncology Biology Physics*, 53(4):822–834.

Sermesant, M., Chabiniok, R., Chinchapatnam, P., Mansi, T., Billet, F., Moireau, P., Peyrat, J., Wong, K., Relan, J., Rhode, K., Ginks, M., Lambiase, P., Delingette, H., Sorine, M., Rinaldi, C., Chapelle, D., Razavi, R., and Ayache, N. (2012). Patient-specific electromechanical models of the heart for the prediction of pacing acute effects in CRT: A preliminary clinical validation. *Medical Image Analysis*, 16(1):201–215.

Simon, B. R., Wu, J. S. S., Carlton, M. W., Kazarian, L. E., France, E. P., Evans, J. H., and Zienkiewicz, O. C. (1985). Poroelastic Dynamic Structural Models of Rhesus Spinal Motion Segments. *Spine*, 10(6):494–507.

Sonke, J.-J., Aznar, M., and Rasch, C. (2019). Adaptive Radiotherapy for Anatomical Changes. *Seminars in Radiation Oncology*, 29(3):245–257.

Spagnolo, P., Balestro, E., Aliberti, S., Cocconcelli, E., Biondini, D., Casa, G. D., Sverzellati, N., and Maher, T. M. (2020). Pulmonary fibrosis secondary to COVID-19: A call to arms? *The Lancet Respiratory Medicine*, 8(8):750–752.

Swigris, J. J. (2005). Health-related quality of life in patients with idiopathic pulmonary fibrosis: A systematic review. *Thorax*, 60(7):588–594.

Tarando, S. R. (2018). *Quantitative Follow-up of Pulmonary Diseases Using Deep Learning Models*. PhD thesis.

Tawhai, M. H., Hunter, P., Tschirren, J., Reinhardt, J., McLennan, G., and Hoffman, E. A. (2004). CT-based geometry analysis and finite element models of the human and ovine bronchial tree. *Journal of Applied Physiology*, 97(6):2310–2321.

Tawhai, M. H., Nash, M. P., Lin, C.-L., and Hoffman, E. A. (2009). Supine and prone differences in regional lung density and pleural pressure gradients in the human lung with constant shape. *Journal of Applied Physiology*, 107(3):912–920.

Tgavalekos, N. T., Tawhai, M., Harris, R. S., Mush, G., Vidal-Melo, M., Venegas, J. G., and Lutchen, K. R. (2005). Identifying airways responsible for heterogeneous ventilation and mechanical dysfunction in asthma: An image functional modeling approach. *Journal of Applied Physiology*, 99(6):2388–2397.

Tian, S., Xiong, Y., Liu, H., Niu, L., Guo, J., Liao, M., and Xiao, S.-Y. (2020). Pathological study of the 2019 novel coronavirus disease (COVID-19) through postmortem core biopsies. *Modern Pathology*, 33(6):1007–1014.

Topol, E. J. (2019). High-performance medicine: The convergence of human and artificial intelligence. *Nature Medicine*, 25(1):44–56.

Viceconti, M. and Hunter, P. (2016). The Virtual Physiological Human: Ten Years After. *Annual Review of Biomedical Engineering*, 18(1):103–123.

Vishnevskiy, V., Gass, T., Szekely, G., Tanner, C., and Goksel, O. (2017). Isotropic Total Variation Regularization of Displacements in Parametric Image Registration. *IEEE Transactions on Medical Imaging*, 36(2):385–395.

Vy, P., Auffret, V., Badel, P., Rochette, M., Le Breton, H., Haigron, P., and Avril, S. (2016). Review of patient-specific simulations of transcatheter aortic valve implantation. *International Journal of Advances in Engineering Sciences and Applied Mathematics*, 8(1):2–24.

Weibel, E. R., Sapoval, B., and Filoche, M. (2005). Design of peripheral airways for efficient gas exchange. *Respiratory Physiology & Neurobiology*, 148(1-2):3–21.

West, J. B. and Matthews, F. L. (1972). Stresses, strains, and surface pressures in the lung caused by its weight. *Journal of Applied Physiology*, 32(3):332–345.

Wiechert, L. and Wall, W. (2010). A nested dynamic multi-scale approach for 3D problems accounting for micro-scale multi-physics. *Computer Methods in Applied Mechanics and Engineering*, 199(21-22):1342–1351.

Wu, H., Yu, Y., Huang, H., Hu, Y., Fu, S., Wang, Z., Shi, M., Zhao, X., Yuan, J., Li, J., Yang, X., Bin, E., Wei, D., Zhang, H., Zhang, J., Yang, C., Cai, T., Dai, H., Chen, J., and Tang, N. (2019). Progressive Pulmonary Fibrosis Is Caused by Elevated Mechanical Tension on Alveolar Stem Cells. *Cell*, 180(1):107–121.e17.

Introduction (Français)

Contexte général

Contexte clinique

Médecine *in silico*

La médecine *in silico*, également appelée médecine numérique, est l'utilisation d'outils numériques en médecine, qui peuvent être par exemple des modèles mathématiques et les simulations informatiques associées, pour le diagnostic, le pronostic, les procédures chirurgicales, les traitements ou encore les essais cliniques. Bien que les approches statistiques soient également largement utilisées pour des applications médicales, ce travail se concentre principalement sur les modèles biophysiques, auxquels les termes « modèles *in silico* » ou « modèles numériques » feront référence tout au long du document.

Largement utilisés dans les domaines de l'aéronautique et de l'automobile, les outils numériques comme les modèles *in silico* commencent à être utilisés en médecine, ce qui ouvre de nouvelles perspectives dans le domaine des soins de santé [Naseer et al., 2008; Lim et al., 2020] et fait de la médecine *in silico* un domaine émergent et prometteur. Pour preuve, le marché mondial de la santé numérique a été estimé à 234,5 milliards d'euros d'ici 2023, soit une augmentation de 160 % par rapport à 2019[3]. Cette évolution rapide est motivée par des questions de société (comme le vieillissement de la population, la nécessité de maîtriser les coûts de santé ou le désir de meilleurs soins) et est renforcée par le développement de nouveaux modèles mathématiques efficaces, combiné à une augmentation de la capacité de calcul. Ces derniers aspects techniques ont connu une grande amélioration au cours des dernières décennies et sont maintenant en mesure de répondre aux besoins de la médecine *in silico*.

La médecine *in silico* peut être appliquée à une grande variété de domaines médicaux, par le développement d'outils numériques spécifiques, qui visent à reproduire des phénomènes biologiques réels dans un environnement virtuel. Ces technologies nécessitent le développement de modèles *in silico*, qui décrivent les fonctions biologiques de divers organes ou même du corps entier, en considérant les interactions entre les différentes physiques impliquées. Un modèle *in silico* devient ainsi un jumeau numérique d'un système physique réel, mis à jour en temps réel avec des données, sur lequel des tests peuvent être effectués, des hypothèses peuvent être étudiées, des paramètres peuvent être modifiés pour évaluer les conséquences, etc. Certains de ces modèles peuvent être spécifiques à un patient. Ils apportent des informations personnalisées au patient sur son état, difficiles voire impossibles à mesurer. Des informations prédictives peuvent également être fournies, comme la prédiction d'un comportement futur. Ces deux types d'information sont utiles pour des décisions cliniques ultérieures et l'utilisation de ces outils offre de nouvelles possibilités à la médecine.

Nous présentons ici quelques exemples d'applications de la médecine *in silico*.

- Le développement de nouveaux médicaments est amélioré par les modèles numériques [Bharath et al., 2011]. Tout d'abord, les modèles *in silico* permettent de réduire les essais expérimentaux lors des essais cliniques, tant sur les animaux que sur l'homme, conformément à la nouvelle législation régissant ces essais[4]. Ainsi, la performance, la toxicité et les effets secondaires de nouvelles molécules peuvent être testés en amont

---

[3] Données issues de l'analyse de la société Frost & Sullivan *Global Digital Health Outlook, 2020*. Site internet : https://ww2.frost.com/

[4] Directive européenne 2010/63/EU sur la protection des animaux utilisés à des fins scientifiques, adoptée le 22 septembre 2010

sur des modèles, ce qui permet de rejeter certaines d'entre elles avant tout test *in vivo*, de réduire le nombre d'animaux testés et de diminuer le risque pour les patients volontaires de ces essais cliniques [Claude et al., 2009; Gleeson et al., 2012]. De plus, les tests *in silico* accélèrent la recherche pharmacologique en analysant une plus grande quantité de molécules ou de combinaisons de molécules que les tests *in vivo* et stimulent ainsi la découverte de nouvelles molécules prometteuses [Ekins et al., 2007; Kazmi et al., 2019]. Alors que les essais cliniques sont risqués et s'étalent sur environ une décennie avant le lancement du médicament en cas de résultat concluant [Dickson and Gagnon, 2004], l'utilisation de modèles *in silico* permet une réduction de leur durée, et par conséquent une diminution des coûts de recherche ainsi que du prix des produits [Michelson et al., 2006].

- La performance des procédures chirurgicales commence à être testée par des modèles *in silico*, en suivant le processus décrit dans la Figure 4. Les interventions chirurgicales peuvent être simulées sur des modèles spécifiques au patient qui prennent en compte ses propres caractéristiques physiologiques [Vy et al., 2016]. Par exemple, l'impact sur la déformation artérielle de l'insertion d'un fil de guidage lors d'une réparation endovasculaire peut être calculé en utilisant les géométries artérielles personnalisées aux patients, afin de préparer et de guider l'intervention [Gindre et al., 2017]. À partir de ces modèles, plusieurs stratégies chirurgicales peuvent être testées *in silico* pour choisir celle qui convient le mieux au patient et pour évaluer virtuellement le succès de l'intervention, avant de la réaliser pour de vrai [Carniel et al., 2017, 2020]. Ainsi, pour la thérapie de resynchronisation cardiaque, des modèles du cœur spécifiques au patient sont capables de prédire l'impact de la stimulation pour différentes localisations et d'aider ensuite à choisir parmi elles la meilleure pour le patient [Sermesant et al., 2012]. Une autre application, très difficile car elle nécessite une simulation en temps réel, est l'utilisation de ces modèles pour assister la chirurgie pendant l'intervention, afin de suivre l'état du patient et d'aider les cliniciens à prendre une décision [Marescaux et al., 1998; Khor et al., 2016]. Les écoles de médecine utilisent également des modèles numériques pour éviter de recourir aux cadavres pour enseigner l'anatomie ou pour former les futurs médecins aux procédures chirurgicales difficiles [Courtecuisse et al., 2014].

- Les dispositifs médicaux bénéficient de la médecine *in silico*, de leur conception et de leur positionnement à la prédiction de leur comportement *in vivo* et de leur durabilité. Ils sont de plus en plus personnalisés au patient, ce qui les rend plus adaptés, plus efficaces et moins risqués pour le patient. De nombreux dispositifs médicaux sont concernés. Dans le domaine cardiovasculaire, les stents peuvent maintenant être développés avec une géométrie spécifique au patient, adaptée à la forme de ses vaisseaux sanguins, forme souvent affectée par la maladie ciblée, tel l'anévrisme [Perrin et al., 2016]. Différentes procédures pour le déploiement de valves aortiques transcathéter peuvent être simulées pour étudier les complications possibles et aider les cliniciens dans le choix de la valve [Bianchi et al., 2019]. Dans d'autres domaines, la résistance à la fatigue des implants de la hanche peut être améliorée par l'utilisation de modèles numériques [Colic et al., 2016], la distribution des contraintes osseuses causées par les implants dentaires peut être calculée pour déterminer les indicateurs de surcharge osseuse [Baggi et al., 2008] et un modèle d'éléments finis d'endoprothèse permet d'étudier la relation entre leur conception et leur flexibilité pour prévenir toute complication [Demanget et al., 2012].

- Le diagnostic de maladies est amélioré par les outils numériques puisque les algorithmes fonctionnent plus vite que l'homme, réduisent les erreurs et peuvent apporter plus d'informations que celles disponibles directement dans les données. L'intelligence artificielle est l'un des principaux outils numériques lorsque le diagnostic est effectué à partir d'images. Les algorithmes d'apprentissage automatique doivent souvent d'abord être entraînés à partir de données fournies par les cliniciens, puis ils peuvent être utilisés pour détecter des maladies. Ces outils sont très utiles pour les cliniciens car le diagnostic manuel à partir d'images est souvent délicat, biaisé et fastidieux. Ils peuvent également apporter des informations quantitatives (comme des caractéristiques morphologiques) en plus des observations qualitatives des cliniciens [Topol, 2019; Tarando, 2018]. Les modèles *in silico* n'examinent pas seulement la mesure directe de quantités biologiques, mais calculent également d'autres quantités d'intérêt impossibles à mesurer, comme la contractilité du myocarde pour évaluer des pathologies cardiaques [Chabiniok et al., 2012] ou les paramètres matériaux des aortes atteintes d'anévrisme pour évaluer la probabilité de rupture de l'anévrisme [Kim et al., 2012], qui ne sont pas mesurables *in vivo*. L'estimation de ces quantités supplémentaires peut être réalisée par des problèmes inverses, qui minimisent la différence entre les données et le modèle par rapport à ces quantités inconnues, pondérée par la confiance dans le modèle [Moireau et al., 2008; Avril et al., 2008]. L'interaction entre le modèle et les données est illustrée dans la Figure 5. La surveillance médicale assistée par des modèles constitue également un nouveau défi, notamment pour la surveillance cardiovasculaire des patients en soins intensifs. Par exemple, Le Gall et al. [2020] obtient, à l'aide de modèles cardiaques spécifiques au patient, la boucle pression-volume cardiaque uniquement à partir des données disponibles. Elle apporte des informations supplémentaires sur l'état physiologique du patient, utiles pour guider les stratégies thérapeutiques.

- Le pronostic des patients est régulièrement anticipé à l'aide de modèles numériques prédictifs. La prévision de l'évolution du patient peut conduire à de meilleures décisions cliniques. Le développement de ces modèles numériques nécessite une bonne compréhension de la maladie et la prise en compte de multiples facteurs qui pourraient avoir un impact sur le pronostic (par exemple, des facteurs physiologiques, des facteurs environnementaux, etc). A partir de la détermination de ces facteurs spécifiques au patient, on peut calculer la probabilité de la survenue d'un état donné (par exemple, guérir d'une maladie, mourir, ...) dans un délai donné. À titre d'exemple, le pronostic des patients ayant subi un traumatisme crânien peut être estimé en connaissant l'âge du patient, son pays, la réaction de ses pupilles à la lumière, la gravité de la lésion extra-crânienne et un score de coma [MRC CRASH Trial Collaborators, 2008]. L'assimilation de données est un ensemble de méthodes qui permettent de prédire le devenir futur d'un système à partir de données réelles, également appelées observations, et d'un modèle dynamique du système. La prédiction du modèle est continuellement corrigée par de nouvelles observations dans le temps (approche séquentielle), et conduit à une meilleure détermination des états précédents du système (approche variationnelle principalement). En particulier, cette dernière approche permet de retrouver les conditions initiales du système, qui sont souvent mal connues lorsque l'on considère des systèmes aussi complexes que les systèmes biologiques. Ces méthodes ont déjà fait leurs preuves en météorologie [Ghil and Malanotte-Rizzoli, 1991] et sont maintenant appliquées en biomécanique, tant pour des questions de diagnostic que de pronostic [Moireau, 2008].

Cette liste d'exemples n'est pas exhaustive mais donne un bon aperçu de ce qui peut être réalisé avec de tels outils numériques. Cependant, la plupart des travaux mentionnés

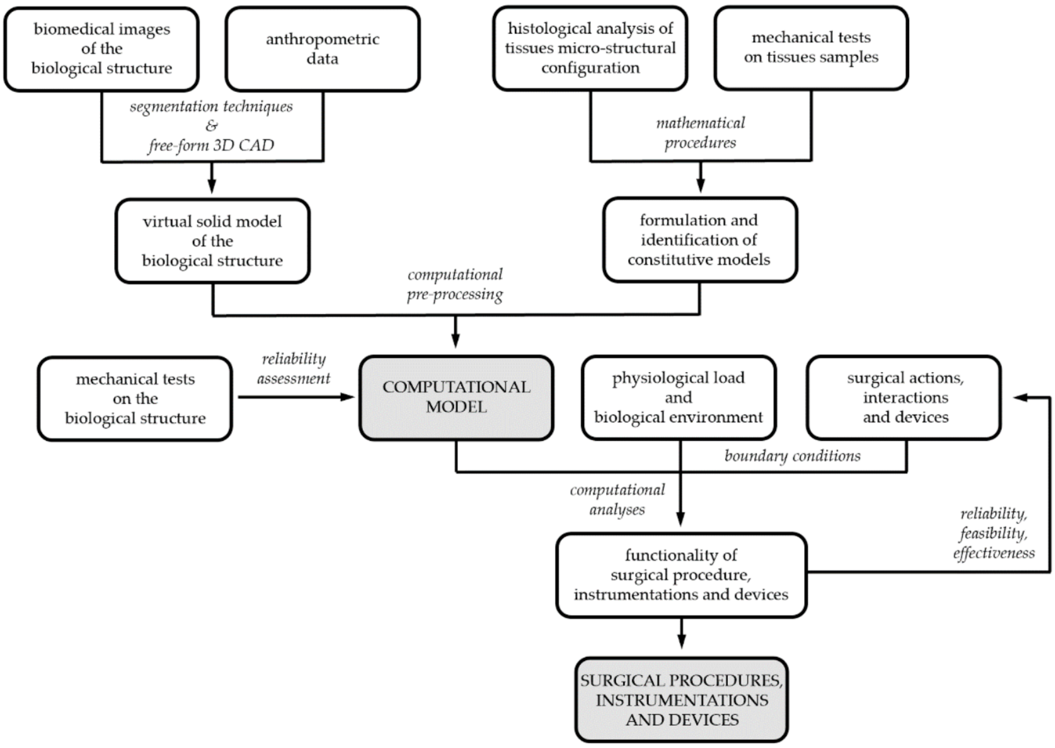

FIGURE 4 – Développement de modèles pour concevoir, optimiser et certifier les procédures, les instruments et les dispositifs chirurgicaux. Figure tirée de Carniel et al. [2020].

FIGURE 5 – Interaction entre le modèle et les données cliniques pour répondre aux questions cliniques. Figure tirée de Chabiniok et al. [2016].

sont encore au stade de la recherche et seules des preuves de concept ont été présentées. De nombreuses initiatives sont mises en place pour connecter ces travaux de recherche mondiaux, comme le Virtual Physiological Human (VPH). Ce projet européen vise à rassembler toutes ces connaissances fragmentaires pour construire un modèle prédictif et personnalisé du corps entier, en assurant une collaboration entre la recherche et la médecine [Viceconti and Hunter, 2016]. Plus proche des applications industrielles, le Living Heart Project (LHP), mené par la société Dassault Systems, rassemble des chercheurs, des cliniciens et des fabricants de dispositifs médicaux pour développer un modèle numérique de cœur, spécifique au patient et de haute précision [Baillargeon et al., 2014]. L'objectif principal est de passer rapidement de ces outils innovants à une meilleure qualité des soins de santé. Enfin, outre les grandes entreprises du secteur de la santé, comme General Electric Healthcare, Air Liquide Healthcare, Siemens Healthcare ou Philips Healthcare, de nombreuses start-up émergent pour traiter ces problèmes de santé. Par exemple, Predisurge développe des modèles numériques pour mieux concevoir et implanter des dispositifs médicaux cardiovasculaires, comme les endoprothèse aortiques, et Ebenbuild crée des jumeaux numériques des poumons de patients atteints de Syndrome de Détresse Respiratoire Aiguë (SDRA) pour aider leur thérapie. En France, le secteur de la santé est le premier secteur représenté dans le programme *French Tech 2020*, une sélection des start-ups françaises les plus prometteuses, puisqu'il concerne environ 20 % d'entre elles.

Les technologies *in silico* doivent encore être améliorées, à la fois pour prendre en compte toute la complexité de l'environnement biologique du corps humain et être intégrées dans les protocoles cliniques. Certaines limitations à leur utilisation doivent également être supprimées. Les modèles numériques doivent être validés afin de certifier que leurs prévisions sont suffisamment précises. Ainsi, les modèles sont souvent basés sur des données bruitées et l'incertitude qui s'y rattache se propage aux résultats. Une analyse de la propagation de l'incertitude doit être effectuée pour garantir la qualité des modèles [Lin et al., 2015]. La médecine *in silico* pose également des problèmes de confidentialité et de sécurité. Les données des patients, en tant qu'éléments essentiels des modèles spécifiques aux patients, doivent être manipulées avec beaucoup de précaution conformément aux lois en vigueur, comme le Règlement Général sur la Protection des Données (RGPD) dans l'Union européenne. En outre, la question de l'acceptation de ces technologies par les cliniciens et les patients est essentielle, car les premiers peuvent craindre d'être remplacés par des ordinateurs alors que les seconds peuvent avoir des difficultés à faire confiance à des « boîtes noires ». Les essais *in silico* commencent à être pris en compte par les organismes de réglementation, ce qui montre que la situation évolue.

Questions spécifiques à la pneumologie

Toutes les disciplines médicales peuvent bénéficier de ces avancées techniques, comme le montrent les exemples précédents, et la pneumologie ne fait pas exception. L'utilisation des technologies numériques permet de répondre à de nombreuses questions : une meilleure compréhension de la physiopathologie et de la fonction pulmonaire, ainsi qu'un meilleur diagnostic et un meilleur pronostic des pathologies, ce qui permet aussi d'améliorer les traitements. En pneumologie, l'oncologie, l'administration de médicaments et la ventilation mécanique sont trois domaines qui peuvent bénéficier des modèles *in silico*.

Le cancer du poumon est traité par radiothérapie, qui consiste à envoyer des radiations pour détruire les cellules cancéreuses et les empêcher de se multiplier. La préservation des cellules saines autour des cellules cancéreuses ciblées est cruciale et délicate en raison du mouvement des poumons pendant la respiration. En effet, ce mouvement induit le déplacement des nodules cancéreux, ce qui rend leur ciblage difficile : chaque séance de radiothérapie dure quelques minutes alors qu'un cycle inhalation-expiration dure quelques secondes. La direction du faisceau doit alors suivre la zone cancéreuse, car elle atteindrait les zones saines si elle restait fixe. Finalement, le principal problème est de prévoir les déplacements des nodules pendant la séance d'irradiation, même si l'ampleur de la respiration est irrégulière et que les déplacements des nodules le sont tout autant, afin de synchroniser le faisceau de radiation avec le mouvement de la tumeur [Seppenwoolde et al., 2002; Sonke et al., 2019]. Des substituts internes et externes du mouvement de la tumeur sont étudiés [Savanovic et al., 2020]. La dose de rayonnement est également impactée par l'incertitude sur la justesse du ciblage de la zone cancéreuse : elle est réduite pour diminuer les risques pour la zone saine, alors qu'elle pourrait être augmentée si la zone cancéreuse était atteinte à coup sûr.

En ce qui concerne la circulation de l'air dans les poumons, l'administration de médicaments est un sujet d'intérêt pour les pneumologues, afin d'améliorer les traitements de maladies comme l'asthme ou la bronchopneumopathie chronique obstructive (BPCO). Ces deux maladies nécessitent l'inhalation d'un bronchodilatateur pour dilater les voies respiratoires et améliorer l'apport en oxygène. Mais ce type de traitement soulève des questions sur le transport des particules dans les voies respiratoires, qui sont complexes et non homogènes, sur le dépôt de particules sur les zones ciblées et sur les dispositifs d'inhalation. En effet, les voies respiratoires ont des propriétés intrinsèques de défense pour protéger l'intérieur du poumon de particules étrangères, comme les cils présents à leur surface pour éliminer ces particules. Certaines maladies peuvent également rendre difficile la circulation des particules, lorsque les voies respiratoires sont rétrécies par exemple. Seul 20 % de la dose délivrée par l'inhalateur atteint les poumons [Borgström et al., 2006]. L'interaction des particules avec la surface ciblée pour le dépôt doit également être prise en compte, car les interactions chimiques avec les couches de surface, comme le mucus, le surfactant ou les enzymes, peuvent entraîner la dégradation des particules, qui est la manifestation des barrières immunologiques. Tous ces défis doivent être pris en compte lors de la formulation des médicaments et de la conception des inhalateurs afin d'optimiser les traitements [Newman, 2017; Ehrmann et al., 2020].

Alors que la radiothérapie pulmonaire concernait le mouvement des poumons et l'administration des médicaments les écoulements d'air pulmonaires, le comportement de la microstructure est une préoccupation majeure en anesthésie et en soins intensifs lors de l'utilisation d'un respirateur pour un patient. La ventilation mécanique avec un ventilateur est utilisée pour les patients souffrant d'une détresse respiratoire aiguë, sous anesthésie générale ou dans les unités de soins intensifs. L'air est apportée aux poumons du patient sous certaines caractéristiques de pression, de fréquence et de flux. De nombreux paramètres peuvent être réglés sur un respirateur et sont très importants pour que la ventilation soit adéquate pour le patient. Une pression positive est nécessaire pour recruter les alvéoles, gonfler les poumons et ainsi fournir de l'oxygène au corps. Cependant, une pression excessive peut endommager la microstructure des poumons, en particulier les alvéoles, et entraîner ce que l'on appelle une lésion pulmonaire induite par le ventilateur. Le réglage de la ventilation mécanique est un compromis entre une bonne oxygénation du patient et la protection de ses poumons contre des lésions. Il pourrait être facilité par des modèles spécifiques au patient qui prendraient en compte les paramètres du patient, comme la pathologie mais aussi l'état physiologique actuel, et qui pourraient optimiser les paramètres de la ventilation mécanique en utilisant la réponse en direct du patient [Goligher et al., 2016]. Le même principe pourrait être appliqué pour la surveillance cardiovasculaire en utilisant un modèle biomécanique du cœur comme outil périopératoire pour estimer de nouvelles informations, non mesurables, mais utiles pour les cliniciens [Le Gall et al., 2020].

COVID-19 Les défis de la ventilation mécanique ont trouvé un écho dans les événements actuels concernant la COVID-19, puisque le nouveau coronavirus peut affecter les poumons. Les patients en état grave sont placés sous ventilation mécanique car ils sont sous-oxygénés et souffrent d'une insuffisance respiratoire aiguë.

La COVID-19 entraîne dans certains cas graves un œdème pulmonaire [Kuebler et al., 2020; Archer et al., 2020], caractérisé par l'accumulation de liquide à l'intérieur des poumons, ce qui restreint les échanges gazeux dans les alvéoles et semble avoir un impact sur la compliance pulmonaire. Plus il y a de liquide dans les poumons, moins il y a d'alvéoles disponibles pour les échanges gazeux, et moins le corps reçoit d'oxygène, ce qui entraîne une hypoxie. Pour améliorer la compliance pulmonaire ainsi que les échanges gazeux, les anesthésistes ont la possibilité de modifier la position du patient (couché ou allongé) et de régler les pressions de fin d'expiration et de fin d'inspiration. Cependant, ils ne connaissent pas à l'avance le degré d'amélioration de la compliance pour un réglage spécifique ni les meilleurs réglages à appliquer. Par conséquent, ils doivent essayer plusieurs réglages jusqu'à ce qu'ils trouvent le meilleur. Des modèles spécifiques au patient pourraient les aider à améliorer le processus de ventilation.

Un autre aspect de la maladie concerne l'évolution à long terme des lésions pulmonaires. Une hypothèse d'évolution vers une maladie pulmonaire interstitielle fibrosante, qui pourrait toucher 20 % à 30 % des cas graves, a été formulée [George et al., 2020; Spagnolo et al., 2020]. Les données sont encore de la toute première phase de l'épidémie, cependant une multiplication fibroblastique avec dépôt de matrice extracellulaire en grappe a été rapportée dans certaines autopsies [Tian et al., 2020] et conforte l'hypothèse. L'évolution supposée doit être étudiée car elle pourrait conduire à l'avenir à un problème de santé publique lié à une incapacité respiratoire secondaire.

Fibrose Pulmonaire Idiopathique La Fibrose Pulmonaire Idiopathique (FPI) est une pathologie pulmonaire, qui est le point de départ de ce sujet de thèse ainsi que sa principale application.

Description La Fibrose Pulmonaire Idiopathique appartient à un groupe d'environ 200 maladies pulmonaires appelées maladies pulmonaires interstitielles, qui affectent l'interstitium pulmonaire, c'est-à-dire le tissu conjonctif autour des alvéoles qui s'étend autour des voies aériennes et des vaisseaux sanguins et dans la plèvre viscérale. La FPI est une maladie chronique caractérisée par des phénomènes cicatricielles, causées par une inflammation et entraînant un épaississement des tissus, comme le montre la Figure 6. En conséquence, les échanges gazeux dans les alvéoles sont moins efficaces et les poumons sont moins compliants [Plantier et al., 2018]. La maladie touche majoritairement les hommes de plus de 50 ans [Lederer and Martinez, 2018]. Son incidence est d'environ 10 nouveaux cas pour 100 000 individus chaque année [Nalysnyk et al., 2012], ce qui en fait une maladie rare même si elle est la plus courante des pneumopathies interstitielles.

Les patients souffrant de FPI présentent deux symptômes principaux. Le premier est une dyspnée, ou essoufflement, qui affecte la vie quotidienne [Swigris, 2005] et qui s'aggrave avec l'évolution de la maladie. Le second est une toux chronique.

Les causes de la FPI sont inconnues, comme l'indique le terme « idiopathique ». Cependant, certains facteurs de risque ont été identifiés, tels des facteurs génétiques ou environnementaux. Il a également été démontré que le tabagisme augmentait le risque de survenue de la maladie [Sauleda et al., 2018]. Le sexe et l'âge peuvent également être considérés comme des facteurs de risque, car l'incidence de la maladie est plus élevée chez les hommes de plus de 50 ans.

Le diagnostic de la FPI est difficile, car il nécessite d'exclure les causes connues de d'autres pneumopathies interstitielles. Il implique généralement une combinaison de techniques [Poletti et al., 2013]. Les tests de la fonction pulmonaire permettent de mesurer le taux d'absorption d'oxygène ainsi que le volume d'air inhalé pendant la respiration, qui sont tous deux réduits en cas de FPI. Un autre outil majeur est la tomodensitométrie à rayons X, aussi appelée scanner, une modalité d'imagerie médicale qui permet de visualiser la texture des poumons. Certains motifs sont typiques des maladies pulmonaires interstitielles, comme la structure en nid d'abeille ou le verre dépoli, et jouent un rôle important dans le diagnostic (voir la Figure 6). Toutefois, cette technique ne peut pas être utilisée seule car elle ne permet pas de distinguer la FPI des autres pneumopathies interstitielles. La biopsie pulmonaire, qui consiste à prélever un petit morceau de tissu pulmonaire au cours d'une opération chirurgicale, peut également être pratiquée [Hübner et al., 2008; Cavazza et al., 2010]. Le tissu est ensuite observé au microscope pour un examen histologique, afin de mettre en évidence les caractéristiques spécifiques des pneumopathies interstitielles, mais là encore, elles ne sont pas propres à la FPI. Enfin, bien que difficile, un diagnostic précoce est nécessaire pour améliorer le devenir du patient à long terme.

Alors que le diagnostic est difficile et peut prendre beaucoup de temps, le pronostic est défavorable puisque l'espérance de vie moyenne après le diagnostic est de trois à cinq ans [Poletti et al., 2013]. L'évolution de la maladie se caractérise par un déclin progressif des fonctions pulmonaires associé à l'expansion de la zone pulmonaire affectée et fibreuse. Certaines exacerbations, caractérisées par une progression plus rapide, sont observées, mais restent imprévisibles [King et al., 2011].

Il n'existe aucun traitement pour guérir la maladie [Rogliani et al., 2016]. Les médicaments administrés aux patients atteints de FPI, la pirfénidone et le nintédanib, ne font que ralentir le déclin et prévenir les exacerbations, ce qui améliore par conséquent l'espérance de vie [King et al., 2011]. D'autres médicaments peuvent également réduire les symptômes, comme la toux. Cependant, ces deux principaux médicaments ont des effets secondaires importants et réduisent la qualité de vie des patients. Finalement, la seule solution est la transplantation pulmonaire, mais elle n'est pas accessible à tous car plusieurs critères doivent être remplis et il existe une liste d'attente pour y avoir droit.

Enjeux La FPI est mal comprise, mal diagnostiquée et mal traitée. Ainsi, une meilleure compréhension, un meilleur diagnostic et un meilleur pronostic sont les trois principaux enjeux pour les pneumologues confrontés à la FPI.

Toutefois, certaines améliorations sont en cours. Récemment, une hypothèse a été formulée sur le mécanisme d'évolution de la maladie [Liu et al., 2010; Hinz and Suki, 2016; Haak et al., 2018; Wu et al., 2019]. Il a été supposé qu'un cercle vicieux, dans lequel la fibrose conduirait à plus de fibrose, régirait la FPI. En effet, la fibrose pulmonaire induit un tissu cicatriciel plus rigide par la formation de fibres de collagène. Lors de la respiration, ce tissu plus rigide subit des contraintes plus importantes, stimulant les fibroblastes, qui produisent alors plus de fibres de collagène et plus de fibrose, et ainsi de suite. Ce cercle vicieux, dans lequel la mécanique joue un rôle majeur, doit être étudié et validé plus en profondeur, et pourrait améliorer considérablement la compréhension de la maladie.

Toutes ces questions peuvent être abordées par des modèles, notamment des modèles *in silico*. Ils pourraient être utilisés pour étudier l'hypothèse du cercle vicieux mécanique et pour améliorer le diagnostic en apportant de nouvelles informations par la combinaison des outils existants. Le pronostic serait également amélioré par une meilleure connaissance de la maladie, et l'impact des médicaments pourrait être étudié à l'aide de modèles.

Ces questions sont celles qui ont amené ce sujet de thèse. Les ayant identifiées, les

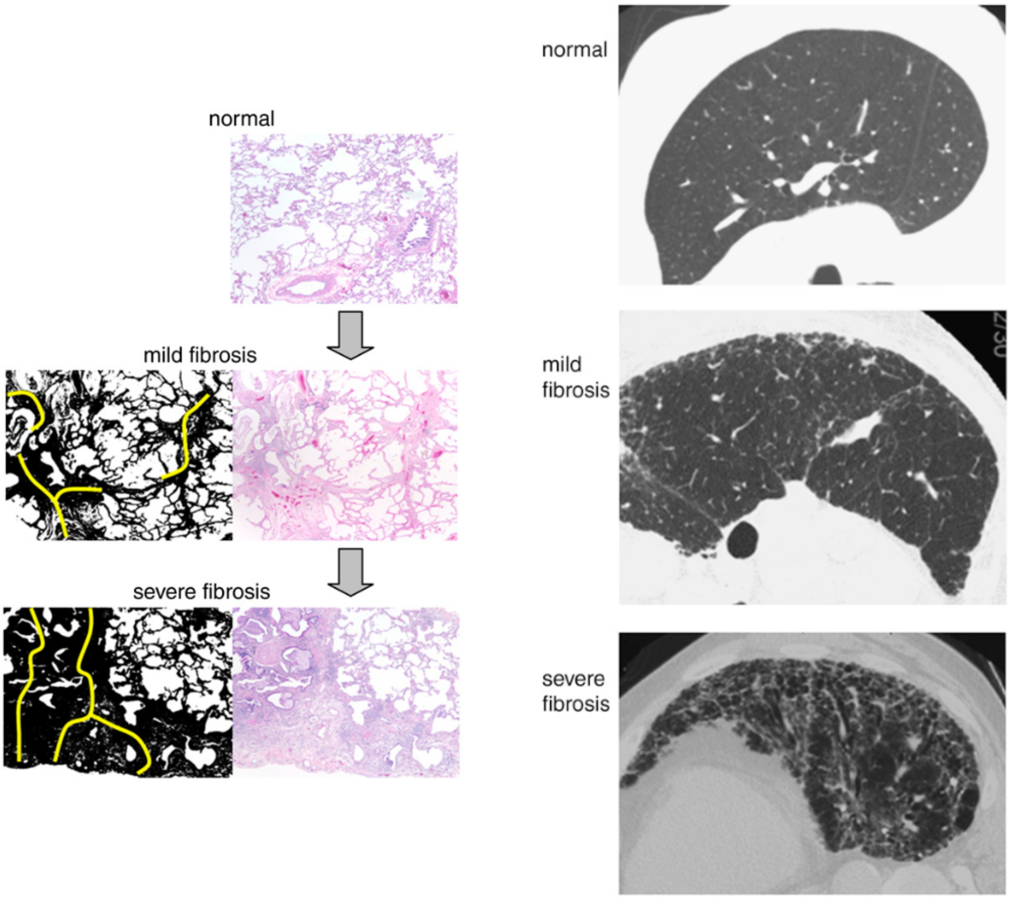

Figure 6 – Illustrations de l'impact de la FPI sur la microstructure pulmonaire. (Gauche) Coupes histologiques d'une biopsie pulmonaire. (Droite) Images scanner de poumon. Figure tirée de Bates et al. [2007].

cliniciens et radiologues de l'hôpital APHP Avicenne de Bobigny, en France, experts en pneumopathies interstitielles, ont contacté l'équipe MΞDISIM pour faire appel à son expertise afin de mieux comprendre le rôle de la mécanique dans le développement de la FPI. C'est ainsi qu'a débuté cette thèse ainsi que la collaboration sur l'utilisation de la mécanique numérique pour des applications pulmonaires.

Modélisation pulmonaire

La modélisation des poumons vise à répondre aux applications cliniques pulmonaires mentionnées précédemment. Nous nous concentrons ici sur les modèles physiques, sans considérer les outils numériques relatifs aux données et à l'analyse statistique comme l'intelligence artificielle.

Les poumons sont des organes complexes, de par leur composition en trois phases (air, sang et tissu solide), qui peuvent interagir les unes avec les autres, de par leur microstructure, évoluant au cours de la respiration, et de par leur environnement. La modélisation des poumons est un réel défi car elle peut impliquer une grande diversité de phénomènes physiques. En outre, plusieurs échelles – échelle de temps ou échelle spatiale – peuvent être considérées, selon le type de phénomènes étudiés et l'échelle à laquelle ils se produisent. La respiration correspond à une échelle de temps court par rapport à l'échelle de temps long du remodelage pathologique, et l'échelle spatiale alvéolaire est une échelle microscopique qui est liée à la microstructure pulmonaire par opposition à l'échelle macroscopique de l'organe. Enfin, les aspects multi-échelle, multi-physique et multi-phase doivent être pris en compte pour la modélisation des poumons [Burrowes et al., 2008]. Les poumons peuvent être décrits par différentes disciplines physiques, comme la mécanique des fluides, les interactions fluide-structure, la mécanique des solides, la poromécanique, la chimie, etc. Un modèle ne peut pas prendre en compte tous ces domaines et des choix de modélisation doivent être faits en fonction de l'objectif visé. En effet, plus le modèle est complexe, plus le temps de calcul est long et plus la calibration du modèle est difficile.

Nous nous concentrons ici sur la mécanique, plus particulièrement la mécanique des fluides et la mécanique des solides, qui peuvent être utilisées indépendamment, mais aussi couplées [Cazeaux and Grandmont, 2015; Berger et al., 2016], ce qui augmente la complexité des modèles et le temps de calcul.

Aspects de mécanique des fluides La mécanique des fluides permet d'étudier les écoulements d'air à l'intérieur des poumons. Les modèles sont construits en une dimension ou peuvent prendre en compte la complexité de la géométrie des voies respiratoires et des caractéristiques du flux d'air (vitesse, turbulence [Lin et al., 2007], compressibilité, etc) en utilisant des simulations de la mécanique des fluides numérique (MFN) en trois dimensions [Lin et al., 2013]. La géométrie des voies aériennes peut être générique [Mauroy et al., 2003], mais les améliorations des techniques d'imagerie médicale permettent d'obtenir une géométrie spécifique au patient [Tawhai et al., 2004; Fetita et al., 2004]. Des modèles statistiques sont également développés pour prendre en compte la variabilité géométrique entre les personnes [Koblinger and Hofmann, 1990].

Ces modèles 3D permettent de décrire l'écoulement d'air dans les poumons malades comme ceux souffrant d'asthme, en prenant en compte le changement de diamètre des voies respiratoires inflammées qui influe sur leur résistance, ainsi que le type d'écoulement, laminaire ou turbulent [Martonen et al., 2003; Tgavalekos et al., 2005]. Une fois l'écoulement d'air modélisé, l'étude du transport des particules avec l'écoulement et leur dépôt dans la section 3D des voies aériennes [Hofmann and Koblinger, 1990; Annapragada and Mishchiy, 2007; Lambert et al., 2011; Boudin et al., 2015] peut également être réalisée, avec des particules décrites de manière discrète [Oakes et al., 2014] ou continue [Chen et al., 2006]. Les informations locales sur les dépôts de médicaments, non disponibles avec les modèles 1D globaux, sont apportées avec ces modèles 3D [Longest and Holbrook, 2012].

Alors que les premières bifurcations des voies aériennes sont le lieu de phénomènes de convection, les voies aériennes périphériques présentent des phénomènes de diffusion. Les échanges gazeux se produisent alors à une plus petite échelle, l'échelle alvéolaire, à l'extrémité des voies aériennes périphériques. C'est pourquoi la géométrie des alvéoles avec la dernière bifurcation des voies aériennes périphériques est utilisée pour décrire la diffusion de l'oxygène à travers l'interface entre l'air et le sang. Le paramètre clé d'une telle modélisation est la pression partielle de l'oxygène dans les voies aériennes et les vaisseaux sanguins.

Aspects de mécanique des solides Lorsqu'il s'agit d'étudier la déformation des poumons pendant la respiration, un autre type de physique est utilisé. La mécanique des solides donne des informations sur la cinématique, qui décrit comment les poumons se déforment tout au long du cycle respiratoire et quantifie les déplacements et les déformations. La cinématique peut être calculée à partir d'images avec des outils de corrélation d'images [Hurtado et al., 2016; Vishnevskiy et al., 2017]. Les applications en radiothérapie utilisent de telles informations, mais, pour d'autres applications, comme la ventilation mécanique ou l'étude de la FPI, des informations mécaniques supplémentaires de dynamique, l'étude des forces et des contraintes, sont nécessaires. Les interactions entre les poumons et leur environnement sont alors modélisées par des forces, ce qui permet de mieux comprendre le comportement des poumons. Les contraintes sont reliées à la déformation par le comportement du matériau, qui est l'un des ingrédients essentiels de la modélisation mécanique des poumons. Le comportement du matériau peut être considéré comme homogène ou hétérogène pour modéliser les pathologies pulmonaires ayant un impact sur la mécanique, et peut inclure plusieurs paramètres caractérisant le tissu pulmonaire, comme l'élasticité, la viscosité, l'isotropie, etc.

Les modèles mécaniques solides peuvent utiliser une géométrie basée sur des formes mathématiques [West and Matthews, 1972; Denny and Schroter, 2006], générique [Gefen et al., 1999] ou spécifique au patient [Tawhai et al., 2009], quelle que soit échelle spatiale. Les géométries spécifiques aux patients sont plus complexes et nécessitent une plus grande capacité de calcul. Cependant, elles permettent de construire des modèles prédictifs spécifiques au patient.

Du fait de leur microstructure complexe, les poumons ont des propriétés multi-échelles, ce qui est important pour la modélisation mécanique des poumons. Comme les modèles de dynamique des fluides, les modèles de mécanique des solides peuvent prendre en compte différentes échelles pour décrire la microstructure, de l'échelle de l'organe à l'échelle alvéolaire [Rausch et al., 2011; Concha et al., 2018]. L'échelle alvéolaire est plus appropriée pour décrire l'impact de la ventilation sur la structure alvéolaire, car elle permet de quantifier les contraintes et les déformations dans la paroi alvéolaire. De nouveaux éléments, tels que les tensioactifs ou les fibres de collagène, peuvent être inclus dans ces modèles. Les deux échelles peuvent être liées par des procédures d'homogénéisation [Wiechert and Wall, 2010] pour étudier l'impact à l'échelle de l'organe des paramètres décrivant la microsctructure ou pour décrire certains paramètres macroscopique par des modèles à l'échelle microscopique [Lauzon et al., 2012].

La matière pulmonaire est également multiphasique, puisque les poumons sont composés de plusieurs phases, tissu solide, air et sang principalement. La poromécanique, qui est la mécanique des milieux poreux, est ainsi pertinente pour décrire le tissu pulmonaire en considérant sa porosité. Les théories de la poromécanique ont déjà été largement utilisées dans les géosciences pour l'étude des roches et des sols [Biot and Temple, 1972; Coussy, 2004; Dormieux et al., 2006] et ont ensuite été introduites en biomécanique [Mow et al., 1980; Simon et al., 1985; Chapelle and Moireau, 2014]. La théorie des mélanges considère la superposition de chaque phase en tout point du milieu poreux, avec une physique spécifique et un couplage entre elles. Par rapport aux approches d'homogénéisation, la poromécanique présente plusieurs avantages. Aucune microstructure complexe n'est supposée, la porosité étant utilisée comme caractéristique de la microstructure homogénéisée, ce qui permet de gagner du temps de calcul. On peut également supposer une microstructure par la suite pour revenir à l'échelle microscopique. En outre, le comportement mécanique effectif peut être dérivé de tests expérimentaux, ce qui est plus difficile pour le comportement de la partie solide requis dans les approches multi-échelles.

Parmi l'ensemble des modèles qui peuvent être construits pour décrire les poumons, nous avons choisi de travailler dans cette thèse avec des outils de poromécanique. En effet, la poromécanique est une compétence majeure de l'équipe MΞDISIM, qui a déjà développé une théorie poromécanique générale pour la biomécanique [Chapelle and Moireau, 2014] et l'a appliquée pour des modèles de perfusion cardiaque [Burtschell, 2016].

Objectifs : de la théorie aux applications cliniques

L'objectif de ce travail est de développer un modèle pulmonaire afin de répondre aux enjeux cliniques soulevés par la Fibrose Pulmonaire Idiopathique. Comme la mécanique semble être essentielle dans cette maladie, à la fois par son impact sur la physiologie des poumons atteints et par son rôle dans l'évolution de la maladie, le modèle développé est un modèle mécanique, et plus précisément un modèle poromécanique, pour considérer la porosité des poumons. Afin d'utiliser le modèle dans un but de diagnostic et de pronostic personnalisés, le modèle doit être spécifique au patient, ce qui nécessite des données sur le patient. Ainsi, des images biomédicales, acquises par l'hôpital APHP Avicenne de Bobigny, sont utilisées pour personnaliser les différents éléments du modèle.

Les trois principaux objectifs de cette thèse sont les suivants :

Objectif 1 - Construire un modèle de poumon dans un cadre poromécanique.
Le point de départ pour construire le modèle de poumon est la formulation poromécanique générale de Chapelle and Moireau [2014]. L'objectif est de l'adapter au contexte du poumon en proposant des hypothèses spécifiques. En outre, tous les éléments d'un modèle mécanique classique doivent être définis, principalement la géométrie, le comportement du matériau et les conditions aux limites, afin de décrire le processus de la respiration. Cela nécessite une bonne compréhension de la physiologie respiratoire.

Objectif 2 - Personnaliser le modèle au patient avec des données.
Une fois le modèle de poumon général construit, un processus de personnalisation utilisant les données du patient doit être mis en place pour rendre le modèle spécifique au patient. Idéalement, tous les éléments du modèle doivent être personnalisés pour obtenir le jumeau numérique reproduisant le plus fidèlement la physiologie du poumon. Un premier objectif est de déterminer quel type de données est nécessaire pour personnaliser le modèle et quel type de données les cliniciens ont la possibilité d'acquérir sur les patients. Cette étape nécessite une interaction étroite avec les cliniciens. Ensuite, ces données disponibles doivent être exploitées pour obtenir les informations nécessaires : des géométries spécifiques nécessitent des outils de traitement d'images et une loi de comportement spécifique implique une procédure d'optimisation mathématique.

Objectif 3 - Construire des biomarqueurs mécaniques pour répondre aux questions cliniques sur la fibrose.
Enfin, le modèle de poumon personnalisé doit être pleinement exploité pour répondre aux questions cliniques sur la FPI soulevées par les cliniciens. Le modèle mécanique peut étudier les effets mécaniques de la maladie sur les poumons et apporter des informations sur la compliance locale pour compléter les informations globales déjà acquises par les cliniciens, ce qui pourrait aider au diagnostic de la maladie. L'hypothèse d'un cercle vicieux mécanique peut également être explorée en examinant l'impact de la FPI sur les contraintes et les déformations du poumon.

Structure et contributions

Cette thèse est organisée en trois chapitres. Leur contenu et leurs principales contributions sont présentés ici.

Chapitre 1 - De la physiologie pulmonaire à la modélisation mécanique des poumons

Dans le premier chapitre, nous présentons les principaux éléments de physiologie pulmonaire nécessaires à une bonne compréhension de la modélisation mécanique des poumons. La fonction et l'anatomie pulmonaires sont décrites, ainsi que les mécanismes de la respiration. Diverses façons d'évaluer la fonction pulmonaire sont également mentionnées. Ensuite, nous nous référons à ces éléments de physiologie pour les relier à la modélisation des poumons. Différents types de modèles mécaniques sont passés en revue : modèles à l'échelle de l'organe, avec des discussions sur le choix des conditions limites et de la loi de comportement, et modèles multi-échelles. Enfin, la poromécanique est introduite, en particulier le modèle général sur lequel se basent ces travaux et les chapitres suivants.

Chapitre 2 - Un modèle poromécanique des poumons

Dans le deuxième chapitre, nous abordons le premier objectif de cette thèse en construisant un modèle poromécanique pulmonaire à l'échelle de l'organe et à l'échelle de la respiration. Sur la base du cadre poromécanique de Chapelle and Moireau [2014], des hypothèses spécifiques aux poumons sont formulées. Ensuite, tous les éléments d'un modèle mécanique sont incorporés. Une loi de comportement est conçue pour considérer la non linéarité du comportement volumique des poumons avec la pression. Des conditions limites utilisant le contact et prenant en compte le type de respiration (spontanée ou mécanique) sont définies. Un problème spécifique à la biomécanique est aussi résolu pour estimer la configuration non chargée des poumons. Enfin, un problème spécifique à la poromécanique en grande déformation, qui consiste à contraindre la porosité à être positive, est abordé et deux solutions sont proposées. A la fin, plusieurs illustrations du modèle sont proposées pour étudier l'impact de différents choix faits dans le modèle, comme la loi de comportement (compliance, énergie de porosité) et les conditions aux limites (propriétés de contact, gravité, pression).

Ce chapitre prend la forme d'un article à soumettre co-écrit par Cécile Patte, Martin Genet et Dominique Chapelle, intitulé *A poromechanical model of the lungs.*

Chapitre 3 - Estimation de la compliance pulmonaire régionale pour la FPI basée sur la modélisation poromécanique pulmonaire

Dans le troisième chapitre, nous présentons d'abord le processus de personnalisation du modèle qui a été développé, ce qui correspond au deuxième objectif. Les données utilisées sont des scans 3D de patients ; des données de pression auraient également été nécessaires pour réaliser une personnalisation plus avancée, mais il était impossible d'acquérir de telles données sur les patients considérés. Les images sont ensuite utilisées pour personnaliser à la fois la porosité et la géométrie avec des outils de segmentation, pour différencier les régions saines des régions malades et pour estimer la compliance. Cette dernière étape est formulée comme un problème d'optimisation pour minimiser la différence des mouvements respiratoires entre le modèle et les données. Deux fonctions coût, exploitant les images de deux manières différentes, sont étudiées.

Des résultats sont ensuite obtenus pour des patients souffrant de la FPI. D'une part, la performance du processus de personnalisation est étudiée en comparant les deux fonctions coût, l'utilisation de deux régions par rapport à une seule région et l'utilisation de la compliance absolue par rapport à la compliance effective. D'autre part, les quantités pertinentes pour répondre au troisième objectif sont déterminées et analysées. Les compliances régionales sont estimées à la fois dans les régions saines et dans les régions malades, ce qui permet de quantifier le raidissement des tissus induit par la FPI. La corrélation entre le rapport de compliances et le déclin induit par la maladie est également explorée, tout comme l'impact de la FPI sur les contraintes mécaniques.

Ce chapitre prend la forme d'un article à soumettre co-écrit par Cécile Patte, Pierre-Yves Brillet, Catalin Fetita, Thomas Gille, Jean-François Bernaudin, Hilario Nunes, Dominique Chapelle et Martin Genet, intitulé *Estimation of regional pulmonary compliance in IPF based on lung poromechanical modeling.*

Communications

Ce travail a été présenté dans plusieurs conférences sous forme de présentations orales et a donné lieu à deux articles à soumettre. Ces différentes contributions sont présentées par ordre chronologique.

Présentations orales

- **Présentation orale au « 14ème Colloque National en Calcul des Structures » (CSMA 2019).**
  Giens, France - 13-17 mai 2019.

- **Présentation orale au Symposium Jean Mandel 2020.**
  École Polytechnique, Palaiseau, France - 18-19 juin 2020.

- **Présentation orale à la conférence VPH 2020.**
  France (en ligne) - 25-28 août 2020.

Publications

Articles de conférence

- **Mécanique pulmonaire personnalisée : modélisation et estimation – Application à la fibrose pulmonaire [Patte et al., 2019].**
  C. Patte, M. Genet, C. Fetita, P.-Y. Brillet et D. Chapelle.
  14ème Colloque National en Calcul des Structures, mai 2019, Giens, France.

- **Personalized Pulmonary Poromechanics [Genet et al., 2020a].**
  M. Genet, C. Patte et D. Chapelle.
  14th World Congress on Computational Mechanics (WCCM), 2020, Paris, France.

- **Estimation of patient-specific mechanical parameters in pulmonary diseases [Patte et al., 2020].**
  C. Patte, P.-Y. Brillet, C. Fetita, T. Gille, J.-F. Bernaudin, H. Nunes, D. Chapelle et M. Genet.
  VPH2020 conference, août 2020, Paris, France.

- **Personalized Pulmonary Poromechanics [Genet et al., 2020b].**
  M. Genet, C. Patte, C. Fetita, P.-Y. Brillet et D. Chapelle.
  45ème Congrès de la Société de Biomécanique (SB), octobre 2020, Metz, France.

Articles de journaux

- **A poromechanical model of the lungs.**
  C. Patte, M. Genet et D. Chapelle.
  A soumettre, à soumettre en octobre 2020 dans *Annals of Biomedical Engineering.*

- **Estimation of regional pulmonary compliance in IPF based on lung poromechanical modeling.**
  C. Patte, P.-Y. Brillet, C. Fetita, T. Gille, J.-F. Bernaudin, H. Nunes, D. Chapelle et M. Genet.
  A soumettre.

Bibliographie

Annapragada, A. and Mishchiy, N. (2007). In silico modeling of aerosol deposition in lungs. *Drug Discovery Today : Disease Models*, 4(3) :155–161.

Archer, S. L., Sharp, W. W., and Weir, E. K. (2020). Differentiating COVID-19 Pneumonia From Acute Respiratory Distress Syndrome and High Altitude Pulmonary Edema : Therapeutic Implications. *Circulation*, 142(2) :101–104.

Avril, S., Bonnet, M., Bretelle, A.-S., Grédiac, M., Hild, F., Ienny, P., Latourte, F., Lemosse, D., Pagano, S., Pagnacco, E., and Pierron, F. (2008). Overview of Identification Methods of Mechanical Parameters Based on Full-field Measurements. *Experimental Mechanics*, 48(4) :381–402.

Baggi, L., Cappelloni, I., Maceri, F., and Vairo, G. (2008). Stress-based performance evaluation of osseointegrated dental implants by finite-element simulation. *Simulation Modelling Practice and Theory*, 16(8) :971–987.

Baillargeon, B., Rebelo, N., Fox, D. D., Taylor, R. L., and Kuhl, E. (2014). The Living Heart Project : A robust and integrative simulator for human heart function. *European Journal of Mechanics - A/Solids*, 48 :38–47.

Bates, J. H. T., Davis, G. S., Majumdar, A., Butnor, K. J., and Suki, B. (2007). Linking Parenchymal Disease Progression to Changes in Lung Mechanical Function by Percolation. *American Journal of Respiratory and Critical Care Medicine*, 176(6) :617–623.

Berger, L., Bordas, R., Burrowes, K., Grau, V., Tavener, S., and Kay, D. (2016). A poroelastic model coupled to a fluid network with applications in lung modelling : A poroelastic model coupled to a fluid network with applications in lung modelling. *International Journal for Numerical Methods in Biomedical Engineering*, 32(1).

Bharath, E. N., Manjula, S. N., and Vijaychand, A. (2011). In silico drug design-tool for overcoming the innovation deficit in the drug discovery process. 3(2).

Bianchi, M., Marom, G., Ghosh, R. P., Rotman, O. M., Parikh, P., Gruberg, L., and Bluestein, D. (2019). Patient-specific simulation of transcatheter aortic valve replacement : Impact of deployment options on paravalvular leakage. *Biomechanics and Modeling in Mechanobiology*, 18(2) :435–451.

Biot, M. A. and Temple, G. (1972). Theory of Finite Deformations of Porous Solids. *Indiana University Mathematics Journal*, 21(7) :597–620.

Borgström, L., Olsson, B., and Thorsson, L. (2006). Degree of Throat Deposition Can Explain the Variability in Lung Deposition of Inhaled Drugs. *Journal of Aerosol Medicine*, 19(4) :473–483.

Boudin, L., Grandmont, C., Lorz, A., and Moussa, A. (2015). Modelling and Numerics for Respiratory Aerosols. *Communications in Computational Physics*, 18(3) :723–756.

Burrowes, K., Swan, A., Warren, N., and Tawhai, M. (2008). Towards a virtual lung : Multiscale, multi-physics modelling of the pulmonary system. *Philosophical Transactions of the Royal Society A : Mathematical, Physical and Engineering Sciences*, 366(1879) :3247–3263.

Burtschell, B. (2016). *Mechanical Modeling and Numerical Methods for Poromechanics : Application to Myocardium Perfusion*. PhD thesis.

Carniel, E. L., Frigo, A., Fontanella, C. G., De Benedictis, G. M., Rubini, A., Barp, L., Pluchino, G., Sabbadini, B., and Polese, L. (2017). A biomechanical approach to the analysis of methods and procedures of bariatric surgery. *Journal of Biomechanics*, 56 :32–41.

Carniel, E. L., Toniolo, I., and Fontanella, C. G. (2020). Computational Biomechanics : In-Silico Tools for the Investigation of Surgical Procedures and Devices. *Bioengineering*, 7(2) :48.

Cavazza, A., Rossi, G., Carbonelli, C., Spaggiari, L., Paci, M., and Roggeri, A. (2010). The role of histology in idiopathic pulmonary fibrosis : An update. *Respiratory Medicine*, 104 :S11–S22.

Cazeaux, P. and Grandmont, C. (2015). Homogenization of a multiscale viscoelastic model with nonlocal damping, application to the human lungs. *Mathematical Models and Methods in Applied Sciences*, 25(06) :1125–1177.

Chabiniok, R., Moireau, P., Lesault, P.-F., Rahmouni, A., Deux, J.-F., and Chapelle, D. (2012). Estimation of tissue contractility from cardiac cine-MRI using a biomechanical heart model. *Biomechanics and Modeling in Mechanobiology*, 11(5) :609–630.

Chabiniok, R., Wang, V. Y., Hadjicharalambous, M., Asner, L., Lee, J., Sermesant, M., Kuhl, E., Young, A. A., Moireau, P., Nash, M. P., Chapelle, D., and Nordsletten, D. A. (2016). Multiphysics and multiscale modelling, data–model fusion and integration of organ physiology in the clinic : Ventricular cardiac mechanics. *Interface Focus*, 6(2) :20150083.

Chapelle, D. and Moireau, P. (2014). General coupling of porous flows and hyperelastic formulations—From thermodynamics principles to energy balance and compatible time schemes. *European Journal of Mechanics - B/Fluids*, 46 :82–96.

Chen, F., Yu, S. C., and Lai, A. C. (2006). Modeling particle distribution and deposition in indoor environments with a new drift–flux model. *Atmospheric Environment*, 40(2) :357–367.

Claude, N., Goldfain-Blanc, F., and Guillouzo, A. (2009). La place des méthodes *in silico, in vitro, in omic* dans l'évaluation de la sécurité des médicaments. *médecine/sciences*, 25(1) :105–110.

Colic, K., Sedmak, A., Grbovic, A., Burzić, M., Hloch, S., and Sedmak, S. (2016). Numerical Simulation of Fatigue Crack Growth in Hip Implants. *Procedia Engineering*, 149 :229–235.

Concha, F., Sarabia-Vallejos, M., and Hurtado, D. E. (2018). Micromechanical model of lung parenchyma hyperelasticity. *Journal of the Mechanics and Physics of Solids*, 112 :126–144.

Courtecuisse, H., Allard, J., Kerfriden, P., Bordas, S. P., Cotin, S., and Duriez, C. (2014). Real-time simulation of contact and cutting of heterogeneous soft-tissues. *Medical Image Analysis*, 18(2) :394–410.

Coussy, O. (2004). *Poromechanics.* Wiley, Chichester.

Demanget, N., Avril, S., Badel, P., Orgéas, L., Geindreau, C., Albertini, J.-N., and Favre, J.-P. (2012). Computational comparison of the bending behavior of aortic stent-grafts. *Journal of the Mechanical Behavior of Biomedical Materials*, 5(1) :272–282.

Denny, E. and Schroter, R. (2006). A model of non-uniform lung parenchyma distortion. *Journal of Biomechanics*, 39(4) :652–663.

Dickson, M. and Gagnon, J.-P. (2004). The cost of new drug discovery and development. *Discovery Medicine*, 4(22) :172–179.

Dormieux, L., Kondo, D., and Ulm, F.-J. (2006). *Microporomechanics.* John Wiley & Sons, Chichester, West Sussex, England ; Hoboken, NJ.

Ehrmann, S., Schmid, O., Darquenne, C., Rothen-Rutishauser, B., Sznitman, J., Yang, L., Barosova, H., Vecellio, L., Mitchell, J., and Heuze-Vourc'h, N. (2020). Innovative preclinical models for pulmonary drug delivery research. *Expert Opinion on Drug Delivery*, 17(4) :463–478.

Ekins, S., Mestres, J., and Testa, B. (2007). *In Silico* pharmacology for drug discovery : Applications to targets and beyond. *British Journal of Pharmacology*, 152(1) :21–37.

Fetita, C., Preteux, F., Beigelman-Aubry, C., and Grenier, P. (2004). Pulmonary Airways : 3-D Reconstruction From Multislice CT and Clinical Investigation. *IEEE Transactions on Medical Imaging*, 23(11) :1353–1364.

Gefen, A., Elad, D., and Shiner, R. (1999). Analysis of stress distribution in the alveolar septa of normal and simulated emphysematic lungs. *Journal of Biomechanics*, 32(9) :891–897.

Genet, M., Patte, C., and Chapelle, D. (2020a). Personalized Pulmonary Poromechanics. *14th World Congress on Computational Mechanics (WCCM).*

Genet, M., Patte, C., and Fetita, C. (2020b). Personalized Pulmonary Poromechanics. *45ème Congrès de la Société de Biomécanique.*

George, P. M., Wells, A. U., and Jenkins, R. G. (2020). Pulmonary fibrosis and COVID-19 : The potential role for antifibrotic therapy. *The Lancet Respiratory Medicine*, 8(8) :807–815.

Ghil, M. and Malanotte-Rizzoli, P. (1991). Data Assimilation in Meteorology and Oceanography. In *Advances in Geophysics*, volume 33, pages 141–266. Elsevier.

Gindre, J., Bel-Brunon, A., Rochette, M., Lucas, A., Kaladji, A., Haigron, P., and Combescure, A. (2017). Patient-Specific Finite-Element Simulation of the Insertion of Guidewire During an EVAR Procedure : Guidewire Position Prediction Validation on 28 Cases. *IEEE Transactions on Biomedical Engineering*, 64(5) :1057–1066.

Gleeson, M. P., Modi, S., Bender, A., L. Marchese Robinson, R., Kirchmair, J., Promkatkaew, M., Hannongbua, S., and C. Glen, R. (2012). The Challenges Involved in Modeling Toxicity Data In Silico : A Review. *Current Drug Metabolism*, 18(9) :1266–1291.

Goligher, E. C., Ferguson, N. D., and Brochard, L. J. (2016). Clinical challenges in mechanical ventilation. *The Lancet*, 387(10030) :1856–1866.

Haak, A. J., Tan, Q., and Tschumperlin, D. J. (2018). Matrix biomechanics and dynamics in pulmonary fibrosis. *Matrix Biology*, 73 :64–76.

Hinz, B. and Suki, B. (2016). Does Breathing Amplify Fibrosis ? *American Journal of Respiratory and Critical Care Medicine*, 194(1) :9–11.

Hofmann, W. and Koblinger, L. (1990). Monte Carlo modeling of aerosol deposition in human lungs. Part II : Deposition fractions and their sensitivity to parameter variations. *Journal of Aerosol Science*, 21(5) :675–688.

Hübner, R.-H., Gitter, W., Eddine El Mokhtari, N., Mathiak, M., Both, M., Bolte, H., Freitag-Wolf, S., and Bewig, B. (2008). Standardized quantification of pulmonary fibrosis in histological samples. *BioTechniques*, 44(4) :507–517.

Hurtado, D. E., Villarroel, N., Retamal, J., Bugedo, G., and Bruhn, A. (2016). Improving the Accuracy of Registration-Based Biomechanical Analysis : A Finite Element Approach to Lung Regional Strain Quantification. *IEEE Transactions on Medical Imaging*, 35(2) :580–588.

Kazmi, S. R., Jun, R., Yu, M.-S., Jung, C., and Na, D. (2019). In silico approaches and tools for the prediction of drug metabolism and fate : A review. *Computers in Biology and Medicine*, 106 :54–64.

Khor, W. S., Baker, B., Amin, K., Chan, A., Patel, K., and Wong, J. (2016). Augmented and virtual reality in surgery—the digital surgical environment : Applications, limitations and legal pitfalls. *Annals of Translational Medicine*, 4(23) :454–454.

Kim, J.-H., Avril, S., Duprey, A., and Favre, J.-P. (2012). Experimental characterization of rupture in human aortic aneurysms using a full-field measurement technique. *Biomechanics and Modeling in Mechanobiology*, 11(6) :841–853.

King, T. E., Pardo, A., and Selman, M. (2011). Idiopathic pulmonary fibrosis. *The Lancet*, 378(9807) :1949–1961.

Koblinger, L. and Hofmann, W. (1990). Monte Carlo modeling of aerosol deposition in human lungs. Part I : Simulation of particle transport in a stochastic lung structure. *Journal of Aerosol Science*, 21(5) :661–674.

Kuebler, W. M., Jordt, S.-E., and Liedtke, W. B. (2020). Urgent reconsideration of lung edema as a preventable outcome in COVID-19 : Inhibition of TRPV4 represents a promising and feasible approach. *American Journal of Physiology-Lung Cellular and Molecular Physiology*, 318(6) :L1239–L1243.

Lambert, A. R., O'shaughnessy, P. T., Tawhai, M. H., Hoffman, E. A., and Lin, C.-L. (2011). Regional Deposition of Particles in an Image-Based Airway Model : Large-Eddy Simulation and Left-Right Lung Ventilation Asymmetry. *Aerosol Science and Technology*, 45(1) :11–25.

Lauzon, A.-M., Bates, J. H. T., Donovan, G., Tawhai, M., Sneyd, J., and Sanderson, M. J. (2012). A Multi-Scale Approach to Airway Hyperresponsiveness : From Molecule to Organ. *Frontiers in Physiology*, 3.

Le Gall, A., Vallée, F., Pushparajah, K., Hussain, T., Mebazaa, A., Chapelle, D., Gayat, É., and Chabiniok, R. (2020). Monitoring of cardiovascular physiology augmented by a patient-specific biomechanical model during general anesthesia. A proof of concept study. *PLOS ONE*, 15(5).

Lederer, D. J. and Martinez, F. J. (2018). Idiopathic Pulmonary Fibrosis. *New England Journal of Medicine*, 378(19) :1811–1823.

Lim, K. Y. H., Zheng, P., and Chen, C.-H. (2020). A state-of-the-art survey of Digital Twin : Techniques, engineering product lifecycle management and business innovation perspectives. *Journal of Intelligent Manufacturing*, 31(6) :1313–1337.

Lin, C.-L., Tawhai, M. H., and Hoffman, E. A. (2013). Multiscale image-based modeling and simulation of gas flow and particle transport in the human lungs : Gas flow and particle transport in the human lungs. *Wiley Interdisciplinary Reviews : Systems Biology and Medicine*, 5(5) :643–655.

Lin, C.-L., Tawhai, M. H., McLennan, G., and Hoffman, E. A. (2007). Characteristics of the turbulent laryngeal jet and its effect on airflow in the human intra-thoracic airways. *Respiratory Physiology & Neurobiology*, 157(2-3) :295–309.

Lin, X., Zong, Z., and Niu, J. (2015). Finite element model validation of bridge based on structural health monitoring—Part II : Uncertainty propagation and model validation. *Journal of Traffic and Transportation Engineering (English Edition)*, 2(4) :279–289.

Liu, F., Mih, J. D., Shea, B. S., Kho, A. T., Sharif, A. S., Tager, A. M., and Tschumperlin, D. J. (2010). Feedback amplification of fibrosis through matrix stiffening and COX-2 suppression. *The Journal of Cell Biology*, 190(4) :693–706.

Longest, P. W. and Holbrook, L. T. (2012). In silico models of aerosol delivery to the respiratory tract — Development and applications. *Advanced Drug Delivery Reviews*, 64(4) :296–311.

Marescaux, J., Clément, J.-M., Tassetti, V., Koehl, C., Cotin, S., Russier, Y., Mutter, D., Delingette, H., and Ayache, N. (1998). Virtual Reality Applied to Hepatic Surgery Simulation : The Next Revolution :. *Annals of Surgery*, 228(5) :627–634.

Martonen, T., Fleming, J., Schroeter, J., Conway, J., and Hwang, D. (2003). In silico modeling of asthmaq. *Advanced Drug Delivery Reviews*, 55(7) :829–849.

Mauroy, B., Filoche, M., Andrade, J. S., and Sapoval, B. (2003). Interplay between Geometry and Flow Distribution in an Airway Tree. *Physical Review Letters*, 90(14) :148101.

Michelson, S., Sehgal, A., and Friedrich, C. (2006). In silico prediction of clinical efficacy. *Current Opinion in Biotechnology*, 17(6) :666–670.

Moireau, P. (2008). *Assimilation de Données Par Filtrage Pour Les Systèmes Hyperboliques Du Second Ordre - Applications à La Mécanique Cardiaque.* PhD thesis.

Moireau, P., Chapelle, D., and Tallec, P. L. (2008). Joint state and parameter estimation for distributed mechanical systems. *Computer Methods in Applied Mechanics and Engineering*, 197(6-8) :659–677.

Mow, V. C., Kuei, S. C., Lai, W. M., and Armstrong, C. G. (1980). Biphasic Creep and Stress Relaxation of Articular Cartilage in Compression : Theory and Experiments. *Journal of Biomechanical Engineering*, 102(1) :73–84.

MRC CRASH Trial Collaborators (2008). Predicting outcome after traumatic brain injury : Practical prognostic models based on large cohort of international patients. *BMJ*, 336(7641) :425–429.

Nalysnyk, L., Cid-Ruzafa, J., Rotella, P., and Esser, D. (2012). Incidence and prevalence of idiopathic pulmonary fibrosis : Review of the literature. *European Respiratory Review*, 21(126) :355–361.

Naseer, A., Jahangirian, M., and Stergioulas, L. (2008). Potential applications of simulation modelling techniques in healthcare : Lessons learned from aerospace & military. page 13.

Newman, S. P. (2017). Drug delivery to the lungs : Challenges and opportunities. *Therapeutic Delivery*, 8(8) :647–661.

Oakes, J. M., Marsden, A. L., Grandmont, C., Shadden, S. C., Darquenne, C., and Vignon-Clementel, I. E. (2014). Airflow and Particle Deposition Simulations in Health and Emphysema : From In Vivo to In Silico Animal Experiments. *Annals of Biomedical Engineering*, 42(4) :899–914.

Patte, C., Brillet, P.-Y., Fetita, C., Gille, T., Bernaudin, J.-F., Nunes, H., Chapelle, D., and Genet, M. (2020). Estimation of patient-specific mechanical parameters in pulmonary diseases. *VPH2020 conference.*

Patte, C., Genet, M., Fetita, C., Brillet, P.-Y., and Chapelle, D. (2019). Mécanique pulmonaire personnalisée : modélisation et estimation - Application à la fibrose pulmonaire. *14ème Colloque National en Calcul des Structures (CSMA2019).*

Perrin, D., Badel, P., Orgeas, L., Geindreau, C., rolland du Roscoat, S., Albertini, J.-N., and Avril, S. (2016). Patient-specific simulation of endovascular repair surgery with tortuous aneurysms requiring flexible stent-grafts. *Journal of the Mechanical Behavior of Biomedical Materials*, 63 :86–99.

Plantier, L., Cazes, A., Dinh-Xuan, A.-T., Bancal, C., Marchand-Adam, S., and Crestani, B. (2018). Physiology of the lung in idiopathic pulmonary fibrosis. *European Respiratory Review*, 27(147) :170062.

Poletti, V., Ravaglia, C., Buccioli, M., Tantalocco, P., Piciucchi, S., Dubini, A., Carloni, A., Chilosi, M., and Tomassetti, S. (2013). Idiopathic Pulmonary Fibrosis : Diagnosis and Prognostic Evaluation. *Respiration*, 86(1) :5–12.

Rausch, S. M. K., Haberthür, D., Stampanoni, M., Schittny, J. C., and Wall, W. A. (2011). Local Strain Distribution in Real Three-Dimensional Alveolar Geometries. *Annals of Biomedical Engineering*, 39(11) :2835–2843.

Rogliani, P., Calzetta, L., Cavalli, F., Matera, M. G., and Cazzola, M. (2016). Pirfenidone, nintedanib and N-acetylcysteine for the treatment of idiopathic pulmonary fibrosis : A systematic review and meta-analysis. *Pulmonary Pharmacology & Therapeutics*, 40 :95–103.

Sauleda, J., Núñez, B., Sala, E., and Soriano, J. (2018). Idiopathic Pulmonary Fibrosis : Epidemiology, Natural History, Phenotypes. *Medical Sciences*, 6(4) :110.

Savanovic, M., Strbac, B., Jaros, D., Cazic, D., Kolarevic, G., and Foulquier, J.-N. (2020). Assessment of Internal and External Surrogates for Lung Stereotactic Body Radiation Therapy. *Iranian Journal of Medical Physics*.

Seppenwoolde, Y., Shirato, H., Kitamura, K., Shimizu, S., van Herk, M., Lebesque, J. V., and Miyasaka, K. (2002). Precise and real-time measurement of 3D tumor motion in lung due to breathing and heartbeat, measured during radiotherapy. *International Journal of Radiation Oncology Biology Physics*, 53(4) :822–834.

Sermesant, M., Chabiniok, R., Chinchapatnam, P., Mansi, T., Billet, F., Moireau, P., Peyrat, J., Wong, K., Relan, J., Rhode, K., Ginks, M., Lambiase, P., Delingette, H., Sorine, M., Rinaldi, C., Chapelle, D., Razavi, R., and Ayache, N. (2012). Patient-specific electromechanical models of the heart for the prediction of pacing acute effects in CRT : A preliminary clinical validation. *Medical Image Analysis*, 16(1) :201–215.

Simon, B. R., Wu, J. S. S., Carlton, M. W., Kazarian, L. E., France, E. P., Evans, J. H., and Zienkiewicz, O. C. (1985). Poroelastic Dynamic Structural Models of Rhesus Spinal Motion Segments. *Spine*, 10(6) :494–507.

Sonke, J.-J., Aznar, M., and Rasch, C. (2019). Adaptive Radiotherapy for Anatomical Changes. *Seminars in Radiation Oncology*, 29(3) :245–257.

Spagnolo, P., Balestro, E., Aliberti, S., Cocconcelli, E., Biondini, D., Casa, G. D., Sverzellati, N., and Maher, T. M. (2020). Pulmonary fibrosis secondary to COVID-19 : A call to arms ? *The Lancet Respiratory Medicine*, 8(8) :750–752.

Swigris, J. J. (2005). Health-related quality of life in patients with idiopathic pulmonary fibrosis : A systematic review. *Thorax*, 60(7) :588–594.

Tarando, S. R. (2018). *Quantitative Follow-up of Pulmonary Diseases Using Deep Learning Models*. PhD thesis.

Tawhai, M. H., Hunter, P., Tschirren, J., Reinhardt, J., McLennan, G., and Hoffman, E. A. (2004). CT-based geometry analysis and finite element models of the human and ovine bronchial tree. *Journal of Applied Physiology*, 97(6) :2310–2321.

Tawhai, M. H., Nash, M. P., Lin, C.-L., and Hoffman, E. A. (2009). Supine and prone differences in regional lung density and pleural pressure gradients in the human lung with constant shape. *Journal of Applied Physiology*, 107(3) :912–920.

Tgavalekos, N. T., Tawhai, M., Harris, R. S., Mush, G., Vidal-Melo, M., Venegas, J. G., and Lutchen, K. R. (2005). Identifying airways responsible for heterogeneous ventilation and mechanical dysfunction in asthma : An image functional modeling approach. *Journal of Applied Physiology*, 99(6) :2388–2397.

Tian, S., Xiong, Y., Liu, H., Niu, L., Guo, J., Liao, M., and Xiao, S.-Y. (2020). Pathological study of the 2019 novel coronavirus disease (COVID-19) through postmortem core biopsies. *Modern Pathology*, 33(6) :1007–1014.

Topol, E. J. (2019). High-performance medicine : The convergence of human and artificial intelligence. *Nature Medicine*, 25(1) :44–56.

Viceconti, M. and Hunter, P. (2016). The Virtual Physiological Human : Ten Years After. *Annual Review of Biomedical Engineering*, 18(1) :103–123.

Vishnevskiy, V., Gass, T., Szekely, G., Tanner, C., and Goksel, O. (2017). Isotropic Total Variation Regularization of Displacements in Parametric Image Registration. *IEEE Transactions on Medical Imaging*, 36(2) :385–395.

Vy, P., Auffret, V., Badel, P., Rochette, M., Le Breton, H., Haigron, P., and Avril, S. (2016). Review of patient-specific simulations of transcatheter aortic valve implantation. *International Journal of Advances in Engineering Sciences and Applied Mathematics*, 8(1) :2–24.

West, J. B. and Matthews, F. L. (1972). Stresses, strains, and surface pressures in the lung caused by its weight. *Journal of Applied Physiology*, 32(3) :332–345.

Wiechert, L. and Wall, W. (2010). A nested dynamic multi-scale approach for 3D problems accounting for micro-scale multi-physics. *Computer Methods in Applied Mechanics and Engineering*, 199(21-22) :1342–1351.

Wu, H., Yu, Y., Huang, H., Hu, Y., Fu, S., Wang, Z., Shi, M., Zhao, X., Yuan, J., Li, J., Yang, X., Bin, E., Wei, D., Zhang, H., Zhang, J., Yang, C., Cai, T., Dai, H., Chen, J., and Tang, N. (2019). Progressive Pulmonary Fibrosis Is Caused by Elevated Mechanical Tension on Alveolar Stem Cells. *Cell*, 180(1) :107–121.e17.

CHAPTER 1

From pulmonary physiology to lung modeling

This chapter is composed of two parts. In a first part, the main elements of pulmonary physiology required for a good understanding of lung mechanical modeling are given. Lung function and anatomy are described, as well as breathing mechanisms. Various ways to evaluate lung functions are also mentioned. In a second part, various types of mechanical models are reviewed: organ scale models, with discussions about the choice of boundary conditions and constitutive behavior, and multiscale models. Finally, poromechanics is introduced, especially the general model on which this work is based.

Contents

1.1 From pulmonary physiology ...

1.1.1 Lung functions

Breathing, the main function Lungs are vital organs as they play a major role in both the respiratory system and the circulatory system.

The goal of breathing is, on the one hand, to provide oxygen (O_2) to the body, and more specifically to the body cells, and, on the other hand, to reject carbon dioxide (CO_2). Indeed, cells require O_2 to produce energy that will be used by the body to grow, live and function. As a consequence, cells produce and reject CO_2 as a waste product. Oxygen should enter the body continuously in time to be renewed, and should also be distributed to organs. Thus, two phenomena occur: *ventilation*, to induce airflow and renew O_2 inside respiratory tract, and *circulation*, to transport O_2 along blood vessels and provide it to organs and cells. The same phenomena are also present for CO_2, but in the inverse direction, as it is produced by cells and rejected into air. The circulation system is represented in Figure 1.1.

Lungs are then the interface between both systems: airflow and blood flow. They are the place of gas exchanges where O_2 and CO_2 move in and out: O_2 present in inhaled air enters the blood circulation, whereas CO_2 in blood goes into airflow to be ejected to the atmosphere.

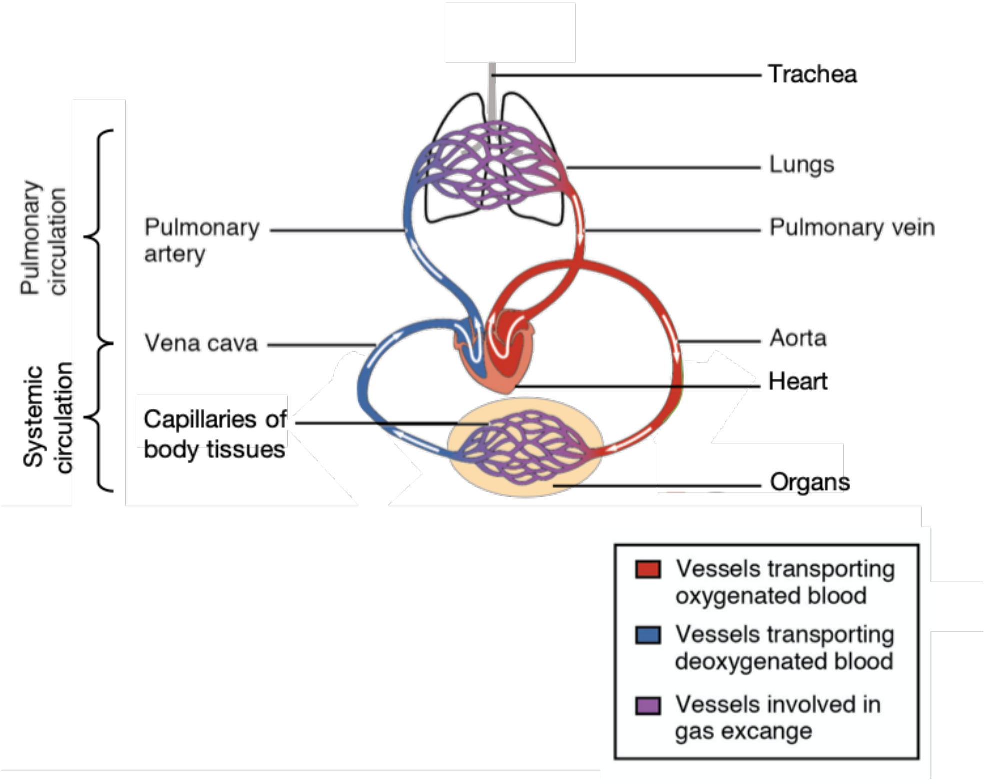

Figure 1.1 – Circulation system in the human body. Figure modified from OpenStax College - Anatomy & Physiology, licensed under CC BY 3.0.

Other functions Lungs have a role in the regulation of the pH of the body by controlling CO_2 quantity present in the body. Since CO_2 is acid, pH is impacted by its concentration. Lungs can impact the quantity of CO_2 in modifying the rate and depth of breathing to reject it more or less. These ventilation parameters are controlled by a chemoreceptors system [Kane, 1973].

Moreover, lungs have also other functions, not linked to breathing but important for normal physiology [Joseph et al., 2013]. Lungs contribute to the defense mechanisms with cough and sneeze, which are reflexes after mechanical or chemical stimuli, or with the mucociliary clearance, which eliminates foreign particles. They also participate to the innate and adaptative immune system through the various macrophages and lymphocytes subpopulations. They filter both air-born particles and bloodstream, they are a vascular reservoir with pulmonary capillaries and the other pulmonary blood vessels and they play a role in metabolism. They take part in the regulation of the body temperature since breathing allows heat loss by making fresh air circulate. This last function is significant in dogs: as they cannot sweat, breathing is their main way to regulate their temperature [Crawford, 1962].

1.1.2 Respiratory system anatomy

1.1.2.1 Lungs anatomy

The human chest contains two lungs in the pleural space. The upper part of lungs, close to the neck, is called *apex*, while the bottom part is the *base*. Each lung is composed of several *lobes* separated from each other by *fissures*: two lobes for the left lung and three lobes for the right lung. Each lobe is divided into pulmonary segments and lobules.

Lungs are composed of three different structures: the lower respiratory tract, filled with air, the blood vessels, transporting blood, and the supporting pulmonary tissue. Each of them is described in the following paragraphs.

Respiratory tract The respiratory tract is a set of airways, which leads air from the atmosphere to lungs and alveoli during breathing. It is divided into two parts: the upper respiratory tract and the lower respiratory tract.

The *upper respiratory tract* is the entrance of air in the body. Air is entering the body from the mouth and the nose. Then, it goes to nasal cavities and the pharynx, and finally to the larynx.

The *lower respiratory tract*, represented in Figure 1.2, starts with the trachea, located just after the larynx. Then it divides into two bronchi, each of them entering one lung at the *hilum*, the “root” of lungs, where blood vessels, pulmonary arteries and veins, and airways enter the lungs. The bronchial tree is composed of a dichotomous fractal splitting of airways [Mauroy et al., 2004]. In total, the lower respiratory tract is composed of 23 divisions from the trachea to the smallest pulmonary units, the *alveoli*, with bronchi and bronchioles as intermediate state. Each division makes airways diameter and thickness smaller. The first divisions, also called *conducting airways*, do not contribute to gas exchanges and are useful to direct air to the *acinar airways*, or *respiratory airways*. The second category, starting from the 17th division, is the place of gas exchanges and allows to fulfill lung function since acinar airways are highly vascularized.

The different divisions of airways define different pulmonary units. Lungs are supplied in air by bronchi, lobes by secondary bronchi, and *segments* by tertiary bronchi. Each terminal bronchiole supplies in air a part of the lung, called *lobule*, (previously called secondary lobule). Lobules are wrapped and separated by *interlobular septa*. A lobule measures about 13 to 20 mm. It contains three to five *acini*, the terminal respiratory unit, supplied by a respiratory bronchiole. An acinus measures 6 to 20 mm and includes a set of alveoli. Both lobules and acini are important anatomical and physiological units of lungs and are mostly involved in pulmonary diseases [Osborne et al., 1983] (see Figure 1.3).

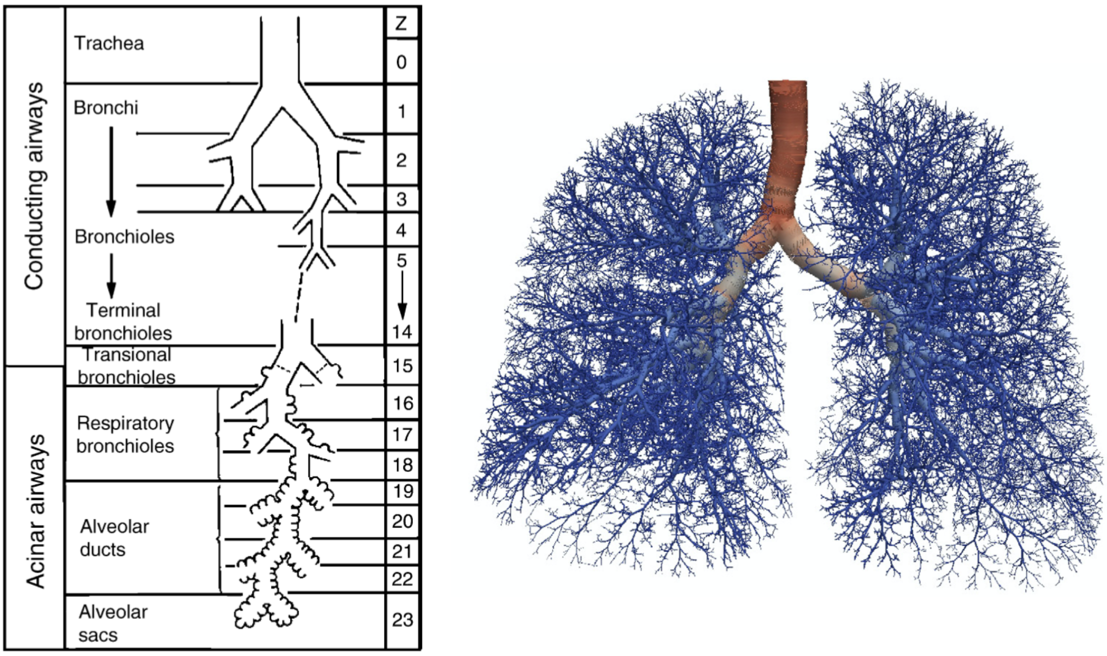

(a) (b)

Figure 1.2 – Lower respiratory tract. (a) Representation of the 23 divisions of the respiratory tract from the trachea to alveoli. Figure taken from Weibel et al. [2005]. (b) 3D reconstruction of the pulmonary airways. Figure taken from Bordas et al. [2015].

Alveoli Alveoli are small sacs at the termination of pulmonary airways and are the place of gas exchanges. Their diameter is of the order of 250 to 300 µm [Weibel, 1963]. Human lungs contain about 300 million alveoli. Their total surface area is estimated between either 70 to 80 m^2 [Weibel, 1963] or 91 to 118 m^2 [Colebatch and Ng, 1992]. Such a surface area associated with an amount of volume in the order of a few liters is made possible only by these numerous divisions. Illustrations of alveoli are given in Figure 1.3.

The extremely thin and vascularized alveolar wall and the large available total surface area allow efficient gas exchanges. Indeed, gas are diffusing through the alveolar wall from alveolar air to blood capillaries for O_2 and inversely for CO_2. The driving force of gas diffusion is the difference in partial pressure: blood coming into lungs is poor in O_2 and rich in CO_2, whereas air inside alveoli is rich in O_2 and poor in CO_2. That is why O_2 diffuses towards blood and CO_2 is rejected into air.

Alveoli tend to collapse because of their spherical shape and the air-liquid interface of the alveoli surface. Thus, the alveoli surface is covered by a thin liquid layer containing tensioactive material, called *surfactant*, which modifies the surface tension of the interface. In reducing the surface tension of the alveoli surface, it facilitates alveoli expansion and collapsed airways recruitment during inhalation and keeps alveoli open during exhalation. Surfactant is then essential for a normal breathing.

Pulmonary blood vessels A dense network of blood vessels is located in the lungs. Deoxygenated blood, ejected by the right ventricle of the heart, is coming to the lungs through pulmonary arteries. These arteries divide to capillaries, which circulate into the alveolar wall where gas exchanges happen. There, blood becomes rich in O_2. Then, pulmonary veins bring back the oxygenated blood to the left atrium of the heart to be sent to the various organs of the body.

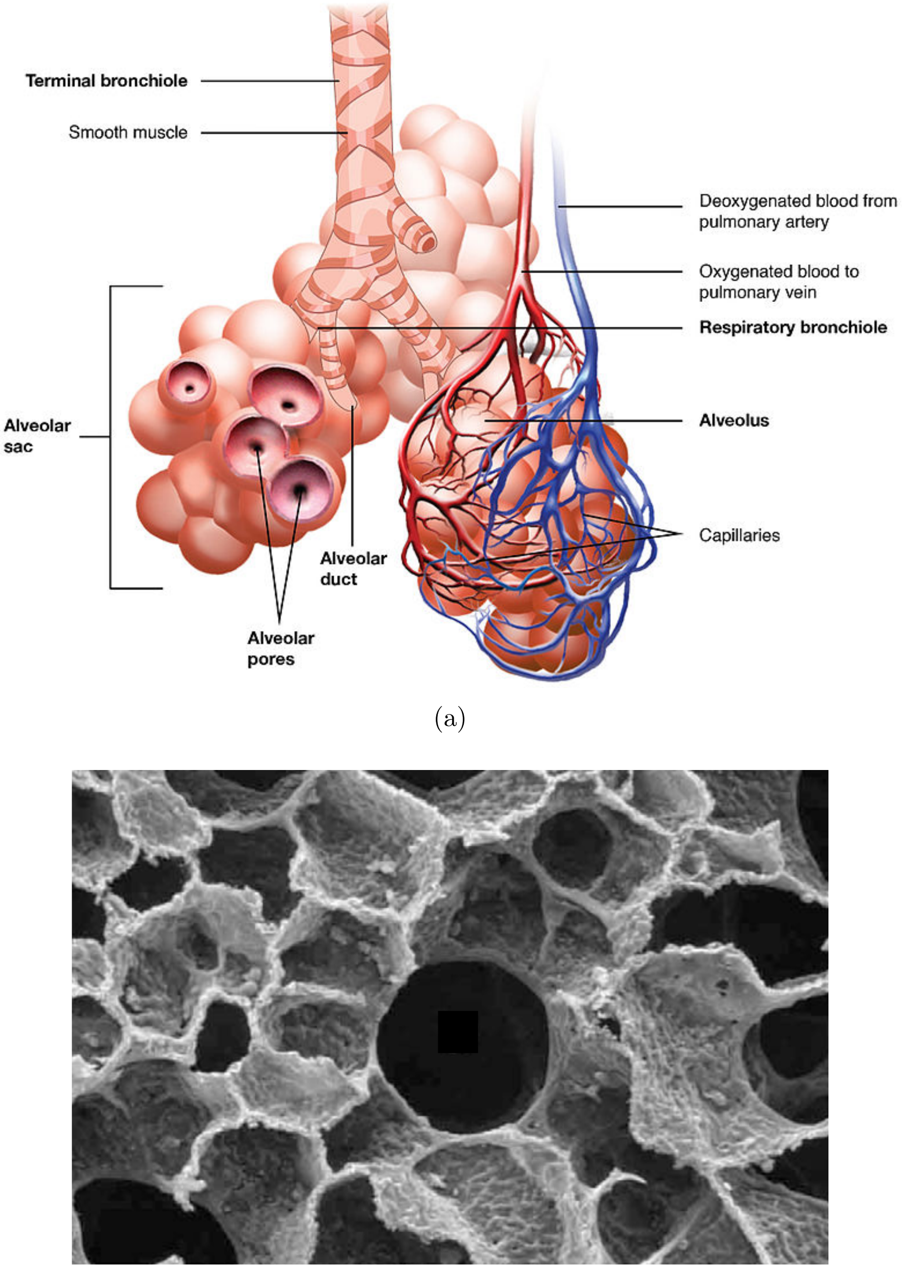

(a)

(b)

Figure 1.3 – Representation of alveoli. (a) Schematic of the respiratory zone, composed of a set of alveoli. Figure by OpenStax College - Anatomy & Physiology, licensed under CC BY 3.0. (b) Scanning electron micrograph of a lung cross-section. Figure modified from Weibel et al. [2005].

Interstitium tissue The interstitium tissue is the connective tissue that supports the pulmonary structure. Indeed, it constitutes the alveolar wall, where gas exchanges take place. It is mainly composed of collagen and elastin fibers, which give its mechanical properties.

1.1.2.2 Lungs surroundings

During breathing, lungs surroundings play a major role. The main elements involved during the breathing process are described in the following paragraphs. They are represented in Figure 1.4.

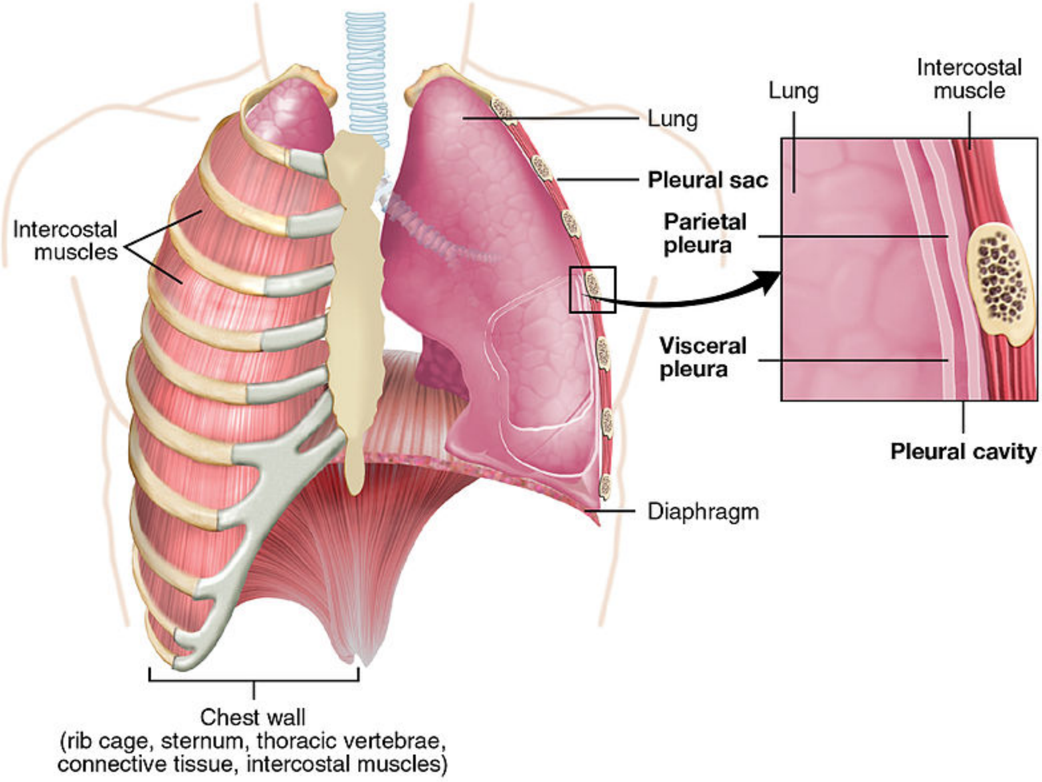

Figure 1.4 – Lungs surroundings. With lungs, the pleura, the chest wall and the diaphragm are the main components involved in breathing. Figure by OpenStax College - Anatomy & Physiology, licensed under CC BY 3.0.

Rib cage The *rib cage*, enclosing the lungs, is a bony structure which has a protective role towards the lungs and other vital organs. It is composed of several bones: the spine at the back, the sternum at the front and twelve pairs of ribs, curved and joining the spine to the sternum.

Between ribs are located the *intercostal muscles*, which allow the rib cage movement during breathing. They can be activated during forced inhalation and forced exhalation. In that case, they contract to decrease the distance between each rib and induce an overall volume change of the rib cage.

Pleura Lungs are surrounded on the whole surface by the *pleura*. It is a serous membrane located between the lungs and the rib cage and composed of two sheets: the *visceral pleura*, covering the lung surface, even between lobes, and the *parietal pleura*, covering the rib cage surface, the diaphragm and the mediastinum (see below details about the mediastinum). The continuity between both sheets takes place at the root of each lung, where bronchi, pulmonary arteries and pulmonary veins enter lungs.

The space between both pleura sheets is called *pleural cavity.* A small quantity of liquid is present to allow the sliding between sheets during breathing. It acts as a lubricant and decreases friction during sliding. A negative pressure is present inside the pleural cavity and allows both pleural sheets to remain in contact together. Consequently, it maintains lungs inflated: without this negative pleural pressure, lungs would deflate. The variation of pleural pressure, mainly under the action of diaphragm or intercostal muscles, has an impact on inflation and deflation of lungs

Diaphragm The diaphragm is a muscle underneath the lung base with a convex surface, looking like a C-shaped structure. It separates the thoracic cavity and the abdominal cavity and is attached to the thorax. Several openings in the diaphragm allow other structures, like the aorta, the vena cava and the esophagus, to join both cavities. Its contractions and releases are the key of breathing as they impact the pleural pressure, hence lungs inflation and deflation during inhalation and exhalation, respectively. The diaphragm contractions are periodic and happen at the beginning of each breathing cycle.

Mediastinum The mediastinum is the central area of the thoracic cage and is placed between lungs. It contains the heart, the esophagus, the trachea and the bronchi.

1.1.3 Breathing mechanics

Breathing is a phenomenon involving lungs, but also lungs surroundings, which concerns lungs inflation. A breathing cycle is composed of one inhalation and one exhalation and lasts about four seconds. In general, the inhalation is active, whereas the exhalation is passive. For our purposes, two types of breathing should be distinguished, differing by the driving force of inhalation: the spontaneous breathing, which is the physiological breathing, and the mechanical ventilation.

Spontaneous breathing Spontaneous breathing is the normal breathing. Lungs surroundings have a central role, since lungs cannot inflate on their own. The main contributor of breathing is the diaphragm.

Inhalation is initiated by the diaphragm contraction. Diaphragm flattens and pulls on the pleura, decreasing the pleural pressure, making it more negative. The pleural pressure decrease tends to increase lungs volume and creates a small depression inside the airways, which makes air enter lungs. In case of a forced inhalation, intercostal muscles can contract in the same time as the diaphragm, leading to an increase of the rib cage diameter, which then pulls also on the pleura and impacts the pleural pressure. The pleural pressure becomes more negative than during normal inhalation and lungs inflation is larger. During normal breath, the diaphragm contraction leads to a diaphragm displacement of about 1 cm, but it can reach 10 cm between a forced exhalation and a forced inhalation [West and Nadeau, 2003].

On the contrary, exhalation occurs with the diaphragm relaxation. As elastic organs, lungs tend to come back to the initial position on their own. Consequently, lungs deflate, which induces a small overpressure inside pulmonary airways, ejecting air from lungs. In the case of a forced exhalation, intercostal muscles can contract to eject more air, by reducing the rib cage diameter and pushing on lungs. Whereas normal exhalation is passive, forced exhalation is active.

Mechanical ventilation Mechanical ventilation aims to mechanically assist or replace spontaneous breathing. It requires the use of a machine called *ventilator*, which provides air to the patient. This process is invasive for the patient since a tube is inserted into the throat and the trachea. Mechanical ventilation is used for patients which are unable to breathe on their own, for example during anesthesia or coma. Indeed, anesthetics drugs disrupt a regular breathing by impacting the diaphragm and can lead to apnea. In this type of breathing, the diaphragm, which does not fulfill his role anymore, is replaced by the ventilator.

In that case, lungs inflation is induced by the positive air pressure provided by the ventilator. Alveoli pressure increases with the ventilated pressure and air flows inside lungs. Then the positive air pressure decreases for exhalation, lungs tend to come back to their unloaded position and air flows out of lungs. The end-expiratory air pressure is kept positive to prevent alveoli from collapsing.

Contrary to the pleural pressure during spontaneous breathing that leads to lungs inflation only, the ventilated pressure inflates lungs as well as expands rib cage and pushes diaphragm. Indeed, lungs surroundings resist to lung inflation as breathing muscles (diaphragm and intercostal muscles) remain passive. That is why the ventilated pressure is larger than the pleural pressure for a same amount of inflation.

The parameters of the ventilator can be tuned to control the patient breathing: the breathing rate, the flux, the amount of air provided during inhalation, the end-inhalation pressure, etc.

1.1.4 Evaluation of pulmonary function

Several characteristics can be measured to evaluate the pulmonary function. They give important information about the respiratory system during breathing. Such measurements are performed for diagnostic purposes for patients suffering from respiratory symptoms and to follow diseases evolution. They are also useful to build personalized models.

Volumes measurement Air volumes involved in breathing under different conditions can be measured using *spirometry*. It is one of the most common tests used to evaluate pulmonary function. It measures air volumes but also airflow rates.

The test is performed with a device called spirometer, which is placed into the mouth of the patient. Then the patient performs inhalations and exhalations, both normal and forced, and at different breathing rates. The process is repeated several times to ensure repeatability.

The different lung volumes are represented in Figure 1.5. A spirometry test can measure the tidal volume, which is the air volume inhaled or exhaled during normal breathing. The inspiratory and expiratory reserve volumes are measured during a forced inhalation or exhalation respectively. They correspond to the air volume inhaled or exhaled beyond the tidal volume. The vital capacity is then the sum of these three volumes. Airflow rates give also information about airways resistance.

Pathologies can affect lung volumes. Restrictive diseases tend to decrease volumes, whereas volumes increase in the case of obstructive diseases.

The residual volume cannot be measured with this method since it is not possible to breathe out the whole air of lungs. Other techniques exist to estimate it like body plethysmography. It is an indirect method where the patient is sitting in a closed box. Breathing movements and lung volume variations impact the pressure and the volume of the box, since it is a closed system. The residual volume is then estimated from the volume variation of the box and the pressure variation to the patient mouth [Criée et al., 2011].

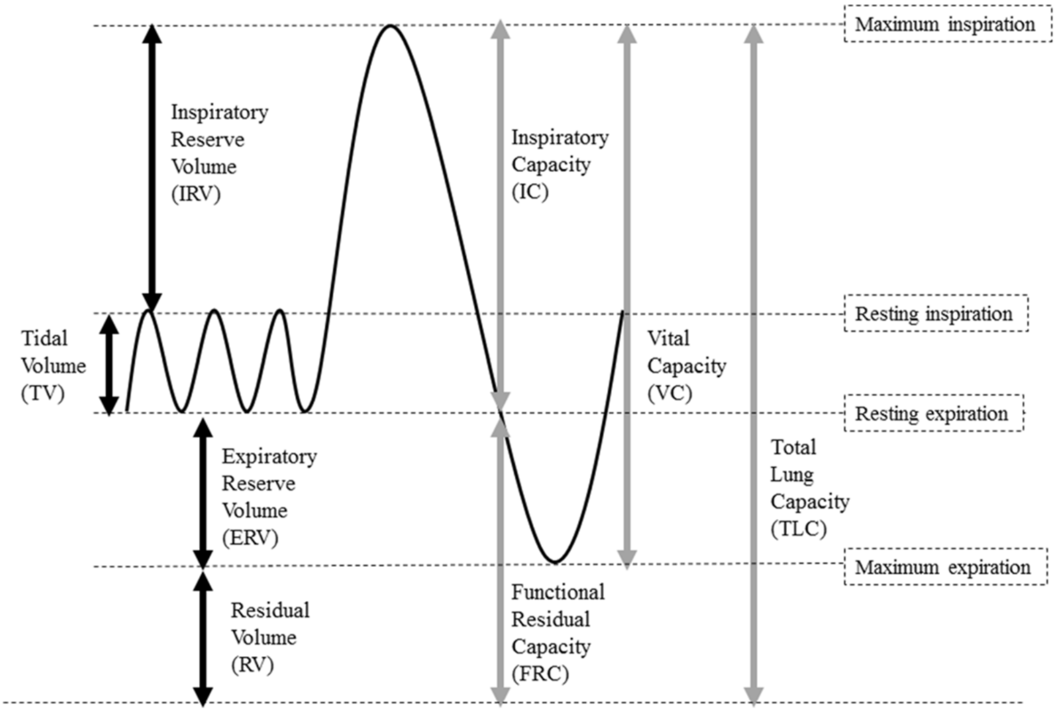

Figure 1.5 – Lung volumes and capacities. Figure taken from Lutfi [2017].

Pressures measurement Pressures are the driving force of breathing as seen in Section 1.1.3: either the pleural pressure or the ventilated pressure depending on the breathing type. They correspond to the forces required to inflate lungs. The way to measure each of these pressures are different.

Air pressure measurement During mechanical ventilation, air pressure inside lungs and airways is the ventilated pressure induced by the ventilator. In the case of a high breathing rate, the ventilated pressure could be not well equilibrated with the airways pressure because of airways resistance. Airways pressure can also be measured with a pressure transducer positioned in the mouth during a breath hold.

However, air pressure gives information about forces needed to expand both lungs and rib cage and does not allow to separate both contributions.

Pleural pressure measurement The pleural pressure is very complicated to measure. A direct measure of the pleural pressure means having access to the pleura. It involves an invasive surgical act, which could lead to complications like pneumothorax. This direct measure can happen during a surgical biopsy, which consists in removing a piece of lung in order to examine it with a microscope. The needle biopsy uses a needle going through the rib cage and the pleura to the lungs. Because of the invasiveness of the process, it cannot be performed for patients who do not need a biopsy.

Another method exists to estimate the pleural pressure using an esophageal balloon which is inserted into the esophagus from the mouth. The esophageal balloon measures the esophageal pressure, which is considered as a surrogate of the pleural pressure [Hoppin et al., 1969; Agostoni, 1972; Akoumianaki et al., 2014]. Indeed, the esophagus is in contact with the pleura and forces are transmitted through the contact surface. This measure is difficult and its reliability is still questioned because of the variety of possible artifacts. The measure can be impacted by the balloon position, the patient position or the patient disease [Knowles et al., 1959; Hoppin et al., 1969; Pecchiari et al., 2013; Akoumianaki et al., 2014]. Still, it is considered that the esophageal pressure is a good approximation of the global average pleural pressure [Pecchiari et al., 2013]. This indirect method gives only an approximation of the pleural pressure and does not give pleural pressure values in various sites of the pleura.

Compliance Lung *compliance* characterizes the ability of the lung to change its volume (ΔV) in response to a change of pressure (ΔP). It describes the lung ability to stretch and inflate. It is defined as:

$$C = \frac{\Delta V}{\Delta P} \tag{1.1}$$

It is then the slope of the curve representing the lung volume as a function of pressure. Since such a curve is not linear, the compliance is not constant during breathing. Compliance decreases with increasing pressure, because the more inflated the lung is, the harder it is to inflate it more.

Lung compliance is impacted by several diseases and can be used to diagnose them. A low compliance results in a stiff lung, like in the case of the pulmonary fibrosis, whereas a large compliance can be evidence of emphysema (see Figure 1.6).

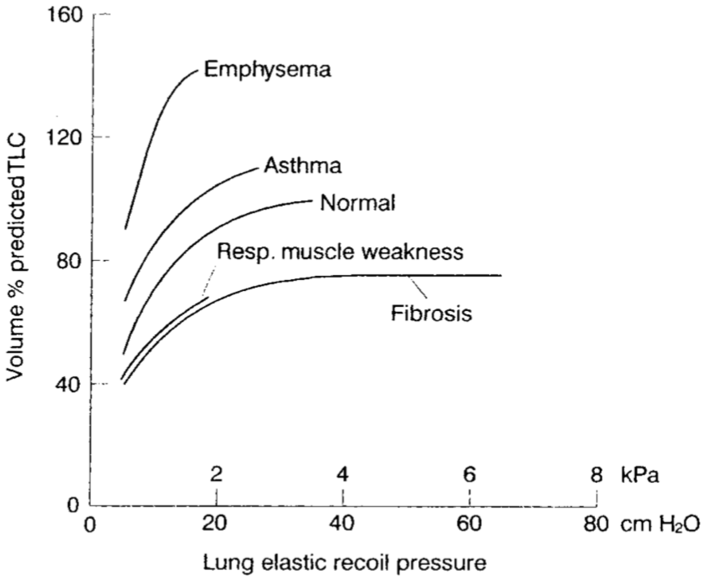

Figure 1.6 – Pressure-volume curves for healthy and diseased lungs. Figure taken from Gibson [2001].

Imaging Anatomical information, highly linked to the pulmonary function, are obtained through lung medical imaging, which is not invasive. The main techniques are chest radiography, computer tomography and magnetic resonance imaging.

Chest radiography, based on X-rays, is a frontal image, as a projection of the chest (3D volume) on a 2D surface. The main pulmonary structures are observed and many pathologies can be detected. In particular, radiography allows to control the lung realignment or the drain position after a surgery. The radiation dose is low compared to other techniques. However, radiography technique is not precise enough for the visualization of small pulmonary features. It should often be combined with an additional imaging technique for diagnosis.

Computer tomography, or CT-scan, produces a 3D image composed of a set of 2D images. The voxel intensity is based on the ability of the tissue to absorb X-rays. It allows to visualize the texture of lung tissue, especially the difference of density inside the organ, and to detect the associated diseases, like interstitial lung diseases. The spatial resolution is very good, between 0.5 mm and 1 mm, and small airways or blood vessels can be reconstructed [Bordas et al., 2015]. The visualization is better than for radiography since structures are not superimposed on a 2D plane. However, the radiation dose is high and the technique cannot be reproduced too often for the same patient. Special care should be paid to get a sharp image since breathing movements induce blur. Thus, patients need to hold their breath during image acquisition, which lasts a few seconds.

The lung MRI (Magnetic Resonance Imaging) is the latest technique being developed for lung imaging [Biederer et al., 2012a]. Commonly used in other clinical applications like cardiac imaging, lung MRI remains challenging because of various pulmonary specificities [Boucneau, 2019]. The tissue is low density and the magnetic resonance signal has a short lifetime because of the large differences in magnetic susceptibility at the gas-tissue interface. Another difficulty is lung movements due to the acquisition time, which is longer than a breathing cycle. It is now recommended for some pathologies but CT remains the preferred choice in case of interstitial lung disease [Biederer et al., 2012b].

Diffusing capacity measurement Other exams can be performed to examine lung function in analyzing gas. The measurement of the diffusing capacity gives information about the gas diffusion through the alveolar wall, from air to blood. The test consists in a single breath from full exhalation to full inhalation, of a gas containing a small quantity of carbon monoxide and an inert gas. When the carbon monoxide diffuses into the blood, the inert gas does not cross the alveolar wall and remains inside pulmonary airways. Then the patient breathes out and the composition in carbon monoxide and in inert gas of the inhaled and exhaled air is analyzed.

The quantity called $\mathrm{D_{LCO}}$, generally measured in mL/min/kPa, is computed to quantify the diffusing capacity of carbon monoxide. The result gives information about the diffusing capacity of oxygen ($\mathrm{D_{LO_2}}$). Defined as the oxygen absorption rate of lung divided by the partial pressure of oxygen between alveoli and blood, $\mathrm{D_{LO_2}}$ cannot be measured easily since it requires an invasive procedure to get the partial pressure of oxygen in the pulmonary artery. On the other hand, the partial pressure of carbon monoxide in blood is neglected because carbon monoxide has a strong affinity with red blood cells and is easily absorbed by them. That is why the $\mathrm{D_{LCO}}$ is used instead of $\mathrm{D_{LO_2}}$ to estimate the pulmonary diffusing capacity [West and Nadeau, 2003].

1.2 ... to lung mechanical modeling

A lung pulmonary model intends to reproduce lungs behavior with mathematics in order to perform analytical analysis or numerical simulations. Tests can then be performed on the model to study for example the impact of parameters or to predict the future behavior in case of a parameter change. In this Section, only continuum solid mechanics models are discussed; the fluid mechanics aspects are not covered.

A mechanical model includes different elements:

- the system geometry;
- the fundamental principle of dynamics, also called Cauchy's first law of motion, and

derived from the principle of conservation of linear momentum:

$$\boldsymbol{\nabla} \cdot \underline{\underline{\sigma}} + \rho \left(\underline{f} - \underline{a} \right) = 0, \tag{1.2}$$

with $\underline{\underline{\sigma}}$ the Cauchy stress tensor, ρ the density, $\underline{f}$ the body forces applied on the system and $\underline{a}$ the acceleration;

- the constitutive behavior, to characterize the relationship between stress and strain, *i.e.,* how the system deforms for a certain loading;
- boundary conditions, to describe the loadings that lead to the system deformation.

A good knowledge of the real system, here the lungs physiology, is required to build a realistic model. Different models could be proposed depending on what they focus on, mainly concerning the spatial scale and the time scale. Indeed, considering the organ scale or the alveoli scale will lead to different modeling choice, as well as considering the breathing scale or the remodeling scale. In the following Section, pulmonary mechanical models at the organ scale are reviewed. Then, a special attention is given to multiscale models, which explicitly consider the pulmonary microstructure.

1.2.1 Organ scale models

1.2.1.1 Constitutive behavior

The constitutive behavior of a material is a key aspect of a mechanical model. It corresponds to the relationship between stress and strain in the material and expresses its mechanical properties, like anisotropy, compressibility or viscoelasticity. Both the expression of the constitutive law and the parameters should be defined. In order to best represent the physical material properties, the final law should match data, which could be difficult to obtain in biomechanics since *in vivo* data acquisition can be invasive and *ex vivo* or *in vitro* properties can be different from *in vivo* ones. A specificity of biomechanics is also that parameters often differ from one person to another, unlike industrial materials which are built according to predefined specifications and whose constitutive behavior is as desired by the manufacturer. Consequently, parametrization should be subject-specific, even though some average parameters can also be used if the modeling is not personalized.

Despite the complex microstructure, lung parenchyma is often considered as a homogeneous continuum in organ scale mechanical modeling. This kind of models are reviewed in this Section, whereas considerations on microstructure, and especially the porosity, are discussed in Sections 1.2.2 and 1.2.3.

Pulmonary parenchyma properties At the organ scale, the mechanical properties of the pulmonary parenchyma as a continuum are often assumed to be the following, according to various experimental investigations:

- nonlinear. As most biological tissues, pulmonary tissue presents a nonlinear behavior, both for isochoric and volumetric transformations. It is highlighted by the stress-strain relationship achieved from uniaxial tests as shown in Figure 1.7a, as well as the pressure-volume curve of Figure 1.6. The non-linearity is a consequence of the composition of the interstitium tissue, with collagen and elastin fibers mainly, which are the main load-bearing elements. The impact of fibers presence on the stress-strain relationship is investigated by Birzle et al. [2019].

- elastic [Mead et al., 1970; Fung, 1974; Budiansky and Kimmel, 1987]. The lung tissue is deformed when a loading is applied and tends to recover its initial state when the loading is no longer active, as most biological materials.

- highly deformable. During breathing, lungs are highly deformed as the lung volume is increased by more than 100 % from exhalation to inhalation [Lai-Fook et al., 1976] and the displacements at the base can reach 10 cm [West and Nadeau, 2003].

- isotropic. Tai and Lee [1981] investigate the directional dependency of lung deformation in testing cubes of dog lung tissue with triaxial force-extension tests. It is shown that pulmonary parenchyma can be assumed to be isotropic. This assumption is also supported by Hoppin et al. [1975] with dog lung testing. A more recent investigation is also performed by Weed et al. [2015], who tests porcine lungs with compression tests. The isotropy can be explained by the random orientation of alveoli and fibers inside the interstitium tissue [Hoppin et al., 1975].

- spatially homogeneous. This assumption depends on the scale considered. With the same tests as for studying isotropy, Tai and Lee [1981] show that lung can be assumed to be homogeneous, since no significant dependency in the location is observed between upper and lower lobes for example. This assumption should be taken carefully since a piece of tissue including the conducting airways or the pulmonary artery does not have the same behavior as a piece of tissue corresponding to an alveolar sac. However, it means that two pieces of tissue around an alveolar sac in different locations will behave the same. Moreover, it is valid only in the healthy case and not in the diseased case for obvious reasons. This assumption is commonly accepted at the organ scale for normal cases [Lai-Fook, 1981; Al-Mayah et al., 2011].

- compressible. The compressibility of the parenchyma is illustrated by the pressure - volume curves (see Figure 1.6), which can be obtained either with inflation or triaxial tests [Birzle et al., 2018b] or with *in vivo* data [Shirzadi et al., 2013]. This property is fundamental to ensure the pulmonary function of inhaling air. When lung inflates, the porosity increases and more air flows in. The compressibility of the pulmonary organ does not mean anything about the compressibility of the solid tissue which composes lungs. Indeed, pulmonary interstitium is considered as quasi-incompressible, as described in Section 1.2.2. Both compressibility properties, of the organ and of the solid tissue, are independent.

- viscoelastic. Like most soft biological tissues [Fung, 1993], lungs have a viscoelastic behavior, which combines a solid behavior and a fluid behavior. It means that the stress is not maintained constant under a constant deformation, which is also called the stress relaxation. This property has been studied by several works [Bayliss and Robertson, 1939; Bachofen, 1968; Suki et al., 1994; Suki and Lutchen, 2006; Mortola, 2013]. The interstitium tissue is also viscous by itself as it is composed partly of water Birzle and Wall [2018].

- pressure-volume hysteresis. The pressure-volume curve during the whole breathing cycle is a loop, since the pressure value is different during inflation and deflation at the same level of strain or volume, as shown in Figure 1.7b. This hysteresis is caused by the presence of the surfactant [Mead et al., 1957; Smith and Stamenovic, 1986; Otis et al., 1994], which reduces the air-solid surface tension of the alveoli surface and decreases then the amount of work for breathing [Hills, 1981]. Indeed, the surface tension of the alveoli surface tends to reduce the alveoli surface area by collapsing alveoli [West and Nadeau, 2003]. It is enhanced by the comparison with the pressure - volume curve of lung under saline condition (see Figure 1.7b), in which the air-solid interface is removed: the compliance is much higher than under air condition and the hysteresis nearly disappears.

- prestressed. The *in vivo* lung is in a state of expansion because it is loaded by the pleural pressure [Lai-Fook, 1977]. In an *ex vivo* configuration, the lung would deflate to recover its unloaded configuration, alveoli would collapse and air would flow out. It could be a similar configuration as the pneumothorax. This *in vivo* loading state generates then a prestress field in the organ.

Constitutive model used in mechanical models The knowledge of the material properties of the lung parenchyma is useful for lung mechanical modeling. A realistic mechanical model needs realistic material properties to reproduce a realistic behavior. Depending on what a mechanical model focuses on, some aspects of the whole material properties could be neglected.

Despite the evident non-linearity of the pulmonary constitutive behavior, numerous mechanical models are considering a simple linear model with two parameters, Young's modulus and the Poisson ratio [Baudet et al., 2003; Zhang et al., 2004; Brock et al., 2005; Werner et al., 2009; Fuerst et al., 2015]. However, the values used for these parameters do not reach a consensus, as proved by Werner's literature review [Werner et al., 2009] (see Table 1.1). West and Matthews [1972] try to consider the non-linearity in defining Young's modulus E dependent from the amount of strain ϵ:

$$E = 0.8\frac{E_0}{0.8-\epsilon}, \tag{1.3}$$

with E_0 the Young's modulus value for zero strain.

Reference	Elasticity modulus E (kPa)	Poisson's ratio ν
Al-Mayah et al. [2008]	7.8	0.43
Brock et al. [2005]	5.0	0.45
De Wilde et al. [1981]	0.73	0.3
Sundaram and Gee [2005]	0.1	0.2
Villard et al. [2005]	0.823	0.25 - 0.35
West and Matthews [1972]	0.25	0.3
Zhang et al. [2004]	4.0	0.35

Table 1.1 – Different values of Young's modulus and Poisson ratio used in the literature. Table reproduced from [Werner et al., 2009].

Others deal with the non-linearity in using a Neo-Hookean hyperelastic potential [Berger et al., 2016; Han et al., 2017]. A more complex hyperelastic potential is developed by Zeng et al. [1987] with a biaxial experimental test:

$$\begin{aligned} W =& \frac{1}{2}c\Big[\exp\left(a_1E_x^2 + a_2E_y^2 + 2a_4E_xE_y\right) + \exp\left(a_1E_x^2 + a_2E_z^2 + 2a_4E_xE_z\right) \\ &+ \exp\left(a_1E_z^2 + a_2E_y^2 + 2a_4E_zE_y\right)\Big], \end{aligned} \tag{1.4}$$

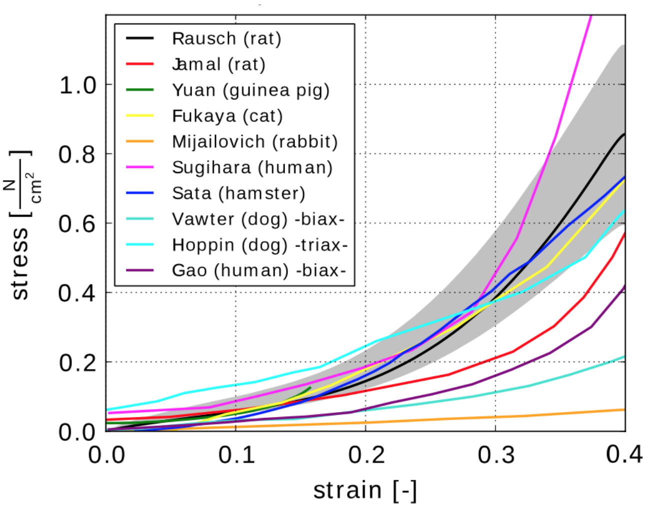

(a) Stress-strain curves obtained from experimental uniaxial tension tests. Figure taken from Rausch et al. [2011a].

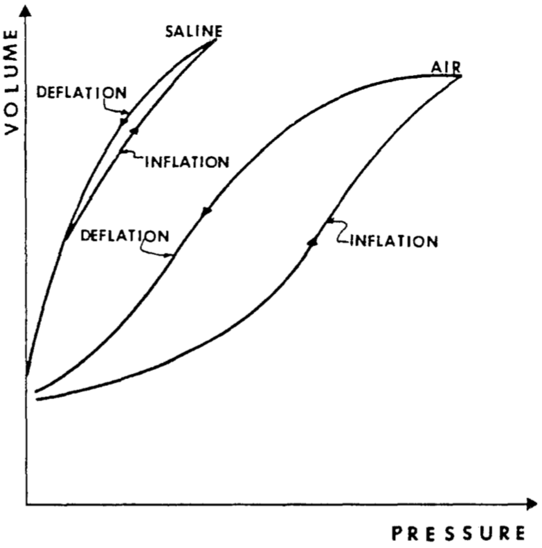

(b) Pressure-volume curve in deflation and inflation showing the lung hysteresis. Figure taken from Kowalczyk [1993].

Figure 1.7 – Mechanical behavior of the pulmonary parenchyma.

with c, a_1, a_2 and a_4 four parameters determined in the experiment and E_i the strain components in the direction i. Under the isotropy assumption, the following equality can be taken $a_1 = a_2$ to reduce the number of parameters. This potential is used also by Al-Mayah et al. [2009] and Eom et al. [2010]. However, this potential cannot reproduce the volumetric behavior of the lung well, because it has been elaborated from biaxial test, which cannot detect the change of volume with a change of pressure. Tawhai et al. [2009] is using such a potential, accurate to the compressibility behavior of the lung parenchyma. It takes the following shape:

$$W = c \exp\left(aI_1 + bI_2\right), \tag{1.5}$$

with a, b and c three parameters and I_1 and I_2 the first two invariants of the Green strain tensor.

The use of a linear model could be sufficient depending on the need. Al-Mayah et al. [2011] compared the accuracy of their model using either a linear elastic model or a hyperelastic model and showed that the material property has little effect on the deformation. The conclusion seems to be true in the range of applications considered in the study, *i.e.,* radiotherapy, where the lung volume change is less than 10 %. However, it may not be applicable for other applications with forced exhalation or forced inhalation.

The consideration of the prestress in the *in vivo* configuration is necessary in case of a nonlinear behavior where the change of strain depends on the stress state. This aspect is not taken into account in some studies [Al-Mayah et al., 2009; Eom et al., 2010]. A uniform scaling is used by Tawhai et al. [2009] and Berger et al. [2016] to compute the unloaded configuration from a known configuration.

Development of more complex potentials with experiments In order to improve the characterization of the pulmonary mechanical properties, various studies established complex experimental protocols and identification procedures. Experiments should be representative of the mechanical behavior, whereas parameters identification requires the formulation of an inverse problem.

Bel-Brunon et al. [2014] performs uniaxial tensile test to identify in the same time the isochoric, volumetric and viscoelastic behavior. Several combinations of hyperelastic potentials are tested to find the best match with data. The identification is performed in building a finite element model of the experimental test and in minimizing the difference between displacements from the numerical model and from the experiment (computed by image registration). The following potential was determined:

$$W = W_{\text{vol}} + W_{\text{iso}} + W_{\text{vis}} \text{ with } \begin{cases} W_{\text{vol}} = \dfrac{\kappa}{4}\left(-2\ln J + J^2 - 1\right) \\ W_{\text{iso}} = \dfrac{k_1}{2k_2}\left[\exp\left(k_2\left(\frac{\bar{I}_1}{3} - 1\right)\right) - 1\right] \\ W_{\text{vis}} = f\left(\tau\right), \end{cases} \tag{1.6}$$

where all the parameters κ, c_1, c_3, k_1, k_2 and τ have been identified and $\bar{I}_1$ and J are the first and third reduced invariants of the right Cauchy-Green strain tensor. The study is improved by Birzle et al. [2018a] in adding a second experiment. Indeed, the compressibility behavior of the pulmonary material is not well represented in a uniaxial test. Consequently, a pressure - volume test was coupled with the uniaxial test and the identification procedure takes into account both experiments, leading to:

$$W = c\left(I_1 - 3\right) + \frac{c}{\beta}\left(I_3^{-\beta} - 1\right) + c_1\left(I_3^{-\frac{1}{3}} I_1 - 3\right)^{d_1} + c_3\left(I_3^{\frac{1}{3}} - 1\right)^{d_3}, \tag{1.7}$$

with c, β, c_1, c_3, d_1 and d_3 are the parameters identified and I_1 and I_3 are the first and third invariants of the right Cauchy-Green strain tensor. They also show that this potential is the one that best fits the data, among others potentials proposed in the literature, both for volumetric and isochoric deformation.

1.2.1.2 Boundary conditions

Two main kinds of boundary conditions exist:

- Dirichlet boundary conditions, which prescribe displacements;
- Neumann boundary conditions, which prescribe forces.

A combination of these boundary conditions can also be used.

In the context of pulmonary mechanical modeling, both boundary conditions can be encountered.

Dirichlet boundary conditions Some existing models apply a displacement field on the lung surface depending on scaling parameters [Berger et al., 2016]. The imposed displacement field could also be extracted from two images (exhalation and inhalation for example). Brock et al. [2005] and Al-Mayah et al. [2008] perform an orthogonal projection of the exhaled lung surface nodes to the inhaled body surface, configurations known from images. The displacement field can also be applied on another surface than the lung surface. Tawhai et al. [2009] create a second surface, the pleural cavity surface, matching with the lung surface. Then, the pleural cavity surface is deformed according a displacement field, and the lung surface is set in contact with it all along the transformation, leading to lung deformation.

To improve these Dirichlet boundary conditions, contact condition are used by Al-Mayah et al. [2008] and Tawhai et al. [2009]. They are frictionless in order to represent the lubrification effect of the pleural liquid. This characteristic is validated by Al-Mayah et al. [2009], which studied the impact of the friction coefficient and showed that the frictionless condition gives more accurate results.

However, the prescription of displacements does not seem to be the most natural choice regarding lung physiology. Indeed, Section 1.1 was mentioning the importance of lung surroundings and specifically highlighted the pleura pressure role in breathing.

Neumann boundary conditions The pleura has a strong impact on lungs through the pleural pressure variations during a breathing cycle. Consequently, Neumann boundary conditions model reality better, which is why this choice is made in several models [Baudet et al., 2003; Zhang et al., 2004; Villard et al., 2005; Werner et al., 2009; Han et al., 2017]. All these studies apply a negative pressure on the whole lung surface in order to inflate the lungs. They also consider the target shape of the transformation, extracted from images, on which the initial configuration will come into contact, allowing frictionless sliding. Villard et al. [2005] and Werner et al. [2009] assume also that the root of the lung is fixed during breathing.

Nevertheless, such approaches cannot be predictive since boundary conditions come directly from a final geometric state and do not model the exact physiology. Moreover, the applied pressure is assumed to be homogeneous, although various studies have highlighted the inhomogeneity of the pleural pressure [Hoppin et al., 1969; D'Angelo et al., 1970; Lai-Fook and Rodarte, 1991]. Fuerst et al. [2015] is going in that direction in computing patient-specific boundary conditions, *i.e.,* the regional value of pressure is estimated through an optimization process.

Further investigations about pleural pressure boundary conditions Considering the inhomogeneity of the pleural pressure would allow to better model the lung behavior. However, the main difficulty is to measure such an inhomogeneity, which requires invasive tools [Agostoni, 1972; Lai-Fook, 2004], as already mentioned in Section 1.1.

It has been shown that the pleural pressure presents a gradient from apex to base, of about 7.5 cmH_2O, where the apex pressure is more negative than the base pressure [Kallet, 2015]. The consequence of this gradient is that the ventilation is not homogeneous in all the alveoli: alveoli closer from the apex are more inflated and have a better ventilation than alveoli closer from the base [Milic-Emili et al., 1966; Millar and Denison, 1989]. The pleural pressure inhomogeneity can be explained by two phenomena:

- gravity, which induces a pleural pressure gradient of 1 cmH_2O/cm from apex to base, with a smaller pressure at the apex than at the base [Agostoni, 1972; Lai-Fook, 2004]. This amount of gradient corresponds to the expected gradient in the pleural liquid in hydrostatic equilibrium and would lead to a total gradient of about 20 cmH_2O.
- pressure loss due to a non-equilibrated pleural liquid. Indeed, it can exist some contact zones of both pleural membranes, where the pressure is not negative anymore. They are the consequence of the presence of fatty tissues between ribs and the parietal membranes. Their thickness is about 1 to 2 mm [Im et al., 1989], which is large compared to the thickness of the pleural liquid, between 1 to 10 µm thick [Agostoni et al., 1968]. These contact zones lead to a disruption of the hydrostatic equilibrium and a pressure loss effect, which reduces the theoretical gradient computed from the hydrostatic equilibrium.

Numerical illustration of the impact of the fatty tissue An illustration of the impact of the fatty tissue on the contact pressure is performed using a finite element model which includes a lung and a rib cage with a simplified geometry, including or not the fatty tissue.

The whole model is represented in Figure 1.8a. The rib cage is modeled as a surface cylinder, opened in the bottom part, and the lung as another volume cylinder. At start, both rib cage and lung are in contact. The top lung surface can only move according to the x-axis, whereas a pressure is applied on the lateral and bottom parts to model the pleural pressure which inflates lungs. The rib cage is a fixed surface. Frictionless contact conditions between the lung lateral surface and the rib cage lateral surface are applied. The contact is also considered with no separation, which means that once the surfaces are in contact, they cannot separate. The whole model is 2D-axisymmetric with the longitudinal axis as the rotation axis. Two cases are studied, differing by the geometry: one case, where lateral surfaces are flat (reference), and one case, where lateral surfaces have a bump to model the fatty tissue.

The contact pressure between the lung and the rib cage at the lateral surface is plotted as a function of the z-coordinate in Figure 1.8b. For the reference, the contact pressure is homogeneous in the whole surface. Without the contact condition, the transformation would be isochoric and the diameter of the lung cylinder would decrease when the pressure in the z-direction increases, whereas inflation is allowed with such contact conditions. The contact pressure is impacted by the presence of the bump. The top part of the lung, above the bump, has a slightly higher contact pressure than in the reference case because the displacement in the z-direction is slightly restricted by the bump and decreases the force required to maintain the lung and the rib cage in contact. On the top part of the bump, the lung should be compressed to be able to take the form of the bump. That is why the contact pressure increases until it reaches a positive value. On the contrary, on the bottom part of the bump, the contact pressure is more negative, since a higher loading is needed to make the diameter as above the bump. Finally, the contact pressure below the bump is not impacted at all.

This increase of the contact pressure until a positive value in case of the presence of a bump reflects what can happen with the presence of the fatty tissue. It could then be the cause of a loading loss, since it brings a discontinuity in the pleural liquid and in its hydrostatic equilibrium.

1.2.2 Multiscale approaches

Unlike macroscopic approaches that assume a constitutive behavior without taking into account the complex microstructure of lungs, multiscale approaches make the link between microscale and macroscale. They allow to better understand pulmonary mechanics across spatial scales, as well as the pulmonary function, and how the different scales interact with each other [Tawhai and Bates, 2011]. Indeed, the interactions between the multiple constituents of lungs, mainly tissue, air and blood, take place in different physical phenomena according to the scale considered. Most often in pulmonary multiscale mechanics study, two scales are considered [Yoshihara et al., 2013; Concha et al., 2018], *i.e.,* the alveolar scale and the organ scale, but other scales could be interesting, like acinus scale or lobule scale, that could also be involved since they correspond to functional units as described in Section 1.1.2.1.

1.2.2.1 Micromechanical model

Multiscale approaches require a micromechanical model of the microstructure, with a geometry, a constitutive behavior and boundary conditions. We focus in this Section on the first two aspects. The models mentioned in this Section are not all part of a multiscale model. Some of them, like [Budiansky and Kimmel, 1987], were developed by their authors to describe the relationship between the microstructure and the properties only, without considering a macroscopic model. The main goal is to explain what is a micromechanical model to highlight the difference with poromechanical approaches.

Geometrical model Several strategies have been employed in the literature to generate a geometry of the microstructure, as can be seen in Figure 1.9.

The simple way to model the geometry is to use a simplified mathematical shape. To represent a single alveolus, Dale et al. [1980], Denny and Schroter [2006], Roth et al. [2017] and Concha et al. [2018] are using truncated octahedra, also called Kelvin's tetrakaidecahedra, whereas Budiansky and Kimmel [1987] are using regular dodecahedra. An alveolar sac is modeled by de Ryk et al. [2007] with a central rhombic dodecahedron surrounded by twelve adjoining dodecahedra, in which the central dodecahedron walls are removed to connect all the dodecahedra together and a wall of an external dodecahedra is removed to stand for an airway connection. Ferrara [2009] is also modeling alveolar sacs but uses a cylinder surrounded by thirteen spheres. The dimensions of elements in these models can be determined by the knowledge on the alveolar geometry from [Weibel et al., 2005] for example.

Various recent studies use more complex geometrical shapes derived from images. Gefen et al. [1999] develop a two-dimensional model of an alveolar sac extracted from a scanning electron micrograph of a mouse lung. Three-dimensional models are developed by Rausch et al. [2011b] and Koshiyama et al. [2018] from the segmentation of high-resolution synchrotron CT images of a mouse lung and a rat lung respectively. In order to obtain a satisfactory geometry from images, image acquisition should be performed on a piece of

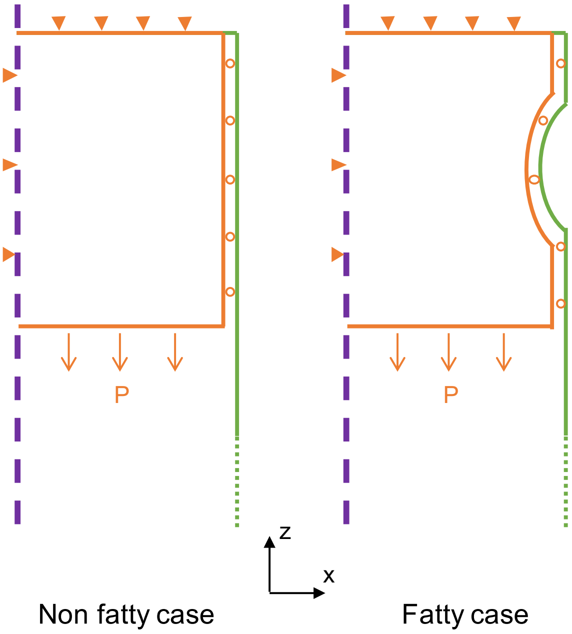

(a) 2D-axisymmetric model, with the rotation axis (z-axis) in purple. The rib cage is in green and the lung, as well as its boundary conditions, in orange. The triangles represent a fixed displacement in a specific direction, the circles sliding conditions and the arrows a pressure loading. The rib cage can be flat or with a curve representing fatty tissues.

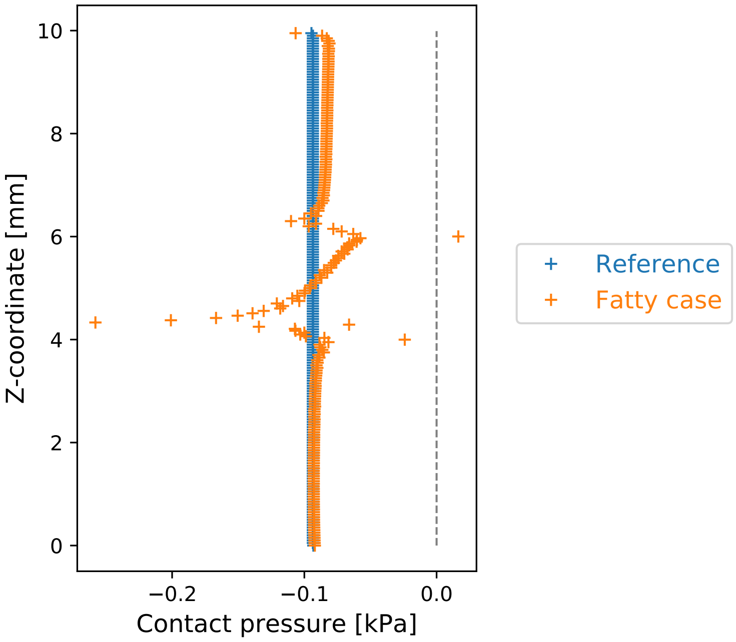

(b) Contact pressure as a function of the z-coordinate.

Figure 1.8 – Impact of the fatty tissue on the contact pressure. The zero of the z-coordinate is the initial z-coordinate of the bottom lung surface. The bump is between the z-coordinate 4 mm and 6 mm.

lung kept under pressure. Otherwise, alveoli tend to collapse and the geometry would not be representative of the *in vivo* lung microstructure.

The image-extracted geometries are closer to the real geometry and take into account the porosity. However, they require a high computational capacity, contrary to mathematical geometries. Concha et al. [2018] develop a mathematical micromechanical model, validated with multiple responses of a real micromechanical model under different boundary conditions.

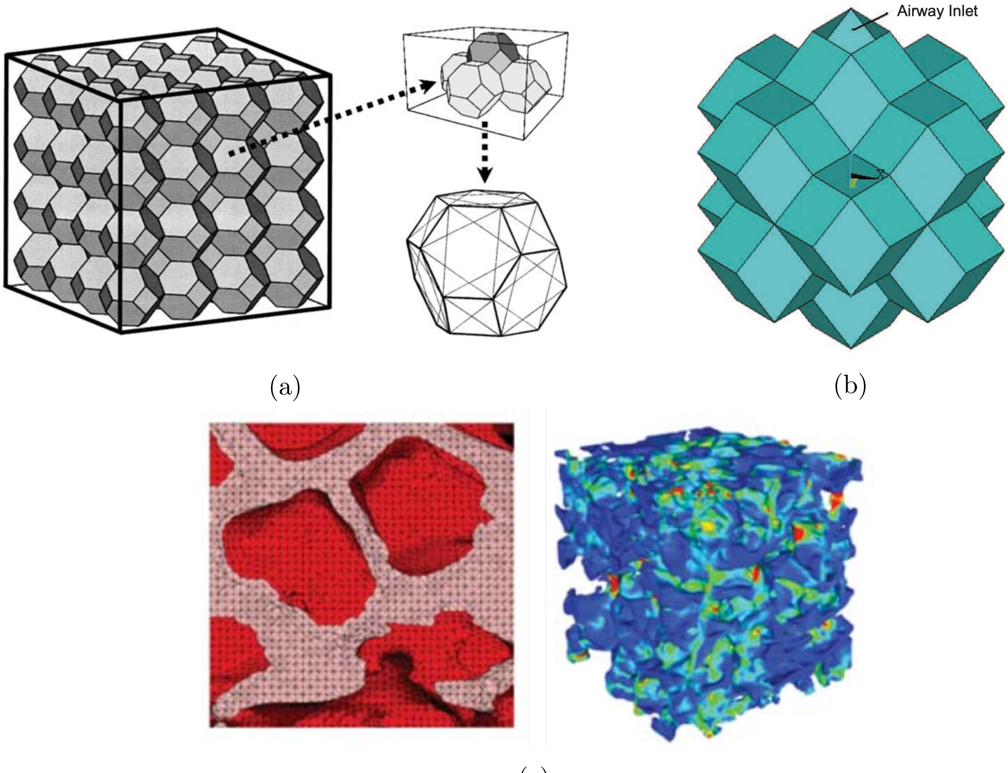

(a)

(b)

(c)

Figure 1.9 – Various microstructures of alveoli or alveolar sacs used in the literature. (a) Tetrakaidecahedra. Figure taken from Denny and Schroter [2006]. (b) Assembly of dodecahedra. Figure taken from de Ryk et al. [2007]. (c) Geometry extracted from images. Figure taken from Wiechert et al. [2011].

Constitutive behavior of the solid phase In addition to a geometry, a constitutive behavior should be given to the interstitium tissue composing the alveolar wall, also called *interalveolar septa*.

The alveolar wall is considered to be isotropic. Indeed, the main components are collagen and elastin fibers and have a major role in the mechanical properties of the tissue [Toshima et al., 2004]: collagen fibers limit the deformation of the tissue and provide cohesion to the material, whereas elastin fibers bring elasticity properties and allow the tissue to come back to the initial state after loading. It has been shown that the orientation of these fibers is random and that they are uniformly distributed in all directions [Sobin et al., 1988], justifying the isotropy assumption.

Another assumption commonly used is the incompressibility or quasi-incompressibility of the alveolar tissue, since the main content of the tissue is water, like most biological tissue [Concha et al., 2018].

Various hyperelastic potentials have been proposed according these hypotheses. Concha et al. [2018] use the following Neo-Hookean energy using a Lagrange multiplier to deal with the incompressibility:

$$W = \frac{\mu}{2}\left(\mathrm{tr}\left(\underline{\underline{F}}^T \cdot \underline{\underline{F}}\right) - 3\right) - p\left(\det \underline{\underline{F}} - 1\right), \tag{1.8}$$

with μ the Lame coefficient, p the Lagrange multiplier and $\underline{\underline{F}}$ the deformation gradient. Rausch et al. [2011b] attributes the following Neo-Hookean energy to the solid tissue:

$$W = \frac{E}{4-4\nu}\left(I_1 - 3\right) + \frac{E\left(1-2\nu\right)}{4\nu+4\nu^2}\left(I_3^{-\dfrac{\nu}{1-2\nu}} - 1\right), \tag{1.9}$$

where E is Young's modulus, ν the Poisson ratio and I_1 and I_3 the first and third invariants of the right Cauchy-Green deformation tensor, respectively. This constitutive law is also used by Roth et al. [2017]. Wiechert et al. [2011] decompose the solid tissue energy into two components:

$$W = W_{\mathrm{vol}} + W_{\mathrm{iso}}, \tag{1.10}$$

where W_{vol} describes the volumetric part of the energy, *i.e.,* the quasi-incompressibility, and W_{iso} the isochoric part. This last term is itself divided into two terms:

$$W_{\mathrm{iso}} = W_{\mathrm{iso}}^{\mathrm{gs}} + W_{\mathrm{iso}}^{\mathrm{fib}} \text{ with } \begin{cases} W_{\mathrm{iso}}^{\mathrm{gs}} = c\left(\bar{I}_1 - 3\right) \\ W_{\mathrm{iso}}^{\mathrm{fib}} = \begin{cases} \dfrac{k_1}{2k_2}\left(\exp\left(k_2\left(\frac{1}{3}\bar{I}_1 - 1\right)^2\right) - 1\right) & \text{if } \bar{I}_1 \geq 3 \\ 0 & \text{if } \bar{I}_1 < 3, \end{cases} \end{cases} \tag{1.11}$$

with c, k_1 and k_2 are three parameters and $\bar{I}_1$ is the modified first invariant of the right Cauchy-Green deformation tensor. The energy $W_{\mathrm{iso}}^{\mathrm{gs}}$ stands for the contribution of the ground substance and the elastin fibers, whereas the energy $W_{\mathrm{iso}}^{\mathrm{fib}}$ is related to the collagen fibers network. Finally, an energy expression with an exponential, like that developed by Demiray [1972] or Fung [1993], is suggested by Karakaplan et al. [1980].

An additional element of the constitutive behavior modeling at the alveolar scale is the consideration of the surface tension generated by the surfactant as it acts at this spatial scale. The surfactant effect is taken into account in different studies. Fung [1974] assumes that the surface tension is a function of the surface area. Along the same idea, Koshiyama et al. [2018] is using the following surface tension model:

$$\gamma = \gamma_{\max}\left(1 - d_1 \exp\frac{\Gamma}{\Gamma_0}\right), \tag{1.12}$$

with γ the surface tension, $\gamma_{\max}$ its maximal value, Γ the current surface area of the alveoli, Γ_0 its initial value and d_1 a parameter. Karakaplan et al. [1980] use a function of the surface area change as well as the rate of surface area change, with two different functions for inflation and deflation. Including the rate of surface change allows to take into account the time-dependency of the hysteresis. Wiechert et al. [2011] applies the study about the surfactant behavior of Otis et al. [1994], in which the local surface stress is computed according to the surface area and the surfactant concentration. The transport of surfactant between bulk fluid and the surface is also modeled. Several regimes are distinguished according to the surfactant concentration, compared to the equilibrium and maximal value of surfactant concentration. In the first regime where the surfactant concentration ζ is less than the equilibrium concentration $\zeta^\star$, the surface tension is:

$$\gamma = \gamma_0 - m_1\frac{\zeta}{\zeta^\star}. \tag{1.13}$$

In these studies, the surfactant is not explicitly described, but is incorporated into the global model by its energy.

The main difficulty concerning the constitutive behavior of the interstitium tissue is the identification of the parameters. Very few experimental data exist since testing only the solid part is very challenging [Karakaplan et al., 1980]. Indeed, a mechanical test on a piece of lung does not allow to access directly the alveolar septum parameters, but allows only the direct identification of the parenchyma parameters. However, this kind of test would allow to indirectly identify the alveolar septum parameters with an inverse problem [Rausch and Wall, 2009].

1.2.2.2 Upscaling strategy

Once the micromechanical model is built, a method to link the micromechanical model to the macromechanical model should be established. The micromechanical model is heterogeneous with the solid and fluid phases defined explicitly, whereas at the macroscale each point is considered as homogeneous in averaging the microscopic quantities. This upscaling method is called *homogenization*. The microscopic element size should satisfy several conditions: being large enough to be representative of the microstructure and being small compared to the macroscale. The averaging over this microscopic element, also called *Representative Volume Element* (RVE), gives its effective behavior.

Homogenization methods could be either mathematical or numerical. Concha et al. [2018] mathematically derive the effective behavior of the RVE as a function of four parameters, mainly the alveolar wall elasticity and the porosity, from a mathematical dodecahedron alveolar unit. However, when using a more complex geometry extracted from images, the numeric approach is more adapted [Wiechert, 2011]. It consists in numerically applying to the RVE the boundary conditions prescribed by the macroscale model to compute the stress and strain in the RVE and the effective stress and strains of the RVE. An illustration of the homogenization process is given in Figure 1.10. Other studies apply homogenization methods for pulmonary applications [Lewis and Owen, 2001; Cazeaux and Grandmont, 2015; Yoshihara et al., 2017]. However, they focus on airflow and not on solid mechanics.

1.2.3 Contribution of a poromechanical framework

As a porous organ where the pores are small compared to the organ size, lung is a multiphase and multiscale organ, which justifies the use of poromechanics to describe its behavior.

1.2.3.1 Poromechanics in general

Poromechanics is a discipline of continuum mechanics which investigates the behavior of porous media with several phases, like fluid-saturated solid media. Unlike homogenization approaches, it brings a macroscopic approach of porous media, called *mixture theory*, in which the porous medium is considered to be the superposition of a solid phase and a fluid phase at each point. The microstructure is not described explicitly and only average quantities are given at each point. It can be applied to several kinds of materials, like rocks, soils, foams or biological tissues.

This discipline has been extensively used in civil engineering for soil mechanics investigations [Siddique et al., 2017], to understand water, oil or gas flows inside soils and interactions between those fluids and the soil matrix. Such a knowledge is useful for geology,

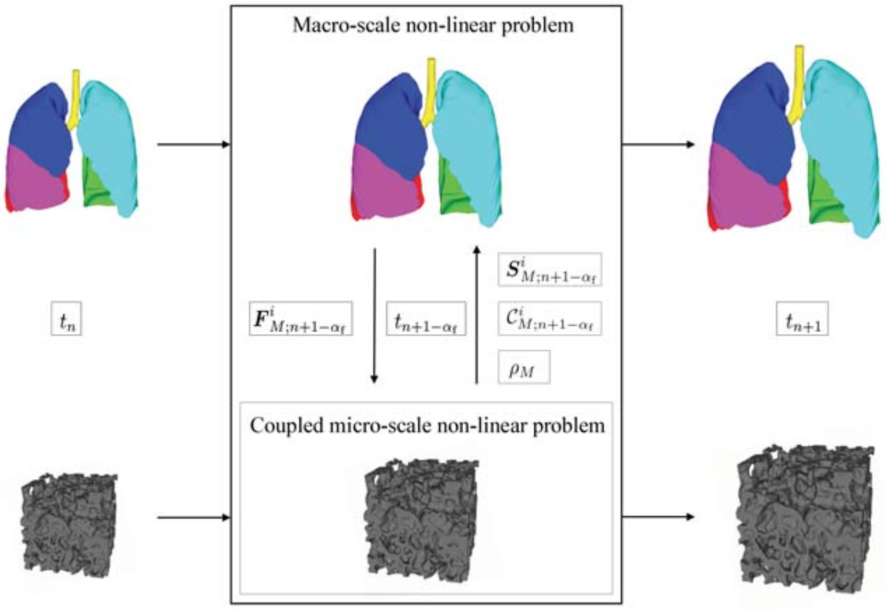

Figure 1.10 – Illustration of the homogenization method. Figure taken from Wiechert [2011].

seismology [Frenkel, 2005] or agriculture applications for example. The work of Terzaghi [1943] is considered as a pioneer [de Boer and Ehlers, 1988], but a three-dimensional general theory of poromechanics was developed by Biot [Biot, 1941, 1962; Biot and Temple, 1972]. The mixture theory has then been widely investigated [Bedford and Drumheller, 1979; Bowen, 1982; Coussy, 2004]. However, these pioneering works cannot be used in biomechanics, like in cardiology or pulmonology, because the formulated hypotheses are not relevant for these applications. Indeed, the hypothesis of small deformation is not appropriate to describe highly deformable organs and the fluid inertia cannot be neglected for cardiac blood circulation. Some works already took into account finite strains [Biot and Temple, 1972; Almeida and Spilker, 1998; Li et al., 2004], but formulate hypotheses about the constitutive behavior instead of deriving the conservation and thermodynamics principles.

Chapelle and Moireau [2014] propose a general poromechanical formulation, based on the work of Coussy [2004]. Their theory satisfies the fundamental physical principles, mainly conservation and thermodynamics laws. It is also compatible with large strains with no specific assumptions, using nonlinear constitutive behavior. Thus, the formulation allows to describe the behavior of biological tissue, like cardiac perfusion [Chapelle et al., 2010; Burtschell, 2016] or lungs, as it will be largely discussed in this thesis.

Concerning pulmonary applications of poromechanics, very few studies model the lung as a porous organ. Kowalczyk [1993] proposes a numerical approach for two-phases media applied to pulmonary parenchyma and airflow, considering a simplified lung geometry. Lande and Mitzner [2006] investigate theoretically the viscoelasticity and time-dependency properties of the porous parenchyma with a dynamic model. Finally, Berger et al. [2016] develop a poroelastic model of lungs, focusing on airflow using a strong coupling with airways.

1.2.3.2 Poromechanical formulation

Before going into the pulmonary poromechanical model developed in this thesis, it is necessary to introduce the general theory of Chapelle and Moireau [2014] on which the present work is based, since simplifications under pulmonary-specific assumptions will be achieved. It is constructed with the derivation of the mass conservation laws, the conservation of momentum, as well as the first and the second fundamental principles of thermodynamics, leading to the energy conservation law and a Clausius-Duhem inequality, respectively.

We consider a mixture occupying the domain ω at any time t. Considering a Lagrangian approach, we will denote by Ω the reference domain with respect to which the position of each material point is defined. Distributed volume forces are applied on the mixture, which can be for example gravity, and are denoted by $\underline{f}$. The mapping $\underline{\chi}$ from Ω to ω gives the position in time of each point:

$$\underline{\chi} = \begin{cases} \Omega \to \omega \\ \underline{X} \mapsto \underline{x} = \underline{\chi}\left(\underline{X}, t\right). \end{cases} \tag{1.14}$$

The displacement is given by:

$$\underline{U} = \underline{x} - \underline{X}, \tag{1.15}$$

and the deformation gradient is defined as:

$$\underline{\underline{F}}\left(\underline{X}, t\right) = \underline{\underline{\nabla}}_{\underline{X}}\,\underline{\chi}. \tag{1.16}$$

The quantity $J = \det \underline{\underline{F}}$ gives the local volume variation of the mixture. The right Cauchy-Green deformation tensor is:

$$\underline{\underline{C}} = \underline{\underline{F}}^T \cdot \underline{\underline{F}}. \tag{1.17}$$

The mixture stress in the reference configuration is given by the second Piola-Kirchhoff stress tensor $\underline{\underline{\Sigma}}$ and is related to the Cauchy stress $\underline{\underline{\sigma}}$ with the following relation:

$$\underline{\underline{\sigma}} = \frac{1}{J}\underline{\underline{F}} \cdot \underline{\underline{\Sigma}} \cdot \underline{\underline{F}}^T. \tag{1.18}$$

Following the mixture theory, the mixture is composed of a fluid phase and a solid phase, in the proportions ϕ_{f} and $1 - \phi_{\mathrm{f}}$, at each point. The quantity ϕ_{f}, called *porosity*, is the volume fraction of fluid in the deformed configuration. In the reference configuration, the reference porosity is denoted by Φ_{f0}.

The fluid flows into the solid matrix with velocity $\underline{v}_{\mathrm{f}}$, pressure p_{f} and current fluid density ϱ_{f}. Fluid can flow in and out, which can be described by either the distributed mass source term θ or the added fluid mass density $\overline{\rho}_{\mathrm{f}+}$. These two quantities are linked with the fluid mass conservation law. The fluid contribution to the mixture stress is composed of two terms:

$$\underline{\underline{\Sigma}}_{\mathrm{f}} = \phi_{\mathrm{f}}\underline{\underline{\Sigma}}_{\mathrm{vis}} - \phi_{\mathrm{f}} p_{\mathrm{f}} J \underline{\underline{C}}^{-1}, \tag{1.19}$$

where $\underline{\underline{\Sigma}}_{\mathrm{vis}}$ is the fluid viscous stress and the second term is the fluid hydrostatic stress.

The solid phase, also called *skeleton* or *matrix*, is characterized by the reference solid density ρ_{s0} and the solid velocity $\underline{v}_{\mathrm{s}}$, defined as $\underline{v}_{\mathrm{s}} = \left.\dfrac{\partial \underline{x}}{\partial t}\right|_{\underline{X}}$. A poromechanics-specific quantity is the local variation of the solid volume J_{s}, expressed as $J_{\mathrm{s}} = J\left(1 - \phi_{\mathrm{f}}\right)$. The solid contribution in the mixture stress tensor is:

$$\underline{\underline{\Sigma}}_{\mathrm{s}} = \underline{\underline{\Sigma}} - \underline{\underline{\Sigma}}_{\mathrm{f}}. \tag{1.20}$$

Finally, both phases interact with each other through the permeability tensor $\underline{\underline{k}}_{\mathrm{f}}$, which describes how the fluid flows into the solid. It can be impacted by the solid properties, such as anisotropy, or interactions between both phases, like friction.

The strong formulation of the poromechanical theory of Chapelle and Moireau [2014] is then the following:

$$\begin{cases} \rho_{\mathrm{s}0}\left(1-\Phi_{\mathrm{f}0}\right)\dfrac{\mathrm{d}\underline{v}_{\mathrm{s}}}{\mathrm{d}t} - \underline{\nabla}_{\underline{X}}\cdot\left(\underline{\underline{F}}\cdot\underline{\underline{\Sigma}}_{\mathrm{s}}\right) - J\phi_{\mathrm{f}}^{2}\underline{\underline{k}}_{\mathrm{f}}^{-1}\cdot\left(\underline{v}_{\mathrm{f}}-\underline{v}_{\mathrm{s}}\right) + p_{\mathrm{f}}J\underline{\underline{F}}^{-T}\cdot\underline{\nabla}_{\underline{X}}\phi_{\mathrm{f}} \\ \qquad\qquad = \rho_{\mathrm{s}0}\left(1-\Phi_{\mathrm{f}0}\right)\underline{f},\ \text{in } \Omega \\ \dfrac{1}{J}\dfrac{\mathrm{d}}{\mathrm{d}t}\left(J\varrho_{\mathrm{f}}\Phi_{\mathrm{f}0}\underline{v}_{\mathrm{f}} + \underline{\nabla}_{\underline{x}}\cdot\left(\varrho_{\mathrm{f}}\Phi_{\mathrm{f}0}\underline{v}_{\mathrm{f}}\otimes\left(\underline{v}_{\mathrm{f}}-\underline{v}_{\mathrm{s}}\right)\right)\right) - \theta\underline{v}_{\mathrm{f}} + \Phi_{\mathrm{f}0}^{2}\underline{\underline{k}}_{\mathrm{f}}^{-1}\cdot\left(\underline{v}_{\mathrm{f}}-\underline{v}_{\mathrm{s}}\right) \\ \qquad\qquad +\Phi_{\mathrm{f}0}\underline{\nabla}_{\underline{x}}p_{\mathrm{f}} - \underline{\nabla}_{\underline{x}}\cdot\left(\Phi_{\mathrm{f}0}\underline{\underline{\sigma}}_{\mathrm{vis}}\right) = \varrho_{\mathrm{f}}\Phi_{\mathrm{f}0}\underline{f},\ \text{in } \omega \\ \dfrac{1}{J}\dfrac{\mathrm{d}}{\mathrm{d}t}\left(J\varrho_{\mathrm{f}}\Phi_{\mathrm{f}0}\right) + \underline{\nabla}_{\underline{x}}\cdot\left(\varrho_{\mathrm{f}}\Phi_{\mathrm{f}0}\left(\underline{v}_{\mathrm{f}}-\underline{v}_{\mathrm{s}}\right)\right) = \theta,\ \text{in } \omega. \end{cases} \tag{1.21}$$

The formulation takes the form of a system with three equations. The three unknowns are the solid displacement $\underline{U}$, the fluid velocity $\underline{v}_{\mathrm{f}}$ and the porosity ϕ_{f}. The first equation is the fundamental law of dynamics, derived from the momentum conservation law, and describes the solid deformation. The second one describes the fluid flow and the last one the fluid mass conservation.

It should be noticed that no specific assumption was formulated to get this system of equations. In particular, no hypothesis is done on the compressibility of the solid and fluid phase.

Compared to the mechanical models discussed in Section 1.2, poromechanical models have more unknowns and more equations. Indeed, unknowns and equations are required to describe the fluid phase and the interaction between both phases of a mixture. Mechanical models can be recovered from poromechanical models by taking the limit case where there is no fluid in the mixture, *i.e.*, $\phi_{\mathrm{f}} = 0$ at any time t. The boundary conditions and constitutive behaviors described for the mechanical models can be incorporated in the poromechanical models, except that they concern only the solid phase. Thus, they should be augmented by boundary conditions and constitutive behaviors specific to the fluid phase.

Treatment of boundary conditions Concerning boundary conditions, several common combinations for both solid and fluid phases are mentioned in Chapelle and Moireau [2014]:

- Dirichlet boundary conditions for both phases: prescribed solid displacement $\underline{U}$ and fluid velocity $\underline{v}_{\mathrm{f}}$,
- Neumann boundary conditions for both phases,
- Neumann boundary conditions for the global mixture and equal velocities of both phases to prevent sliding ($\underline{v}_{\mathrm{f}} = \underline{v}_{\mathrm{s}}$).

Treatment of the constitutive behavior The integration of the constitutive behavior of a mechanical model into a poromechanical model is less straightforward than for the boundary conditions. More details should be given on the description of the mixture constitutive behavior.

The mixture constitutive behavior is defined by the Helmholtz free energy $\overline{\psi}$, which characterizes the energy of the whole mixture. A common assumption is the decomposition of the mixture energy into two terms [Coussy, 2004; Chapelle and Moireau, 2014]:

$$\overline{\psi} = \overline{\psi}_{\mathrm{s}} + \overline{\psi}_{\mathrm{f}}, \tag{1.22}$$

where $\overline{\psi}_{\mathrm{s}}$ and $\overline{\psi}_{\mathrm{f}}$ are the free energies of the solid and fluid phases respectively. With such a decomposition, the contribution of each phase is described separately.

The solid energy takes into account several physical phenomena. The first one is the deformation of the solid phase, considering it as a structure. This deformation energy depends on the microstructure, especially the porosity, but also the microscopic geometry. Another one is the compressibility of the solid phase, *i.e.,* the variation of the solid phase volume with the fluid pressure exerted in the pores. For example, in the case of pulmonary alveoli, it reflects the energy related to the variation of the alveolar wall thickness with the alveolar air pressure. A natural way to construct such a solid energy is to consider that the effects are additive. It gives the following expression [Chapelle and Moireau, 2014]:

$$\overline{\psi}_{\mathrm{s}} = \overline{W}_{\mathrm{skel}} + \overline{W}_{\mathrm{bulk}}, \tag{1.23}$$

where $\overline{W}_{\mathrm{skel}}$ is the deformation energy of the solid structure and $\overline{W}_{\mathrm{bulk}}$ is the energy associated with the compressibility property of the solid. It should be noticed that the energy produced by the global variation of the mixture volume is present in the $\overline{W}_{\mathrm{skel}}$ term, since it corresponds to the volume variation of the global solid structure and not of the solid phase.

The constitutive behavior used in a mechanical model, where a mixture is considered as a structure without taking into account the biphasic characteristics of the mixture, corresponds to the skeleton energy $\overline{W}_{\mathrm{skel}}$ of the poromechanical model. It means that the constitutive behavior built from experimental tests on a mixture should be incorporated there. Moreover, biological tissues are often quasi-incompressible or incompressible, leading to the adequate energy $\overline{W}_{\mathrm{bulk}}$ depending on a solid bulk modulus which should be taken large.

The fluid energy depends on the fluid present in the mixture. However, when studying living tissue, some assumptions can be formulated, resulting in a simplified expression of $\overline{\psi}_{\mathrm{f}}$. Indeed, fluids are considered as incompressible, which is an acceptable hypothesis regarding the applications for blood or pulmonary airflow. Furthermore, the temperature is constant at the body temperature and homogeneous. Then, living tissue deformations are under isothermal conditions. Under these two assumptions, the fluid energy is expressed as [Chapelle and Moireau, 2014]:

$$\overline{\psi}_{\mathrm{f}} = -p_{\mathrm{f0}} J \phi_{\mathrm{f}}, \tag{1.24}$$

with p_{f0} a reference pressure. The fluid energy is then independent from the deformation, which means that the fluid does not store any energy. Consequently, the associated stress is zero.

As a conclusion, such a poromechanical framework can be relevant for pulmonary modeling as lungs are biphasic materials. It can incorporate the elements of a solid mechanical model, but also use additional elements concerning the fluid phase, like the porosity or the fluid velocity, which gives more information on the microstructure evolution throughout the deformation.

Comparing to multiscale approaches discussed in Section 1.2, the microstructure is not explicitly described. Consequently, no microscopic quantity is available and only average quantities on the microstructure at a given point are computed. However, the computations are more efficient in poromechanical approach. If needed, a microstructure can be assumed and post-processing computations can be performed on it using as boundary conditions the result of the poromechanical computations. This method allows then to recover some microscopic information from a poromechanical approach at a lower cost.

This poromechanical framework forms the basis of the pulmonary poromechanical model, which will be described in Chapter 2. In particular, some pulmonary-specific assumptions will be formulated.

Bibliography

Agostoni, E. (1972). Mechanics of the pleural space. *Physiological Reviews*, 52(1):57–128.

Agostoni, E., D'Angelo, E., and Roncoroni, G. (1968). The thickness of the pleural liquid. *Respiration Physiology*, 5(1):1–13.

Akoumianaki, E., Maggiore, S. M., Valenza, F., Bellani, G., Jubran, A., Loring, S. H., Pelosi, P., Talmor, D., Grasso, S., Chiumello, D., Guérin, C., Patroniti, N., Ranieri, V. M., Gattinoni, L., Nava, S., Terragni, P.-P., Pesenti, A., Tobin, M., Mancebo, J., and Brochard, L. (2014). The Application of Esophageal Pressure Measurement in Patients with Respiratory Failure. *American Journal of Respiratory and Critical Care Medicine*, 189(5):520–531.

Al-Mayah, A., Moseley, J., and Brock, K. K. (2008). Contact surface and material nonlinearity modeling of human lungs. *Physics in Medicine and Biology*, 53(1):305–317.

Al-Mayah, A., Moseley, J., Velec, M., and Brock, K. (2011). Toward efficient biomechanical-based deformable image registration of lungs for image-guided radiotherapy. *Physics in Medicine and Biology*, 56(15):4701–4713.

Al-Mayah, A., Moseley, J., Velec, M., and Brock, K. K. (2009). Sliding characteristic and material compressibility of human lung: Parametric study and verification: Sliding characteristic and material compressibility of human lung. *Medical Physics*, 36(10):4625–4633.

Almeida, E. S. and Spilker, R. L. (1998). Finite element formulations for hyperelastic transversely isotropic biphasic soft tissues. *Computer Methods in Applied Mechanics and Engineering*, 151(3-4):513–538.

Bachofen, H. (1968). Lung tissue resistance and pulmonary hysteresis. *Journal of Applied Physiology*, 24(3):296–301.

Baudet, V., Villard, P.-F., Jaillet, F., Beuve, M., and Shariat, B. (2003). Towards accurate tumour tracking in lungs. In *Proceedings on Seventh International Conference on Information Visualization, IV 2003.*, pages 338–343. IEEE Comput. Soc.

Bayliss, L. E. and Robertson, G. W. (1939). The visco-elastic properties of the lungs. *Quarterly Journal of Experimental Physiology and Cognate Medical Sciences*, 29(1):27–47.

Bedford, A. and Drumheller, D. (1979). A variational theory of porous media. *International Journal of Solids and Structures*, 15(12):967–980.

Bel-Brunon, A., Kehl, S., Martin, C., Uhlig, S., and Wall, W. (2014). Numerical identification method for the non-linear viscoelastic compressible behavior of soft tissue using uniaxial tensile tests and image registration – Application to rat lung parenchyma. *Journal of the Mechanical Behavior of Biomedical Materials*, 29:360–374.

Berger, L., Bordas, R., Burrowes, K., Grau, V., Tavener, S., and Kay, D. (2016). A poroelastic model coupled to a fluid network with applications in lung modelling: A poroelastic model coupled to a fluid network with applications in lung modelling. *International Journal for Numerical Methods in Biomedical Engineering*, 32(1).

Biederer, J., Beer, M., Hirsch, W., Wild, J., Fabel, M., Puderbach, M., and Van Beek, E. J. R. (2012a). MRI of the lung (2/3). Why ... when ... how? *Insights into Imaging*, 3(4):355–371.

Biederer, J., Mirsadraee, S., Beer, M., Molinari, F., Hintze, C., Bauman, G., Both, M., Van Beek, E. J. R., Wild, J., and Puderbach, M. (2012b). MRI of the lung (3/3)—current applications and future perspectives. *Insights into Imaging*, 3(4):373–386.

Biot, M. A. (1941). General Theory of Three-Dimensional Consolidation. *Journal of Applied Physics*, 12(2):155–164.

Biot, M. A. (1962). Mechanics of Deformation and Acoustic Propagation in Porous Media. *Journal of Applied Physics*, 33(4):1482–1498.

Biot, M. A. and Temple, G. (1972). Theory of Finite Deformations of Porous Solids. *Indiana University Mathematics Journal*, 21(7):597–620.

Birzle, A. M., Hobrack, S. M. K., Martin, C., Uhlig, S., and Wall, W. A. (2019). Constituent-specific material behavior of soft biological tissue: Experimental quantification and numerical identification for lung parenchyma. *Biomechanics and Modeling in Mechanobiology*, 18:1383–1400.

Birzle, A. M., Martin, C., Uhlig, S., and Wall, W. A. (2018a). A Coupled Approach for Identification of Nonlinear and Compressible Material Models for Soft Tissue Based on Different Experimental Setups – Exemplified and Detailed for Lung Parenchyma. *Journal of the Mechanical Behavior of Biomedical Materials*, 94:126–143.

Birzle, A. M., Martin, C., Yoshihara, L., Uhlig, S., and Wall, W. A. (2018b). Experimental characterization and model identification of the nonlinear compressible material behavior of lung parenchyma. *Journal of the Mechanical Behavior of Biomedical Materials*, 77:754–763.

Birzle, A. M. and Wall, W. A. (2018). A Viscoelastic Nonlinear Compressible Material Model of Lung Parenchyma - Experiments and Numerical Identification. *Journal of the Mechanical Behavior of Biomedical Materials*, 94:164–175.

Bordas, R., Lefevre, C., Veeckmans, B., Pitt-Francis, J., Fetita, C., Brightling, C. E., Kay, D., Siddiqui, S., and Burrowes, K. S. (2015). Development and Analysis of Patient-Based Complete Conducting Airways Models. *Plos One*, 10(12).

Boucneau, T. (2019). *Magnetic Resonance Imaging of Respiratory Mechanics*. PhD thesis.

Bowen, R. M. (1982). Compressible porous media models by use of the theory of mixtures. *International Journal of Engineering Science*, 20(6):697–735.

Brock, K. K., Sharpe, M. B., Dawson, L. A., Kim, S. M., and Jaffray, D. A. (2005). Accuracy of finite element model-based multi-organ deformable image registration: Accuracy of FEM-based multi-organ deformable image registration. *Medical Physics*, 32(6Part1):1647–1659.

Budiansky, B. and Kimmel, E. (1987). Elastic Moduli of Lungs. *Journal of Applied Mechanics*, 54(2):351–358.

Burtschell, B. (2016). *Mechanical Modeling and Numerical Methods for Poromechanics: Application to Myocardium Perfusion*. PhD thesis.

Cazeaux, P. and Grandmont, C. (2015). Homogenization of a multiscale viscoelastic model with nonlocal damping, application to the human lungs. *Mathematical Models and Methods in Applied Sciences*, 25(06):1125–1177.

Chapelle, D., Gerbeau, J.-F., Sainte-Marie, J., and Vignon-Clementel, I. E. (2010). A poroelastic model valid in large strains with applications to perfusion in cardiac modeling. *Computational Mechanics*, 46(1):91–101.

Chapelle, D. and Moireau, P. (2014). General coupling of porous flows and hyperelastic formulations—From thermodynamics principles to energy balance and compatible time schemes. *European Journal of Mechanics - B/Fluids*, 46:82–96.

Colebatch, H. and Ng, C. (1992). Estimating alveolar surface area during life. *Respiration Physiology*, 88(1-2):163–170.

Concha, F., Sarabia-Vallejos, M., and Hurtado, D. E. (2018). Micromechanical model of lung parenchyma hyperelasticity. *Journal of the Mechanics and Physics of Solids*, 112:126–144.

Coussy, O. (2004). *Poromechanics*. Wiley, Chichester.

Crawford, E. C. (1962). Mechanical aspects of panting in dogs. *Journal of Applied Physiology*, 17(2):249–251.

Criée, C., Sorichter, S., Smith, H., Kardos, P., Merget, R., Heise, D., Berdel, D., Köhler, D., Magnussen, H., Marek, W., Mitfessel, H., Rasche, K., Rolke, M., Worth, H., and Jörres, R. (2011). Body plethysmography – Its principles and clinical use. *Respiratory Medicine*, 105(7):959–971.

Dale, P., Matthews, F. L., and Schroter, R. C. (1980). Finite element analysis of lung alveolus. *Journal of Biomechanics*, 13(10):865–873.

D'Angelo, E., Bonanni, M., Michelini, S., and Agostoni, E. (1970). Topography of the pleural surface pressure in rabbits and dogs. *Respiration Physiology*, 8(2):204–229.

de Boer, R. and Ehlers, W. (1988). A historical review of the formulation of porous media theories. *Acta Mechanica*, 74(1-4):1–8.

de Ryk, J., Thiesse, J., Namati, E., and McLennan, G. (2007). Stress distribution in a three dimensional, geometric alveolar sac under normal and emphysematous conditions. *International Journal of COPD*, 2(1):81–91.

De Wilde, R., Clement, J., Hellemans, J. M., Decramer, M., Demedts, M., Boving, R., and Van de Woestijne, K. P. (1981). Model of elasticity of the human lung. *Journal of Applied Physiology*, 51(2):254–261.

Demiray, H. (1972). A note on the elasticity of soft biological tissues. *Journal of Biomechanics*, 5(3):309–311.

Denny, E. and Schroter, R. (2006). A model of non-uniform lung parenchyma distortion. *Journal of Biomechanics*, 39(4):652–663.

Eom, J., Shi, C., Xu, X. G., and De, S. (2010). In vivo Characterization of Lung Tissue Properties from 4D CT Images for Cancer Radiation Therapy. In Magjarevic, R., Lim, C. T., and Goh, J. C. H., editors, *6th World Congress of Biomechanics (WCB 2010). August 1-6, 2010 Singapore*, volume 31, pages 698–701. Springer Berlin Heidelberg, Berlin, Heidelberg.

Ferrara, J. M. (2009). *Determination of 3-Dimensional Deformations of the Alveolar Sac during Simulated Breathing*. PhD thesis.

Frenkel, J. (2005). On the Theory of Seismic and Seismoelectric Phenomena in a Moist Soil. *Journal of Engineering Mechanics*, 131(9):879–887.

Fuerst, B., Mansi, T., Carnis, F., Salzle, M., Zhang, J., Declerck, J., Boettger, T., Bayouth, J., Navab, N., and Kamen, A. (2015). Patient-Specific Biomechanical Model for the Prediction of Lung Motion From 4-D CT Images. *IEEE Transactions on Medical Imaging*, 34(2):599–607.

Fung, Y.-C. (1974). A Theory of Elasticity of the Lung. *Journal of Applied Mechanics*, 41(1).

Fung, Y.-C. (1993). *Biomechanics: Mechanical Properties of Living Tissues*. Springer-Verlag New York.

Gefen, A., Elad, D., and Shiner, R. (1999). Analysis of stress distribution in the alveolar septa of normal and simulated emphysematic lungs. *Journal of Biomechanics*, 32(9):891–897.

Gibson, G. (2001). Lung volumes and elasticity. *Clinics in Chest Medicine*, 22(4):623–635.

Han, L., Dong, H., McClelland, J. R., Han, L., Hawkes, D. J., and Barratt, D. C. (2017). A hybrid patient-specific biomechanical model based image registration method for the motion estimation of lungs. *Medical Image Analysis*, 39:87–100.

Hills, B. A. (1981). What is the true role of surfactant in the lung? *Thorax*, 36(1):1–4.

Hoppin, F. G., Green, I. D., and Mead, J. (1969). Distribution of pleural surface pressure in dogs. *Journal of Applied Physiology*, 27(6):863–873.

Hoppin, F. G., Lee, G. C., and Dawson, S. V. (1975). Properties of lung parenchyma in distortion. *Journal of Applied Physiology*, 39(5):742–751.

Im, J. G., Webb, W. R., Rosen, A., and Gamsu, G. (1989). Costal pleura: Appearances at high-resolution CT. *Radiology*, 171(1):125–131.

Joseph, D., Puttaswamy, R. K., and Krovvidi, H. (2013). Non-respiratory functions of the lung. *Continuing Education in Anaesthesia Critical Care & Pain*, 13(3):98–102.

Kallet, R. H. (2015). A Comprehensive Review of Prone Position in ARDS. *Respiratory Care*, 60(11):1660–1687.

Kane, K. K. (1973). The Role of the Lungs in the Adjustment of Acid-Base Balance. *Annals of Clinical Laboratory Science*, 3(5).

Karakaplan, A. D., Bieniek, M. P., and Skalak, R. (1980). A Mathematical Model of Lung Parenchyma. *Journal of Biomechanical Engineering*, 102(2):124–136.

Knowles, J. H., Hong, S. K., and Rahn, H. (1959). Possible errors using esophageal balloon in determination of pressure-volume characteristics of the lung and thoracic cage. *Journal of Applied Physiology*, 14(4):525–530.

Koshiyama, K., Nishimoto, K., Ii, S., Sera, T., and Wada, S. (2018). Heterogeneous structure and surface tension effects on mechanical response in pulmonary acinus: A finite element analysis. *Clinical Biomechanics*, 66:32–39.

Kowalczyk, P. (1993). Mechanical model of lung parenchyma as a two-phase porous medium. *Transport in Porous Media*, 11(3):281–295.

Lai-Fook, S. J. (1977). Lung parenchyma described as a prestressed compressible material. *Journal of Biomechanics*, 10(5-6):357–365.

Lai-Fook, S. J. (1981). Elasticity analysis of lung deformation problems. *Annals of Biomedical Engineering*, 9(5-6):451–462.

Lai-Fook, S. J. (2004). Pleural Mechanics and Fluid Exchange. *Physiological Reviews*, 84(2):385–410.

Lai-Fook, S. J. and Rodarte, J. R. (1991). Pleural pressure distribution and its relationship to lung volume and interstitial pressure. *Journal of Applied Physiology*, 70(3):967–978.

Lai-Fook, S. J., Wilson, T. A., Hyatt, R. E., and Rodarte, J. R. (1976). Elastic constants of inflated lobes of dog lungs. *Journal of Applied Physiology*, 40(4):508–513.

Lande, B. and Mitzner, W. (2006). Analysis of lung parenchyma as a parametric porous medium. *Journal of Applied Physiology*, 101(3):926–933.

Lewis, M. A. and Owen, M. R. (2001). The Mechanics of Lung Tissue under High-Frequency Ventilation. *SIAM Journal on Applied Mathematics*, 61(5):1731–1761.

Li, C., Borja, R. I., and Regueiro, R. A. (2004). Dynamics of porous media at finite strain. *Computer Methods in Applied Mechanics and Engineering*, 193(36-38):3837–3870.

Lutfi, M. F. (2017). The physiological basis and clinical significance of lung volume measurements. *Multidisciplinary Respiratory Medicine*, 12(1):3.

Mauroy, B., Filoche, M., Weibel, E. R., and Sapoval, B. (2004). An optimal bronchial tree may be dangerous. *Nature*, 427(6975):633–636.

Mead, J., Takishima, T., and Leith, D. (1970). Stress distribution in lungs: A model of pulmonary elasticity. *Journal of Applied Physiology*, 28(5):596–608.

Mead, J., Whittenberger, J. L., and Radford, E. P. (1957). *Surface Tension as a Factor in Pulmonary Volume-Pressure Hysteresis*. *Journal of Applied Physiology*, 10(2):191–196.

Milic-Emili, J., Henderson, J. A., Dolovich, M. B., Trop, D., and Kaneko, K. (1966). Regional distribution of inspired gas in the lung. *Journal of Applied Physiology*, 21(3):749–759.

Millar, A. B. and Denison, D. M. (1989). Vertical gradients of lung density in healthy supine men. *Thorax*, 44(6):485–490.

Mortola, J. P. (2013). Lung Viscoelasticity: Implications on Breathing and Forced Expiration. *Clinical Pulmonary Medicine*, 20(3):144–148.

Osborne, D., Effmann, E., and Hedlund, L. (1983). Postnatal growth and size of the pulmonary acinus and secondary lobule in man. *American Journal of Roentgenology*, 140(3):449–454.

Otis, D. R., Ingenito, E. P., Kamm, R. D., and Johnson, M. (1994). Dynamic surface tension of surfactant TA: Experiments and theory. *Journal of Applied Physiology*, 77(6):2681–2688.

Pecchiari, M., Loring, S. H., and D'Angelo, E. (2013). Esophageal pressure as an estimate of average pleural pressure with lung or chest distortion in rats. *Respiratory Physiology & Neurobiology*, 186(2):229–235.

Rausch, S., Martin, C., Bornemann, P., Uhlig, S., and Wall, W. (2011a). Material model of lung parenchyma based on living precision-cut lung slice testing. *Journal of the Mechanical Behavior of Biomedical Materials*, 4(4):583–592.

Rausch, S. and Wall, W. A. (2009). Parameter identification for modelling alveolar tissue on different scales. In *7th EUROMECH Solid Mechanics Conference*, Lisbon, Portugal.

Rausch, S. M. K., Haberthür, D., Stampanoni, M., Schittny, J. C., and Wall, W. A. (2011b). Local Strain Distribution in Real Three-Dimensional Alveolar Geometries. *Annals of Biomedical Engineering*, 39(11):2835–2843.

Roth, C. J., Yoshihara, L., and Wall, W. A. (2017). A simplified parametrised model for lung microstructures capable of mimicking realistic geometrical and mechanical properties. *Computers in Biology and Medicine*, 89:104–114.

Shirzadi, Z., Sadeghi-Naini, A., and Samani, A. (2013). Toward *in vivo* lung's tissue incompressibility characterization for tumor motion modeling in radiation therapy: Toward *in vivo* lung's tissue incompressibility characterization. *Medical Physics*, 40(5):051902.

Siddique, J., Ahmed, A., Aziz, A., and Khalique, C. (2017). A Review of Mixture Theory for Deformable Porous Media and Applications. *Applied Sciences*, 7(9):917.

Smith, J. C. and Stamenovic, D. (1986). Surface forces in lungs. I. Alveolar surface tension-lung volume relationships. *Journal of Applied Physiology*, 60(4):1341–1350.

Sobin, S. S., Fung, Y. C., and Tremer, H. M. (1988). Collagen and elastin fibers in human pulmonary alveolar walls. *Journal of Applied Physiology*, 64(4):1659–1675.

Suki, B., Barabasi, A. L., and Lutchen, K. R. (1994). Lung tissue viscoelasticity: A mathematical framework and its molecular basis. *Journal of Applied Physiology*, 76(6):2749–2759.

Suki, B. and Lutchen, K. R. (2006). Lung Tissue Viscoelasticity. In Akay, M., editor, *Wiley Encyclopedia of Biomedical Engineering*. John Wiley & Sons, Inc., Hoboken, NJ, USA.

Sundaram, T. A. and Gee, J. C. (2005). Towards a model of lung biomechanics: Pulmonary kinematics via registration of serial lung images. *Medical Image Analysis*, 9(6):524–537.

Tai, R. C. and Lee, G. C. (1981). Isotropy and homogeneity of lung tissue deformation. *Journal of Biomechanics*, 14(4):243–252.

Tawhai, M. H. and Bates, J. H. T. (2011). Multi-scale lung modeling. *Journal of Applied Physiology*, 110(5):1466–1472.

Tawhai, M. H., Nash, M. P., Lin, C.-L., and Hoffman, E. A. (2009). Supine and prone differences in regional lung density and pleural pressure gradients in the human lung with constant shape. *Journal of Applied Physiology*, 107(3):912–920.

Terzaghi, K. (1943). *Theoretical Soil Mechanics*. John Wiley & Sons, Inc., Hoboken, NJ, USA.

Toshima, M., Ohtani, Y., and Ohtani, O. (2004). Three-dimensional architecture of elastin and collagen fiber networks in the human and rat lung. *Archives of Histology and Cytology*, 67(1):31–40.

Villard, P.-F., Beuve, M., Shariat, B., Baudet, V., and Jaillet, F. (2005). Simulation of Lung Behaviour with Finite Elements: Influence of Bio-Mechanical Parameters. In *Third International Conference on Medical Information Visualisation–BioMedical Visualisation*, pages 9–14, London, England. IEEE.

Weed, B., Patnaik, S., Rougeau-Browning, M., Brazile, B., Liao, J., Prabhu, R., and Williams, L. (2015). Experimental Evidence of Mechanical Isotropy in Porcine Lung Parenchyma. *Materials*, 8(5):2454–2466.

Weibel, E. R. (1963). *Morphometry of the Human Lung*. Springer Berlin Heidelberg, Berlin, Heidelberg.

Weibel, E. R., Sapoval, B., and Filoche, M. (2005). Design of peripheral airways for efficient gas exchange. *Respiratory Physiology & Neurobiology*, 148(1-2):3–21.

Werner, R., Ehrhardt, J., Schmidt, R., and Handels, H. (2009). Patient-specific finite element modeling of respiratory lung motion using 4D CT image data: Finite element modeling of respiratory lung motion. *Medical Physics*, 36(5):1500–1511.

West, J. B. and Matthews, F. L. (1972). Stresses, strains, and surface pressures in the lung caused by its weight. *Journal of Applied Physiology*, 32(3):332–345.

West, J. B. and Nadeau, M. (2003). *La physiologie respiratoire*.

Wiechert, L. (2011). *Computational Modeling of Multi-Field and Multi-Scale Phenomena in Respiratory Mechanics*. PhD thesis.

Wiechert, L., Comerford, A., Rausch, S., and Wall, W. A. (2011). Advanced Multi-scale Modelling of the Respiratory System. In Hirschel, E. H., Schröder, W., Fujii, K., Haase, W., Leer, B., Leschziner, M. A., Pandolfi, M., Periaux, J., Rizzi, A., Roux, B., Shokin, Y. I., Klaas, M., Koch, E., and Schröder, W., editors, *Fundamental Medical and Engineering Investigations on Protective Artificial Respiration*, volume 116, pages 1–32. Springer Berlin Heidelberg, Berlin, Heidelberg.

Yoshihara, L., Ismail, M., and Wall, W. A. (2013). Bridging Scales in Respiratory Mechanics. In Holzapfel, G. A. and Kuhl, E., editors, *Computer Models in Biomechanics*, pages 395–407. Springer Netherlands, Dordrecht.

Yoshihara, L., Roth, C. J., and Wall, W. A. (2017). Fluid-structure interaction including volumetric coupling with homogenised subdomains for modeling respiratory mechanics: Fluid-structure interaction including volumetric coupling with homogenised subdomains for modeling respiratory mechanics. *International Journal for Numerical Methods in Biomedical Engineering*, 33(4).

Zeng, Y. J., Yager, D., and Fung, Y. C. (1987). Measurement of the Mechanical Properties of the Human Lung Tissue. *Journal of Biomechanical Engineering*, 109(2):169–174.

Zhang, T., Orton, N. P., Mackie, T. R., and Paliwal, B. R. (2004). Technical note: A novel boundary condition using contact elements for finite element based deformable image registration. *Medical Physics*, 31(9):2412–2415.

CHAPTER 2

A poromechanical model of the lungs

In the second chapter, we aim to build a pulmonary poromechanical model at the organ scale and at the breathing scale. Based on a previous work of MΞDISIM team about poromechanics, pulmonary-specific hypotheses are formulated. Then, all the elements of a mechanical model are incorporated. A constitutive behavior is designed to consider the non-linearity of the volume behavior of lungs with pressure. Boundary conditions using contact and taking into account the breathing type (spontaneous or mechanical) are defined. A specific problem in biomechanics is solved to estimate the unloaded configuration of lungs. Finally, a specific problem to poromechanics in high deformation, which is to constrain the porosity to be positive, is addressed and two solutions are proposed. At the end, several illustrations of the model are proposed by studying the impact of different modeling choices, like the constitutive behavior (compliance, porosity energy) and boundary conditions (contact properties, gravity, pressure).
This chapter takes the form of a pre-print article co-authored by Cécile Patte, Martin Genet and Dominique Chapelle, entitled *A poromechanical model of the lungs*.

Contents

A poromechanical model of the lungs

C. Patte[1,2], M. Genet[2,1], D. Chapelle[1,2]

[1] Inria, {cecile.patte, dominique.chapelle}@inria.fr
[2] LMS, École Polytechnique, Institut Polytechnique de Paris, CNRS,
martin.genet@polytechnique.edu

to be submitted

Abstract

Lung vital function of providing oxygen to the body is dependent on the mechanical behavior of pulmonary tissue. During air inhalation, lung inflation is allowed by the pulmonary tissue, which is highly compliant and porous. The driving forces of breathing involve a complex environment, with diaphragm, pleura, rib cage and intercostal muscles. We developed a poromechanical model of the lungs during breathing, adapted from a general poromechanics theory by the formulation of lung-specific assumptions. Our model includes physiological boundary conditions and a hyperelastic potential reproducing the volume response of the pulmonary mixture to a change of pressure. A strategy is established to estimate the unloaded, reference configuration with a particular focus on ensuring a positive porosity, since this issue occurs for large deformation problems. Finally we emphasize through several illustrations the relevance of our model and its possible clinical applications.

Keywords— Pulmonary Mechanics, Poromechanics, Modeling, Finite Element Method

2.1 Introduction

Context Pulmonary diseases are among the main causes of death in the world [OMS, 2016] and represent an important health burden. Among them, interstitial lung diseases (ILD) affect the pulmonary tissue and the organ structure, and consequently alter the pulmonary function. Indeed, the main lung function, consisting in providing oxygen to the whole body, is made possible by the alveoli pulmonary structure. The high deformability of lungs throughout the breathing cycle plays also a role, letting air enter lungs to the alveoli. Lung mechanical deformations and lung function are then tightly linked. Moreover, mechanics is also assumed to be a driving force of the propagation of some diseases like pulmonary fibrosis, in which a vicious circle, where fibrosis leads to high stresses which in turn induce fibrosis spreading, may occur [Hinz and Suki, 2016].

Pulmonary physiology and pathology involve many scales, from the organ scale to the alveoli scale through the lobe, segment, lobule and acini scales [Burrowes et al., 2019; Osborne et al., 1983]. Lung microstructure is highly complex and can be "homogenized" using the air volume fraction quantity called porosity. Like other organs, bones or brain for example, lungs are porous organs composed of air, present into the airways and the alveoli, on one side, and tissue, composed mainly of respiratory epithelium, elastic fibers, capillary endothelium and blood, on the other side [Weibel, 1965]. The lung porosity varies during breathing when air goes in and out and impacts lung compliance. More than mechanics, lung poromechanics seems to describe well the lung behavior.

Understanding lung physiology allows to model it and then to create a numerical model of the organ. Digital medicine is a growing field since models reach a high level of accuracy along with the development of computational tools. Computational modeling is well developed in some disciplines like cardiology [Chabiniok et al., 2016; Winslow et al., 2012] where clinical applications are achieved, whereas numerical pulmonology is still an emergent area [Kaul, 2019]. Lung modeling and simulation have been initiated mainly for radiotherapy purposes [Eom et al., 2010] and for airflow study in asthma or chronic obstructive pulmonary disease (COPD) [Bordas et al., 2015]. High hopes are placed in these new numerical tools that aim to help clinicians in taking decisions. They pave the way for improvements of diagnostic and prognosis and can be used to test *in silico* therapeutic strategies [Sermesant et al., 2012]. Numerical tools will allow to reduce healthcare costs and risks for patients, as well as optimize procedures for each patient.

Lung poromechanical modeling Lung modeling, and especially pulmonary mechanical modeling, is a real challenge, given the high level of complexity of the organ and the environment [Clark et al., 2017], which should be overcome to improve the digital lung. Lung mechanical models have been proposed at the organ scale, with varying complexity depending on their objective. Radiotherapy applications mainly require displacements knowledge, that can be acquired with image registration [Sundaram and Gee, 2005; Hurtado et al., 2017]. Mechanical models integrate more information like boundary conditions or material constitutive behavior. Some existing models apply a displacement field to the lung surface, obtained by image registration, [Berger et al., 2016] or perform an orthogonal projection of surface nodes from initial to the deformed configurations known from images [Al-Mayah et al., 2011; Brock et al., 2005]. Tawhai et al. [2009] proposed to create the pleural cavity surface, matching to the lung surface, and to deform the pleural cavity keeping the lung surface in contact with the pleural cavity, allowing a frictionless sliding. These Dirichlet boundary conditions do not represent the negative pleural pressure function, that is why other models decided to apply a pressure on the lung surface [Werner et al., 2009; Baudet et al., 2003; Zhang et al., 2004; Han et al., 2017]. Nevertheless, they all impose the final shape, considering a surface with which the lung surface will come into contact and slide. As far material constitutive behavior, lung parenchyma is often considered as a linear material defined with a Young modulus and a Poisson ratio [Werner et al., 2009; Brock et al., 2005; Baudet et al., 2003; Fuerst et al., 2015; Zhang et al., 2004] or with a neohookean hyperelastic law [Berger et al., 2016; Han et al., 2017]. In order to take into account the non linearity of the lung behavior, West and Matthews [1972] used a strain-dependent Young modulus. Zeng et al. [1987] developed a more complex hyperelastic potential using an experimental mechanical tests to capture the non linearity of the lung behavior. Their hyperelastic potential has then been used by [Al-Mayah et al., 2011; Eom et al., 2010]. However, as it comes from biaxial tension tests, it could not reproduce well the volume lung behavior with a change of pressure, on the contrary to inflation tests as realized by Richardson et al. [2019]. Only Tawhai et al. [2009] used an hyperelastic potential able to reproduce the pressure volume behavior of lungs. The studies using a non linear behavior either do not take into account that the initial configuration extracted from images is not an unloaded configuration [Al-Mayah et al., 2011; Eom et al., 2010] or use a scaling to get the unloaded configuration from the initial configuration [Tawhai et al., 2009; Berger et al., 2016].

Other modeling approaches have been focusing on the lung microstructure, in order to investigate structure-properties relationship. Models of the alveoli microstructure have been developed using geometrical shape [Dale et al., 1980; Budiansky and Kimmel, 1987; Denny and Schroter, 2006] or image segmentation [Sarabia-Vallejos et al., 2019]. The link between organ scale and alveolar scale can then be performed by homogenization techniques [Wiechert and Wall, 2010; Cazeaux and Grandmont, 2015]. Considering lungs as porous media has been little studied, although general poromechanics theories [Biot and Temple, 1972; Coussy, 2004; Dormieux et al., 2006] have been widely used in geophysics and have then been adapted for the need of biomechanics by Chapelle and Moireau [2014], with a theory compatible with large strains and thermodynamics. Such a poromechanical framework has been successfully applied in biomechanics for cardiac perfusion [Chapelle et al., 2010; Burtschell, 2016; Reeve et al., 2014] or bones [Scheiner et al., 2013], but lungs poroelastic models just started to be developed with Kowalczyk [1993] and focused mainly on air flows [Seyfi et al., 2016; Berger et al., 2016].

Our work In this work, we propose to model lung mechanical behavior using poromechanics. We use the general poromechanics theory of Chapelle and Moireau [2014], which is compatible with large deformation, and we adapt it to the pulmonary case with the formulation of lung-specific hypotheses. Our model includes physiological boundary conditions and an hyperelastic potential reproducing the volume response of the pulmonary mixture to a change of pressure. A strategy is established to estimate the unloaded, reference configuration with a particular focus on ensuring a positive porosity, since this issue occurs for large deformation problems. Finally we emphasize through several illustrations the relevance of our model and its possible clinical applications.

2.2 Lung model

2.2.1 Poromechanical framework

As discussed in the Introduction, we propose in this paper a model of the lung biomechanics at the organ spatial scale and the breathing temporal scale. The material behavior is written in the framework of Biot's macroscopic theory of poromechanics [Biot, 1941; Biot and Temple, 1972; Coussy, 2004; Chapelle and Moireau, 2014]. Thus, the lung constituents (*i.e.,* the parenchymal tissue, air and blood) are not represented explicitly, but through overlapping "solid" (written with the subscript "s") and "fluid" (written with the subscript "f") fields. We chose to represent the air flowing in the airways and alveoli as the fluid phase, and the rest, *i.e.,* tissue and blood, as the solid phase.

2.2.1.1 Basic assumptions for the pulmonary setting

Besides standard considerations in continuum poromechanics [Coussy, 2004], the proposed model is based on the following specific assumptions:

- The mixture temperature is constant and uniform, as lungs are part of the human body. This is a natural hypothesis for biological tissues.
- The fluid is incompressible, as the Reynolds number of the airflow inside the lungs is low [Baffico et al., 2010].
- The breathing stages considered are associated with static equilibrium. Inertia and viscous terms are then neglected, both for the fluid and the solid phases.
- The fluid pressure is homogeneous throughout the lungs, as a consequence of the previous assumption. Its actual value depends on the breathing configuration considered: in case of free breathing the fluid pressure is equal to the atmospheric pressure; whereas in case of ventilated breathing it is prescribed by the ventilator.

The first two assumptions have already been used in [Chapelle and Moireau, 2014] and are also valid in the case of cardiac perfusion modeling for example [Burtschell, 2016]. The last two are specific to pulmonary modeling.

2.2.1.2 Continuum poromechanics

Kinematics We consider a mixture deforming under some loading, and occupying the domain ω with boundary γ. Following the total Lagrangian approach, we denote by Ω_0 a supposedly known reference configuration (which is not necessarily unloaded or stress-free, or even equal to $\omega_{t=0}$) with boundary Γ_0, on which we will formulate the problem, so that all quantities must be defined or transported onto Ω_0. Quantities defined over the reference configuration will be written in uppercase, while quantities defined over the deformed configuration will be written in lowercase. Furthermore, to distinguish quantities characterizing the reference and the current configurations, we will write the former ones with a subscript "0". The deformation, *i.e.,* the mapping from Ω_0 to ω, is denoted by $\underline{\chi}$, and the displacement is given by

$$\underline{U}\left(\underline{X}\right) := \underline{\chi}\left(\underline{X}\right) - \underline{X} = \underline{x}\left(\underline{X}\right) - \underline{X}. \tag{2.1}$$

The deformation gradient is then

$$\underline{\underline{F}} := \underline{\underline{\nabla}}\;\underline{\chi} = \underline{\underline{\mathbb{1}}} + \underline{\underline{\nabla}}\;\underline{U}, \tag{2.2}$$

so that the relative volume change of the mixture is

$$J := \det \underline{\underline{F}}. \tag{2.3}$$

We also introduce the right Cauchy-Green deformation tensor

$$\underline{\underline{C}} := \underline{\underline{F}}^T \cdot \underline{\underline{F}}, \tag{2.4}$$

as well as the Green-Lagrange strain tensor

$$\underline{\underline{E}} := \frac{1}{2}\left(\underline{\underline{C}} - \underline{\underline{\mathbb{1}}}\right). \tag{2.5}$$

Specific poromechanics variables

Porosities To formally define poromechanics variables, we consider the infinitesimal domains of matter surrounding $\underline{X}$ (denoted $d\Omega_0$) and $\underline{x}$ (denoted $d\omega$). Both can be decomposed into solid and fluid parts, *i.e.,* $\mathrm{d}\Omega_0 = \mathrm{d}\Omega_{\mathrm{f}0} \cup \mathrm{d}\Omega_{\mathrm{s}0}$ and $\mathrm{d}\omega = \mathrm{d}\omega_{\mathrm{f}} \cup \mathrm{d}\omega_{\mathrm{s}}$. It is important to note that $d\omega$ is the image of $d\Omega_0$ through the mapping $\underline{\chi}$, such that it contains the same solid matter; the fluid, however, can flow in and out of $d\omega$ and is not necessarily conserved locally.

The key quantity of poromechanics is the porosity, defined as the volume fraction of fluid in the mixture. We will denote

$$\Phi_{\mathrm{f}0} := \frac{|\mathrm{d}\Omega_{\mathrm{f}0}|}{|\mathrm{d}\Omega_0|} \qquad \text{and} \qquad \phi_{\mathrm{f}} := \frac{|\mathrm{d}\omega_{\mathrm{f}}|}{|\mathrm{d}\omega|} \tag{2.6}$$

the porosity in the reference and the current configurations, respectively.

We also introduce

$$\Phi_{\mathrm{s}} := \left(1 - \phi_{\mathrm{f}} \circ \underline{\chi}\right) \cdot J = \frac{|\mathrm{d}\omega_{\mathrm{s}}|}{|\mathrm{d}\Omega_0|} \tag{2.7}$$

the current volume fraction of solid pulled back on the reference configuration, which will be used in the following as a state variable. Finally, we denote $\Phi_{\mathrm{f}} := \phi_{\mathrm{f}} \circ \underline{\chi} \cdot J$ the current volume fraction of fluid pulled back on the reference configuration such that $\Phi_{\mathrm{f}} = J - \Phi_{\mathrm{s}}$.

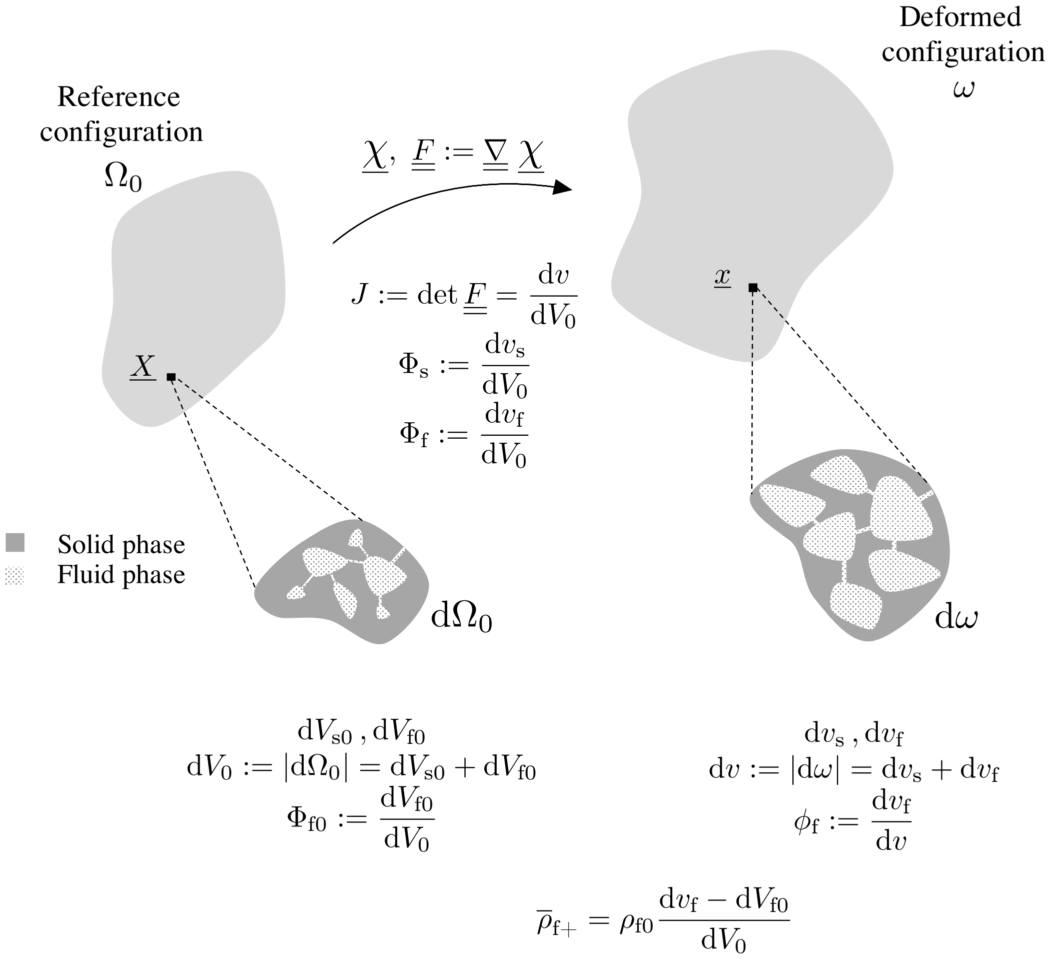

Figure 2.1 – Schematic of the reference and deformed configurations with associated local quantities, volumes and porosity. $\mathrm{d}V_0$, $\mathrm{d}v$, $\mathrm{d}V_{\mathrm{f}0}$, $\mathrm{d}v_\mathrm{f}$, $\mathrm{d}V_{\mathrm{s}0}$ $\mathrm{d}v_\mathrm{s}$ are the infinitesimal volumes of the mixture, the fluid and solid phases, in the reference and deformed configurations, respectively. $\Phi_{\mathrm{f}0}$ and ϕ_f are the porosities in the reference and deformed configurations, respectively. $\overline{\rho}_{\mathrm{f}+}$ is the added fluid mass density defined in the reference configuration. J, Φ_s, Φ_f are the local volume ratios.

Mass densities We distinguish between constituent (fluid or solid) actual densities, which are defined as mass per unit constituent volume, from apparent densities, which are defined as mass per unit mixture volume and written with a bar. Thus, the reference fluid and solid mass densities are denoted $\rho_{\mathrm{f}0}$ and $\rho_{\mathrm{s}0}$, respectively. The mixture reference mass density is decomposed into a fluid and a solid part:

$$\overline{\rho}_0 = \overline{\rho}_{\mathrm{f}0} + \overline{\rho}_{\mathrm{s}0}, \tag{2.8}$$

with $\overline{\rho}_{\mathrm{f}0} := \rho_{\mathrm{f}0} \Phi_{\mathrm{f}0}$ and $\overline{\rho}_{\mathrm{s}0} := \rho_{\mathrm{s}0} \left(1 - \Phi_{\mathrm{f}0}\right)$ the fluid and solid mass per unit volume of the mixture in the reference configuration, *i.e.,* the reference apparent densities.

We could define the current mass densities similarly to the reference mass densities using the current fluid and solid mass densities, denoted as ϱ_{f} and ϱ_{s}, respectively. However, as the equations in the paper are written on the reference configuration, we focus on the current mass densities pulled back on the reference configuration. Then, we express the current mass density of the mixture pulled back on the reference configuration as:

$$\overline{\rho} = \overline{\rho}_{\mathrm{f}} + \overline{\rho}_{\mathrm{s}}, \tag{2.9}$$

with $\overline{\rho}_{\mathrm{f}} := \varrho_{\mathrm{f}} J \phi_{\mathrm{f}} \circ \underline{\chi}$ and $\overline{\rho}_{\mathrm{s}} := \varrho_{\mathrm{s}} J \left(1 - \phi_{\mathrm{f}} \circ \underline{\chi}\right)$ the pull backs of the fluid and solid apparent mass densities, *i.e.,* the fluid and solid current mass per unit reference mixture volume.

As the solid mass is conserved, we have:

$$\overline{\rho}_{\mathrm{s}} = \overline{\rho}_{\mathrm{s}0}. \tag{2.10}$$

We can now define the "added" fluid mass per unit reference mixture volume as:

$$\overline{\rho}_{\mathrm{f}+} := \overline{\rho}_{\mathrm{f}} - \overline{\rho}_{\mathrm{f}0} = \overline{\rho} - \overline{\rho}_0. \tag{2.11}$$

Using the fluid incompressibility assumption whereby $\varrho_{\mathrm{f}} = \rho_{\mathrm{f}0}$, we get:

$$\overline{\rho}_{\mathrm{f}+} = \rho_{\mathrm{f}0} \left(\Phi_{\mathrm{f}} - \Phi_{\mathrm{f}0}\right). \tag{2.12}$$

It can be positive, for instance when lungs inflate, or negative, for instance when lungs deflate. However, one cannot remove more fluid than there was initially, so $\overline{\rho}_{\mathrm{f}+} \geq -\overline{\rho}_{\mathrm{f}0}$. It is important to notice that the porosity ϕ_{f} and the added mass density $\overline{\rho}_{\mathrm{f}+}$ are two independent variables. Indeed, the porosity can for instance remain constant while the mixture deforms and fluid flows through it; conversely, even when there is no fluid flow within the mixture the porosity can vary as it deforms.

Force balance At any time the mixture is in equilibrium with external loadings, such as boundary tractions or gravity. The stress is denoted $\underline{\underline{\sigma}}$ on ω (Cauchy stress tensor) and $\underline{\underline{\Sigma}} := J \underline{\underline{F}}^{-1} \cdot \underline{\underline{\sigma}} \circ \underline{\chi} \cdot \underline{\underline{F}}^{-T}$ (second Piola-Kirchhoff stress tensor) on Ω_0. Mechanical equilibrium of the mixture can be expressed in weak form through the principle of virtual work written in reference configuration [Chapelle and Moireau, 2014]:

$$\forall \underline{U}^*, \; W_{\mathrm{int}}\left(\underline{U}, \underline{U}^*\right) = W_{\mathrm{ext}}\left(\underline{U}, \underline{U}^*\right), \tag{2.13}$$

where W_{int} is the virtual work of internal forces of the mixture and W_{ext} is the virtual work of external forces applied to the mixture. Following standard objectivity and locality considerations, the virtual work of internal forces can be expressed as

$$W_{\mathrm{int}}\left(\underline{U}, \underline{U}^*\right) = \int_{\Omega_0} \underline{\underline{\Sigma}} : \mathrm{d}_{\underline{U}} \underline{\underline{E}} \cdot \underline{U}^* \, \mathrm{d}\Omega_0 \,, \tag{2.14}$$

where $\mathrm{d}_{\underline{U}}\,\underline{\underline{E}} \cdot \underline{U}^* = \left(\underline{\underline{F}}^T \cdot \underline{\nabla}\,\underline{U}^*\right)_{\mathrm{sym}}$ is the first differential of the Green-Lagrange strain tensor. The virtual work of internal forces W_{int} will be detailed in Section 2.2.1.3 through the choice of a free energy function, while the virtual work of external forces W_{ext} will be detailed in Section 2.2.3 through the definition of loading conditions. General poromechanics formulations usually require other balance equations for the fluid flow and fluid mass conservation [Chapelle and Moireau, 2014]; they are, however, not required here because of the specific assumptions made for the pulmonary setting.

2.2.1.3 Constitutive behavior

Mixture free energy Under the hypotheses considered in the paper, namely isothermal and static equilibrium conditions, the mixture local state is characterized by two independent variables, associated with the mixture deformation and the added fluid mass [Coussy, 2004; Dormieux et al., 2006; Chapelle and Moireau, 2014]. Classically, we choose the Green-Lagrange strain tensor $\underline{\underline{E}}$ and the added fluid mass density $\overline{\rho}_{\mathrm{f}+}$ as state variables. We define the mixture constitutive behavior through its Helmholtz free energy density potential, denoted $\overline{\psi}$, which is thus a function of $\underline{\underline{E}}$ and $\overline{\rho}_{\mathrm{f}+}$. It is additively decomposed into solid and fluid parts [Coussy, 2004]:

$$\overline{\psi} = \overline{\psi}_{\mathrm{s}} + \overline{\psi}_{\mathrm{f}}, \tag{2.15}$$

where $\overline{\psi}_{\mathrm{s}}$ and $\overline{\psi}_{\mathrm{f}}$ are the solid and fluid free energies per unit mixture volume in the reference configuration.

It is convenient to express the solid free energy density $\overline{\psi}_{\mathrm{s}}$ as a function of the Green-Lagrange strain tensor $\underline{\underline{E}}$ and the pulled back solid volume fraction Φ_{s}. Indeed, we will see that the energy conjugate of Φ_{s} is directly involved in the fundamental poromechanical equilibrium principle between fluid and solid hydrostatic stresses, making it a very natural variable. And this choice is possible since Φ_{s} can be expressed from the state variables $\underline{\underline{E}}$ and $\overline{\rho}_{\mathrm{f}+}$ as shown in Equation (2.12).

Regarding the fluid, since it is assumed to be incompressible and in isothermal conditions, its free energy density can be expressed as a function of the pulled back fluid volume fraction Φ_{f} only:

$$\overline{\psi}_{\mathrm{f}}\left(\Phi_{\mathrm{f}}\right) = -p_{\mathrm{f}0}\;\Phi_{\mathrm{f}}, \tag{2.16}$$

where $p_{\mathrm{f}0}$ is a reference pressure (see [Chapelle and Moireau, 2014] for more details). Note that Φ_{f} depends only on the state variable $\overline{\rho}_{\mathrm{f}+}$, not $\underline{\underline{E}}$, as can be seen in Equation (2.12).

Thus, we consider a mixture free energy density of the form:

$$\overline{\psi}\left(\underline{\underline{E}}, \overline{\rho}_{\mathrm{f}+}\right) = \overline{\psi}_{\mathrm{s}}\left(\underline{\underline{E}}, \Phi_{\mathrm{s}}\right) + \overline{\psi}_{\mathrm{f}}\left(\Phi_{\mathrm{f}}\right), \tag{2.17}$$

where the intermediate variables Φ_{f} and Φ_{s} have simple expressions in terms of the state variables $\underline{\underline{E}}$ and $\overline{\rho}_{\mathrm{f}+}$:

$$\begin{cases} \Phi_{\mathrm{s}} = J\left(\underline{\underline{E}}\right) - \Phi_{\mathrm{f}} \\ \Phi_{\mathrm{f}} = \Phi_{\mathrm{f}0} + \dfrac{\overline{\rho}_{\mathrm{f}+}}{\rho_{\mathrm{f}0}}. \end{cases} \tag{2.18}$$

Since all dissipative processes have been neglected, the second principle of thermodynamics implies that the second Piola-Kirchhoff stress tensor simply derives from the free energy potential. We then have:

$$\underline{\underline{\Sigma}} = \left.\frac{\partial \overline{\psi}\left(\underline{\underline{E}}, \overline{\rho}_{\mathrm{f}+}\right)}{\partial \underline{\underline{E}}}\right|_{\overline{\rho}_{\mathrm{f}+}} = \left.\frac{\partial \overline{\psi}_{\mathrm{s}}\left(\underline{\underline{E}}, \Phi_{\mathrm{s}}\right)}{\partial \underline{\underline{E}}}\right|_{\overline{\rho}_{\mathrm{f}+}} + \left.\frac{\partial \overline{\psi}_{\mathrm{f}}\left(\Phi_{\mathrm{f}}\right)}{\partial \underline{\underline{E}}}\right|_{\overline{\rho}_{\mathrm{f}+}}. \tag{2.19}$$

Introducing Equations (2.17) and (2.18) into this expression, we obtain:

$$\underline{\underline{\Sigma}}\left(\underline{\underline{E}},\overline{\rho}_{\mathrm{f}+}\right)=\frac{\partial\overline{\psi}_{\mathrm{s}}}{\partial\underline{\underline{E}}}+\frac{\partial\overline{\psi}_{\mathrm{s}}}{\partial\Phi_{\mathrm{s}}}\frac{\partial\Phi_{\mathrm{s}}}{\partial\underline{\underline{E}}}+\frac{\partial\overline{\psi}_{\mathrm{f}}}{\partial\Phi_{\mathrm{f}}}\frac{\partial\Phi_{\mathrm{f}}}{\partial\underline{\underline{E}}}=\frac{\partial\overline{\psi}_{\mathrm{s}}}{\partial\underline{\underline{E}}}-p_{\mathrm{s}}J\underline{\underline{C}}^{-1}, \tag{2.20}$$

where $p_{\mathrm{s}}:=-\frac{\partial\overline{\psi}_{\mathrm{s}}}{\partial\Phi_{\mathrm{s}}}$ is the solid hydrostatic stress induced by volume fraction change, *i.e.,* by fluid pressure changes, fluid addition or fluid removal. Internal equilibrium of the mixture requires that [Coussy, 2004; Chapelle and Moireau, 2014]

$$p_{\mathrm{s}}=p_{\mathrm{f}}, \tag{2.21}$$

leading to the following expression:

$$\underline{\underline{\Sigma}}\left(\underline{\underline{E}},\overline{\rho}_{\mathrm{f}+}\right)=\frac{\partial\overline{\psi}_{\mathrm{s}}}{\partial\underline{\underline{E}}}-p_{\mathrm{f}}J\underline{\underline{C}}^{-1}, \tag{2.22}$$

with the following relation:

$$p_{\mathrm{f}}=-\frac{\partial\overline{\psi}_{\mathrm{s}}}{\partial\Phi_{\mathrm{s}}}. \tag{2.23}$$

We will now define a specific solid free energy density potential for the parenchyma.

Solid free energy Following [Chapelle and Moireau, 2014], we choose an additive form of the solid free energy density potential split into skeleton and bulk parts:

$$\overline{\psi}_{\mathrm{s}}\left(\underline{\underline{E}},\Phi_{\mathrm{s}}\right)=\overline{W}_{\mathrm{skel}}\left(\underline{\underline{E}}\right)+\overline{W}_{\mathrm{bulk}}\left(\Phi_{\mathrm{s}}\right), \tag{2.24}$$

where $\overline{W}_{\mathrm{skel}}$ represents the mechanical behavior of the porous solid, or skeleton, as a structure subjected to deformation, and $\overline{W}_{\mathrm{bulk}}$ its mechanical behavior with regard to solid volume fraction changes. Such a decomposition leads to the following expressions for the stress and internal hydrostatic equilibrium:

$$\underline{\underline{\Sigma}}\left(\underline{\underline{E}},\overline{\rho}_{\mathrm{f}+}\right)=\frac{\partial\overline{W}_{\mathrm{skel}}}{\partial\underline{\underline{E}}}\left(\underline{\underline{E}}\right)-p_{\mathrm{f}}J\underline{\underline{C}}^{-1}\quad\text{and}\quad p_{\mathrm{f}}=-\frac{\partial\overline{W}_{\mathrm{bulk}}}{\partial\Phi_{\mathrm{s}}}\left(\Phi_{\mathrm{s}}\right). \tag{2.25}$$

It is possible to express these potentials directly, in which case they are effective potentials, depending both on the solid behavior and the solid volume fraction. Another option, fully exploiting the poromechanical framework, is to assume the dependence of the effective potentials to the solid volume fraction. For instance, assuming that the effective potentials vary linearly with respect to the solid volume fraction, we have:

$$\left\{\begin{array}{lll}\overline{\psi}_{\mathrm{s}} & = & \left(1-\Phi_{\mathrm{f}0}\right)\ \widetilde{\psi}_{\mathrm{s}}\\ \overline{W}_{\mathrm{skel}} & = & \left(1-\Phi_{\mathrm{f}0}\right)\ \widetilde{W}_{\mathrm{skel}}\\ \overline{W}_{\mathrm{bulk}} & = & \left(1-\Phi_{\mathrm{f}0}\right)\ \widetilde{W}_{\mathrm{bulk}},\end{array}\right. \tag{2.26}$$

where $\widetilde{\psi}_{\mathrm{s}}$, $\widetilde{W}_{\mathrm{skel}}$ and $\widetilde{W}_{\mathrm{bulk}}$ are the absolute free energy potentials, characterizing the solid matter itself. It allows to distinguish the effect of porosity and the effect of solid tissue stiffness, both present in the effective parameters.

The pulmonary parenchyma is assumed to behave as an isotropic, non linear, hyperelastic material. Even though it is assumed to be quasi-incompressible, its response as a structure is not incompressible, as fluid can flow in and out of each local volume. Thus we use the following compressible potential for the skeleton free energy:

$$\widetilde{W}_{\text{skel}}\left(\underline{\underline{E}}\right) = \widetilde{\beta}_1 \left(I_1 - 3 - 2\ln J\right) + \widetilde{\beta}_2 \left(I_2 - 3 - 4\ln J\right) + \widetilde{\alpha}\left(\mathrm{e}^{\delta\left(J^2-1-2\ln J\right)} - 1\right), \qquad (2.27)$$

where $I_1 := \operatorname{tr}\underline{\underline{C}}$ and $I_2 := \frac{1}{2}(\operatorname{tr}\left(\underline{\underline{C}}\right)^2 - \operatorname{tr}\left(\underline{\underline{C}}^2\right))$ are the first two invariants of $\underline{\underline{C}}$, and $\widetilde{\beta}_1$, $\widetilde{\beta}_2$, $\widetilde{\alpha}$ and δ are four material parameters. The potential contains standard neo-hookean and Mooney-Rivlin terms, and an exponential of the Ciarlet-Geymonat bulk term [Ciarlet and Geymonat, 1982]. The use of an exponential term, initiated by Demiray [1972] and popularized by Fung [1981], is common in soft tissues modeling [Weiss et al., 1996; Caruel et al., 2014; Genet et al., 2015a]. Here it was motivated by the shape of the clinical data representing the lung volume with respect to the pleural pressure Gibson and Pride [1976].

The effective hyperelastic potential $\overline{W}_{\text{skel}}$ depends on the four material constants $\overline{\alpha}$, $\overline{\beta}_1$, $\overline{\beta}_2$, δ, such as

$$\left\{\begin{array}{lcl} \overline{\alpha} & = & (1-\Phi_{\text{f0}})\ \widetilde{\alpha} \\ \overline{\beta}_1 & = & (1-\Phi_{\text{f0}})\ \widetilde{\beta}_1 \\ \overline{\beta}_2 & = & (1-\Phi_{\text{f0}})\ \widetilde{\beta}_2, \end{array}\right. \qquad (2.28)$$

whose typical values can be determined by calibration on clinical or experimental data. The volume macroscopic behavior of the pulmonary mixture is usually characterized by P-V curves, with P the pleural pressure and V the lung volume, that are used by clinicians to assess lung compliance [Gibson and Pride, 1976]. These data allow then to characterize the mixture volume change with the pressure and to determine the dependency of the skeleton deformation energy $\overline{W}_{\text{skel}}$ with J (see Figure 2.2). We determined a set of the four effective parameters of the skeleton hyperelastic potential with the data from Gibson and Pride [1976]. The parameters identification is not unique but allows to match available experimental data; further investigation is required to define the range of normal values for these parameters. Typical values for a healthy case were obtained as $\overline{\alpha} = 0.08$, $\overline{\beta_1} = 0.1$, $\overline{\beta_2} = 0.2$, $\delta = 0.5$.

For the bulk term $\overline{W}_{\text{bulk}}$, the following expression, which is an extension of the Ciarlet-Geymonat law to poromechanics, is chosen [Ciarlet and Geymonat, 1982; Chapelle and Moireau, 2014]:

$$\widetilde{W}_{\text{bulk}}\left(\Phi_{\text{s}}\right) = \widetilde{\kappa}\left(\frac{\Phi_{\text{s}}}{(1-\Phi_{\text{f0}})} - 1 - \ln\left(\frac{\Phi_{\text{s}}}{(1-\Phi_{\text{f0}})}\right)\right), \qquad (2.29)$$

where $\widetilde{\kappa}$ is the bulk modulus of the solid phase and is taken large to ensure quasi-incompressibility of the solid phase.

2.2.1.4 Constraints to ensure positive porosity

The above poromechanical model, with the choices made on the energies in Section 2.2.1.3, does not ensure by itself a positive porosity [Chapelle et al., 2010; Chapelle and Moireau, 2014; Genet et al., 2020], which becomes a problem with large strains during mixture compression or, in the pulmonary case, lung deflation (see Figure 2.4).

Use of an additional energy Chapelle and Moireau [2014] proposed adding a penalization term to the solid energy $\overline{\psi}_{\text{s}}$ in order to keep the porosity positive. The additional energy tends to infinity when the porosity ϕ_{f} tends to 0, describing the mechanism that a pore cannot be closed totally, without providing an infinite amount of energy. Indeed,

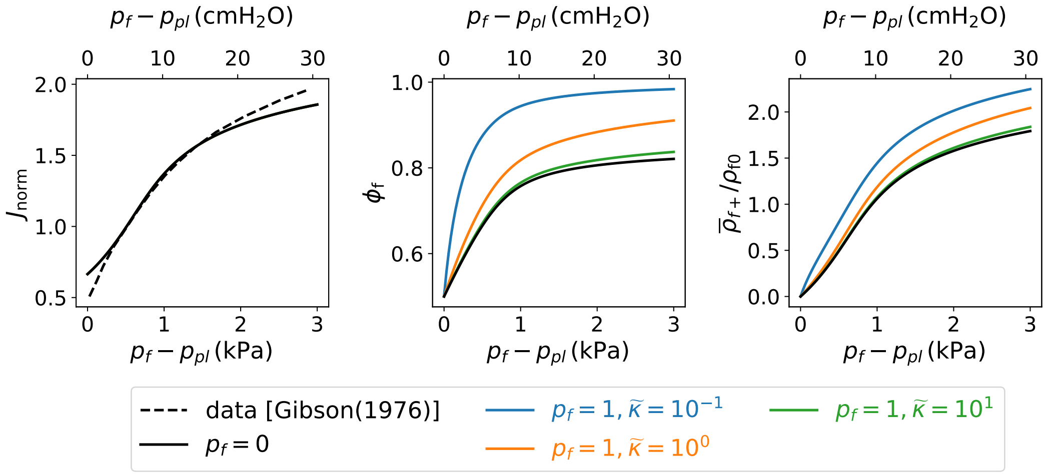

Figure 2.2 – Mechanical behavior of the solid phase resulting from $\overline{W}_{\text{skel}}$ (Equation (2.27)) with different values of bulk modulus $\widetilde{\kappa}$ and fluid pressure p_{f}. The loading is expressed as $p_{\text{f}} - p_{\text{pl}}$ since there are two contributions for the loading: the fluid pressure p_{f} and an external pressure p_{pl}, which will be called pleural pressure (see Section 2.2.3 for more details). (Left) Volume response of a mixture to a pressure loading, with a comparison with data [Gibson and Pride, 1976]. J_{norm} is the mixture volume change J normalized by its value at end-exhalation $J_{0.5}$, *i.e.*, at the pressure 0.5 kPa, which leads to $J_{\text{norm}} = J/J_{0.5} = 1$ at end-exhalation. The curves with $p_{\text{f}} = 1$ kPa are superimposed with the curve with zero fluid pressure because the deformation depends only on $p_{\text{f}} - p_{\text{pl}}$. (Middle) Evolution of the porosity ϕ_{f} with the pressure loading. (Right) Evolution of the added fluid mass with the pressure loading. The following parameters are taken: $\widetilde{\alpha} = 0.16$ kPa, $\widetilde{\beta}_1 = 0.2$ kPa, $\widetilde{\beta}_2 = 0.4$ kPa, $\delta = 0.5$, $\widetilde{\kappa} = 10^2$ kPa, $\Phi_{\text{f0}} = 0.5$. J depends only on $p_{\text{f}} - p_{\text{pl}}$. However, the porosity ϕ_{f} depends on both the fluid pressure p_{f} and the solid bulk modulus $\widetilde{\kappa}$: when the fluid pressure is non zero, the solid phase is compressed according to its bulk modulus. The lower the bulk modulus, the more compressible the solid, the higher the porosity and the more fluid is added.

closing a pore means schematically either reducing a circle to a point or flattening a pore inducing infinite radii of curvature.

However, the energy proposed in Chapelle and Moireau [2014] leads to non zero stresses in the reference configuration. We propose then to use the following penalization term $\overline{W}_{\mathrm{por}}$ to describe the mechanism of collapsing pores:

$$\overline{W}_{\mathrm{por}}^{C^n}(\overline{\rho}_{\mathrm{f}+}) := \begin{cases} \eta\left(\dfrac{\Phi_{\mathrm{f0}}-\Phi_{\mathrm{f}}}{\Phi_{\mathrm{f}}}\right)^{n+1} & \text{if } \overline{\rho}_{\mathrm{f}+}<0 \\ 0 & \text{if } \overline{\rho}_{\mathrm{f}+}\geq 0 \end{cases} \quad \text{for } n \geq 1. \tag{2.30}$$

The condition of zero stresses in the reference configuration is well satisfied. This function $\overline{W}_{\mathrm{por}}$ is C^n on the domain. In mechanics, as the main requirement is a continuous stress, taking $n = 1$ can be sufficient. Note that the following expression is C^∞ and verifies the same requirements:

$$\overline{W}_{\mathrm{por}}^{C^\infty}(\overline{\rho}_{\mathrm{f}+}) := \begin{cases} \eta\,\dfrac{\Phi_{\mathrm{f0}}-\Phi_{\mathrm{f}}}{\Phi_{\mathrm{f}}}\,\mathrm{e}^{-\dfrac{\Phi_{\mathrm{f}}}{\Phi_{\mathrm{f0}}-\Phi_{\mathrm{f}}}} & \text{if } \overline{\rho}_{\mathrm{f}+}<0 \\ 0 & \text{if } \overline{\rho}_{\mathrm{f}+}\geq 0. \end{cases} \tag{2.31}$$

The shape of such a function is visualized in Figure 2.3.

Using such an energy implies that $\overline{\psi}_{\mathrm{s}}$ incorporates a new term:

$$\overline{\psi}_{\mathrm{s}}\left(\underline{\underline{E}},\Phi_{\mathrm{s}}\right) = \overline{W}_{\mathrm{skel}}\left(\underline{\underline{E}}\right) + \overline{W}_{\mathrm{bulk}}\left(\Phi_{\mathrm{s}}\right) + \overline{W}_{\mathrm{por}}(\overline{\rho}_{\mathrm{f}+}), \tag{2.32}$$

where we take $\overline{W}_{\mathrm{por}} = \overline{W}_{\mathrm{por}}^{C^\infty}$ if no specification is given. The presence of the term $\overline{W}_{\mathrm{por}}$ in $\overline{\psi}_{\mathrm{s}}$ and its dependency on Φ_{s} imply that it is also present in Equation (2.23), ensuring that the porosity ϕ_{f} remains positive.

Figure 2.4a illustrates that the porosity ϕ_{f} depends on the solid bulk modulus κ in the term $\overline{W}_{\mathrm{bulk}}$ through Equation (2.23). The coefficient η allows to control the smoothness of the trend change, as illustrated in Figure 2.4b. If η takes small values, the transition becomes sharper.

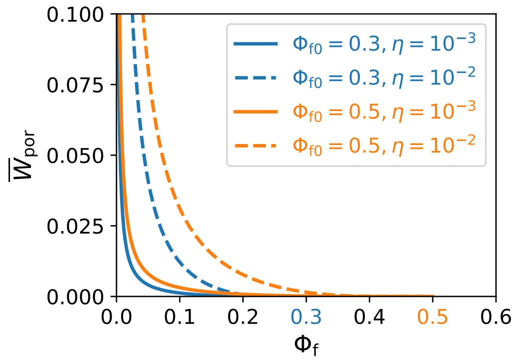

Figure 2.3 – Representation of the $\overline{W}_{\mathrm{por}}^{C^\infty}$ energy, for two different values of Φ_{f0} and of η. The $\overline{W}_{\mathrm{por}}$ energy is zero above Φ_{f0} and tends to infinity when ϕ_{f} comes close to 0. When η decreases, the transition between the nearly-zero porosity and the non-zero porosity is sharper.

Contact-like formulation The asymptotic case ($\eta \to 0$) is a contact-like problem, which can be formulated with two quantities, the porosity ϕ_{f} and the solid auto-contact pressure p_{c}, using the following conditions:

$$\begin{cases} \phi_{\mathrm{f}} \cdot p_{\mathrm{c}} = 0 \\ \phi_{\mathrm{f}} \geq 0 \\ p_{\mathrm{c}} \geq 0. \end{cases} \tag{2.33}$$

An infinitesimal domain of mixture is dual-state: either it is filled with some fluid and the porosity is non-zero while the auto-contact pressure is zero, or the pores are collapsed and the auto-contact pressure is non-zero while the porosity is zero. We define $\mathscr{H}\left(\phi_{\mathrm{f}}\right)$ as:

$$\mathscr{H}\left(\phi_{\mathrm{f}}\right) := \begin{cases} 1 \text{ if } \phi_{\mathrm{f}} > 0 \\ 0 \text{ otherwise,} \end{cases} \tag{2.34}$$

giving the state of the infinitesimal domain. When $\mathscr{H}\left(\phi_{\mathrm{f}}\right) = 1$, fluid is present and the fluid pressure p_{f} is well defined, whereas $\mathscr{H}\left(\phi_{\mathrm{f}}\right) = 0$ means that the fluid totally left the pores and the fluid pressure is not a relevant quantity anymore. The contact pressure p_{c} is then a substitute of the fluid pressure and acts against the solid compression. We define the pressure p as:

$$p := p_{\mathrm{f}} \mathscr{H}\left(\phi_{\mathrm{f}}\right) + p_{\mathrm{c}}\left(1 - \mathscr{H}\left(\phi_{\mathrm{f}}\right)\right), \tag{2.35}$$

which is equal to p_{f} or p_{c} depending on the state of the mixture. By extension of the internal equilibrium principle of Equation (2.21) to the case $\phi_{\mathrm{f}} = 0$, we have:

$$p = -\frac{\partial \overline{\psi}_{\mathrm{s}}}{\partial \Phi_{\mathrm{s}}}. \tag{2.36}$$

Initially, the porosity ϕ_{f} is non zero and the contact pressure p_{c} is zero. When the mixture is compressed, the porosity decreases as air is expelled. Then, the porosity comes to 0, which means that the entire initial air is expelled. If the mixture keeps being compressed, the solid part is compressed according to the solid bulk modulus κ, as shown in Figure 2.4c, and the resulting contact pressure p_{c} starts to increase.

Remark The other constraint $\phi_{\mathrm{f}} < 1$ is well satisfied with the proposed expression of the bulk energy $\overline{W}_{\mathrm{bulk}}$ in the Equation (2.29). Indeed, when the porosity ϕ_{f} tends to 1, Φ_{s} tends to zero, and the bulk energy $\overline{W}_{\mathrm{bulk}}$ tends to infinity.

2.2.2 Geometric model

Our lung model requires several geometric entities as illustrated in Figure 2.5, all described by finite elements meshes. In addition to the lungs themselves, which are volume meshes, two surface meshes are used: the rib cage surface and the inner surface. The rib cage surface is in contact with the lung where the lung is surrounded by hard tissue (*i.e.,* ribs and spine). It corresponds to the costal pleura. The inner surface is in contact with the lung where the lung is surrounded by softer tissues. It matches with the diaphragmatic pleura and mediastinal pleura, *i.e.,* the soft surroundings of lungs. Both rib cage and inner surfaces are surface meshes. The interactions between lungs and both surfaces are detailed in Section 2.2.3, whereas a method to produce these surfaces is detailed in Section 2.2.5.2.

Typically, realistic geometric models can be obtained from biomedical images through segmentation. However, it is important to notice that no image of the unloaded configuration can be acquired *in vivo* as this is a virtual configuration corresponding to a pneumothorax, in which air enters pleura and pleural pressure becomes equal to atmospheric pressure. Consequently, the unloaded configuration associated with image-based geometries must be computed, as described in Section 2.2.4.

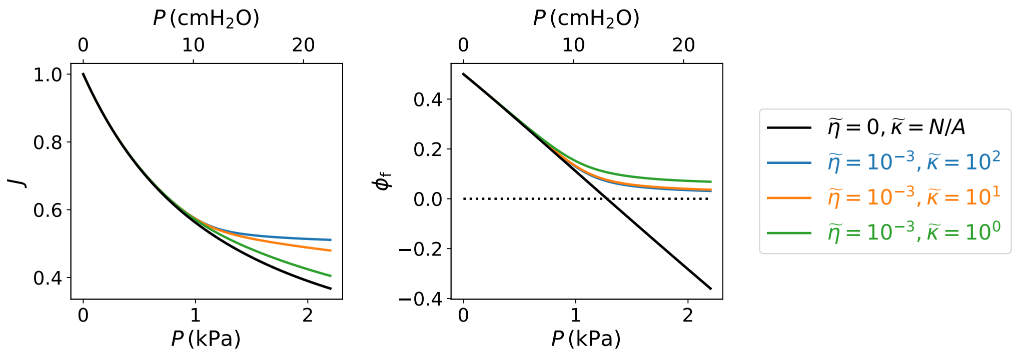

(a) Influence of the solid bulk modulus $\widetilde{\kappa}$ when using $\widetilde{W}_\mathrm{por}$. As long as the porosity is far from zero, the solid bulk modulus has nearly no impact, since the volume decrease is mainly linked to the air ejection and less to the solid compression. Then, when the porosity comes close to zero, little air remains to be ejected and the solid starts to be compressed according to the solid bulk modulus.

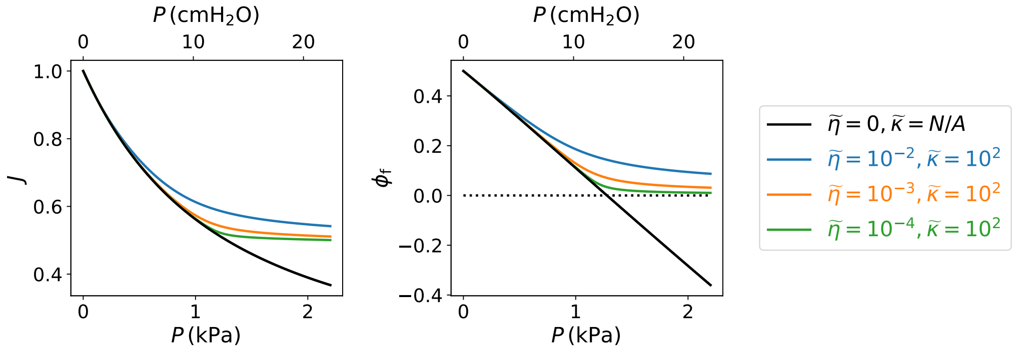

(b) Influence of $\widetilde{\eta}$ when using $\widetilde{W}_\mathrm{por}$. When $\widetilde{\eta}$ decreases, the change of behavior when the porosity comes close to zero becomes sharper.

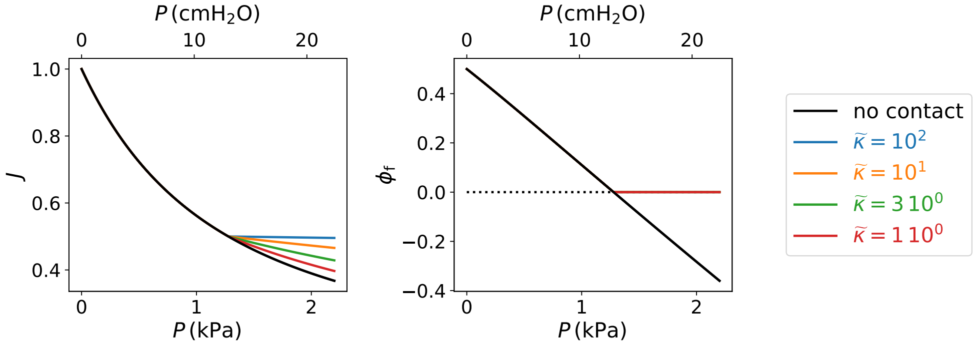

(c) Influence of the solid bulk modulus $\widetilde{\kappa}$ when using the contact-like formulation. The same behavior as in Figure 2.4a is observed but the curves are sharper using the contact-like formulation.

Figure 2.4 – Behavior of a mixture under compression using either the $\widetilde{W}_\mathrm{por}$ term or the contact-like formulation. The mixture is in free breathing condition ($p_\mathrm{f} = 0$). In each case, the evolution of the mixture volume change J and of the porosity ϕ_f with respect to the pressure loading are shown. The black solid line illustrates the weakness of the model regarding negative porosity when neither the $\widetilde{W}_\mathrm{por}$ term nor the contact-like formulation are used. The black dotted line represents $\phi_\mathrm{f} = 0$.

2.2.3 Boundary conditions

Elements of pulmonary physiology A complex environment is involved during breathing. The lungs are surrounded by the pleura, composed of two membranes and applying a negative pressure, called pleural pressure, on the lungs surface. The pleural pressure keeps the lungs inflated and maintains the contact with their close environment (thorax and diaphragm mainly). Two mechanisms of breathing should be distinguished, spontaneous breathing and mechanical ventilation, differing by the driving force for lung inflation. During spontaneous breathing, the diaphragm contracts and pulls on the external layer of the pleura, causing a decrease in the pleural pressure, which induces lungs inflation and air filling. Intercostal muscles play also a role in the thorax inflation during inhalation. Conversely, during mechanical ventilation the diaphragm and intercostal muscles do not contract. Their role is played by the ventilator, which induces a positive air pressure inside the lungs to make them inflate. A part of the ventilated pressure acts to push the rib cage and the diaphragm, which then act against the lung inflation.

Boundary conditions in spontaneous breathing As shown in Figure 2.5, several choices were made to model the complex loading on the lung during spontaneous breathing.

(i) The air pressure is homogeneous and equal to the atmospheric pressure according to the assumptions of Section 2.2.1.1, *i.e.,* $p_{\mathrm{f}} = 0$.

(ii) The pleural pressure p_{pl} is modeled by a negative pressure p_{pl} applied on the lungs surface. This pressure varies under the diaphragm action from $-5\,\mathrm{cmH_2O}$ (*i.e.,* $-0.5\,\mathrm{kPa}$) at end-exhalation to $-8\,\mathrm{cmH_2O}$ (*i.e.,* $-0.8\,\mathrm{kPa}$) at end-inhalation and can reach $-30\,\mathrm{cmH_2O}$ (*i.e.,* $-3\,\mathrm{kPa}$) at full inhalation. The associated boundary traction on γ, whose outward normal is denoted by $\underline{n}$, is $\underline{t} = -p_{\mathrm{pl}}\,\underline{n}$. It corresponds to $\underline{T} = -p_{\mathrm{pl}} J \underline{\underline{F}}^{-T} \underline{N_0}$ on Γ_0, whose outward normal is denoted by $\underline{N_0}$.

(iii) Interactions between the rib cage and the lungs are modeled by a bilateral contact between the lungs external surface and the rib cage surface. The contact is frictionless, in order to take into account the lubrication of pleura by the pleural liquid. As the contact is bilateral, it is permanent, which means that surface elements which are in contact initially or become in contact at some point remain in contact throughout breathing. These interactions are represented by a boundary traction, denoted $\underline{T}_{\mathrm{c,rb}}$, applied on the lung surface in contact with the rib cage $\Gamma_{0,\mathrm{c,rb}}$.

(iv) Rib cage displacements induced by intercostal muscles during breathing is different for everyone. They are imposed in the model through a prescribed motion of the rib cage surface. Patient-specific motion can be extracted from biomedical images, or generic motion (including no motion, *i.e.,* fixed rib cage surface) can be used.

(v) Gravity loading, denoted $\underline{g}$, can be applied considering any position, supine, prone or standing/seated position.

The virtual work of external forces is then:

$$W_{\mathrm{ext}}\left(\underline{U}, \underline{U}^*\right) = -\int_{\Gamma_0} p_{\mathrm{pl}} J \underline{\underline{F}}^{-T} \cdot \underline{N_0} \cdot \underline{U}^* \,\mathrm{d}\Gamma_0 + \int_{\Gamma_{0,\mathrm{c,rb}}} \underline{T}_{\mathrm{c,rb}} \cdot \underline{U}^* \,\mathrm{d}\Gamma_0 + \int_{\Omega_0} \overline{\rho}\, \underline{g} \cdot \underline{U}^* \,\mathrm{d}\Omega_0 \,. \quad (2.37)$$

Boundary conditions in mechanical ventilation In case of mechanical ventilation, the boundary conditions concerning the air pressure and the pleural pressure are different:

(i) Air pressure is controlled by the ventilator. We again assume that air pressure is homogeneous, such as $p_{\mathrm{f}} = p_{\mathrm{vent}}$ with p_{vent} the ventilated pressure. The associated stresses appear in Equation (2.22) as a part of the mixture stresses. According to the homogeneous fluid pressure assumption, the loading can be transformed from a volume loading to a surface loading:

$$\int_{\Omega_0} p_{\mathrm{f}} J \underline{\underline{C}}^{-1} : \mathrm{d}_{\underline{U}}\, \underline{\underline{E}} \cdot \underline{U}^* \,\mathrm{d}\Omega_0 = \int_{\gamma} p_{\mathrm{f}}\, \underline{n} \cdot \underline{U}^* \,\mathrm{d}\gamma = \int_{\Gamma_0} p_{\mathrm{f}} J \underline{\underline{F}}^{-T} \cdot \underline{N_0} \cdot \underline{U}^* \,\mathrm{d}\Gamma_0\,. \tag{2.38}$$

It means that the fluid pressure, acting on the whole lung volume, can be also considered, under the homogeneity assumption, as a following pressure applied on the lung surface γ.

(ii) In the same way as for the interaction with the rib cage, interaction between the internal organs and the lungs are modeled by a bilateral contact between the lungs external surface and the inner surface. The contact is frictionless, as the pleural liquid acts as a lubricant. This contact induces a boundary loading written as $\underline{T}_{\mathrm{c,in}}$, applied on the lung external surface in contact with the inner surface $\Gamma_{0,\mathrm{c,in}}$.

(iii) Internal organs impose a resistance to lung inflation or deflation. This is modeled through Robin boundary conditions applied on the inner surface. The stiffness can be set to model a more or less stiff lung environment. These Robin boundary conditions are not taken into account in the modeling of spontaneous breathing since breathing is induced in that case by the variation of the pleural pressure.

The other boundary conditions, *i.e.,* contact between the lungs and the rib cage, rib cage displacements and gravity are unchanged compared to the case of spontaneous breathing (see the boundary conditions modeling the spontaneous breathing (iii), (iv) and (v) respectively).

The virtual work of external forces is then:

$$W_{\mathrm{ext}}\left(\underline{U}, \underline{U}^*\right) = \int_{\Gamma_{0,\mathrm{c,in}}} \underline{T}_{\mathrm{c,in}} \cdot \underline{U}^* \,\mathrm{d}\Gamma_0 + \int_{\Gamma_{0,\mathrm{c,rb}}} \underline{T}_{\mathrm{c,rb}} \cdot \underline{U}^* \,\mathrm{d}\Gamma_0 + \int_{\Omega_0} \overline{\rho}\, \underline{g} \cdot \underline{U}^* \,\mathrm{d}\Omega_0\,. \tag{2.39}$$

The fluid pressure term is not included into W_{ext} as it is already part of the mixture stress $\underline{\underline{\Sigma}}$ and then of the virtual work of internal forces W_{int}.

Remark about pleural pressure Several studies have shown that pleural pressure is not homogeneous in the whole pleural space. For instance, a pleural pressure gradient of about $-7.5\,\mathrm{cmH_2O}$ has been observed between the apex and the base in the upright position in [Kallet, 2015].

The main explanation given is gravity [Millar and Denison, 1989; Agostoni, 1972], which induces a smaller pressure, *i.e.,* more negative, at apex than at the base in the standing position. If the pleural liquid was in an hydrostatic equilibrium, the gradient of pleural pressure would be about $1\,\mathrm{cmH_2O/cm}$ [Agostoni, 1972; Lai-Fook, 2004], *i.e.,* a difference of $20\,\mathrm{cmH_2O}$ for a 20 cm high lung between the apex and the base.

The difference between the observed gradient and the theoretical gradient implies an intrinsic gradient which reduces the gravity effect. It can possibly be explained by the existence of contact areas between both pleural membranes because of the presence of fatty tissue layers on the ribs, between ribs and parietal pleura. These fatty tissue layers, 1 or 2 mm thick [Im et al., 1989], make a contact between parietal and visceral pleura and must impact the hydrostatic equilibrium of the pleural liquid with a pressure loss [Lai-Fook, 2004].

Since the gradient of pleural pressure between apex and base is also present in the supine position, it means that another process occurs. The change of pleural pressure is induced under the action of the diaphragm, which is close to the basal part of lungs. Then, the negative pleural pressure comes from the base but is not homogeneous in the whole pleural space because of the pressure loss caused by contact as already mentioned.

The role of the pleural liquid in the pleural pressure gradient has also been been raised. Indeed, the pleural liquid is highly viscous and is always circulating in the pleura in order to be renewed. The pleural liquid is produced by capillary filtering from the upper parietal pleural and is resorbed by lymphangions by basal, posterior costal parietal pleura and the diaphragmatic and mediastinal parietal pleura, inducing a downward pleural liquid flow and a depression of $-10\,\mathrm{cmH_2O}$ [Wang, 1975; Miserocchi, 1997; Zocchi, 2002]. The complete turnover of pleural liquid is performed twice a day, since about 15 mL are produced each day and the volume of pleural liquid is about 8 mL [Noppen et al., 2000], which can be considered as negligible compared to the breathing time scale.

Concerning modeling, the pleural pressure will be first assumed to be homogeneous on the whole lung surface. Gradients of pleural pressure will also be considered to take into account the non-homogeneity of the pleural pressure: from apex to base in standing position, from back to stomach in supine or prone position.

2.2.4 End-exhalation stress field

Since in general the initial geometry of the lungs (which may be obtained from biomedical images or from a generic model) is not unloaded as was already mentioned in Section 2.2.2, the unloaded configuration needs to be computed in order to take into account the initial stress field present in the initial geometry. This is a classical problem in biomechanics as many living tissue contain prestresses due to a loaded physiological configuration [Gee et al., 2010; Sellier, 2011; Rausch et al., 2017] or inherent residual stresses [Fung, 1981; Genet et al., 2015b; Genet, 2019].

Let us consider that a pleural pressure $p_{\mathrm{pl,I}}$ is applied on the configuration ω_{I} constructed from an image I. We aim to find the unloaded configuration Ω_0 such that a zero pressure is applied on the lung surface in Ω_0 and Ω_0 is transformed into ω_{I} when $p_{\mathrm{pl,I}}$ is applied onto it. The boundary conditions to describe the transformation from the reference configuration Ω_0 to a real configuration ω_{I} are simplified compared to the boundary conditions used to describe breathing, since only a negative pressure applied on the whole lung surface, which stands for the pleural pressure, is considered (see Figure 2.5). In addition to the negative pleural pressure, the rigid body degrees of freedom are blocked using the nodes defining the best trihedron in the initial configuration mesh.

In this problem, a configuration ω_{I} is given and the unknown is the transformation $\underline{\chi}\left(\underline{x}\right)$ from ω_{I} to the unloaded configuration Ω_0. The boundary conditions applied from Ω_0 to ω_{I} are given. The problem is formulated following Govindjee and Mihalic [1998], where a change of variable is performed from $\underline{X}$ to $\underline{x}$. We denote with small letters the quantities defined on the known deformed configuration ω_{I} (see Figure 2.5), such as:

$$\begin{cases} \underline{\chi} := \underline{\chi}^{-1} \\ \underline{u} := -\underline{U} \circ \underline{\chi} \\ \underline{\underline{f}} := \underline{\underline{F}}^{-1} \circ \underline{\chi} \\ j := J^{-1} \circ \underline{\chi}. \end{cases} \tag{2.40}$$

The variational formulation of the problem is then written as:

$$\forall \underline{u}^{*},\ \int_{\omega_{\mathrm{I}}} \underline{\underline{\sigma}}(\underline{u}) : \underline{\underline{\varepsilon}}(\underline{u}^{*})\,\mathrm{d}\omega = -\int_{\Gamma_{\mathrm{I}}} p_{\mathrm{pl,I}}\ \underline{n} \cdot \underline{u}^{*}\,\mathrm{d}\gamma\,, \tag{2.41}$$

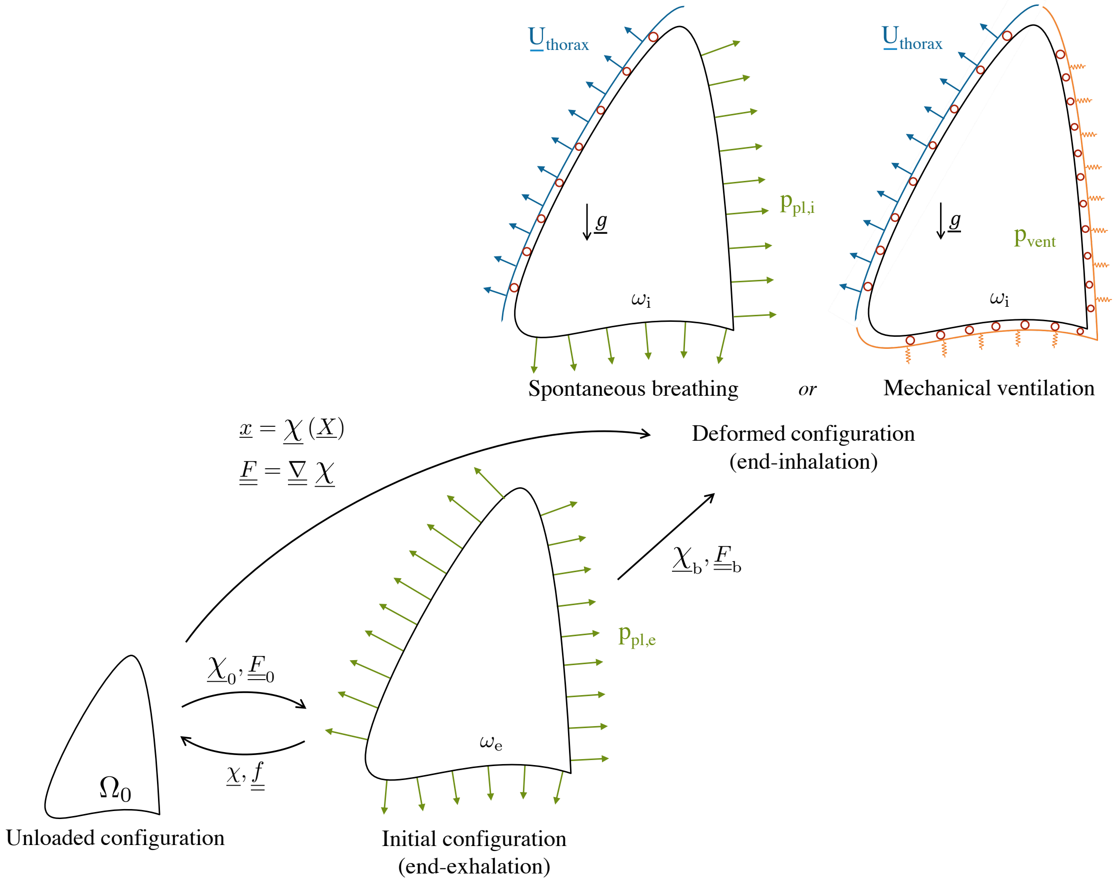

Figure 2.5 – Boundary conditions used to compute the unloaded configuration Ω_0, then the deformed configuration ω_{i} from the initial configuration ω_{e}. In addition to fixing rigid body movements, only pleural pressure $p_{\text{pl,e}}$ is considered for the transformation $\underline{\chi}_0$ between the unloaded and the end-exhalation configurations. However, the breathing transformation $\underline{\chi}_{\text{b}}$ between the end-exhalation to the end-inhalation configurations uses more complex boundary conditions, which depend on the type of breathing. In the case of spontaneous breathing, we consider the rib cage displacements $\underline{U}_{\text{thorax}}$, the pleural pressure at end-inhalation $p_{\text{pl,i}}$, a frictionless bilateral contact between the rib cage surface and lungs surface and the gravity volume loading. In the case of mechanical ventilation, an inner surface subjected to Robin's condition is also in contact with the inner lung surface.

where the Cauchy stress tensor $\underline{\underline{\sigma}}$ is written with the variable change as

$$\begin{aligned}\underline{\underline{\sigma}}\left(\underline{u}\left(\underline{x}\right)\right) &= \frac{1}{J\left(\underline{\chi}\left(\underline{x}\right)\right)}\underline{\underline{F}}\left(\underline{\chi}\left(\underline{x}\right)\right)\cdot\underline{\underline{\Sigma}}\left(\underline{\chi}\left(\underline{x}\right)\right)\cdot\underline{\underline{F}}^{T}\left(\underline{\chi}\left(\underline{x}\right)\right)\\ &= j\underline{\underline{f}}^{-1}\left(\underline{x}\right)\cdot\underline{\underline{\Sigma}}\left(\underline{\chi}\left(\underline{x}\right)\right)\cdot\underline{\underline{f}}^{-T}\left(\underline{x}\right)\end{aligned} \tag{2.42}$$

and the linearized strain tensor $\underline{\underline{\varepsilon}}$ is

$$\underline{\underline{\varepsilon}}\left(\underline{u}\right) := \left(\underline{\underline{\nabla}}\,\underline{u}\right)_{\mathrm{sym}} = \frac{1}{2}\left(\underline{\underline{\nabla}}\,\underline{u} + \underline{\underline{\nabla}}\,\underline{u}^{T}\right). \tag{2.43}$$

In this paper, we choose to estimate the unloaded configuration from the end-exhalation configuration, as shown in Figure 2.5.

Remark about porosity In the same extent as for the direct problem, the porosity should be constrained to remain positive. However, the proposed solutions – the use of a $\overline{W}_{\mathrm{por}}$ term or a contact-like formulation – formulated in the Section 2.2.1.4 are not enough, since they ensure only the deformed porosity ϕ_{f} to be positive. When considering the inverse problem, the porosity ϕ_{f} is given and the reference porosity Φ_{f0} is the quantity which should be constrained to be positive. The contact-like formulation of Equation (2.33) can be easily adapted for the inverse problem, with the two quantities, the reference porosity Φ_{f0} and the contact pressure $p_{\mathrm{c},0}$:

$$\begin{cases}\Phi_{\mathrm{f0}}\cdot p_{\mathrm{c},0} = 0\\ \Phi_{\mathrm{f0}} \geq 0\\ p_{\mathrm{c},0} \geq 0.\end{cases} \tag{2.44}$$

Conversely, the $\overline{W}_{\mathrm{por}}$ terms of Equation (2.30) or Equation (2.31) cannot be used anymore since $\overline{W}_{\mathrm{por}} = 0$ when Φ_{f0} tends to zero ($\Phi_{\mathrm{f0}} < \phi_{\mathrm{f}}$). A similar $\overline{W}_{\mathrm{por}}$ function ensuring Φ_{f0} to be positive could potentially be determined as well.

2.2.5 Resolution

2.2.5.1 Variational formulations

General poromechanics problem The problem to be solved to study the deformation of lungs throughout breathing in a poromechanical framework is described by the following system:

$$\text{Find }\left(\underline{U},\Phi_{\mathrm{f}}\right)/\quad\begin{cases}\forall\underline{U}^{*},\ \displaystyle\int_{\Omega_0}\frac{\partial\overline{\psi}}{\partial\underline{\underline{E}}}:\mathrm{d}_{\underline{U}}\underline{\underline{E}}\cdot\underline{U}^{*}\,\mathrm{d}\Omega_0 = W_{\mathrm{ext}}\left(\underline{U},\underline{U}^{*}\right)\\ p_{\mathrm{f}} = -\dfrac{\partial\overline{\psi}_{\mathrm{s}}}{\partial\Phi_{\mathrm{s}}}.\end{cases} \tag{2.45}$$

In this system, the two equations are coupled with the two unknowns $\underline{U}$ and Φ_{f}. The first one is the global mechanical equilibrium, the second one is the local hydrostatic pressure equilibrium.

Using the decomposition of $\dfrac{\partial\overline{\psi}}{\partial\underline{\underline{E}}}$ as shown in Equation (2.22) as well as the transformation of the fluid pressure term with the homogeneous fluid pressure assumption, the first equation of the system gives:

$$\text{Find } \left(\underline{U}, \Phi_{\mathrm{f}}\right) / \\ \begin{cases} \forall \underline{U}^*, \displaystyle\int_{\Omega_0} \frac{\partial \overline{\psi}_{\mathrm{s}}}{\partial \underline{\underline{E}}} : \mathrm{d}_{\underline{U}}\, \underline{\underline{E}} \cdot \underline{U}^* \, \mathrm{d}\Omega_0 = W_{\mathrm{ext}}\left(\underline{U}, \underline{U}^*\right) + \int_{\Gamma_0} p_{\mathrm{f}} J \underline{\underline{F}}^{-T} \underline{n} \cdot \underline{U}^* \, \mathrm{d}\Gamma_0 \\ p_{\mathrm{f}} = -\dfrac{\partial \overline{\psi}_{\mathrm{s}}}{\partial \Phi_{\mathrm{s}}}. \end{cases} \tag{2.46}$$

It is interesting to notice that a mixture under the lung specific assumptions mentioned in Section 2.2.1.1 behaves as a non porous solid with an extra loading representing the fluid pressure action, which simply acts as a following pressure applied on the boundary of the mixture.

The coupling between equations is weak: since the fluid pressure p_{f} is given, the mechanical equilibrium depends only on the reference porosity $\Phi_{\mathrm{f}0}$ and not on the actual porosity Φ_{f}. The porosity field can then be computed afterwards from an initial porosity field and the deformation of the mixture.

In some cases, the second equation of the system can be simplified. With the choice of $\overline{\psi}_{\mathrm{s}}$ that was made in Equation (2.24), we have:

$$\text{Find } \left(\underline{U}, \Phi_{\mathrm{f}}\right) / \\ \begin{cases} \forall \underline{U}^*, \displaystyle\int_{\Omega_0} \frac{\partial \overline{W}_{\mathrm{skel}}}{\partial \underline{\underline{E}}} : \mathrm{d}_{\underline{U}}\, \underline{\underline{E}} \cdot \underline{U}^* \, \mathrm{d}\Omega_0 = W_{\mathrm{ext}}\left(\underline{U}, \underline{U}^*\right) + \int_{\Gamma_0} p_{\mathrm{f}} J \underline{\underline{F}}^{-T} \underline{n} \cdot \underline{U}^* \, \mathrm{d}\Gamma_0 \\ p_{\mathrm{f}} = -\dfrac{\partial \overline{W}_{\mathrm{bulk}}}{\partial \Phi_{\mathrm{s}}}, \end{cases} \tag{2.47}$$

and from the choice of $\overline{W}_{\mathrm{bulk}}$ made in Equation (2.29), the porosity becomes

$$\Phi_{\mathrm{f}} = J - \Phi_{\mathrm{s}} \quad \text{with} \quad \Phi_{\mathrm{s}} = \frac{1}{\dfrac{p_{\mathrm{f}}}{\overline{\kappa}} + \dfrac{1}{\Phi_{\mathrm{s}0}}} \,. \tag{2.48}$$

In case of free breathing, where $p_{\mathrm{f}} = 0$, or when $\overline{\kappa}$ is high and tend to an incompressible behavior, the quantity Φ_{s} is constant and equal to $\Phi_{\mathrm{s}0}$, and leads to the purely geometric equality

$$1 - \Phi_{\mathrm{f}0} = J\left(1 - \phi_{\mathrm{f}} \circ \underline{\chi}\right), \tag{2.49}$$

valid for an incompressible solid.

Problem with the additional energy $\overline{W}_{\mathrm{por}}$ When using an additional energy $\overline{W}_{\mathrm{por}}$, the energy of the solid part of the mixture is transformed as mentioned in Equation (2.32). The expression of $\underline{\underline{\Sigma}}$ from Equation (2.25) becomes:

$$\underline{\underline{\Sigma}}\left(\underline{\underline{E}}, \overline{\rho}_{\mathrm{f}+}\right) = \frac{\partial \overline{\psi}}{\partial \underline{\underline{E}}} = \frac{\partial \overline{W}_{\mathrm{skel}}}{\partial \underline{\underline{E}}} + \frac{\partial \overline{W}_{\mathrm{bulk}}}{\partial \Phi_{\mathrm{s}}} J \underline{\underline{C}}^{-1} + \frac{\partial \overline{W}_{\mathrm{por}}}{\partial \overline{\rho}_{\mathrm{f}+}} \frac{\partial \overline{\rho}_{\mathrm{f}+}}{\partial \underline{\underline{E}}}. \tag{2.50}$$

However, since $\underline{\underline{E}}$ and $\overline{\rho}_{\mathrm{f}+}$ are two independent variables, the last term is zero and the expression of $\underline{\underline{\Sigma}}$ from Equation (2.25) is unchanged. In addition, the fluid pressure becomes:

$$p_{\mathrm{f}} = -\frac{\partial \overline{\psi}_{\mathrm{s}}}{\partial \Phi_{\mathrm{s}}} = -\left(\frac{\partial \overline{W}_{\mathrm{bulk}}}{\partial \Phi_{\mathrm{s}}} + \frac{\partial \overline{W}_{\mathrm{por}}}{\partial \Phi_{\mathrm{s}}}\right). \tag{2.51}$$

The problem is then the following:

$$\text{Find } \left(\underline{U}, \Phi_{\mathrm{f}}\right) / \\ \begin{cases} \forall \underline{U}^*, \displaystyle\int_{\Omega_0} \frac{\partial \overline{W}_{\mathrm{skel}}}{\partial \underline{\underline{E}}} : \mathrm{d}_{\underline{U}} \underline{\underline{E}} \cdot \underline{U}^* \, \mathrm{d}\Omega_0 = W_{\mathrm{ext}}\left(\underline{U}, \underline{U}^*\right) - \int_{\Omega_0} \frac{\partial \overline{W}_{\mathrm{bulk}}}{\partial \Phi_{\mathrm{s}}} J \underline{\underline{C}}^{-1} : \mathrm{d}_{\underline{U}} \underline{\underline{E}} \cdot \underline{U}^* \, \mathrm{d}\Omega_0 \\ p_{\mathrm{f}} = -\left(\dfrac{\partial \overline{W}_{\mathrm{bulk}}}{\partial \Phi_{\mathrm{s}}} + \dfrac{\partial \overline{W}_{\mathrm{por}}}{\partial \Phi_{\mathrm{s}}}\right). \end{cases} \tag{2.52}$$

The coupling is strong here as $\overline{W}_{\mathrm{por}}$ depends on the current porosity Φ_{f}.

Problem with the contact-like formulation The contact-like formulation to ensure a positive porosity is formulated using an extra unknown, the contact pressure p_{c}:

$$\text{Find } \left(\underline{U}, \Phi_{\mathrm{f}}, p_{\mathrm{c}}\right) / \\ \begin{cases} \forall \underline{U}^*, \displaystyle\int_{\Omega_0} \frac{\partial \overline{\psi}_{\mathrm{s}}}{\partial \underline{\underline{E}}} : \mathrm{d}_{\underline{U}} \underline{\underline{E}} \cdot \underline{U}^* \, \mathrm{d}\Omega_0 = W_{\mathrm{ext}}\left(\underline{U}, \underline{U}^*\right) + \int_{\Omega_0} p J \underline{\underline{C}}^{-1} : \mathrm{d}_{\underline{U}} \underline{\underline{E}} \cdot \underline{U}^* \, \mathrm{d}\Omega_0 \\ p = p_{\mathrm{f}} \mathscr{H}\left(\Phi_{\mathrm{f}}\right) + p_{\mathrm{c}}\left(1 - \mathscr{H}\left(\Phi_{\mathrm{f}}\right)\right) = -\dfrac{\partial \overline{\psi}_{\mathrm{s}}}{\partial \Phi_{\mathrm{s}}} \\ \Phi_{\mathrm{f}} \cdot p_{\mathrm{c}} = 0 \\ \Phi_{\mathrm{f}} \geq 0 \\ p_{\mathrm{c}} \geq 0. \end{cases} \tag{2.53}$$

In practice, as p_{c} is not a quantity of interest in our case, the variational formulation is formulated in a simpler way. If $\mathscr{H}\left(\Phi_{\mathrm{f}}\right) = 1$, the system of Equation (2.46) is still valid, with the two unknowns $\underline{U}$ and ϕ_{f}, since the contact pressure is zero. However, if $\mathscr{H}\left(\Phi_{\mathrm{f}}\right) = 0$, the unknowns are $\underline{U}$ and p_{c} since the porosity is zero. The contact pressure is explicitly given by the second equation of the system and can be inserted into the first equation. Only one equation is left:

$$\text{Find } \underline{U} / \\ \forall \underline{U}^*, \int_{\Omega_0} \frac{\partial \overline{\psi}_{\mathrm{s}}}{\partial \underline{\underline{E}}} : \mathrm{d}_{\underline{U}} \underline{\underline{E}} \cdot \underline{U}^* \, \mathrm{d}\Omega_0 = W_{\mathrm{ext}}\left(\underline{U}, \underline{U}^*\right) - \int_{\Omega_0} \frac{\partial \overline{\psi}_{\mathrm{s}}}{\partial \Phi_{\mathrm{s}}} J \underline{\underline{C}}^{-1} : \mathrm{d}_{\underline{U}} \underline{\underline{E}} \cdot \underline{U}^* \, \mathrm{d}\Omega_0 \,. \tag{2.54}$$

Note that in the case where $\Phi_{\mathrm{f}} = 0$, $\overline{\psi}_{\mathrm{s}}$ is a function of $\underline{\underline{E}}$ and J since $\Phi_{\mathrm{s}} = J$. We can gather both cases:

$$\text{Find } \left(\underline{U}, \Phi_{\mathrm{f}}\right) / \\ \begin{cases} \forall \underline{U}^*, \displaystyle\int_{\Omega_0} \frac{\partial \overline{\psi}_{\mathrm{s}}}{\partial \underline{\underline{E}}} \left(\underline{\underline{E}}\right) : \mathrm{d}_{\underline{U}} \underline{\underline{E}} \cdot \underline{U}^* \, \mathrm{d}\Omega_0 = W_{\mathrm{ext}}\left(\underline{U}, \underline{U}^*\right) \\ \qquad\qquad - \displaystyle\int_{\Omega_0} \frac{\partial \overline{\psi}_{\mathrm{s}}}{\partial \Phi_{\mathrm{s}}} \left(\underline{\underline{E}}, \Phi_{\mathrm{s}}\left(J, \Phi_{\mathrm{f,\ real}} = \Phi_{\mathrm{f}} \mathscr{H}\left(\Phi_{\mathrm{f}}\right)\right)\right) J \underline{\underline{C}}^{-1} : \mathrm{d}_{\underline{U}} \underline{\underline{E}} \cdot \underline{U}^* \, \mathrm{d}\Omega_0 \\ p_{\mathrm{f}} = -\dfrac{\partial \overline{\psi}_{\mathrm{s}}}{\partial \Phi_{\mathrm{s}}} \left(\underline{\underline{E}}, \Phi_{\mathrm{s}}\left(J, \Phi_{\mathrm{f}}\right)\right). \end{cases} \tag{2.55}$$

The quantity Φ_{f} computed through the second equation can be negative. However, the actual porosity in the mixture is $\Phi_{\mathrm{f,\ real}} = \Phi_{\mathrm{f}} \mathscr{H}\left(\Phi_{\mathrm{f}}\right)$ and is the quantity of interest. Consequently, the mechanical equilibrium is a function of $\Phi_{\mathrm{f,\ real}}$ and not of Φ_{f}, which is an auxiliary quantity. Formulating the problem in that way avoids having to perform fixed point iterations on the states $\mathscr{H}\left(\Phi_{\mathrm{f}}\right) = 0$ and $\mathscr{H}\left(\Phi_{\mathrm{f}}\right) = 1$.

As it is well-known in contact theory, the convergence of such formulations can be problematic. In the pulmonary case, some non porous cells could be next to other cells that are still porous; both types of cells differ by the volume ratio J, which can lead to convergence issues, especially with a quasi-incompressible solid.

Inverse problem In the case of the inverse problem to estimate the reference configuration, a loaded configuration ω_{I}, which can be taken from an image, is given, as well as the associated deformed porosity. The two unknowns are the displacement on the deformed configuration and the reference porosity, which was given in the case of the direct problem. The problem is then:

$$\text{Find } \left(\underline{u}, \phi_{\mathrm{f0}}\right) / \begin{cases} \forall \underline{u}^*, \ \displaystyle\int_{\omega_{\mathrm{I}}} \underline{\underline{\sigma}}(\underline{u}) : \underline{\underline{\varepsilon}}(\underline{u}^*) \, \mathrm{d}\omega = -\int_{\Gamma_{\mathrm{I}}} p_{\mathrm{pl}} \, \underline{n} \cdot \underline{u}^* \, \mathrm{d}\gamma \\ p_{\mathrm{f}} = -\dfrac{\partial \overline{\psi}_{\mathrm{s}}}{\partial \Phi_{\mathrm{s}}}(\underline{u}), \end{cases} \tag{2.56}$$

where $\phi_{\mathrm{f0}} := \Phi_{\mathrm{f0}} \circ \underline{\chi} \cdot J^{-1} = \dfrac{\mathrm{d}V_{\mathrm{f0}}}{\mathrm{d}v}$ is the reference volume fraction of fluid pushed forward on the known deformed configuration.

2.2.5.2 Implementation

Generation of the rib cage and inner surfaces geometries The rib cage and inner surfaces generation uses the lung geometries. First, the lung surface is used to compute a binary image. Then, for each surface, a second binary image is performed by drawing contours manually with the software MeVisLab in order to get an extension of the lungs. Finally, surfaces are extracted from each of the binary images and meshed with the software Gmsh to get the rib cage surface and the inner surface.

Computation of the unloaded configuration The reference configuration Ω_0 is computed with a method using a re-parametrization of the weak form of the inverse problem [Govindjee and Mihalic, 1998], as described in Section 2.2.4. It has been implemented in python using the FEniCS library [Alnæs et al., 2015; Logg et al., 2012].

Computation of the end-inhalation configuration The deformed configuration is computed with the Abaqus software. We now present the details of the model implementation.

Elements The lungs are meshed with the linear tetrahedral volume elements, whereas both the rib cage surface and the inner surface are meshed with the linear triangle surface elements. There are called C3D4 and S3 in Abaqus respectively.

Mechanical properties The skeleton energy $\overline{W}_{\mathrm{skel}}$ is written in a subroutine UHYPER. The local equilibrium of the mixture depending on the bulk energy $\overline{W}_{\mathrm{bulk}}$ is inserted in the subroutine in order to compute the deformed porosity as a state variable. The inner surface is defined with a Neo-Hookean material, such that the initial shear modulus is $2 \cdot 10^3$ kPa and the initial bulk modulus is 6.67 kPa.

Contact Concerning the contact with the thorax, a master-slave, finite-sliding, node-to-surface contact pair formulation is used, with the rib cage as master and the lung surface as slave. The surfaces are adjusted at the start of the simulation in order to remove gaps and overclosures. The contact is defined as a frictionless, hard contact which does not allow any separation of surfaces once it is established. In case of the simulation of the mechanical ventilation, the contact with the inner surface have the same properties as the contact with the thorax except that separation between surfaces are possible.

Robin conditions aspect Robin boundary conditions are established using spring elements. Each node of the inner surface is linked to three linear spring elements of type SPRING1, attaching the node to the end-exhalation position of that node, in each direction of the space. The spring stiffness k_{spring} is different for each spring element in order to take into account the size of the surface elements connected to the node linked by each spring element. The spring stiffness is then $k_{\text{spring}} = \lambda_{\text{node}} K$, where λ_{node} is the coefficient of the lumped mass matrix associated to the node defining the spring, and K is a reference stiffness, which means that the three spring elements linked to the same node have the same stiffness.

Solution process The deformed configuration is computed in two steps. First, the stresses and the strains in the initial configuration are computed using the reference nodes coordinates and the reference porosity of the unloaded configuration computed before. It uses the same model as for the estimation of the reference configuration. It is checked that the nodes coordinates are the same as in the initial configuration from which the reference configuration was estimated. Then, the deformed configuration is computed with the more complex boundary conditions, including contact.

2.3 Illustrations

We now present some illustrations of our pulmonary poromechanical model. The end-exhalation pleural pressure $p_{\text{pl,e}}$ and the end-inhalation pleural pressure $p_{\text{pl,i}}$ are chosen in the physiological range, whereas the mechanical parameters are chosen in order to reproduce the volumetric response to a change of pressure as observed in experimental data [Gibson and Pride, 1976] (see Figure 2.2). In all cases, the thorax is fixed. For each illustration, the parameters used are reported in the corresponding table.

2.3.1 Geometries

All the computations in this section use a generic right lung mesh, taken from the Zygote model[1], in the end-exhalation configuration and a thorax mesh, generated from the lung mesh in order to have the thorax surface and the lung surface in contact at the initial configuration. The thorax corresponds to the hard tissue surrounding lungs, mainly the ribs and the spine. The lung mesh is composed of 4052 tetrahedral elements, whereas the thorax and the inner surface are composed of 2678 and 2260 triangle surface elements respectively. Both lung and thorax meshes are shown in Figure 2.6.

---

[1] www.zygote.com

2.3.2 Influence of the positive porosity constraint on the unloaded configuration

The first step to simulate breathing is to estimate the unloaded configuration. As explained in Sections 2.2.1.4 and 2.2.4, the estimation of the unloaded configuration is associated with a problem concerning the porosity to be kept positive. We study in this paragraph the impact of using the contact-like formulation in a real case.

An initial end-exhalation porosity distribution $\phi_{\mathrm{f,\,e}}$ was generated according to a Gaussian distribution (mean: 0.5, std: 0.13) as shown in grey in Figure 2.7. The porosity values are randomly distributed in space in the lung volume. The pressure loading and material parameters used in the simulations are presented in Table 2.1.

Two simulations were performed: one without any constraint on the porosity using the model of Equation (2.24), the other using the contact-like formulation proposed in Equation (2.33). The resulting reference porosity Φ_{f} in both cases is then computed as presented in Figure 2.7, in blue and red, respectively. The estimation of the unloaded configuration implies a shift to the left of the porosity distribution because the porosity decreases when lung deflates. When using no constraint, the left part of the distribution is negative, which is not physiological. However, the use of the contact-like formulation allows to keep the porosity to be positive everywhere. We can notice that the cells with zero porosity do not significantly impact the rest of the global distribution.

Name	Symbol	Unit	Value
Air pressure	p_{f}	[kPa]	0
End-exhalation pleural pressure	$p_{\mathrm{pl,e}}$	[kPa]	-0.5
Skeleton energy parameters	$\widetilde{\alpha}$	[kPa]	$1.6 \cdot 10^{-1}$
	δ	[-]	0.5
	$\widetilde{\beta}_1$	[kPa]	0.2
	$\widetilde{\beta}_2$	[kPa]	0.4
Solid bulk modulus	$\overline{\kappa}$	[kPa]	-

Table 2.1 – Parameters used for the breathing simulations when studying the influence of the porosity constraint on the unloaded configuration. Top rows corresponds to the loading parameters, fluid pressure and pleural pressures, whereas bottom rows are the components of the constitutive behavior of the pulmonary mixture. The solid bulk modulus is not needed when $p_{\mathrm{f}} = 0$.

2.3.3 Influence of the stiffness

We present here an illustration of the model in the free breathing case and the fluid pressure is then zero. The reference configuration is first computed from the initial configuration using the inverse problem described in Section 2.2.4. Then, the deformed configuration is computed using the complex boundary conditions described in Section 2.2.3: a pleural pressure is applied on the lung surface and makes the lung inflate and slide against the thorax surface; the thorax displacement is prescribed (here it is null); the gravity is neglected. The loading and material parameters used for the computation are reported in Table 2.2. The same material parameters are used for both the estimation of the reference configuration and the computation of the deformed configuration.

The impact of the stiffness parameter $\overline{\alpha}$, which is part of the skeleton energy presented in Equation (2.27), is studied using three different values : $8 \cdot 10^{-1}$ kPa, $8 \cdot 10^{-2}$ kPa,

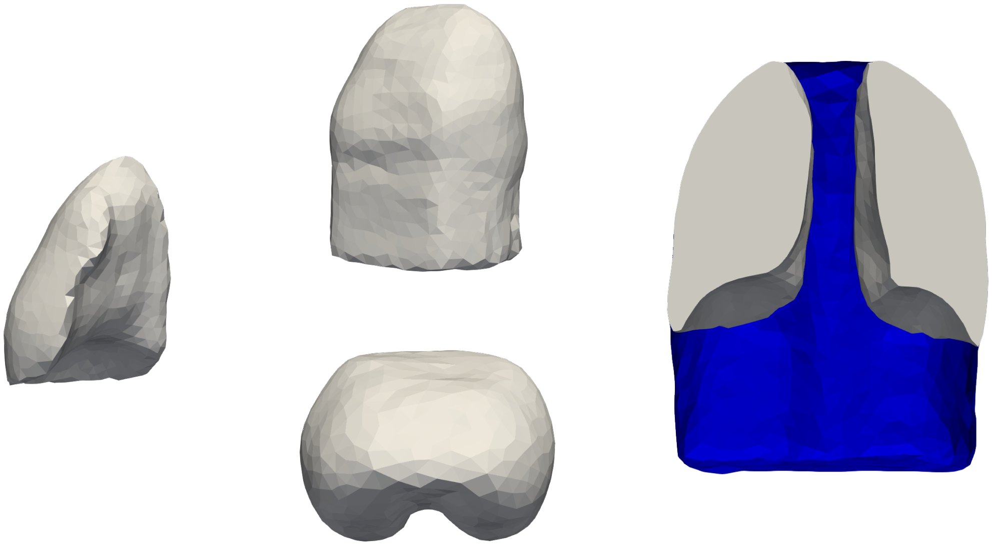

Figure 2.6 – Lung and thorax meshes in the initial configuration, *i.e.,* end-exhalation. (Left) Lung mesh taken from Zygote model[1]. (Middle) Two views of the thorax mesh, lateral view (top) and top view (bottom). (Right) Both meshes together in a coronal view. The lung surface is in contact with the thorax surface.

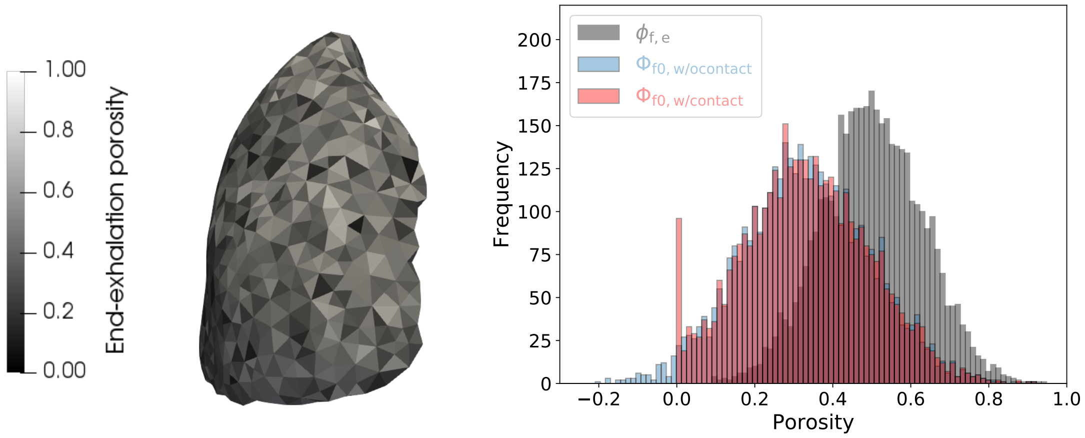

Figure 2.7 – Comparison of the reference porosity field computed without or with the contact-like formulation. (Left) The given end-exhalation porosity is shown on the end-exhalation mesh. (Right) The distribution of the given end-exhalation porosity is plotted in grey on the histogram. The red and blue distributions are the computed reference porosity with or without the contact-like formulation, respectively. When not using any strategy to ensure a positive porosity, the computed reference porosity of some cells is negative, whereas the computed reference porosity remains positive or null when using a contact-like formulation.

$8 \cdot 10^{-3}$ kPa. The results are shown in Figure 2.8. The rigidity parameter $\overline{\alpha}$ impacts the lung compliance. When $\overline{\alpha}$ is increasing, the volumetric change is lower for a given pressure, which means that the lung compliance decreases.

Diseased behaviors could be represented by the model in adjusting the rigidity parameter. Indeed, the green curve ($\overline{\alpha} = 8 \cdot 10^{-1}$ kPa) could represent a fibrosis case, in which the lung becomes stiffer, the orange curve ($\overline{\alpha} = 8 \cdot 10^{-2}$ kPa) could stand for an healthy case, and the blue curve ($\overline{\alpha} = 8 \cdot 10^{-3}$ kPa) could be attributed to an emphysema case, where the lung is more compliant.

Name	Symbol	Unit	Value
Air pressure	p_f	[kPa]	0
End-exhalation pleural pressure	$p_\mathrm{pl,e}$	[kPa]	-0.5
End-inhalation pleural pressure	$p_\mathrm{pl,i}$	[kPa]	-2
Gravity constant	g	[m.s^{-2}]	-
Skeleton energy parameters	$\overline{\alpha}$	[kPa]	$\left[8 \cdot 10^{-3}, 8 \cdot 10^{-2}, 8 \cdot 10^{-1}\right]$
	δ	[-]	0.5
	$\overline{\beta}_1$	[kPa]	0.1
	$\overline{\beta}_2$	[kPa]	0.2
Solid bulk modulus	$\overline{\kappa}$	[kPa]	-

Table 2.2 – Parameters used for the breathing simulations when studying the rigidity impact. Top rows corresponds to the loading parameters, fluid pressure and pleural pressures, whereas bottom rows are the components of the constitutive behavior of the pulmonary mixture. The solid bulk modulus is not needed when $p_\mathrm{f} = 0$.

2.3.4 Influence of gravity

The proposed model also allows to study the impact of gravity on the lung behavior. Two different simulations were performed with or without gravity in supine position, which is meaningful as most of imaging techniques are acquired in supine position. The thorax is fixed and the free breathing case is considered. Gravity is taken into account only from the end-exhalation configuration to the end-inhalation configuration, and not during the estimation of the reference configuration. Both the porosity field and the contact pressure field are investigated.

The impact of gravity on the porosity distribution is presented in Figure 2.9. The histogram representing the porosity distribution into the whole volume is wider when gravity is taken into account. More precisely, we can observe that porosity is lower in the bottom part of the lung and is higher in the top part of the lung, leading to a vertical gradient. It means that the alveoli in the top part are more inflated. The phenomenon was already measured on computed tomography by [Millar and Denison, 1989] on supine subjects or by a gas-dilution technique by [Milic-Emili et al., 1966] on sitting subjects. The relative error in hydrostatic pressure when neglecting gravity, expressed as

$$\frac{\left\| p_{\mathrm{w/o}\ \underline{\mathrm{g}}} - p_{\mathrm{w/}\,\underline{\mathrm{g}}} \right\|_{L^2}}{\left\| p_{\mathrm{w/}\,\underline{\mathrm{g}}} \right\|_{L^2}}, \tag{2.57}$$

is 18 %.

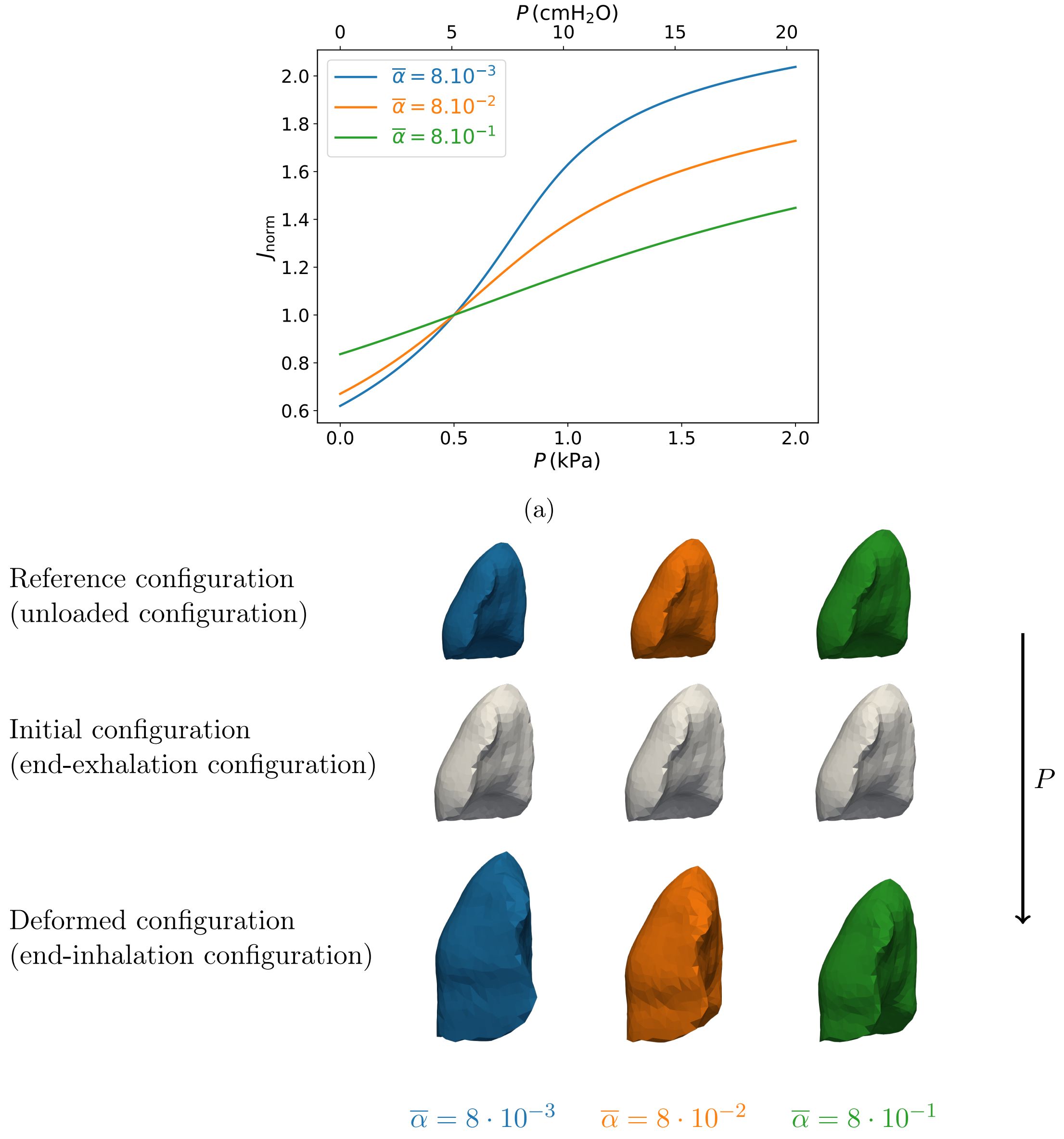

(a)

(b)

Figure 2.8 – Volume response of lung to a change of pleural pressure in the free breathing case for different values of the stiffness parameter $\overline{\alpha}$ in kPa. (a) Lung volume change J normalized by its value at end-exhalation, *i.e.,* at the pressure 0.5 kPa, with respect to the pleural pressure loading. (b) The reference configurations (top row), or unloaded configurations, are computed from the initial configurations (middle row) with simplified boundary conditions using the inverse problem mentioned in Section 2.2.4. Then, the deformed configurations (bottom row) are computed considering a contact between the lungs and the thorax as described in Section 2.2.3.

Gravity also impacts the contact pressure field between the lung surface and the thorax surface. Figure 2.9 shows the distributions of the contact pressure for the case without gravity and the case with gravity. The distribution of the contact pressure without considering gravity is centered around 0. When considering gravity, the distribution is wider and the center is about 0.2 kPa, which is explained by the change in the balance of forces.

Name	Symbol	Unit	Value
Air pressure	p_f	[kPa]	0
End-exhalation pleural pressure	$p_\mathrm{pl,e}$	[kPa]	-0.5
End-inhalation pleural pressure	$p_\mathrm{pl,i}$	[kPa]	-2
Gravity constant	g	[m.s^{-2}]	[0, 9.8]
Solid density	ρ_s0	[g.cm^{-3}]	1
Fluid density	ρ_f0	[g.cm^{-3}]	0
Reference porosity	Φ_f0	[-]	0.4
Skeleton energy parameters	$\overline{\alpha}$	[kPa]	$8 \cdot 10^{-2}$
	δ	[-]	0.5
	$\overline{\beta}_1$	[kPa]	0.1
	$\overline{\beta}_2$	[kPa]	0.2
Solid bulk modulus	$\overline{\kappa}$	[kPa]	-

Table 2.3 – Parameters used for the study of the gravity impact. Top rows corresponds to the loading parameters, fluid and pleural pressures and gravity, whereas bottom rows are the components of the constitutive behavior of the pulmonary mixture. The solid bulk modulus is not needed when $p_\mathrm{f} = 0$.

2.3.5 Comparison between free breathing and ventilated breathing

Mechanical ventilation can produce an injury called Ventilator-Induced Lung Injury (VILI) at the alveolar scale as a consequence of overpressure, which can induce overexpansion or high stresses in the alveoli. Clinicians are interested in improving mechanical ventilation to reduce risks of such a disease. To do so, they can tune several parameters like the Positive End-Expiratory Pressure (PEEP), the plateau pressure or the breathing rate. Lung models could be used to optimize these parameters, by allowing to quantify their impact on the parenchyma. For instance, our model allows to study the impact of fluid pressure induced by the ventilator on stresses, which we illustrate here.

From Equation (2.25), we can decompose the mixture stress as follows:

$$\underline{\underline{\Sigma}} = \underline{\underline{\Sigma}}_\mathrm{skel} + \underline{\underline{\Sigma}}_\mathrm{p} \quad \text{with} \quad \begin{cases} \underline{\underline{\Sigma}}_\mathrm{skel} := \dfrac{\partial \overline{W}_\mathrm{skel}}{\partial \underline{\underline{E}}} \\ \underline{\underline{\Sigma}}_\mathrm{p} := -p_\mathrm{f} J \underline{\underline{C}}^{-1}, \end{cases} \tag{2.58}$$

where $\underline{\underline{\Sigma}}$ represents the total stress in the mixture (that equilibrates the boundary loadings on the mixture as shown by Equation (2.13)), $\underline{\underline{\Sigma}}_\mathrm{skel}$ represents the skeleton stress (it is a function of the global deformation of the mixture that equilibrates the total pressure acting on the system, *i.e.*, $p_\mathrm{tot} = p_\mathrm{pl} - p_\mathrm{f}$, as shown by Equation (2.47)), and $\underline{\underline{\Sigma}}_\mathrm{p}$ is the hydrostatic stress induced by the fluid pressure. Moreover, the mixture hydrostatic stress

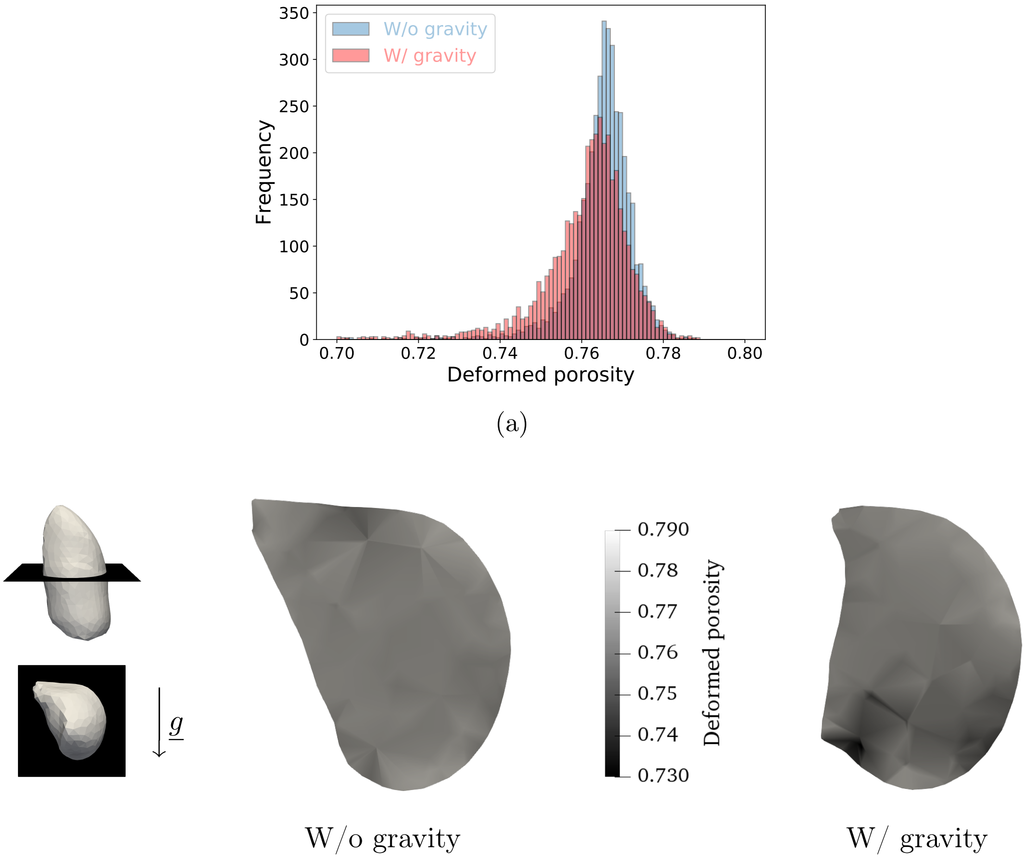

(a)

(b)

Figure 2.9 – Influence of gravity on the porosity in the supine position. (Top) Histogram representing the porosity distribution at end-inhalation with and without considering gravity. The porosity distribution is wider when using the gravity into the model. (Bottom row) Porosity field of an axial cross-section, represented on the left, for both cases. The porosity field is more homogeneous when no gravity is used, whereas a porosity gradient is present when the gravity is applied: the bottom part of the lung is denser and less porous than the top part.

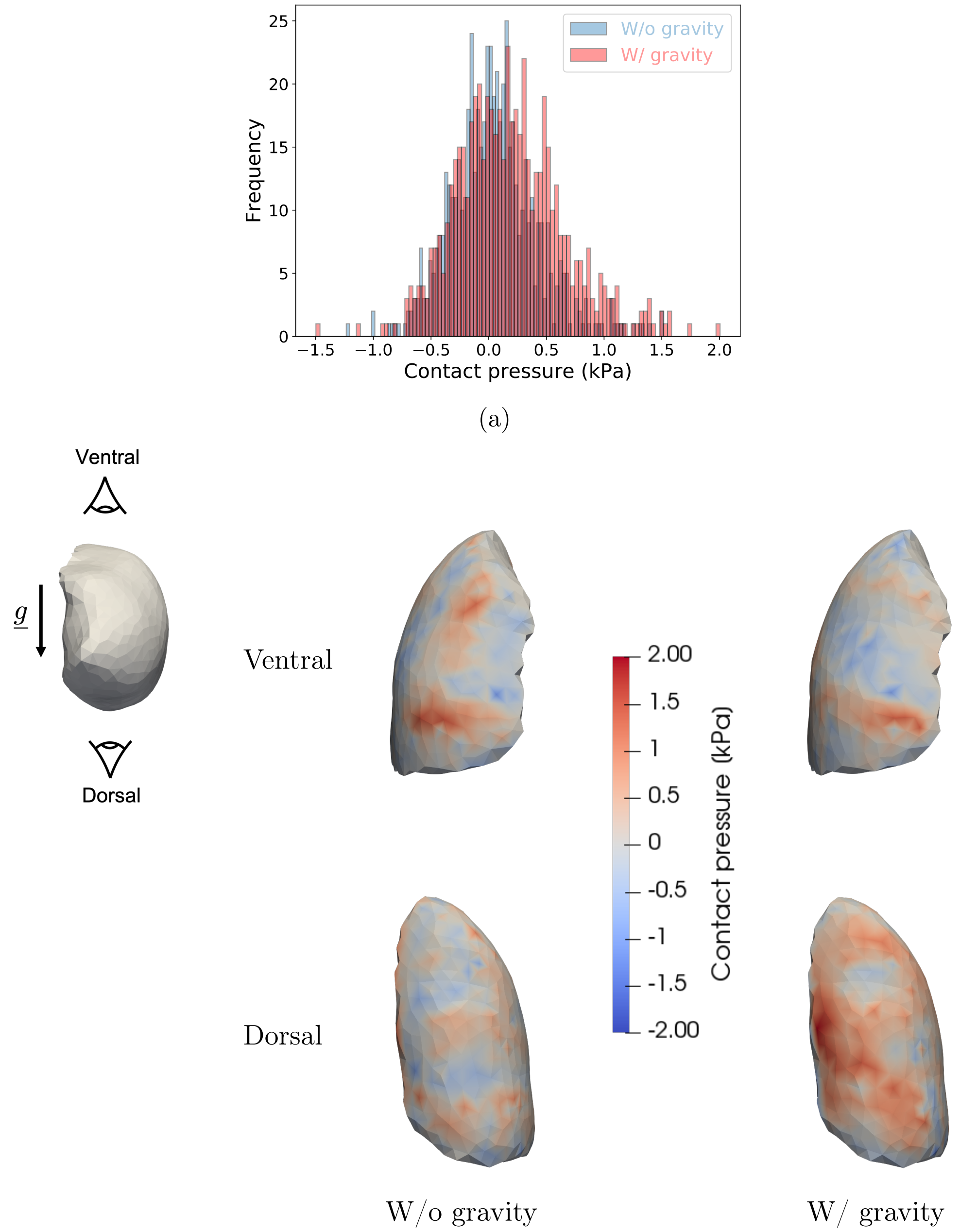

(a)

(b)

Figure 2.10 – Influence of gravity on the contact pressure in the supine position. (Top) Histogram representing the contact pressure distribution w/ and w/o considering gravity. The contact pressure is 0.04±0.38 kPa without considering gravity, whereas it is 0.18±0.47 kPa when considering gravity. (Bottom row) Porosity field represented on the mesh, shown for the ventral and dorsal surface for both cases. With gravity, the contact pressure is more negative for the ventral surface and more positive for the dorsal surface, because gravity is a force acting in the ventral-to-dorsal direction.

can be decomposed into solid and fluid parts, based on the porosity:

$$\underline{\underline{\Sigma}}_{\text{p}} = \underline{\underline{\Sigma}}_{\text{p, s}} + \underline{\underline{\Sigma}}_{\text{p, f}} \quad \text{with} \quad \begin{cases} \underline{\underline{\Sigma}}_{\text{p, s}} := (1-\Phi_{\text{f}})\,\underline{\underline{\Sigma}}_{\text{p}} \\ \underline{\underline{\Sigma}}_{\text{p, f}} := \Phi_{\text{f}}\underline{\underline{\Sigma}}_{\text{p}}. \end{cases} \tag{2.59}$$

Thus, the mixture stress can be decomposed into solid and fluid parts:

$$\underline{\underline{\Sigma}} = \underline{\underline{\Sigma}}_{\text{s}} + \underline{\underline{\Sigma}}_{\text{f}} \quad \text{with} \quad \begin{cases} \underline{\underline{\Sigma}}_{\text{s}} := \underline{\underline{\Sigma}}_{\text{skel}} + (1-\Phi_{\text{f}})\,\underline{\underline{\Sigma}}_{\text{p}} \\ \underline{\underline{\Sigma}}_{\text{f}} := \Phi_{\text{f}}\underline{\underline{\Sigma}}_{\text{p}}, \end{cases} \tag{2.60}$$

since $\underline{\underline{\Sigma}}_{\text{skel}}$ is a solid stress by definition.

Both types of breathing, spontaneous breathing and mechanical ventilation, result in different stresses. Indeed, in the case of spontaneous breathing, the driving force of breathing is the variation of pleural pressure, whereas in the case of ventilated breathing, it is the fluid pressure induced by the ventilator that acts to inflate both lungs and the rib cage. The typical order of magnitude of the pressure variation as well as the volume variation for both types of breathing are reported in Table 2.4. The variation of ventilated pressure is much higher than the variation of pleural pressure while the deformation is smaller, since the ventilated pressure should inflate the rib cage in addition to lungs. In spontaneous breathing, the rib cage inflates thanks to intercostal muscles. In case of spontaneous breathing, we have

$$p_{\text{f}}^{\text{sb}} = 0, \tag{2.61}$$

which induces

$$\begin{cases} \underline{\underline{\Sigma}}_{\text{f}}^{\text{sb}} = \underline{\underline{\Sigma}}_{\text{p}}^{\text{sb}} = 0 \\ \underline{\underline{\Sigma}}_{\text{s}}^{\text{sb}} = \underline{\underline{\Sigma}}^{\text{sb}} = \underline{\underline{\Sigma}}_{\text{skel}}^{\text{sb}}, \end{cases} \tag{2.62}$$

whereas in case of ventilated breathing, we have

$$p_{\text{f}}^{\text{vb}} = p_{\text{vent}}, \tag{2.63}$$

which induces

$$\begin{cases} \underline{\underline{\Sigma}}_{\text{f}}^{\text{vb}} = -\Phi_{\text{f}}\, p_{\text{vent}} J \underline{\underline{C}}^{-1} \\ \underline{\underline{\Sigma}}_{\text{s}}^{\text{vb}} = \underline{\underline{\Sigma}}_{\text{skel}}^{\text{vb}} - (1-\Phi_{\text{f}})\, p_{\text{vent}} J \underline{\underline{C}}^{-1}. \end{cases} \tag{2.64}$$

The main difference is the fluid pressure stress $\underline{\underline{\Sigma}}_{\text{p}}$. Whereas it is zero in case of spontaneous breathing, the fluid pressure is high in ventilated breathing. The skeleton stress $\underline{\underline{\Sigma}}_{\text{skel}}$ is slightly different as the deformation is a bit higher in spontaneous breathing than in ventilated breathing during normal breathing.

The solid stress difference between both types of breathing is illustrated in Figure 2.11. Two simulations were performed using the typical order of magnitude of pressure and volume change for each type of breathing. To do so, the reference stiffness K of the inner surface is tuned to 0.2 kPa. All the parameters used for each simulation are presented in Table 2.5.

The total stress in the solid part $\underline{\underline{\Sigma}}_{\text{s}}$ has then two components: the first one is linked to the skeleton energy and describes the traction coming from the total loading, whereas the second one comes from the fluid pressure which leads to the solid part compression. As both components do not represent the same physical effects, $\underline{\underline{\Sigma}}_{\text{s}}$ is not the relevant quantity to look at in order to study ventilation-induced injuries. Some criterion could be established combining norms of both quantities $\underline{\underline{\Sigma}}_{\text{skel}}$ and $\underline{\underline{\Sigma}}_{\text{p, s}}$ to go into that direction. Moreover, as part of a poromechanical model, stresses are macroscopic and homogenized the microscopic stresses, which are not available directly. To access microscopic stress in the solid part, alveoli geometry could be assumed and such stresses can be computed using the macroscopic deformation. Such microscopic information would provide the most relevant quantities for clinicians to study the impact of mechanical ventilation on the pulmonary tissue.

2.3.6 Pulmonary symphysis

The proposed model also allows to study pathological lung conditions, for instance after a pleural symphysis. A pleural symphysis, where the two pleural membranes are joined together, is performed to prevent pneumothorax from occurring or liquid from accumulating into the pleural space. Consequently, any sliding between the lungs and the thorax becomes impossible.

The simulation of a lung with symphysed pleura can be realized using another type of contact, a tied contact, instead of the frictionless contact as previously used. A comparison between a normal case and this pathological case is now performed. The thorax is fixed and gravity is neglected. The same amount of pressures as well as the same constitutive behavior are applied in both cases. The parameters used are the same for both computations and are reported in Table 2.6.

The results are presented in Figure 2.12. The lung in normal case deforms in the longitudinal direction since the lung can slide against the thorax while the diaphragm pulls on the bottom part of the lung. Conversely, the lung with symphysed pleura cannot deform in the longitudinal direction in the same extent as the healthy lung because of the absence of sliding. However, the pathological lung deforms more in the transverse direction to compensate the absence of sliding. This behavior can explain why it was observed by clinicians that the rib cage diameter in the symphysed lung is higher than in the normal case. Indeed, a larger rib cage would allow the symphysed lung to deform in the only possible direction and to maintain the same ventilation.

2.4 Discussion and conclusions

In contrast to many pulmonary models focusing on air flows [Baffico et al., 2010; Berger et al., 2016], this poromechanical model allows to study the parenchymal stress and strain with the use of an hyperelastic potential describing the skeleton behavior. The non-linear volume response of lungs to a pressure change as well as the solid quasi-incompressibility is well reproduced by the constitutive behavior.

Both effective and absolute mechanical parameters could be used to parametrize the constitutive behavior, depending on whether porosity data are incorporated into the model. Contrary to the effective parameters characterizing the mixture with the effect of the porosity, the absolute parameters characterized the stiffness of the solid tissue. The effective parameters give the same type of porosity-dependent information as the clinical compliance, whereas the absolute parameters bring an additional information which cannot be measured.

Since the constitutive behavior used in the model is non linear and the geometry comes from an *in vivo*, loaded configuration, the unloaded configuration is taken into account. A special attention is paid to ensure the porosity to be positive in the estimated unloaded configuration.

However, the model does not take into account the hysteresis behavior of the lung mechanical behavior, which is commonly attributed to the pulmonary surfactant, present on the alveoli surface [Wiechert, 2011]. An energy describing the surfactant behavior could

		Spontaneous breathing	Mechanical ventilation
Δp_{pl}	[kPa]	$+0.3$	-
Δp_{f}	[kPa]	-	$+3$
ΔV_{air}	[L]	$+0.5$	$+0.3$

Table 2.4 – Order of magnitude of the variation of pressure and fluid volume during a normal inhalation in both types of breathing.

Name	Symbol	Unit	Spontaneous breathing	Mechanical ventilation
End-inhalation air pressure	p_{f}	[kPa]	**0**	**3**
End-exhalation pleural pressure	$p_{\mathrm{pl,e}}$	[kPa]	-0.5	-0.5
End-inhalation pleural pressure	$p_{\mathrm{pl,i}}$	[kPa]	**-0.8**	**-0.5**
Gravity constant	g	[m.s^{-2}]	-	-
Skeleton energy parameters	$\overline{\alpha}$	[kPa]	$8 \cdot 10^{-2}$	$8 \cdot 10^{-2}$
	δ	[-]	0.5	0.5
	$\overline{\beta}_1$	[kPa]	0.1	0.1
	$\overline{\beta}_1$	[kPa]	0.2	0.2
Solid bulk modulus	$\overline{\kappa}$	[kPa]	-	$\mathbf{10^2}$

Table 2.5 – Parameters used for the comparison between spontaneous breathing and ventilated breathing. Top rows corresponds to the loading parameters, fluid pressure and pleural pressures, whereas bottom rows are the components of the constitutive behavior of the pulmonary mixture. The solid bulk modulus is not needed when $p_{\mathrm{f}} = 0$.

Name	Symbol	Unit	Healthy case	Symphysis case
Air pressure	p_{f}	[kPa]	0	0
End-exhalation pleural pressure	$p_{\mathrm{pl,e}}$	[kPa]	-0.5	-0.5
End-inhalation pleural pressure	$p_{\mathrm{pl,i}}$	[kPa]	-2	-2
Gravity constant	g	[m.s^{-2}]	-	-
Sliding type			Frictionless	Tied
Skeleton energy parameters	$\overline{\alpha}$	[kPa]	$8 \cdot 10^{-1}$	$8 \cdot 10^{-1}$
	δ	[-]	0.5	0.5
	$\overline{\beta}_1$	[kPa]	0.1	0.1
	$\overline{\beta}_2$	[kPa]	0.2	0.2
Solid bulk modulus	$\overline{\kappa}$	[kPa]	-	-

Table 2.6 – Parameters used for the comparison between a normal case and a pathological case with a symphysed pleura. Top rows corresponds to the loading parameters, fluid pressure and pleural pressures, whereas bottom rows are the components of the constitutive behavior of the pulmonary mixture. The solid bulk modulus is not needed as $p_{\mathrm{f}} = 0$.

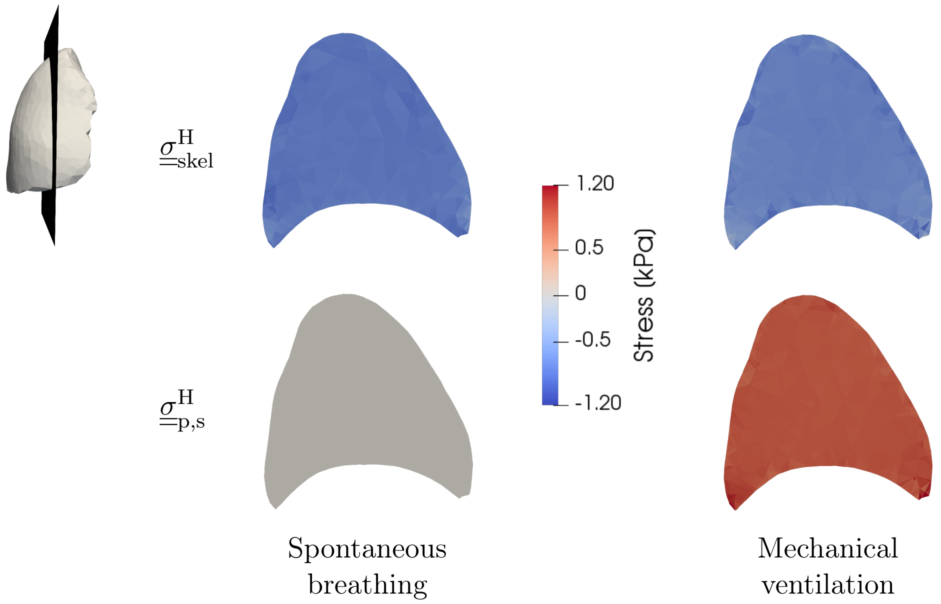

Figure 2.11 – Solid stress components for both types of breathing, spontaneous and ventilated breathing. The quantities represented are the hydrostatic pressure of the solid Cauchy stress tensor, defined as $-\underline{\underline{\sigma}}^{\mathrm{H}} = \frac{1}{3}\,\mathrm{tr}\,\underline{\underline{\sigma}}$, associated with $\underline{\underline{\Sigma}}_{\mathrm{skel}}$ and $\underline{\underline{\Sigma}}_{\mathrm{p,\,s}}$. In case of spontaneous breathing, the skeleton stress is in equilibrium with mixture loading, here the pleural pressure of $-0.8\,\mathrm{kPa}$, and is negative indicating the traction induced by the pleural pressure. In case of ventilated breathing, the skeleton stress is smaller since the deformation is smaller, and $\underline{\underline{\sigma}}^{\mathrm{H}}_{\mathrm{p,s}}$ is positive, showing the compression induced by the fluid pressure imposed by the ventilator.

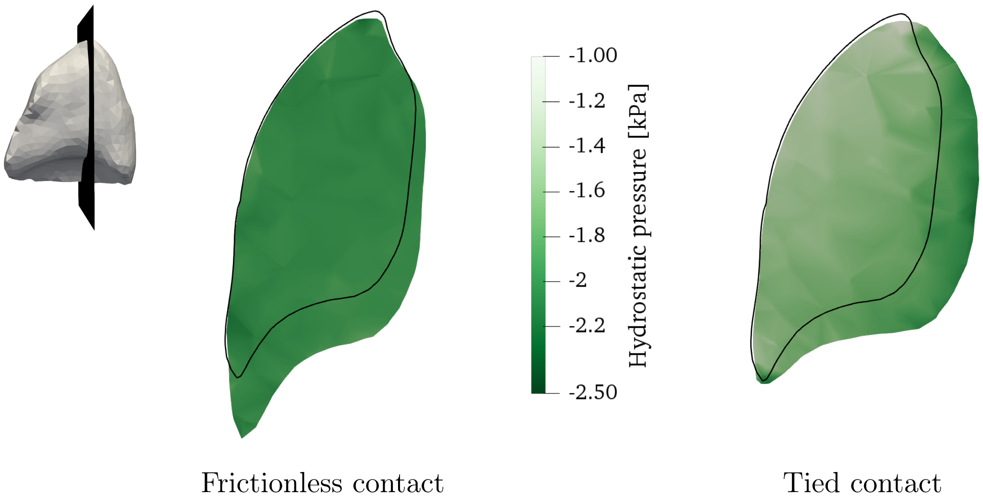

Figure 2.12 – Comparison between two types of contact: the normal case with frictionless contact (left) and the case where pleura is symphysed leading to a tied contact (right). Both cases are shown in a coronal plane. The color scale represents the hydrostatic pressure in kPa. The black line is the surface of the initial configuration.

be incorporated into the solid free energy, in order to improve the model and make it more physiological.

The consideration of the gravity into the model has been illustrated. Nevertheless, it can be improved by applying gravity in the estimation of the unloaded configuration, and not only to compute the deformed configuration. The problem with such boundary conditions (pleural pressure and gravity) is not straightforward because it is ill-posed. Indeed, an infinite number of solutions exist. Boundary conditions should then be better formulated. If gravity is not considered in the unloaded configuration, the model with gravity cannot strictly speaking be used with data like images, since the configuration in medical images involves gravity, but it can be used to study the impact of gravity as comparative modeling.

In the future, this general pulmonary model could be personalized to subjects using clinical data such as images and pressures, and be used for clinical applications. Illustrated here on simple cases, it could be applied in more complex and pathological cases involving mechanics, emphysema or fibrosis for example, in which regional mechanical parameters could be defined instead of homogeneous properties. Applied with a diseased patient, the personalized model could then be used for diagnosis or classification purposes. Another question that such a model could answer is the impact of drugs on the evolution of various diseases, in order to help clinicians to decide on the most appropriate medical treatment.

Acknowledgments

We would like to thank Jean-Francois Bernaudin, Pierre-Yves Brillet, Hilario Nunes and Thomas Gille, clinicians from the Avicenne APHP Hospital for their helpful discussions throughout the development of this work to understand lung physiology and pathologies. We also thank Francois Kimmig for discussions about modeling aspects. This work was supported by the ANR under contract number ANR-10-EQPX-37.

Bibliography

Agostoni, E. (1972). Mechanics of the pleural space. *Physiological Reviews*, 52(1):57–128.

Al-Mayah, A., Moseley, J., Velec, M., and Brock, K. (2011). Toward efficient biomechanical-based deformable image registration of lungs for image-guided radiotherapy. *Physics in Medicine and Biology*, 56(15):4701–4713.

Alnæs, M., Blechta, J., Hake, J., Johansson, A., Kehlet, B., Logg, A., Richardson, C., Ring, J., Rognes, M. E., and Wells, G. N. (2015). The FEniCS Project Version 1.5. *Archive of Numerical Software*, 3(100).

Baffico, L., Grandmont, C., and Maury, B. (2010). Multiscale Modeling of the Respiratory Tract. *Mathematical Models and Methods in Applied Sciences*, 20(01):59–93.

Baudet, V., Villard, P.-F., Jaillet, F., Beuve, M., and Shariat, B. (2003). Towards accurate tumour tracking in lungs. In *Proceedings on Seventh International Conference on Information Visualization, IV 2003.*, pages 338–343. IEEE Comput. Soc.

Berger, L., Bordas, R., Burrowes, K., Grau, V., Tavener, S., and Kay, D. (2016). A poroelastic model coupled to a fluid network with applications in lung modelling: A poroelastic model coupled to a fluid network with applications in lung modelling. *International Journal for Numerical Methods in Biomedical Engineering*, 32(1).

Biot, M. A. (1941). General Theory of Three-Dimensional Consolidation. *Journal of Applied Physics*, 12(2):155–164.

Biot, M. A. and Temple, G. (1972). Theory of Finite Deformations of Porous Solids. *Indiana University Mathematics Journal*, 21(7):597–620.

Bordas, R., Lefevre, C., Veeckmans, B., Pitt-Francis, J., Fetita, C., Brightling, C. E., Kay, D., Siddiqui, S., and Burrowes, K. S. (2015). Development and Analysis of Patient-Based Complete Conducting Airways Models. *Plos One*, 10(12).

Brock, K. K., Sharpe, M. B., Dawson, L. A., Kim, S. M., and Jaffray, D. A. (2005). Accuracy of finite element model-based multi-organ deformable image registration: Accuracy of FEM-based multi-organ deformable image registration. *Medical Physics*, 32(6Part1):1647–1659.

Budiansky, B. and Kimmel, E. (1987). Elastic Moduli of Lungs. *Journal of Applied Mechanics*, 54(2):351–358.

Burrowes, K. S., Iravani, A., and Kang, W. (2019). Integrated lung tissue mechanics one piece at a time: Computational modeling across the scales of biology. *Clinical Biomechanics*, 66:20–31.

Burtschell, B. (2016). *Mechanical Modeling and Numerical Methods for Poromechanics: Application to Myocardium Perfusion.* PhD thesis.

Caruel, M., Chabiniok, R., Moireau, P., Lecarpentier, Y., and Chapelle, D. (2014). Dimensional reductions of a cardiac model for effective validation and calibration. *Biomechanics and Modeling in Mechanobiology*, 13(4):897–914.

Cazeaux, P. and Grandmont, C. (2015). Homogenization of a multiscale viscoelastic model with nonlocal damping, application to the human lungs. *Mathematical Models and Methods in Applied Sciences*, 25(06):1125–1177.

Chabiniok, R., Wang, V. Y., Hadjicharalambous, M., Asner, L., Lee, J., Sermesant, M., Kuhl, E., Young, A. A., Moireau, P., Nash, M. P., Chapelle, D., and Nordsletten, D. A. (2016). Multiphysics and multiscale modelling, data–model fusion and integration of organ physiology in the clinic: Ventricular cardiac mechanics. *Interface Focus*, 6(2):20150083.

Chapelle, D., Gerbeau, J.-F., Sainte-Marie, J., and Vignon-Clementel, I. E. (2010). A poroelastic model valid in large strains with applications to perfusion in cardiac modeling. *Computational Mechanics*, 46(1):91–101.

Chapelle, D. and Moireau, P. (2014). General coupling of porous flows and hyperelastic formulations—From thermodynamics principles to energy balance and compatible time schemes. *European Journal of Mechanics - B/Fluids*, 46:82–96.

Ciarlet, P. and Geymonat, G. (1982). Sur les lois de comportement en élasticité non-linéaire compressible. *C. R. Acad. Sci. Paris Sér. II*, 295:423–426.

Clark, A. R., Kumar, H., and Burrowes, K. (2017). Capturing complexity in pulmonary system modelling. *Proceedings of the Institution of Mechanical Engineers, Part H: Journal of Engineering in Medicine*, 231(5):355–368.

Coussy, O. (2004). *Poromechanics.* Wiley, Chichester.

Dale, P., Matthews, F. L., and Schroter, R. C. (1980). Finite element analysis of lung alveolus. *Journal of Biomechanics*, 13(10):865–873.

Demiray, H. (1972). A note on the elasticity of soft biological tissues. *Journal of Biomechanics*, 5(3):309–311.

Denny, E. and Schroter, R. (2006). A model of non-uniform lung parenchyma distortion. *Journal of Biomechanics*, 39(4):652–663.

Dormieux, L., Kondo, D., and Ulm, F.-J. (2006). *Microporomechanics.* John Wiley & Sons, Chichester, West Sussex, England ; Hoboken, NJ.

Eom, J., Xu, X. G., De, S., and Shi, C. (2010). Predictive modeling of lung motion over the entire respiratory cycle using measured pressure-volume data, 4DCT images, and finite-element analysis: A novel physics-based respiratory modeling for entire breathing cycle. *Medical Physics*, 37(8):4389–4400.

Fuerst, B., Mansi, T., Carnis, F., Salzle, M., Zhang, J., Declerck, J., Boettger, T., Bayouth, J., Navab, N., and Kamen, A. (2015). Patient-Specific Biomechanical Model for the Prediction of Lung Motion From 4-D CT Images. *IEEE Transactions on Medical Imaging*, 34(2):599–607.

Fung, Y. C. (1981). *Biomechanics.* Springer New York, New York, NY.

Gee, M. W., Förster, C., and Wall, W. A. (2010). A computational strategy for prestressing patient-specific biomechanical problems under finite deformation. *International Journal for Numerical Methods in Biomedical Engineering*, 26(1):52–72.

Genet, M. (2019). A relaxed growth modeling framework for controlling growth-induced residual stresses. *Clinical Biomechanics*, 70:270–277.

Genet, M., Chuan Lee, L., Ge, L., Acevedo-Bolton, G., Jeung, N., Martin, A., Cambronero, N., Boyle, A., Yeghiazarians, Y., Kozerke, S., and Guccione, J. M. (2015a). A Novel Method for Quantifying Smooth Regional Variations in Myocardial Contractility Within an Infarcted Human Left Ventricle Based on Delay-Enhanced Magnetic Resonance Imaging. *Journal of Biomechanical Engineering*, 137(8):081009.

Genet, M., Patte, C., and Chapelle, D. (2020). Personalized Pulmonary Poromechanics. *14th World Congress on Computational Mechanics (WCCM).*

Genet, M., Rausch, M., Lee, L., Choy, S., Zhao, X., Kassab, G., Kozerke, S., Guccione, J., and Kuhl, E. (2015b). Heterogeneous growth-induced prestrain in the heart. *Journal of Biomechanics*, 48(10):2080–2089.

Gibson, G. and Pride, N. (1976). Lung distensibility. The static pressure-volume curve of the lungs and its use in clinical assessment. *British Journal of Diseases of the Chest*, 70:143–184.

Govindjee, S. and Mihalic, P. A. (1998). Computational methods for inverse deformations in quasi-incompressible finite elasticity. *International Journal for Numerical Methods in Engineering*, 43(5):821–838.

Han, L., Dong, H., McClelland, J. R., Han, L., Hawkes, D. J., and Barratt, D. C. (2017). A hybrid patient-specific biomechanical model based image registration method for the motion estimation of lungs. *Medical Image Analysis*, 39:87–100.

Hinz, B. and Suki, B. (2016). Does Breathing Amplify Fibrosis? *American Journal of Respiratory and Critical Care Medicine*, 194(1):9–11.

Hurtado, D. E., Villarroel, N., Andrade, C., Retamal, J., Bugedo, G., and Bruhn, A. (2017). Spatial patterns and frequency distributions of regional deformation in the healthy human lung. *Biomechanics and Modeling in Mechanobiology*, 16(4):1413–1423.

Im, J. G., Webb, W. R., Rosen, A., and Gamsu, G. (1989). Costal pleura: Appearances at high-resolution CT. *Radiology*, 171(1):125–131.

Kallet, R. H. (2015). A Comprehensive Review of Prone Position in ARDS. *Respiratory Care*, 60(11):1660–1687.

Kaul, H. (2019). Respiratory healthcare by design: Computational approaches bringing respiratory precision and personalised medicine closer to bedside. *Morphologie*, 103(343):194–202.

Kowalczyk, P. (1993). Mechanical model of lung parenchyma as a two-phase porous medium. *Transport in Porous Media*, 11(3):281–295.

Lai-Fook, S. J. (2004). Pleural Mechanics and Fluid Exchange. *Physiological Reviews*, 84(2):385–410.

Logg, A., Mardal, K., and Wells, G. (2012). *Automated Solution of Differential Equations by the Finite Element Method: The FEniCS Book*. Lecture Notes in Computational Science and Engineering. Springer Berlin Heidelberg.

Milic-Emili, J., Henderson, J. A., Dolovich, M. B., Trop, D., and Kaneko, K. (1966). Regional distribution of inspired gas in the lung. *Journal of Applied Physiology*, 21(3):749–759.

Millar, A. B. and Denison, D. M. (1989). Vertical gradients of lung density in healthy supine men. *Thorax*, 44(6):485–490.

Miserocchi, G. (1997). Physiology and pathophysiology of pleural fluid turnover. *European Respiratory Journal*, 10(1):219–225.

Noppen, M., De Waele, M., Li, R., Gucht, K. V., D'Haese, J., Gerlo, E., and Vincken, W. (2000). Volume and Cellular Content of Normal Pleural Fluid in Humans Examined by Pleural Lavage. *American Journal of Respiratory and Critical Care Medicine*, 162(3):1023–1026.

OMS (2016). The top 10 causes of death in 2016. http://www.who.int/news-room/fact-sheets/detail/the-top-10-causes-of-death.

Osborne, D., Effmann, E., and Hedlund, L. (1983). Postnatal growth and size of the pulmonary acinus and secondary lobule in man. *American Journal of Roentgenology*, 140(3):449–454.

Rausch, M. K., Genet, M., and Humphrey, J. D. (2017). An augmented iterative method for identifying a stress-free reference configuration in image-based biomechanical modeling. *Journal of Biomechanics*, 58:227–231.

Reeve, A. M., Nash, M. P., Taberner, A. J., and Nielsen, P. M. F. (2014). Constitutive Relations for Pressure-Driven Stiffening in Poroelastic Tissues. *Journal of Biomechanical Engineering*, 136(8):081011.

Richardson, S., Gamage, T. P. B., HajiRassouliha, A., Jackson, T., Hedges, K., Clark, A., Taberner, A., Tawhai, M. H., and Nielsen, P. M. F. (2019). Towards a Real-Time Full-Field Stereoscopic Imaging System for Tracking Lung Surface Deformation Under Pressure Controlled Ventilation. In Nielsen, P. M. F., Wittek, A., Miller, K., Doyle, B., Joldes, G. R., and Nash, M. P., editors, *Computational Biomechanics for Medicine*, pages 119–130. Springer International Publishing, Cham.

Sarabia-Vallejos, M. A., Zuñiga, M., and Hurtado, D. E. (2019). The role of three-dimensionality and alveolar pressure in the distribution and amplification of alveolar stresses. *Scientific Reports*, 9(1):8783.

Scheiner, S., Pivonka, P., and Hellmich, C. (2013). Poromechanical Stimulation of Bone Remodeling: A Continuum Micromechanics-Based Mathematical Model and Experimental Validation. In *Poromechanics V*, pages 1867–1876, Vienna, Austria. American Society of Civil Engineers.

Sellier, M. (2011). An iterative method for the inverse elasto-static problem. *Journal of Fluids and Structures*, 27(8):1461–1470.

Sermesant, M., Chabiniok, R., Chinchapatnam, P., Mansi, T., Billet, F., Moireau, P., Peyrat, J., Wong, K., Relan, J., Rhode, K., Ginks, M., Lambiase, P., Delingette, H., Sorine, M., Rinaldi, C., Chapelle, D., Razavi, R., and Ayache, N. (2012). Patient-specific electromechanical models of the heart for the prediction of pacing acute effects in CRT: A preliminary clinical validation. *Medical Image Analysis*, 16(1):201–215.

Seyfi, B., Santhanam, A. P., and Ilegbusi, O. J. (2016). A Biomechanical Model of Human Lung Deformation Utilizing Patient-Specific Elastic Property. *Journal of Cancer Therapy*, 07(06):402–415.

Sundaram, T. A. and Gee, J. C. (2005). Towards a model of lung biomechanics: Pulmonary kinematics via registration of serial lung images. *Medical Image Analysis*, 9(6):524–537.

Tawhai, M. H., Nash, M. P., Lin, C.-L., and Hoffman, E. A. (2009). Supine and prone differences in regional lung density and pleural pressure gradients in the human lung with constant shape. *Journal of Applied Physiology*, 107(3):912–920.

Wang, N.-S. (1975). The Preformed Stomas Connecting the Pleural Cavity and the Lymphatics in the Parietal Pleura. *American Review of Respiratory Disease*, 111(1).

Weibel, E. R. (1965). Morphometry of the Human Lung. *Anesthesiology*, 26(3):367.

Weiss, J. A., Maker, B. N., and Govindjee, S. (1996). Finite element implementation of incompressible, transversely isotropic hyperelasticity. *Computer Methods in Applied Mechanics and Engineering*, 135(1-2):107–128.

Werner, R., Ehrhardt, J., Schmidt, R., and Handels, H. (2009). Patient-specific finite element modeling of respiratory lung motion using 4D CT image data: Finite element modeling of respiratory lung motion. *Medical Physics*, 36(5):1500–1511.

West, J. B. and Matthews, F. L. (1972). Stresses, strains, and surface pressures in the lung caused by its weight. *Journal of Applied Physiology*, 32(3):332–345.

Wiechert, L. (2011). *Computational Modeling of Multi-Field and Multi-Scale Phenomena in Respiratory Mechanics*. PhD thesis.

Wiechert, L. and Wall, W. (2010). A nested dynamic multi-scale approach for 3D problems accounting for micro-scale multi-physics. *Computer Methods in Applied Mechanics and Engineering*, 199(21-22):1342–1351.

Winslow, R. L., Trayanova, N., Geman, D., and Miller, M. I. (2012). Computational Medicine: Translating Models to Clinical Care. *Science Translational Medicine*, 4(158):158rv11.

Zeng, Y. J., Yager, D., and Fung, Y. C. (1987). Measurement of the Mechanical Properties of the Human Lung Tissue. *Journal of Biomechanical Engineering*, 109(2):169–174.

Zhang, T., Orton, N. P., Mackie, T. R., and Paliwal, B. R. (2004). Technical note: A novel boundary condition using contact elements for finite element based deformable image registration. *Medical Physics*, 31(9):2412–2415.

Zocchi, L. (2002). Physiology and pathophysiology of pleural fluid turnover. *European Respiratory Journal*, 20(6):1545–1558.

CHAPTER 3

Estimation of regional pulmonary compliance in IPF based on computational biomechanical modeling

In the third chapter, we first present the personalization pipeline developed for the model based on clinical imaging data. Images are used to personalize geometries using segmentation tools and porosity, as well as to differentiate the healthy and diseased regions and to measure breathing motion. The compliance estimation is formulated as an inverse problem to minimize the difference in breathing motion between model and data. Two cost-functions, exploiting images in two different ways, are investigated. Results are then obtained from patients suffering from IPF. First, the performance of the personalization pipeline is investigated by comparing both cost-functions, the use of two regions and the use of absolute versus effective compliances. Then, relevant quantities are determined and analyzed. Regional compliances are estimated in both healthy and diseased regions, allowing to quantify the IPF-induced tissue stiffening. Correlations between compliance ratio and disease-induced decline are also explored and the impact of IPF on stresses is investigated.
This chapter takes the form of a pre-print article co-authored by Cécile Patte, Pierre-Yves Brillet, Catalin Fetita, Thomas Gille, Jean-Francois Bernaudin, Hilario Nunes, Dominique Chapelle and Martin Genet, entitled *Estimation of regional pulmonary compliance in IPF based on lung poromechanical modeling.*

Contents

Estimation of regional pulmonary compliance in IPF based on lung poromechanical modeling

C. Patte[1,2], P.-Y. Brillet[3,4], C. Fetita[5], T. Gille[3,4], J.-F. Bernaudin[6,3], H. Nunes[3,4], D. Chapelle[1,2], M. Genet[2,1]

[1] Inria, Palaiseau, France, {cecile.patte, dominique.chapelle}@inria.fr
[2] Laboratoire de Mécanique des Solides (LMS), École Polytechnique/CNRS/Institut Polytechnique de Paris, Palaiseau, France, martin.genet@polytechnique.edu
[3] INSERM UMR 1272, Université Paris 13, Bobigny, France
[4] Hôpital Avicenne, APHP, Bobigny, France
[5] ARTEMIS, Telecom SudParis, Institut Polytechnique de Paris, Institut Mines-Telecom, CNRS UMR 8145 - UMR 5157, Evry, France
[6] Médecine Sorbonne Université Paris France

to be submitted

Abstract

Pulmonary function is tightly linked to the lung mechanical behavior, especially large deformation during breathing. Interstitial Lung Diseases, such as Idiopathic Pulmonary Fibrosis (IPF), have an impact on the pulmonary mechanics and consequently alter lung function. However, IPF remains poorly understood, poorly diagnosed and poorly treated. Currently, the mechanical impact of such diseases is assessed by pressure-volume curves, giving only global information. We developed a poromechanical model of the lung that can be partly personalized to a patient based on routine clinical data. The personalization pipeline uses clinical data, mainly CT-images at two timesteps and involves the formulation of an inverse problem to estimate the material behavior. Regional mechanical compliance is estimated for one healthy subject and three patients and the stiffening properties of IPF is assessed. The absolute compliance, characterizing the solid tissue itself without the porosity effect, is also estimated. Such a personalized model could be used by clinicians as an objective and quantitative tool for IPF diagnosis.

Keywords— Pulmonary Mechanics, Poromechanics, Finite Element Method, Image-based Estimation, Simulation

3.1 Introduction

Idiopathic Pulmonary Fibrosis (IPF) is a chronic pulmonary disease with a severe prognosis, affecting the pulmonary interstitium with tissue scarring and leading to tissue thickening and pulmonary microstructure damage. As a consequence, gas exchanges are less efficient because of the thicker alveolar walls. Moreover, lungs become stiffer, impacting lungs function [Plantier et al., 2018]. Patients suffering from IPF are then highly breathless and their difficulties to breathe become worse with the disease evolution. In addition to the mechanical impact of IPF on lungs, mechanics is thought to have a major role in the disease progress. Indeed, a mechanical vicious circle in place in IPF patients has been hypothesized: more fibrosis generates higher stresses, which activates the production of fibers by fibroblasts and then more fibrosis [Hinz and Suki, 2016; Haak et al., 2018]. However, IPF remains poorly understood, poorly diagnosed and poorly treated.

Biomechanical modeling has already been used to help the diagnosis of various diseases, like myocardium infarct detection with the estimation of cardiac contractility [Chabiniok et al., 2012; Genet et al., 2015]. Addressing such applications requires patient-specific models, which have the biophysical characteristics of the patients. Concerning mechanical models, these characteristics are mainly the geometrical description of the organ, but also the specific loading inducing organ deformations and the specific material behavior of the organ. The patient attributes are usually derived from clinical data, like medical imaging, pressures or other relevant measurements.

Mechanical behavior of biological tissues is difficult to personalize. Indeed, contrary to industrial materials that behave as the specifications of design, modulo the uncertainties coming from defects, each individual has different tissue mechanical behavior, which is difficult to characterize directly *in vivo*. It can be characterized *ex vivo*, but this is not viable on patients and can lead to differences from *in vivo*. However, clinical data such as imaging can be used to estimate some parameters of the constitutive law through an inverse problem [Grédiac et al., 2008; Avril and Evans, 2017].

We aim to use our poromechanical model of the lung to tackle diagnosis issues of IPF. To do so, a personalization pipeline was implemented based on available data, provided by the Avicenne APHP hospital, Bobigny, France, and acquired according to the clinical routine procedure for IPF patients. The implementation of an inverse problem is needed to make the model match to the data. Specifically, we investigate two different cost functions: one with a Finite Element Model Updating (FEMU) approach [Hild and Roux, 2006; Avril et al., 2008], the other with an integrated correlation approach [Réthoré et al., 2009; Leclerc et al., 2009]. We intend to assess the pathological features of IPF related to mechanics, *i.e.,* the tissue stiffening and the impact on pulmonary stresses. The mechanical parameters of both healthy and diseased regions are estimated for one reference healthy subject and three diseased patients suffering from IPF.

3.2 Materials and methods

3.2.1 Model

The lung poromechanical model used in this study has been fully described in Patte et al. [2020]. We recall here the main points used in the present work.

3.2.1.1 Direct problem

Poromechanical framework Lungs are porous organs where two phases can be considered: a solid phase, composed of interstitial tissue and blood, and a fluid phase, composed of the air present in airways and alveoli. The porosity $\Phi_{\mathrm{f}0}$ is the volume fraction of the fluid phase in the reference configuration and represents the homogenized microstructure of lungs. In the deformed configuration, the porosity is denoted by ϕ_{f}. The lung density in the reference configuration is then $\overline{\rho}_0 = \rho_{\mathrm{s}0}\left(1 - \Phi_{\mathrm{f}0}\right) + \rho_{\mathrm{f}0}\Phi_{\mathrm{f}0}$, where $\rho_{\mathrm{s}0}$ and $\rho_{\mathrm{f}0}$ are the reference densities of the solid phase and the fluid phase, respectively. During lung deformation, fluid is added to the mixture, as air enters the lungs during inhalation and goes out during exhalation. The added fluid mass per unit volume of the reference configuration is denoted by $\overline{\rho}_{\mathrm{f}+}$.

During breathing, lungs are subjected to an internal fluid pressure p_f, which is the pressure in airways and alveoli, as well as external loadings, like gravity $\underline{g}$ or surface loadings $\underline{T}$ in the reference configuration.

The lung transformation from a reference configuration (Ω_0, Γ_0) to a deformed configuration (ω, γ) is described by the mapping $\underline{\chi}$:

$$\underline{\chi} : \begin{cases} \Omega_0 \to \omega \\ \underline{X} \mapsto \underline{x} = \underline{\chi}\left(\underline{X}, t\right) \end{cases} \tag{3.1}$$

The associated displacement field $\underline{U}$ is

$$\underline{U}(\underline{X}, t) := \underline{x} - \underline{X} \tag{3.2}$$

and the deformation gradient $\underline{\underline{F}}$ is

$$\underline{\underline{F}}(\underline{X}, t) := \underline{\underline{\nabla}}\,\underline{\chi} = \underline{\underline{\nabla}}\,\underline{U} + \underline{\underline{\mathbb{1}}}. \tag{3.3}$$

The local volume change of the mixture is given by $J := \det \underline{\underline{F}}$. The quantities $\Phi_\mathrm{s} := (1 - \phi_\mathrm{f}) \cdot J$ and $\Phi_\mathrm{f} := \phi_\mathrm{f} \cdot J$, such that $\Phi_\mathrm{f} = J - \Phi_\mathrm{s}$, are the contributions of the solid and the fluid phases to J, respectively. The rotation-independent right Cauchy-Green deformation tensor $\underline{\underline{C}}$, defined as $\underline{\underline{C}} := \underline{\underline{F}}^T \cdot \underline{\underline{F}}$, and its three invariants, $I_1 := \operatorname{tr} \underline{\underline{C}}$, $I_2 := \frac{1}{2}\left(\left(\operatorname{tr} \underline{\underline{C}}\right)^2 - \operatorname{tr}\left(\underline{\underline{C}}^2\right)\right)$ and $I_3 := \det \underline{\underline{C}} = J^2$, are more commonly used to describe deformations. Finally, $\underline{\underline{E}}$ is the Green-Lagrange strain tensor:

$$\underline{\underline{E}} := \frac{1}{2}\left(\underline{\underline{C}} - \underline{\underline{\mathbb{1}}}\right). \tag{3.4}$$

The main quantities are represented on a scheme in Figure 3.1.

Hypotheses for the pulmonary settings Lungs can be described by mixture theories [Biot and Temple, 1972; Coussy, 2004], especially that of Chapelle and Moireau [2014] that is compatible with large displacements as required by pulmonary modeling. The fluid is assumed to be incompressible so that $\varrho_\mathrm{f} = \rho_\mathrm{f0}$, with ϱ_f the current fluid density, [Baffico et al., 2010] and the transformation is considered to be under isothermal conditions. In addition to these two general assumptions, two lung-specific hypotheses are formulated: the transformation during breathing is quasi-static and the internal fluid pressure p_f is homogeneous and given, equal to the atmospheric pressure in free breathing ($p_\mathrm{f} = p_\mathrm{atm} \simeq 0$) or imposed by the ventilator in case of ventilated breathing ($p_\mathrm{f} = p_\mathrm{vent}$). In the present work, as only spontaneous cases are studied, the fluid pressure is then taken to be 0.

Mixture constitutive framework The Helmholtz free energy of the mixture $\overline{\psi}$ is decomposed into a solid part and a fluid part:

$$\overline{\psi}\left(\underline{\underline{E}}, \overline{\rho}_{\mathrm{f}+}\right) = \overline{\psi}_\mathrm{s}\left(\underline{\underline{E}}, \Phi_\mathrm{s}\right) + \overline{\psi}_\mathrm{f}\left(\Phi_\mathrm{f}\right), \tag{3.5}$$

where $\overline{\psi}_\mathrm{s}$ and $\overline{\psi}_\mathrm{f}$ are the free energies of the solid and the fluid phase respectively. Since the second Piola-Kirchhoff stress tensor $\underline{\underline{\Sigma}}$ derives from $\overline{\psi}$, we have:

$$\underline{\underline{\Sigma}} = \frac{\partial \overline{\psi}\left(\underline{\underline{E}}, \overline{\rho}_{\mathrm{f}+}\right)}{\partial \underline{\underline{E}}} = \frac{\partial \overline{\psi}_\mathrm{s}}{\partial \underline{\underline{E}}} + \frac{\partial \overline{\psi}_\mathrm{s}}{\partial \Phi_\mathrm{s}} J \underline{\underline{C}}^{-1}. \tag{3.6}$$

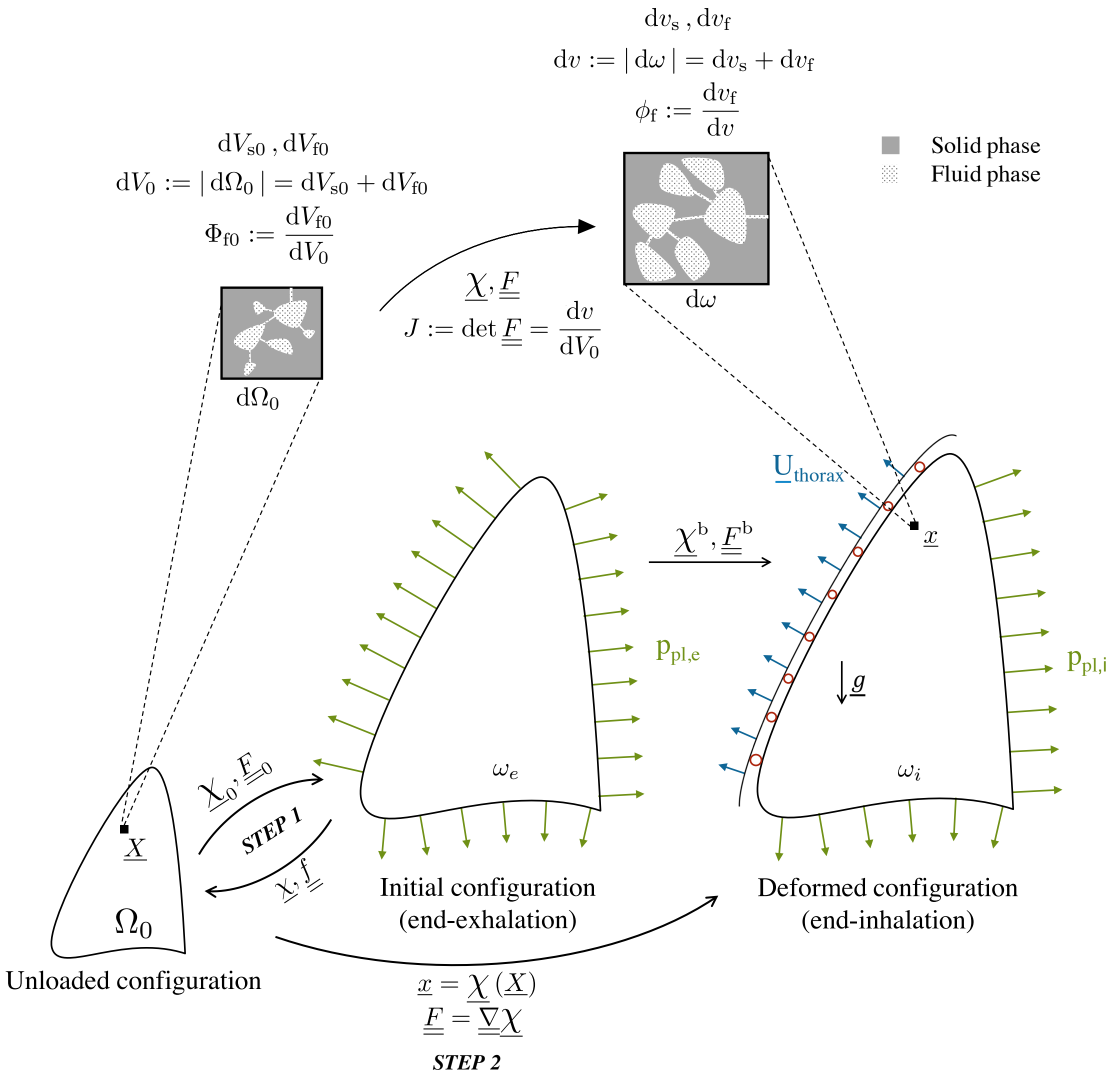

Figure 3.1 – Schematic representation of the main quantities describing the system and the boundary conditions considered in the mechanical problem.

Problem formulation Under the previously mentioned hypotheses, lung poromechanical behavior is described by the following system:

$$\text{Find } \left(\underline{U}, \Phi_{\mathrm{f}}\right), \\ \begin{cases} \forall \underline{U}^*, \displaystyle\int_{\Omega} \frac{\partial \overline{\psi}_{\mathrm{s}}}{\partial \underline{\underline{E}}} : \mathrm{d}_{\underline{U}}\, \underline{\underline{E}}.\underline{U}^*\, \mathrm{d}\Omega_0 = W_{\mathrm{ext}} + \displaystyle\int_{\Omega} p_{\mathrm{f}} J \underline{\underline{C}}^{-1} : \mathrm{d}_{\underline{U}}\, \underline{\underline{E}}.\underline{U}^*\, \mathrm{d}\Omega_0 \\ p_{\mathrm{f}} = -\dfrac{\partial \overline{\psi}_{\mathrm{s}}}{\partial \Phi_{\mathrm{s}}}, \end{cases} \tag{3.7}$$

where W_{ext} is the virtual work of external forces. The first equation is the mechanical equilibrium of the pulmonary mixture. Assuming the previous hypotheses, the pulmonary mixture behaves as a non porous solid with an extra loading representing the action of the fluid pressure as a following pressure applied on the surface of the mixture. In poromechanics, it is classically used that the hydrostatic pressure in the solid phase is equal to the fluid pressure since both phases are equilibrated. It gives the second equation, which links the porosity to the given fluid pressure and the deformation.

3.2.1.2 Solid constitutive behavior

The following decomposition of the solid free energy $\overline{\psi}_{\mathrm{s}}$ is proposed as in [Chapelle and Moireau, 2014]:

$$\overline{\psi}_{\mathrm{s}} = \overline{W}_{\mathrm{skel}}\left(\underline{\underline{E}}\right) + \overline{W}_{\mathrm{bulk}}\left(\Phi_{\mathrm{s}}\right) \tag{3.8}$$

where $\overline{W}_{\mathrm{skel}}\left(\underline{\underline{E}}\right)$ is the free energy of the solid considered as a structure and $\overline{W}_{\mathrm{bulk}}\left(\Phi_{\mathrm{s}}\right)$ describes the compressibility of the solid phase. We propose the following energies:

$$\begin{cases} \overline{W}_{\mathrm{skel}}\left(\underline{\underline{E}}\right) = \overline{\alpha}\left(\mathrm{e}^{\delta\left(J^2-1-2\ln(J)\right)} - 1\right) + \overline{\beta}_1\left(I_1 - 3 - 2\ln(J)\right) + \overline{\beta}_2\left(I_2 - 3 - 4\ln(J)\right) \\ \overline{W}_{\mathrm{bulk}}\left(\Phi_{\mathrm{s}}\right) = \overline{\kappa}\left(\dfrac{\Phi_{\mathrm{s}}}{1-\Phi_{\mathrm{f0}}} - 1 - \ln\left(\dfrac{\Phi_{\mathrm{s}}}{1-\Phi_{\mathrm{f0}}}\right)\right) \end{cases} \tag{3.9}$$

where $\overline{\alpha}, \overline{\beta}_1, \overline{\beta}_2, \delta, \overline{\kappa}$ are some material parameters. $\overline{\kappa}$ is the solid bulk modulus, which should be taken large to ensure quasi-incompressibility of the solid part. These parameters represent the effective behavior of the solid part of the mixture, which depends on the porosity of the mixture. Assuming a linear relation between the effective and the absolute behavior of the solid, we have:

$$\overline{\psi}_{\mathrm{s}} = \left(1 - \Phi_{\mathrm{f0}}\right)\widetilde{\psi}_{\mathrm{s}}, \tag{3.10}$$

which leads to

$$\begin{cases} \overline{W}_{\mathrm{skel}}\left(\underline{\underline{E}}\right) = \left(1 - \Phi_{\mathrm{f0}}\right)\widetilde{W}_{\mathrm{skel}}\left(\underline{\underline{E}}\right) \\ \overline{W}_{\mathrm{bulk}}\left(\Phi_{\mathrm{s}}\right) = \left(1 - \Phi_{\mathrm{f0}}\right)\widetilde{W}_{\mathrm{bulk}}\left(\Phi_{\mathrm{s}}\right), \end{cases} \tag{3.11}$$

where $\widetilde{\psi}_{\mathrm{s}}$, $\widetilde{W}_{\mathrm{skel}}$ and $\widetilde{W}_{\mathrm{bulk}}$ are the absolute free energies per unit solid mass, corresponding to the effective free energies $\overline{\psi}_{\mathrm{s}}$, $\overline{W}_{\mathrm{skel}}$, $\overline{W}_{\mathrm{bulk}}$ respectively. The effective mechanical parameters $\overline{\theta}$ and the absolute mechanical parameters $\widetilde{\theta}$ are then linked by:

$$\overline{\theta} = \left(1 - \Phi_{\mathrm{f0}}\right)\widetilde{\theta} \quad \text{for } \overline{\theta} \in \left\{\overline{\alpha}, \overline{\beta}_1, \overline{\beta}_2, \overline{\kappa}\right\} \tag{3.12}$$

The parameter δ remains the same in both effective and absolute behavior since it describes the non-linear part of the energy $\overline{\psi}_{\mathrm{s}}$.

Compliance We define the compliance of one lung between two mechanical states t_0 and t_1 as the lung volume change divided by the pressure change between these two states:

$$C_{\mathrm{t_0\to t_1}} = \frac{V_{\mathrm{t_1}} - V_{\mathrm{t_0}}}{p_{\mathrm{pl,t_1}} - p_{\mathrm{pl,t_0}}} = \frac{V_{\mathrm{t_0}}\left(\dfrac{J_{t_1}}{J_{t_0}} - 1\right)}{p_{\mathrm{pl,t_1}} - p_{\mathrm{pl,t_0}}} \tag{3.13}$$

In what follows, the compliance will be denoted by C to refer to the compliance between the end-exhalation and end-inhalation state for a normal breathing at rest, *i.e.,* when the pleural pressure value is 0.5 kPa and 0.8 kPa, respectively. In the case of absolute parameters, the porosity used to compute the compliance is 0 ($\Phi_{\mathrm{f0}} = 0$) to reflect the absolute compliance of the non-porous interstitial tissue.

3.2.1.3 Boundary conditions

The initial configuration corresponds to the end-exhalation configuration and the deformed configuration to the end-inhalation configuration. Since the constitutive behavior of the solid phase is non linear and the initial configuration is loaded, the unloaded configuration should be determined. The computation of breathing from the initial to the deformed configuration should be performed in two steps:

1. first, the computation of the unloaded configuration from the initial configuration, which allows to deduce the reference porosity field and the initial stress field,
2. then, the computation of the deformed configuration knowing the unloaded configuration.

Step 1 is an inverse problem which is fully described in Patte et al. [2020] , where the unknown unloaded configuration corresponds to a pneumothorax. The boundary conditions used for this step are only the negative pleural pressure on the whole surface of the lung. The rigid body motion is also blocked using three nodes defining the best trihedron in the mesh.

The boundary conditions in Step 2 are more complex since breathing involves a complex environment (pleura, diaphragm, intercostal muscles...). In addition to the negative pleural pressure on the whole surface of the lung, a contact between the lung surface and the thorax surface is considered. This contact is assumed to be frictionless and with no separation of the surfaces once they are in contact. The thorax displacement is also taken into account. Finally, the gravity can also be imposed.

The boundary conditions of both steps are summarized in Figure 3.1.

3.2.1.4 Implementation

The estimation of the reference configuration (Step 1 of the direct problem) is computed using the method of Govindjee and Mihalic [1998], which has been implemented in python with the FEniCS library [Alnæs et al., 2015; Logg et al., 2012]. Step 2 is computed with the Abaqus software. The contact is defined as a master-slave, finite-sliding and node-to-surface. The master surface and the slave surface, *i.e.,* the thorax surface and the lung surface, respectively, are adjusted at the start of the simulation to remove gaps and overclosures.

3.2.2 Data

Patient data are needed to personalize the above pulmonary poromechanical model. Given the clinical data that can be acquired from a patient, two kinds of data can be used: image and pressure.

3.2.2.1 Synthetic data for validation

In order to validate the mechanical parameters estimation process, which corresponds to the material part of the model personalization, we generate two kinds of synthetic data, displacements and images, for both proposed cost functions. All the elements of the model are chosen: the lung and thorax geometries, a lung partition into two regions, the pleural pressure, the thorax displacements, the material parameters and the porosity.

Synthetic displacements The lung is deformed using the lung poromechanical model described before and the resulting displacement field $\underline{U}_{\text{DIC,synth}}$ will be used as data in the cost function f_{DIC}.

Synthetic images Two images are generated, an initial image $I_{e,\text{synth}}$ and a deformed image $I_{i,\text{synth}}$, corresponding to the end-exhalation and the end-inhalation configurations respectively, to be used as data in the cost function f_{image}. The intensity field of $I_{e,\text{synth}}$ is

$$I_{e,\text{synth}}\left(\underline{X}\right) = \begin{cases} 0 & \text{if } \underline{X} \notin \Omega \\ \left|\sin \dfrac{\pi X_0}{s}\right| \left|\sin \dfrac{\pi X_1}{s}\right| \left|\sin \dfrac{\pi X_2}{s}\right| & \text{if } \underline{X} \in \Omega, \end{cases} \tag{3.14}$$

with X_0, X_1, X_2 the three spatial coordinates of $\underline{X}$ and $s = \frac{1}{3}$ the tagging period. This is the simplest model of tagged MRI, which we use here for its good tracking properties [Škardová et al., 2019]. Such an intensity field means that the image is textured only in the lung volume, and the intensity field of $I_{i,\text{synth}}$ is

$$I_{i,\text{synth}}\left(\underline{x}\right) = I_{e,\text{synth}}\left(\underline{\chi}_{\text{synth}}\left(\underline{x}\right)\right) \tag{3.15}$$

where $\underline{\chi}_{\text{synth}}$ is the transformation associated with the synthetic displacements $\underline{U}_{\text{DIC,synth}}$.

3.2.2.2 Clinical data

Clinical data from one patient without pulmonary disease and normal thoracic scan, which will be called in the following as "healthy subject", and three patients suffering from Idiopathic Pulmonary Fibrosis (IPF) are considered. All the data come from the Avicenne Hospital, Bobigny, APHP.

Images Medical imaging techniques like X-rays, CT (Computed Tomography) scans, MRI (Magnetic Resonance Imaging) and US (Ultrasound) can all be used for lung imaging depending on the need. CT scans are mainly used to image patients suffering from diseases involving mechanics, such as IPF, for the high resolution of the image.

CT scans acquisition were performed for each subject of the study, in the supine position, with the arms above the head and holding breath during the image acquisition. For the purpose of the model, and since it is permitted by the clinical routine [Cottin et al., 2013], two 3D CT scans are acquired, one at full exhalation I_e and one at full inhalation I_i. Details about the characteristics of the images are reported in Table 3.1.

Volume lung displacements by image registration The volume lung displacements $\underline{U}_{\text{DIC}}$ is computed from the two images I_e and I_i with a finite element image registration method [Genet et al., 2016, 2018].

Lung image registration involves several difficulties. First, the large displacements of lungs during breathing, since the lower part is pulled by the diaphragm by several

Subject	Sex	Age	Timestep	Image resolution [mm^3]	Image size [pixels]
Healthy 1 (H1)	M	72	E	$0.636719 \times 0.636719 \times 0.7$	$512 \times 512 \times 455$
			I	$0.720703 \times 0.720703 \times 0.7$	$512 \times 512 \times 455$
Patient 1 (P1)	M	67	E	$0.660156 \times 0.660156 \times 0.7$	$512 \times 512 \times 446$
			I	$0.660156 \times 0.660156 \times 0.7$	$512 \times 512 \times 446$
Patient 2 (P2)	M	61	E	$0.693359 \times 0.693359 \times 0.7$	$512 \times 512 \times 396$
			I	$0.693359 \times 0.693359 \times 0.7$	$512 \times 512 \times 396$
Patient 3 (P3)	F	66	E	$0.681641 \times 0.681641 \times 0.7$	$512 \times 512 \times 475$
			I	$0.615234 \times 0.615234 \times 0.7$	$512 \times 512 \times 423$

Table 3.1 – Characteristics of images used to personalize the model for each subject. For the “Sex” column, F and M stands for Female and Male, respectively. For the “Timestep” column, E and I stands for end-exhalation and end-inhalation, respectively. The patient age in the third column is given in years.

centimeters, cause difficulties to track motion. Secondly, displacement field between both images is not smooth as the lung is sliding against the thorax [Vishnevskiy et al., 2017]. The discontinuity in the displacement field occurring at the interface can result in errors in the lung displacements, mainly in the lung zone close to the surface.

The lung image registration is performed in two steps:

- Lungs are segmented in the 3DCT images I_e and I_i using the algorithm described in Fetita et al. [2016] and two lung binary masks $M_{l,e}$ and $M_{l,i}$ are computed from I_e and I_i respectively. The displacements of the lung shape $\underline{U}_{\text{shape}}$ are then computed by image registration between $M_{l,e}$ and $M_{l,i}$.
- Two images $IM_{l,e}$ and $IM_{l,i}$ are computed as the multiplication of the lung mask M_l and the CT image I, such as pixels inside lungs are textured as in the CT image and pixels out of lungs are 0. The displacement field $\underline{U}_{\text{shape}}$ computed from the first step is then used as a first guess for the image registration between $IM_{l,e}$ and $IM_{l,i}$, which computes the complete lung volume displacement field $\underline{U}_{\text{DIC}}$. This second step is performed on textured mask IM_l to make the result independent from the lung surroundings. Indeed, the image registration is computed using the lung mesh, on which a boundary layer of elements is added by extrusion of the surface. The additional elements layer is needed to track the shape well and the pixels inside the layer are taken into account for the registration.

I, M_l and IM_l can be seen in Figure 3.2 both for end-exhalation and for end-inhalation. The registration process is done for each lung separately.

Pressures Pleural pressure data could also bring useful information for the model. Pleural pressure can be measured directly when placing a drain in case of pneumothorax for example, but the process is highly invasive and is not performed in routine for diseases like IPF. Another way to get the pleural pressure is the esophageal pressure measure using an esophageal balloon, which is considered as a good approximation of the pleural pressure [Gibson and Pride, 1976]. The esophageal pressure measure is not done routinely either. Pleural pressure is then difficult to measure, since it implies invasive procedures.

Consequently, no personalized pressure is used in this work and arbitrary pressures need to be chosen. All the results are then relative to these chosen pressures.

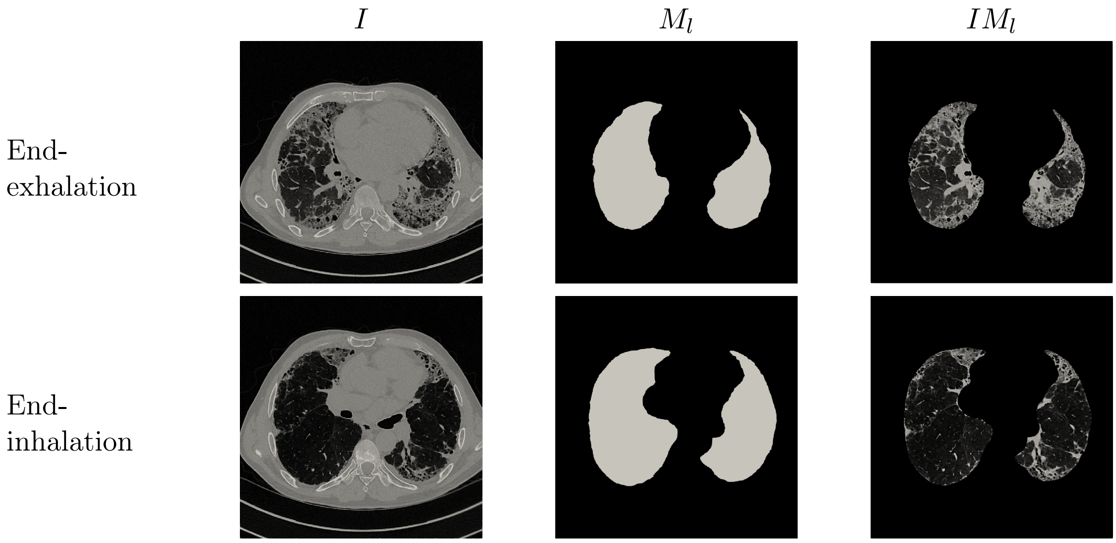

Figure 3.2 – Visualization of the different images used in the whole process of image registration. I are the raw images, M_l are the binary images computed the segmentation of lungs on I, IM_l are the multiplication between I and M_l. The first step of the image registration consists in correlating lung shape between $M_{l,e}$ and $M_{l,i}$. Then lung volume is correlated during the second step using $IM_{l,e}$ and $IM_{l,e}$

3.2.3 Personalization procedure

Using the data previously mentioned, the components of the poromechanical model, i.e., lung and thorax geometries, the boundary conditions, the porosity field and the mechanical parameters, can be personalized to a subject profile. The whole model personalization pipeline is illustrated in Figure 3.3 and each step is detailed in the following paragraphs.

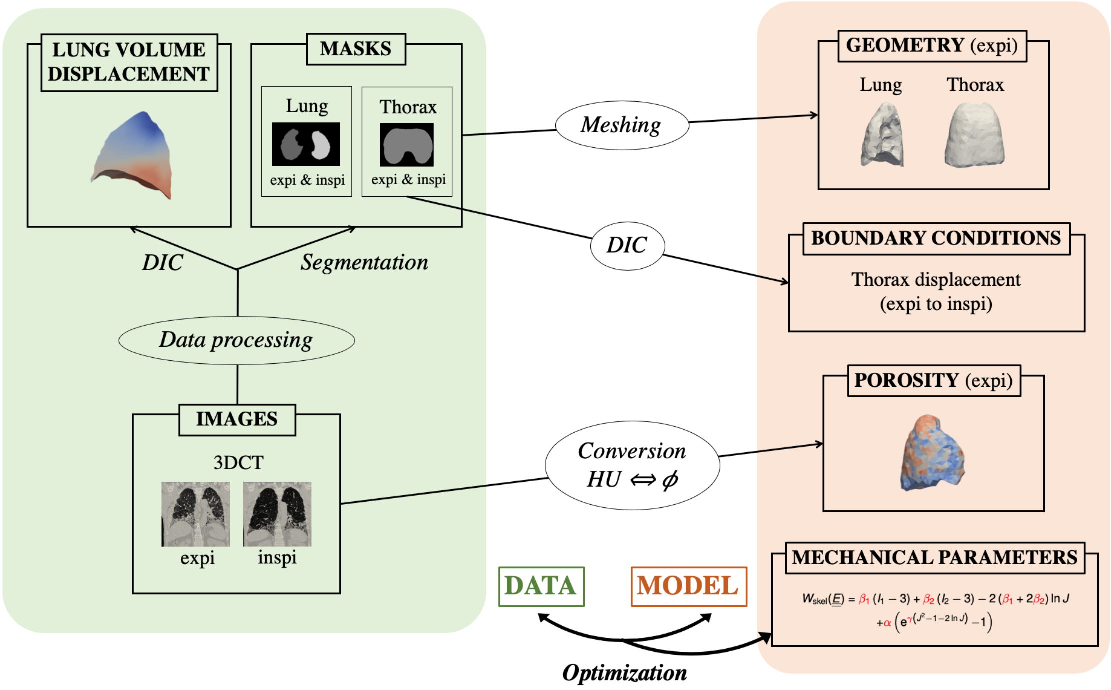

Figure 3.3 – Summary of the personalization pipeline.

3.2.3.1 Patient-specific geometry

Both lung and thorax patient-specific geometries used in the model are 3D finite element meshes, *i.e.,* a volume mesh for the lungs, and a surface mesh for the thorax. Both are generated from the image I_e at end-exhalation.

The lungs are segmented in the 3DCT image I_e using the algorithm described in Fetita et al. [2016] resulting in a lung mask $M_{l,e}$. Healthy lungs, mainly composed of air, are easily distinguishable in CT scans as they match with the darker zones, highly contrasted with the surrounding organs of light intensity. This algorithm is specifically developed for the segmentation of fibrotic lungs where segmentation difficulties are encountered in diseased zones, since fibrotic parts, composed of more tissue, are lighter and have an intensity close to that of the lung surroundings. Lung surface is then extracted from the lung mask $M_{l,e}$ with the software MeVisLab and is used to generate a surface mesh and then a volume mesh using tetrahedral elements with the software Gmsh [Remacle et al., 2009; Geuzaine and Remacle, 2009].

For the rib cage finite element model, only a surface is required. The rib cage shape is manually segmented with MeVisLab in the same image I_e as the lung in order to generate a rib cage surface matching with the lung surface in the contact area between rib cage and lung. The thorax mask $M_{t,e}$ is then generated and the thorax surface is extracted. The rib cage surface is then discretized using shell elements.

3.2.3.2 Disease segmentation

The lungs areas affected by the disease are recognizable since they are lighter than the healthy ones. These areas are manually segmented using the ITK-SNAP software. Then the segmentation is validated by a radiologist. The segmentation is applied on the mesh in a binary way for each element: if more than 50 % of the element is in the healthy area, this element is considered as healthy, otherwise it is considered as diseased. At the end, the mesh is composed of two regions, where different mechanical behavior can be chosen.

3.2.3.3 Patient-specific boundary conditions

Several boundary conditions are prescribed: the pleural pressure, the thorax displacement and a frictionless, permanent contact between lung and thorax surface. The first two can be personalized: thorax displacement and pleural pressure.

As was already mentioned, no pressure data are used in this study. Consequently, pleural pressure is chosen arbitrarily and results are relative to the chosen pleural pressure.

Thorax surface displacements $\underline{U}_{\text{thorax}}$ are computed by image registration between thorax masks at the end-exhalation $M_{t,e}$ and at the end-inhalation $M_{t,i}$. The end-exhalation mask $M_{t,e}$ is obtained during the thorax geometry process from I_e, whereas the deformed mask $M_{t,i}$ is obtained after the manual thorax segmentation on I_i. The displacement field computed is the thorax shape change. Since frictionless sliding is allowed in the model, the exact thorax surface displacements are not necessary.

3.2.3.4 Patient-specific porosity

Porosity information can be computed from CT images [Hedlund et al., 1983]. Indeed, CT technique measures the attenuation of X-rays by tissue, hence the contrast in CT images comes from a difference in tissue density. CT image pixels are displayed according to the mean attenuation of the tissue volume that they represent formulated in the Hounsfield Units (HU) scale. Typically, water and air have an attenuation of 0 HU and −1000 HU respectively.

Considering a linear variation of porosity with HU, the local porosity can be computed for each pixel with the following expression:

$$\phi_{\mathrm{f}}(\underline{x}) = \frac{HU(\underline{x}) - HU_{\mathrm{tissue}}}{HU_{\mathrm{air}} - HU_{\mathrm{tissue}}}, \tag{3.16}$$

with $HU_{\mathrm{tissue}} = 0\,\mathrm{HU}$ considering that biological tissues are mainly composed of water and $HU_{\mathrm{air}} = -1000\,\mathrm{HU}$.

The porosity field, constant by pixel, is then projected into a porosity field constant by element: the value for one element is taken as the mean of the pixel values for all the pixels inside this element. This projection is performed using VTK[1] as described in [Genet et al., 2015]. The initial porosity field is computed using the image I_e.

3.2.3.5 Patient-specific compliance

Problem Patient-specific mechanical parameters of the skeleton energy $\overline{W}_{\mathrm{skel}}$ are estimated using the above lung poromechanical model and clinical data. This inverse problem is an optimization problem, in which the solution is the set of mechanical parameters Θ minimizing the cost function f, describing the error between the model and the data:

$$\Theta = \underset{\theta}{\operatorname{argmin}}\, f(\theta). \tag{3.17}$$

Thus, the model best fits the data for the set of parameters Θ solution of the optimization problem.

Cost function f Two different cost functions are investigated, differing by the nature of the data considered, either the displacement field computed by image registration or the raw images directly.

The first one compares the displacement field $\underline{U}_{\mathrm{model}}(\theta)$ computed with the model for a given set of parameters θ with the displacement field $\underline{U}_{\mathrm{DIC}}$ computed by image registration. It corresponds to the following expression:

$$f_{\mathrm{DIC}}(\theta) = \frac{\|\underline{U}_{\mathrm{model}}(\theta) - \underline{U}_{\mathrm{DIC}}\|_{L^2}}{\|\underline{U}_{\mathrm{DIC}}\|_{L^2}} \tag{3.18}$$

This intuitive approach is also called Finite Element Model Updating (FEMU) and uses the measurement of the kinematic field variable [Hild and Roux, 2006; Avril et al., 2008; Azzouna et al., 2013].

The second cost function partly corresponds to an integrated image correlation approach [Réthoré et al., 2009; Leclerc et al., 2009]. It is composed of two terms weighted by the factor k: f_{reg} is the same energy that is minimized during image registration, comparing image intensities, and f_{shape} quantifies the similarity between the computed and the measured deformed shapes.

$$\begin{aligned} f_{\mathrm{image}}(\theta) &= f_{\mathrm{reg}}(\theta) + k f_{\mathrm{shape}}(\theta) \\ &= \frac{\left\| M_{l,e} M_{l,i} \left(I_i \circ \underline{\chi}_{\mathrm{model}}(\theta) - I_e \right) \right\|_{L^2}}{\left\| M_{l,e} M_{l,i} I_e \right\|_{L^2}} + k\, DICE(\theta), \end{aligned} \tag{3.19}$$

The shape term f_{shape} is needed mainly for fibrosis cases. Indeed, as was already mentioned, the fibrotic parts and lung surroundings have a close pixel intensity. Then, the lung shape

---

[1] http://www.vtk.org

resulting from the estimation process tends to be overinflated. The shape term is computed using the Dice coefficient [Taha and Hanbury, 2015] between two binary images, $M_{l,i}$ coming from the lung segmentation of I_i and $M_{l,i,\text{model}}(\theta)$ masking I_i with the deformed mesh surface computed with the model for a given set of parameters θ, and is defined as:

$$f_{\text{shape}}\left(M_{l,i}, M_{l,i,\text{model}}(\theta)\right) = \frac{2TP}{2TP + FP + FN}, \tag{3.20}$$

where TP, FP and FN are the true positives, the false positives and the false negatives respectively. In the image registration term f_{reg}, the use of the factor $M_{l,e}M_{l,i}$ implies that only the pixels corresponding to the lung area are taken into account, which makes f_{reg} independent from the surrounding area of the image. Computing the cost function f_{image} using I or IM_l will then give the same result. The choice of the weight factor k is made in such a way as to equilibrate the variation of each term of f_{image}.

Estimated parameters Θ Either the effective parameters $\overline{\Theta} = \left\{\overline{\alpha}, \overline{\beta}_1, \overline{\beta}_2, \delta\right\}$ or the absolute parameters $\widetilde{\Theta} = \left\{\widetilde{\alpha}, \widetilde{\beta}_1, \widetilde{\beta}_2, \delta\right\}$ can be estimated: the estimation of the absolute parameters requires a porosity field Φ_{f0} contrary to the estimation of the effective parameters. However, the estimation of four parameters with such data (images at only two different timesteps) is ill-posed. Consequently, only the parameters corresponding to the stiffness, $\widetilde{\Theta} = \{\widetilde{\alpha}\}$ or $\overline{\Theta} = \{\overline{\alpha}\}$, are estimated and the others are set.

The parameters are taken homogeneous by regions. A region is defined as a set of elements. In this study, the lung is considered as composed of either one or two regions, but there is no restriction to consider more than two regions. When two regions are defined, the partition can either be arbitrary, *e.g.,* be defined by a plane cutting the lung geometry in half, mostly used for validation purposes, or match with the segmentation of the disease, one region being the healthy part and the other the diseased part.

Implementation The optimization process is solved using the stochastic derivative-free numerical optimization algorithm called CMA-ES [Hansen and Auger, 2014; Hansen, 2016], which evaluates the direct problem several times with different sets of parameters. For each evaluation of the direct problem, a set of parameters is considered and both steps described in Section 3.2.1 are computed, *i.e.,* the estimation of the unloaded configuration and the computation of the deformed configuration. At each iteration, the evaluations of the cost function are performed in parallel.

3.3 Results

In this section, we present results with both synthetic data and clinical data with four subjects, one healthy subject and three patients suffering from IPF. All the simulations are performed under the free breathing assumption ($p_{\text{f}} = 0$) since all subjects studied were breathing freely. Moreover, gravity is neglected and the pleural pressure is considered as homogeneous on the whole lung surface. Unless specific values are mentioned in the following paragraphs, the model parameters used in the simulations are presented in Table 3.2.

3.3.1 Results with *in silico* data

This section focuses on results with synthetic data. The personalized model of the subject P1 is used (geometry, boundary conditions and porosity). However, the data used in the estimation pipeline, either lung displacements or images, are synthetic.

			Simulations with effective parameters	Simulations with absolute parameters
Loading	p_f	[kPa]	0	
	$p_\mathrm{pl,e}$	[kPa]	-0.5	
	$p_\mathrm{pl,i}$	[kPa]	-1.85	
Material	$\overline{\beta}_1$	[kPa]	0.1	-
	$\overline{\beta}_2$	[kPa]	0.2	-
	$\widetilde{\beta}_1$	[kPa]	-	0.2
	$\widetilde{\beta}_2$	[kPa]	-	0.4
	δ	[-]	0.5	0.5

Table 3.2 – Model parameters used in simulations, with either the effective parameters or the absolute parameters. The parameters are p_f the fluid pressure, $p_\mathrm{pl,e}$ the end-exhalation pleural pressure, $p_\mathrm{pl,i}$ the end-inhalation pleural pressure, $\overline{\theta} = \{\overline{\beta}_1, \overline{\beta}_2, \delta\}$ and the effective parameters of the solid energy $\overline{\psi}_\mathrm{s}$ or $\widetilde{\theta} = \{\widetilde{\beta}_1, \widetilde{\beta}_2, \delta\}$ the absolute parameters of the solid energy $\widetilde{\psi}_\mathrm{s}$. p_f is zero according to the free breathing assumption.

3.3.1.1 Validation of estimation process

We first check the estimation process capacity with synthetic data whose material parameters are known. Such synthetic data are generated in the way described in Section 3.2.2.1: parameters are chosen, then the resulting displacement field is computed through the direct problem (data used with the cost function f_DIC) and the initial image is deformed based on this displacement field to generate the deformed image (data used with the cost function f_image). More specifically, the model components of the subject P1 is used: its lung and thorax geometries, its thorax displacement, its porosity field and its disease segmentation. The model parameters concerning the pressure loading or the fixed material parameters are those presented in Table 3.2. The parameters that were used to generate the synthetic data and that are estimated are reported as Θ_synth in Table 3.3.

The validation is performed for both cost functions, f_DIC and f_image, as well as for both types of parameters, effective and absolute parameters. The results are presented in Table 3.3. Among all the cases, the error in the parameter value is at most $1\,\%$. The synthetic parameters are then well estimated using CMA-ES algorithm, for both cost functions and both types of parameters.

3.3.1.2 Impact of an approximation of the pleural pressure on the compliance ratio

As mentioned in Section 3.2.2.2, the patient-specific end-inhalation pleural pressure is not available in our work. As a consequence, the same value, chosen in the physiological range ($-1.85\,\mathrm{kPa}$), is used for all patients and the results of the parameter estimation are relative to this value. That is why the impact of the pleural pressure incertitude on the compliance is investigated in this section. To that purpose, we consider the same synthetic data as in Section 3.3.1.1 for which the end-inhalation pleural pressure $p_\mathrm{pl,i,synth}$ is known ($p_\mathrm{pl,i,synth} = 1.85\,\mathrm{kPa}$). Then, we estimate the material parameters using this data and a model where the only change is the end-inhalation pleural pressure $p_\mathrm{pl,i}$, which is different from $p_\mathrm{pl,i,synth}$. The four cases considered have the following values for the end-inhalation pleural pressure: $p_\mathrm{pl,i} = \lambda\ p_\mathrm{pl,i,synth}$ with $\lambda \in \{0.8, 0.9, 1.1, 1.2\}$. The material parameters

			f_{DIC}		f_{image}	
		Θ_{synth}	Θ_{estim}	Error (%)	Θ_{estim}	Error (%)
Effective	$\overline{\alpha}_{\text{h}}$	0.052	0.0520	$-3.7 \cdot 10^{-4}$	0.0520	$1.2 \cdot 10^{-2}$
	$\overline{\alpha}_{\text{d}}$	0.67	0.6700	$1.5 \cdot 10^{-5}$	0.6702	$-2.7 \cdot 10^{-2}$
Absolute	$\widetilde{\alpha}_{\text{h}}$	0.09	0.0910	-1.1	0.0910	-1.1
	$\widetilde{\alpha}_{\text{d}}$	0.62	0.6200	$-3.9 \cdot 10^{-3}$	0.6200	$-2.3 \cdot 10^{-4}$

Table 3.3 – Synthetic validation of the estimation process with both criteria (f_{DIC} and f_{image}) and both effective and absolute parameters. $\overline{\alpha}_{\text{h}}$ and $\widetilde{\alpha}_{\text{h}}$ are the effective and absolute parameters of the healthy region respectively, whereas $\overline{\alpha}_{\text{d}}$ and $\widetilde{\alpha}_{\text{d}}$ characterized the diseased region. Θ_{synth} are the parameters chosen to create the synthetic data as explained in Section 3.2.2.1. Θ_{estim} are the estimated parameters, resulting from the optimization algorithm explained in Section 3.2.3.5. The error between the synthetic parameters and the estimated parameters is computed as $(\Theta_{\text{synth}} - \Theta_{\text{estim}})/\Theta_{\text{synth}}$.

are estimated with the cost function f_{DIC} for both effective and absolute parameters.

The results of the four cases studied are presented in Figure 3.4. The regional pressure - volume curves for each pressure value are shown. In a second graph, the regional compliance error as well as the compliance ratio error are plotted as functions of λ for each type of parameters.

The lung appears to have a stiffer behavior when the pressure used in the model is higher than the pressure of the data, which is consistent with the fact that the deformation is the same for a higher pressure. On the contrary, the lung appears to be more compliant when the pressure is smaller than the one from the data. This behavior is the same for both regions and both types of parameters.

The compliance is overestimated when the pressure in the model is larger than in the data. Moreover, the overestimation is much higher when the region is stiffer since the compliance error is higher in the diseased region than in the healthy region. In the case where the pressure in the model is smaller by 20 % than that in the data, the compliance error in the stiffer region is about 40 %. However, the compliance error is reduced when considering the absolute parameters.

On the contrary, a pressure in the model smaller than the real one leads to an underestimation of the compliance. The same trends as for the estimation are observed: higher underestimation for the stiffer region and reduced compliance error for absolute parameters. However, the underestimation is smaller than the overestimation for the same amount of pressure difference.

The compliance ratio is also impacted by the pressure in the model, leading to an underestimation when the pressure is smaller and an overestimation when the pressure is higher. Contrary to the compliance, the compliance ratio is slightly less sensitive to the pressure in the case of effective parameters.

3.3.1.3 Impact of the non-consideration of the porosity

We want to investigate the error done when using effective parameters while data concerns a porous material. The same synthetic data as in Section 3.3.1.1 are used. However, we consider only the data generated with absolute parameters. We then estimate the effective parameters that best match the data with the displacement criterion. The resulting cost function $f(\overline{\Theta}_{\text{estim}})$ is 3.75 %. This error is quite small compared to the errors which are

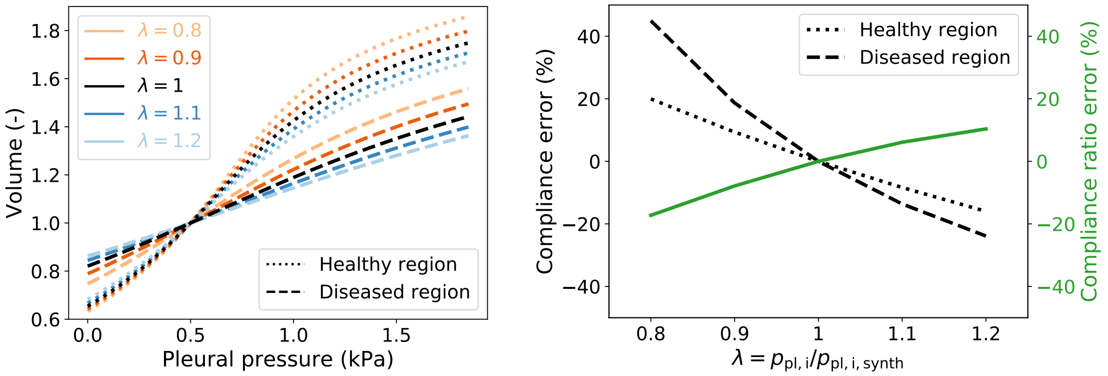

(a) With effective parameters.

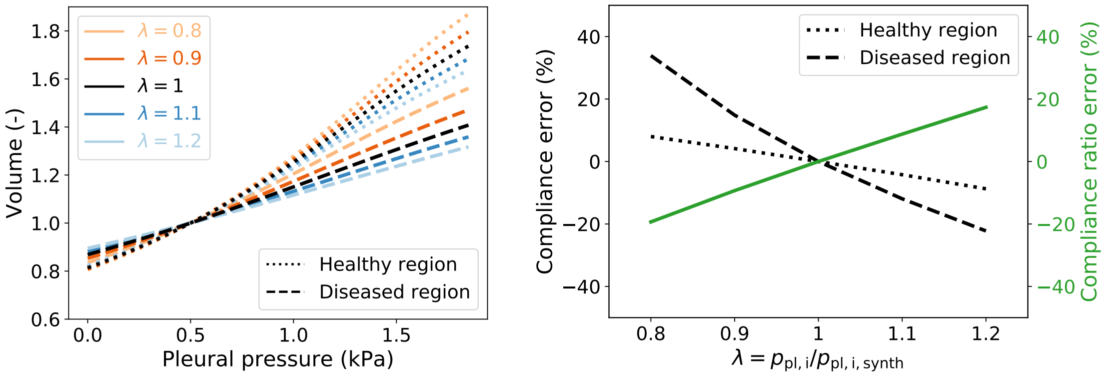

(b) With absolute parameters.

Figure 3.4 – Impact of the non patient-specific pressure applied in the model on the estimated compliance and the compliance ratio, using both effective parameters (a) and absolute parameters (b). λ is the ratio between the pressure of the model used in the estimation and the pressure used to generate the synthetic data. For both types of parameters: (left) Visualization of pressure-volume curves for each pressure case (colored lines), compared to the pressure-volume curves obtained with the pressure used to create the synthetic data (black line); (right) Compliance error for each region as a function of the value of the pressure applied in the model, as well as the compliance ratio error ($C_{\mathrm{h}}/C_{\mathrm{d}}$).

obtained with *in vivo* data in Section 3.3.2 (between 17 and 23 %). This result reflects that the porosity is quite homogeneous in each region. The heterogeneity of porosity, mainly at the interface between regions, does not impact so much the estimation results.

3.3.2 Results with *in vivo* data

This section presents results with one healthy and three diseased subjects. We first study the impact of various modeling choices, like the type of parameters, absolute or effective, the number of regions considered and the cost function used in the minimization. We then focus on clinical results.

3.3.2.1 Estimation performance in relation with modeling and data

Comparison between absolute parameters and effective parameters We compare the results obtained either with effective parameters or absolute parameters in order to investigate whether one of the two choices gives a better accuracy of the model with respect to the data. Both computations are performed for each subject, each cost function and considering one or two regions.

The cost function error, defined as the cost function using absolute parameters compared to the cost function using effective parameters, is presented in Table 3.4. Depending on the subject, the use of one type of parameters is better than the other. The subjects H1 and P1 lead to a better model accuracy with absolute parameters, whereas the models of the subjects P2 and P3 are closer to the data with effective parameters. Consequently, no type of parameter results a better model accuracy in all cases. However, when considering the amount of error, absolute parameters leads to a higher error than effective parameters in the cases where they are not the optimal choice.

	f_{DIC}		f_{image}	
	1 region	2 regions	1 region	2 regions
H1	$-0.46\,\%$	-	$-2.30\,\%$	-
P1	$-0.51\,\%$	$-2.77\,\%$	$-0.02\,\%$	$-0.46\,\%$
P2	34.23 %	9.45 %	10.98 %	6.24 %
P3	15.57 %	13.09 %	4.75 %	9.32 %

Table 3.4 – Evaluation of the contribution of the use of absolute parameters compared to the use of effective parameters. The values, expressed in %, are computed as $(f(\widetilde{\Theta}_{\text{estim}}) - f(\overline{\Theta}_{\text{estim}}))/f(\overline{\Theta}_{\text{estim}})$. They are presented for both criteria f_{DIC} and f_{image}, and for a model using one or two regions (from disease segmentation).

Contribution of the use of two regions We investigate here the contribution of the use of two regions in the model compared to the use of only one region and if the definition of regions from disease segmentation is significant compared to regions arbitrarily defined. As in Section 3.3.1, the model of the subject P1 is used. Twenty-six different lung divisions into two regions are defined. In all the cases, the organ is divided into two parts by a plane defined by its normal. We consider the thirteen normals of a cube to define each plane. Since the disease affects 31 % of the lung volume for the subject P1, all the divisions keep that proportion. For each division, the estimation of the material parameters is performed using the displacement criterion f_{DIC} and the absolute parameters.

The result is presented as a boxplot representing the distribution of the final value of the cost function in Figure 3.5. The two-regions model is better in all the cases than the one-region model, since the number of degrees of freedom is higher. Only four cases with two regions are better than the case using the disease segmentation.

A Shapiro-Wilk test is performed to determine whether the distribution is normally distributed. The p-value is 0.13 %, which is not enough to accept the hypothesis of a normal distribution. As a consequence, the Student's t test cannot be realized to compare means. A non-parametric Mann–Whitney U test is performed to evaluate the probability that the cost function of a random two-regions definition is lower and greater than the cost functions for a one-region model and a two-regions model from the disease segmentation, respectively. The resulting p-values are 5.4 % and 13.7 %, respectively, which allows to accept that the probability of a cost function of any two-regions model is lower than that of a one-zone model. However, it is more difficult to conclude when the comparison is done with the two-regions model from the disease segmentation.

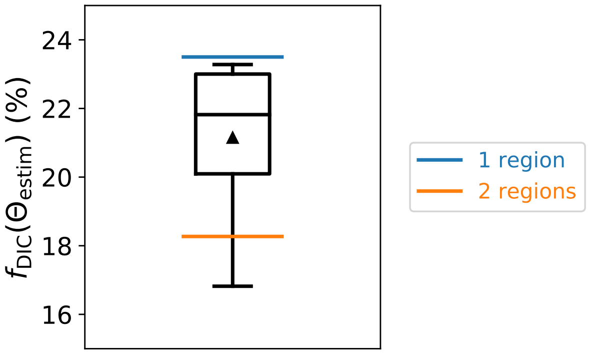

Figure 3.5 – Boxplot representing the value of $f_{\mathrm{DIC}}(\widetilde{\Theta}_{\mathrm{estim}})$ for the 26 cases of divisions into two regions. The box extends from the lower to upper quartile values. The horizontal black line is the median, whereas the triangle is the mean. The lower and upper whiskers extend to $Q_1 - 1.5(Q_3 - Q_1)$ and $Q_3 + 1.5(Q_3 - Q_1)$ respectively, with Q_1 and Q_3 the lower and upper quartiles, respectively. The box plot can be compared to the value of $f_{\mathrm{DIC}}(\Theta_{\mathrm{estim}})$ in the case of the use of one region (blue line) and the case where the two regions come from the disease segmentation (orange line).

Comparison between displacement and image criteria Another question raised in this work is the comparison of both criteria, to explore whether or not they lead to similar results. For each subject, each type of parameters and each number of regions, we compare the compliance estimated from displacement data and the compliance estimated from images.

The result is represented in a Bland-Altman plot, shown in Figure 3.6. The difference between compliances from both criteria is plotted as a function of both compliances. The bias in the difference between compliances is 0.04 ± 0.21 L/kPa, which means that the criterion f_{image} gives a slightly higher compliance than the criterion f_{DIC} statistically. However, the bias is small and can be neglected. Consequently, both criteria can be considered as equivalent.

3.3.2.2 Clinical implications

The results in this Section are those obtained with the image criterion, since we justified previously that both criteria are equivalent.

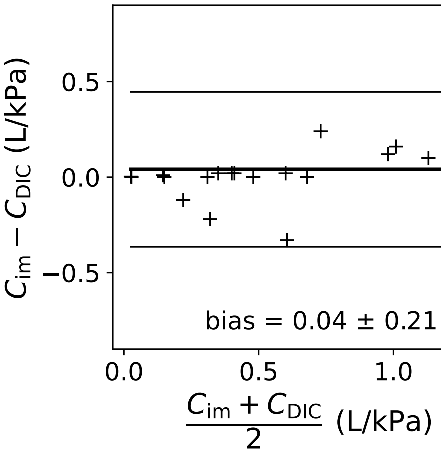

Figure 3.6 – Bland–Altman plot to compare both criteria. The quantities used for the comparison is the compliance computed by both criteria. C_{DIC} and C_{im} are the compliances computed with the displacement criterion and the image criterion, respectively.

Compliance of healthy and diseased regions The global pulmonary compliance is already a biomarker for clinicians to study the impact of pulmonary fibrosis on the organ. With our model, the regional compliance can be also estimated, which is an information not accessible with direct measurements. The compliances, global and regional, are shown for each subject in Figure 3.7.

The results of the subject P2 are different from those of subjects P1 and P3. This can be explained by a different amount of breathing, since the volume variation between end-exhalation and end-inhalation is only 14 %, whereas it is between 80 and 90 % for the other subjects. In what follows, we consider only subjects H1, P1 and P3.

For both subjects P1 and P3, the global compliance is between both regional compliance, which can be easily understood since the global compliance aggregates the contributions of both regions. Moreover, the healthy region is more compliant than the diseased region, which is consistent with the current knowledge of pulmonary fibrosis [Gibson, 2001; Plantier et al., 2018].

Effective compliance is smaller than absolute compliance in all the cases. Indeed, the effective compliance takes into account two aspects: the porosity and the solid tissue compliance, also called absolute compliance. The absolute compliance results then in the effective compliance after the removal of the porosity effect and is smaller than the effective compliance since the solid tissue is non porous.

Finally, compliances cannot be directly compared between subjects since the value is relative to the pleural pressure value used in this work, which is not patient-specific.

Stress distribution It is assumed that the mechanics plays a major role in the pulmonary fibrosis evolution. Indeed, the assumption of a mechanical vicious circle in place for this disease has been formulated: fibrosis leads to stiffer tissue and increases stresses, which activates the production of collagen fibers by fibroblasts and induces more fibrosis [Liu et al., 2010; Hinz and Suki, 2016; Haak et al., 2018; Wu et al., 2019]. Our model allows to investigate the impact of the disease on the stress field, as shown in Figure 3.8. It can be observed that the stress field is largely heterogeneous close to the interface between both regions, the healthy and the diseased regions. In some interfacial areas, the stress is up to twice as large as far from the interface. This stress concentration seems to support the mechanical vicious circle assumption, though a more quantitative analysis, with more

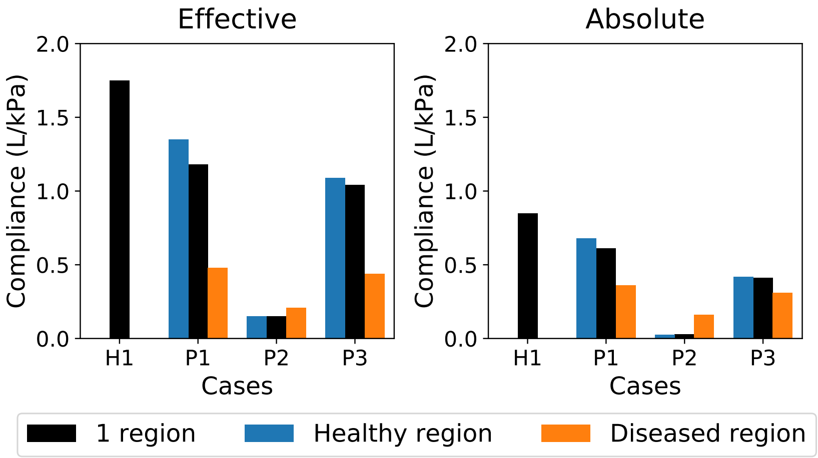

Figure 3.7 – Effective and absolute compliances estimated for each case. For each case, the global compliance, in black, is estimated with a one-region model, whereas the compliance of both healthy and diseased regions, in blue and orange respectively, are estimated with a two-regions model. For the healthy case H1, only the global compliance is estimated. Two types of compliance are estimated: (left) the effective compliance, associated with the mixture, and (right) the absolute compliance, associated with the tissue.

data, will be necessary to conclude.

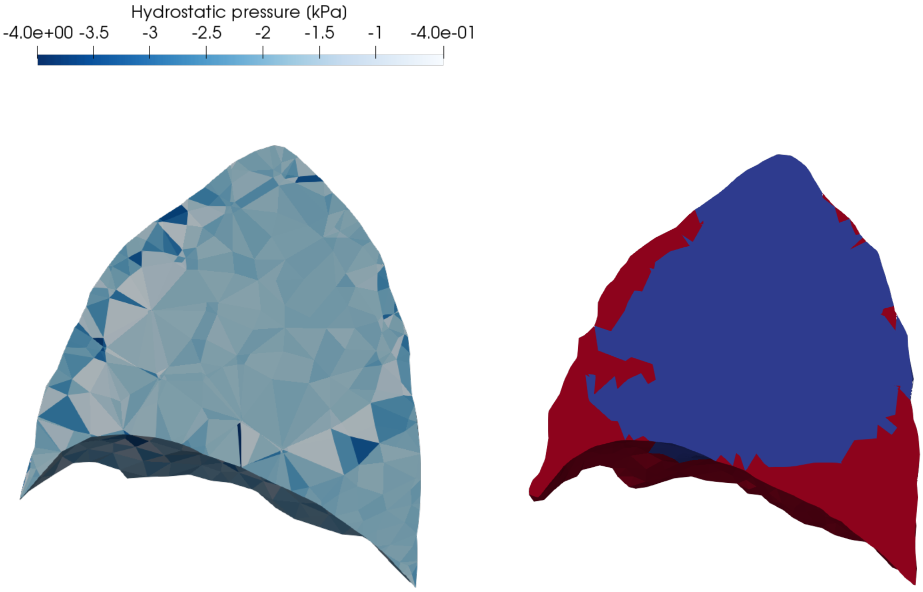

Figure 3.8 – Comparison of the hydrostatic pressure and the disease segmentation in the same slice. (left) Visualization of the hydrostatic pressure in a sagittal slice of the lung. (right) Visualization of the segmentation of the fibrosis. The fibrotic region is in red, whereas the healthy region is in blue.

3.4 Discussion

We have presented a poromechanical model of the lung that can be personalized to a patient using medical images. In particular, patient-specific regional mechanical parameters are estimated, which cannot be measured *in vivo*. The model personalization has been applied with one healthy and three diseased patients.

The choice of using poromechanics was made to consider the porosity of the organ. Even though the results of the present work do not show in all the cases that the use of poromechanics makes the model more accurate to the data, it brings useful information about the material properties of the solid tissue, which are difficult to measure. Indeed, it allows to remove the effect of the porosity from the effective compliance, as effective compliance results from both the compliance of the solid tissue and from the porosity. Such a model can also be used to study the impact of porosity or of porosity gradient in the organ.

We have shown that a two-regions model is more accurate with respect to the data than a one-region model, since more degrees of freedom are present in a two-regions model. Based on our study, the definition of two regions matching with the disease segmentation seems also to bring better results than the definition of two random regions, which is a promising result. However, more data are needed to further conclude whether the result is significant or not.

We assumed homogeneous material properties in each region. In particular, in the case of the healthy subject, we assumed that the whole lung has homogeneous material properties. This assumption could be studied by defining several regions for the healthy subject or by defining several healthy regions and several diseased regions for the diseased cases. Then, the variability of material parameters in each region would give information about the lung inhomogeneity.

Two criteria have been investigated: one using a displacement field, computed from images, like in FEMU approaches, whereas the other exploits images directly, as an integrated image correlation approach. The displacement criterion is easier to understand since the result can be expressed in terms of a length, the RMSE error. For example, the RMSE errors for the cases P1 and P3 are 4.9 mm and 11.4 mm, respectively. It allows to quantify the accuracy of the method in a simple way and clinicians can understand and use it easily. However, the use of the displacement method requires to perform image registration between both images and can lead to errors, on which the estimation process is based. On the other hand, the image criterion includes the same term of similarity between images than in image registration and allows to perform in one step what is done in two steps with the other criterion (registration and estimation). Nevertheless, the value of this criterion is less understandable. Moreover, it is not differentiable, which restricts its use in other minimization tools.

The clinical results obtained in this work are consistent with the current knowledge of the disease. Indeed, the effective compliance of the healthy subject H1 is 1.75 L/kPa, whereas Galetke et al. [2007] showed that the compliance of one lung is 1.67 ± 0.55 L/kPa. The result has an adequate value, even though it is relative to the non patient-specific pressure of the model. Then, the personalization on the diseased subjects led to a stiffer diseased region than the healthy region, which is consistent with the literature [Georges et al., 2007; Booth et al., 2012; Liu et al., 2015; Haak et al., 2018]. More precisely, when considering absolute parameters, we obtained that the solid tissue in the diseased region is stiffer than in the healthy region, which is an information difficult to measure experimentally. The personalization pipeline allows then to quantify the stiffening of the organ with the pulmonary fibrosis.

When applied with more patients, stiffening quantification obtained from the personalized model can be studied in relation to other clinical quantities in order to investigate any correlation. In particular, stiffening could be linked to the disease severity, either determined by the volume of the disease region or DLCO, or the disease decline at six or twelve months.

The highlighting of a stress concentration at the border to the fibrotic region is also a major clinical result. It is a first step towards the confirmation of the hypothesis of the mechanical vicious circle which would govern pulmonary fibrosis. The validation of this phenomenon on more cases would help to better understand and then predict the disease progress.

Some limitations appeared with the patient P2. The diseased region for this patient appeared to have the same or higher compliance than the one of the healthy region, which seems non consistent with what is known on the pulmonary fibrosis. One hypothesis would be that it would correspond to some specific characteristics of the disease. After further investigations, it is more likely that the cause comes from the data. Indeed, the image registration does not show smaller deformation in the diseased region. The diseased region is also quite small (about 7 % of the total volume), very discontinuous and not significantly thick compared to the element size. These characteristics make difficult a good image registration and a finer mesh would be needed.

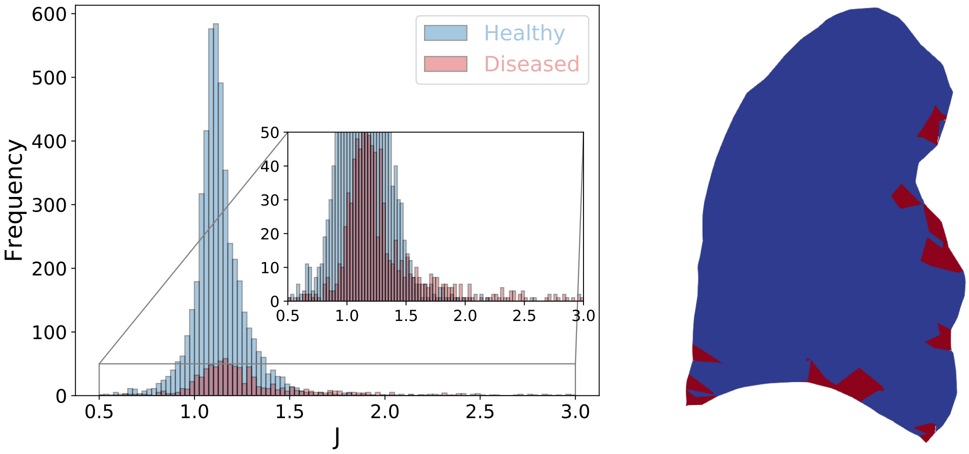

(a) (b)

Figure 3.9 – Details about the patient P2 to understand the related results. (a) Distribution of the local variation of volume J for each region. In the healthy region, $J_{\text{healthy}} = 1.13 \pm 0.15$, whereas in the diseased region, $J_{\text{diseased}} = 1.32 \pm 0.42$ (b) Visualization of the regions in a plane : the blue part is the healthy region, whereas the red part is the diseased region.

As already mentioned, the results presented here are relative to the pleural pressure applied at the end of inhalation, since no patient-specific pressure is available. Consequently, the compliances are relative to that pressure and not absolute. Knowing the patient-specific pressure applied in reality would allow to compute the absolute compliance and to make comparisons between subjects. Such data could be acquired using an esophageal balloon to measure the esophageal pressure, considered as very close to the pleural pressure [Hoppin et al., 1969; Agostoni, 1972; Akoumianaki et al., 2014], under the scanner. However, this measurement is not part of the clinical routine for patients suffering from pulmonary fibrosis.

Another way to improve the personalization process is to use more images. In some cases, like in radiotherapy of pulmonary tumors, 4DCT scans can be acquired in a standard protocol with ten images during the breathing cycle to investigate the nodule displacement during breathing. However, the guidelines for the diagnosis of idiopathic pulmonary fibrosis propose to acquire maximum two CT images in order to limit the radiation exposure of the patients [Cottin et al., 2013]. This is the reason why this study was limited to two

3DCT images. It is clear that using more images during the breathing cycle would enable a more accurate parameters estimation.

3.5 Conclusion

We presented a poromechanical model of the lung, which is personalized to patients using medical images. Applied with one healthy subject and three diseased subjects suffering from idiopathic pulmonary fibrosis, it allows in particular to quantify the regional pulmonary compliance. The results are consistent with the knowledge of the disease, especially the associated stiffening. The estimation process brings information about regional effective compliances, which are not available *in vivo*, but also about regional absolute compliances, which are difficult to measure even *ex vivo*. This work brings a proof of concept and still needs to be applied with more patients before being used in clinical routine for diagnosis purposes. A first step towards a better understanding of the IPF physiology is also provided by the evidence of a stress concentration at the border of the fibrotic zone, that would confirm the hypothesis of the mechanical vicious circle underlying IPF progress. In the longer term, this personalized model could be used with longitudinal data to study the prognosis of the disease, as well as the mechanical impact of drugs.

Ethical statement

Patients data were retrospectively retrieved according to the French law on medical research and compiled as required by the Commission Nationale de l'Informatique et des Libertés (CNIL; the French data protection authority). The study not requiring an informed consent received authorization CLEA-2019-96 from the Comité Local d'Ethique Avicenne.

Bibliography

Agostoni, E. (1972). Mechanics of the pleural space. *Physiological Reviews*, 52(1):57–128.

Akoumianaki, E., Maggiore, S. M., Valenza, F., Bellani, G., Jubran, A., Loring, S. H., Pelosi, P., Talmor, D., Grasso, S., Chiumello, D., Guérin, C., Patroniti, N., Ranieri, V. M., Gattinoni, L., Nava, S., Terragni, P.-P., Pesenti, A., Tobin, M., Mancebo, J., and Brochard, L. (2014). The Application of Esophageal Pressure Measurement in Patients with Respiratory Failure. *American Journal of Respiratory and Critical Care Medicine*, 189(5):520–531.

Alnæs, M., Blechta, J., Hake, J., Johansson, A., Kehlet, B., Logg, A., Richardson, C., Ring, J., Rognes, M. E., and Wells, G. N. (2015). The FEniCS Project Version 1.5. *Archive of Numerical Software*, 3(100).

Avril, S., Bonnet, M., Bretelle, A.-S., Grédiac, M., Hild, F., Ienny, P., Latourte, F., Lemosse, D., Pagano, S., Pagnacco, E., and Pierron, F. (2008). Overview of Identification Methods of Mechanical Parameters Based on Full-field Measurements. *Experimental Mechanics*, 48(4):381–402.

Avril, S. and Evans, S., editors (2017). *Material Parameter Identification and Inverse Problems in Soft Tissue Biomechanics*, volume 573 of *CISM International Centre for Mechanical Sciences*. Springer International Publishing, Cham.

Azzouna, M. B., Feissel, P., and Villon, P. (2013). Identification of elastic properties from full-field measurements: A numerical study of the effect of filtering on the identification results. *Measurement Science and Technology*, 24(5):055603.

Baffico, L., Grandmont, C., and Maury, B. (2010). Multiscale Modeling of the Respiratory Tract. *Mathematical Models and Methods in Applied Sciences*, 20(01):59–93.

Biot, M. A. and Temple, G. (1972). Theory of Finite Deformations of Porous Solids. *Indiana University Mathematics Journal*, 21(7):597–620.

Booth, A. J., Hadley, R., Cornett, A. M., Dreffs, A. A., Matthes, S. A., Tsui, J. L., Weiss, K., Horowitz, J. C., Fiore, V. F., Barker, T. H., Moore, B. B., Martinez, F. J., Niklason, L. E., and White, E. S. (2012). Acellular Normal and Fibrotic Human Lung Matrices as a Culture System for *In Vitro* Investigation. *American Journal of Respiratory and Critical Care Medicine*, 186(9):866–876.

Chabiniok, R., Moireau, P., Lesault, P.-F., Rahmouni, A., Deux, J.-F., and Chapelle, D. (2012). Estimation of tissue contractility from cardiac cine-MRI using a biomechanical heart model. *Biomechanics and Modeling in Mechanobiology*, 11(5):609–630.

Chapelle, D. and Moireau, P. (2014). General coupling of porous flows and hyperelastic formulations—From thermodynamics principles to energy balance and compatible time schemes. *European Journal of Mechanics - B/Fluids*, 46:82–96.

Cottin, V., Crestani, B., Valeyre, D., Wallaert, B., Cadranel, J., Dalphin, J., Delaval, P., Israel-Biet, D., Kessler, R., Reynaud-Gaubert, M., Cordier, J., Aguilaniu, B., Bouquillon, B., Carré, P., Danel, C., Faivre, J.-B., Ferreti, G., Just, N., Kouzan, S., Lebargy, F., Marchand Adam, S., Philippe, B., Prévot, G., Stach, B., and Thivolet-Béjui, F. (2013). Recommandations pratiques pour le diagnostic et la prise en charge de la fibrose pulmonaire idiopathique. Élaborées par le centre national de référence et les centres de compétence pour les maladies pulmonaires rares sous l'égide de la Société de pneumologie de langue française. *Revue des Maladies Respiratoires*, 30(10):879–902.

Coussy, O. (2004). *Poromechanics*. Wiley, Chichester.

Fetita, C., Tarando, S., Brillet, P.-Y., and Grenier, P. A. (2016). Robust lung identification in MSCT via controlled flooding and shape constraints: Dealing with anatomical and pathological specificity. In Gimi, B. and Krol, A., editors, *SPIE Medical Imaging*, volume 97881A, San Diego, California, United States.

Galetke, W., Feier, C., Muth, T., Ruehle, K.-H., Borsch-Galetke, E., and Randerath, W. (2007). Reference values for dynamic and static pulmonary compliance in men. *Respiratory Medicine*, 101(8):1783–1789.

Genet, M., Chuan Lee, L., Ge, L., Acevedo-Bolton, G., Jeung, N., Martin, A., Cambronero, N., Boyle, A., Yeghiazarians, Y., Kozerke, S., and Guccione, J. M. (2015). A Novel Method for Quantifying Smooth Regional Variations in Myocardial Contractility Within an Infarcted Human Left Ventricle Based on Delay-Enhanced Magnetic Resonance Imaging. *Journal of Biomechanical Engineering*, 137(8):081009.

Genet, M., Stoeck, C., von Deuster, C., Lee, L., and Kozerke, S. (2018). Equilibrated warping: Finite element image registration with finite strain equilibrium gap regularization. *Medical Image Analysis*, 50:1–22.

Genet, M., Stoeck, C., von Deuster, C., Lee, L. C., Guccione, J. M., and Kozerke, S. (2016). Finite Element Digital Image Correlation for Cardiac Strain Analysis from 3D Whole-Heart Tagging. In *ISMRM 24rd Annual Meeting and Exhibition 2016*, Singapore, Singapore.

Georges, P. C., Hui, J.-J., Gombos, Z., McCormick, M. E., Wang, A. Y., Uemura, M., Mick, R., Janmey, P. A., Furth, E. E., and Wells, R. G. (2007). Increased stiffness of the rat liver precedes matrix deposition: Implications for fibrosis. *American Journal of Physiology-Gastrointestinal and Liver Physiology*, 293(6):G1147–G1154.

Geuzaine, C. and Remacle, J.-F. (2009). Gmsh: A three-dimensional finite element mesh generator with built-in pre- and post-processing facilities. *International Journal for Numerical Methods in Engineering*, 79(11):1309–1331.

Gibson, G. (2001). Lung volumes and elasticity. *Clinics in Chest Medicine*, 22(4):623–635.

Gibson, G. and Pride, N. (1976). Lung distensibility. The static pressure-volume curve of the lungs and its use in clinical assessment. *British Journal of Diseases of the Chest*, 70:143–184.

Govindjee, S. and Mihalic, P. A. (1998). Computational methods for inverse deformations in quasi-incompressible finite elasticity. *International Journal for Numerical Methods in Engineering*, 43(5):821–838.

Grédiac, M., Pierron, F., Avril, S., and Toussaint, E. (2008). The Virtual Fields Method for Extracting Constitutive Parameters From Full-Field Measurements: A Review. *Strain*, 42(4):233–253.

Haak, A. J., Tan, Q., and Tschumperlin, D. J. (2018). Matrix biomechanics and dynamics in pulmonary fibrosis. *Matrix Biology*, 73:64–76.

Hansen, N. (2016). The CMA Evolution Strategy: A Tutorial.

Hansen, N. and Auger, A. (2014). Principled Design of Continuous Stochastic Search: From Theory to Practice. In Borenstein, Y. and Moraglio, A., editors, *Theory and Principled Methods for the Design of Metaheuristics*, pages 145–180. Springer Berlin Heidelberg, Berlin, Heidelberg.

Hedlund, L., Vock, P., and Effmann, E. (1983). Evaluating Lung Density by Computed Tomography. *Seminars in Respiratory and Critical Care Medicine*, 5(01):76–88.

Hild, F. and Roux, S. (2006). Digital Image Correlation: From Displacement Measurement to Identification of Elastic Properties - a Review. *Strain*, 42(2):69–80.

Hinz, B. and Suki, B. (2016). Does Breathing Amplify Fibrosis? *American Journal of Respiratory and Critical Care Medicine*, 194(1):9–11.

Hoppin, F. G., Green, I. D., and Mead, J. (1969). Distribution of pleural surface pressure in dogs. *Journal of Applied Physiology*, 27(6):863–873.

Leclerc, H., Périé, J.-N., Roux, S., and Hild, F. (2009). Integrated Digital Image Correlation for the Identification of Mechanical Properties. In Gagalowicz, A. and Philips, W., editors, *Computer Vision/Computer Graphics CollaborationTechniques*, volume 5496, pages 161–171. Springer Berlin Heidelberg, Berlin, Heidelberg.

Liu, F., Lagares, D., Choi, K. M., Stopfer, L., Marinković, A., Vrbanac, V., Probst, C. K., Hiemer, S. E., Sisson, T. H., Horowitz, J. C., Rosas, I. O., Fredenburgh, L. E., Feghali-Bostwick, C., Varelas, X., Tager, A. M., and Tschumperlin, D. J. (2015). Mechanosignaling through YAP and TAZ drives fibroblast activation and fibrosis. *American Journal of Physiology-Lung Cellular and Molecular Physiology*, 308(4):L344–L357.

Liu, F., Mih, J. D., Shea, B. S., Kho, A. T., Sharif, A. S., Tager, A. M., and Tschumperlin, D. J. (2010). Feedback amplification of fibrosis through matrix stiffening and COX-2 suppression. *The Journal of Cell Biology*, 190(4):693–706.

Logg, A., Mardal, K., and Wells, G. (2012). *Automated Solution of Differential Equations by the Finite Element Method: The FEniCS Book.* Lecture Notes in Computational Science and Engineering. Springer Berlin Heidelberg.

Patte, C., Genet, M., and Chapelle, D. (2020). A poromechanical model of the lungs. *to be submitted.*

Plantier, L., Cazes, A., Dinh-Xuan, A.-T., Bancal, C., Marchand-Adam, S., and Crestani, B. (2018). Physiology of the lung in idiopathic pulmonary fibrosis. *European Respiratory Review*, 27(147):170062.

Remacle, J.-F., Geuzaine, C., Compere, G., and Marchandise, E. (2009). High Quality Surface Remeshing Using Harmonic Maps. *International Journal for Numerical Methods in Engineering*, 83(4):403–425.

Réthoré, J., Roux, S., and Hild, F. (2009). An extended and integrated digital image correlation technique applied to the analysis of fractured samples: The equilibrium gap method as a mechanical filter. *European Journal of Computational Mechanics*, 18(3-4):285–306.

Škardová, K., Rambausek, M., Chabiniok, R., and Genet, M. (2019). Mechanical and Imaging Models-Based Image Registration. In Tavares, J. M. R. S. and Natal Jorge, R. M., editors, *VipIMAGE 2019*, Lecture Notes in Computational Vision and Biomechanics, pages 77–85. Springer International Publishing.

Taha, A. A. and Hanbury, A. (2015). Metrics for evaluating 3D medical image segmentation: Analysis, selection, and tool. *BMC Medical Imaging*, 15(1):29.

Vishnevskiy, V., Gass, T., Szekely, G., Tanner, C., and Goksel, O. (2017). Isotropic Total Variation Regularization of Displacements in Parametric Image Registration. *IEEE Transactions on Medical Imaging*, 36(2):385–395.

Wu, H., Yu, Y., Huang, H., Hu, Y., Fu, S., Wang, Z., Shi, M., Zhao, X., Yuan, J., Li, J., Yang, X., Bin, E., Wei, D., Zhang, H., Zhang, J., Yang, C., Cai, T., Dai, H., Chen, J., and Tang, N. (2019). Progressive Pulmonary Fibrosis Is Caused by Elevated Mechanical Tension on Alveolar Stem Cells. *Cell*, 180(1):107–121.e17.

Conclusions and perspectives

Conclusions

This work belongs to the growing and promising field of digital medicine. It focused on pulmonology issues, and more specifically on interstitial lung diseases like idiopathic pulmonary fibrosis, for which doctors are seeking the help of physical and numerical modeling to better address their clinical issues – disease understanding, as well as diagnosis, prognosis and treatment improvement. This subject arose precisely from discussions between clinicians from the Avicenne APHP hospital, experts in these pulmonary diseases, and the MΞDISIM Inria team, which has been working for more than ten years on cardiac modeling issues.

The main goal of this work was to bring modeling tools to tackle these pulmonary clinical issues. Considering the mechanical impact of the targeted diseases on lungs, the porosity of lungs and the expertise of MΞDISIM with poromechanics, the choice of poromechanical modeling was the starting point. We aimed to develop a poromechanical model of the lung, derived from [Chapelle and Moireau, 2014], by formulating pulmonary-specific hypotheses and defining the various elements of the model (constitutive behavior and boundary conditions, mainly). Clinical issues of diagnosis required to make the model patient-specific, using clinical data. A close interaction with data was required to fully exploit them. The use of routine data only was important considering the future perspective of a clinical use of the developed tools. Finally, the patient-specific model should bring understandable and usable biomarkers for clinicians to answer their initial clinical need.

In what follows, we summarize the main achievements of this work in the same order as presented in the present manuscript.

- We have first highlighted that modeling choices should be tightly linked to the physiology. We overviewed the main elements of pulmonary physiology for a good understanding of the phenomena studied in this work. Then, we largely reviewed mechanical models of the literature, considering the multiscale and multiphase characteristics of lungs. We discussed organ scale models, in focusing on boundary conditions and constitutive behavior aspects, as well as multiscale models, which take into account the microstructure. We finally presented poromechanical models, which are in between, analyzing advantages and drawbacks of this approach.
- We have developed a poromechanical model of the lung, at the breathing time scale and the organ spatial scale, which includes:
  - the formulation of lung-specific assumptions to derive a simplified description of the poromechanical framework of [Chapelle and Moireau, 2014];
  - the use of a constitutive law reproducing the volume behavior of the lung with a change of pressure, calibrated from experimental data, and considering the quasi-incompressibility of the solid part;
  - the integration of the porosity in the constitutive law in order to distinguish two physical effects present in the effective behavior of the whole mixture, the porosity and the absolute behavior of the solid tissue;
  - the implementation of two kinds of boundary conditions, depending on the type of breathing considered, either spontaneous breathing or mechanical ventilation. We modeled the role of the various elements involved in breathing, from the diaphragm and the pleura to the rib cage and the mediastinum;
  - the consideration of the unloaded configuration, and especially the modeling of the mixture behavior when the local porosity comes close to zero. We proposed either the use of an additional specific energy or a contact-like formulation.

We have finally presented various illustrations of the performance of the model with the impact of some modeling choices or the consideration of pulmonary pathologies.

- We have personalized the model using clinical data, directly acquired in routine, for one healthy subject and three diseased patients suffering from idiopathic pulmonary fibrosis. We made each element of the model patient-specific from two images in the breathing cycle employing various tools: image segmentation for the lung and thorax geometries, image registration for the lung and thorax displacements, conversion of the image intensities for the porosity, optimization of the material behavior. We proposed two different criteria for the optimization, differing by the data considered, and we showed that, in this framework, the FEMU (Finite Element Model Updating) approach, using explicit displacements, is equivalent to the integrated approach. We managed to estimate the material stiffening, or equivalently the compliance, of the diseased region of the lung suffering from pulmonary fibrosis and we obtained results consistent with the current knowledge of the disease. We also observed a stress concentration at the border of the fibrotic region, which supports the hypothesis of the mechanical vicious circle governing the IPF progress.

This work provides a proof of concept that the regional compliance can be estimated from routine clinical data. The developed tool allows to quantify the mechanical impact of pulmonary interstitial diseases, on the organ but also on the solid tissue composing the organ. This information cannot be obtained by direct measurements. It could then be used as an objective and quantitative tool for diagnosis, in addition to the current clinical tools. Indeed, the compliance of the diseased region, and more specifically the ratio of compliances between the healthy and the diseased region, is an understandable biomarker for clinicians. Finally, this work also brings a first insight into the understanding of the IPF physiology, and in particular its progress controlled by mechanics.

Perspectives

Many aspects of the work can be pushed further, from a modeling point of view but also concerning clinical applications. The main perspectives are presented here:

- Improving the boundary conditions of the model by taking into account the gravity. We showed the impact of gravity during breathing with comparative modeling. However, gravity should also be applied in the estimation of the unloaded configuration in order to compare with data, since the *in vivo* configurations are subjected to gravity. An investigation on the integration of gravity in the inverse problem should be done, to make it well-posed. Thus, the inverse problem has an infinite number of solutions, since any configuration spatially above the deformed configuration in the direction of gravity could be solution, and the method of Govindjee and Mihalic [1996] used in this work could not converge. Moreover, applying gravity during breathing for an upright case can lead to an infinite sliding of the lung downwards. Indeed, in our model of spontaneous breathing, the absence of explicit structures close to the mediastinum lung surface does not allow to keep the lung in its physiological place.
- Improving the modeling of lungs material behavior by modeling hysteresis. The hysteresis present in the pressure - volume curves, coming from the presence of the surfactant, is not taken it into account in our work. The main reason is that the available data in this work (two images in the breathing cycle) do not allow to highlight it. We could model the surfactant impact through an additional dissipative contribution in the stress tensor.
- Improving the estimation process:

  - The main limitation of the material parameters estimation in this work is the absence of patient-specific pressures, which implies that the results are relative to the pleural pressure applied in the model. Being able to acquire these patient-specific pressures would allow to make the results absolute. However, for the time being, the clinical routine does not provide for this examination. An idea to bypass this limitation is to set the healthy material parameter and to estimate the pressure in the same time as the diseased material parameter. As a consequence, we could compare patients with each other, assuming that the fixed healthy parameter is accurate.
  - Another kind of data which could be enriched is the medical images. Acquiring more images in the breathing cycle would allow to better estimate the material parameters and also to consider the hysteresis mentioned in the previous point. 4DCT images with about 10 timesteps are already acquired for other applications like radiotherapy, but the resulting high dose of radiation prevents it from being performed on patients suffering from interstitial lung disease.
  - Information of the segmentation of the disease should be provided in order to estimate the regional material parameters. We could circumvent the need for this information by estimating the geometric regions together with the mechanical parameters. Several methods could be used to achieve this goal, like the use of a parameters field [Genet et al., 2015] or shape analysis methods.
- Studying correlations between the stiffening generated by the pulmonary fibrosis, or the compliance ratio between healthy and diseased regions, with others quantities. Several quantities are of interest for clinicians, like the percentage of the measured $\mathrm{D_{LCO}}$ in relation to the predicted $\mathrm{D_{LCO}}$ value and the equivalent quantity with the FVC (Forced Vital Capacity). The evolution of these quantities with time, after six and twelve months for example, is also interesting, to evaluate a relation between stiffening and the disease progression. This information would deepen the knowledge of pulmonary fibrosis. However, the model should be applied to more patients to perform such correlations.
- Building an automatic tool to estimate regional parameters based on this PhD work. Indeed, the current tool is still largely manual and requires about three days to be applied on a patient, where an operator should perform many tasks. We need a more automatic tool to faster apply the model on patients with minimal actions from the operator. This perspective concerns both deeper research to get results on large cohorts of patients, as well as applications towards a clinical practice where clinicians would be the operators. Another challenge is the computation time (about 15 h), which should be reduced and adapted to the clinics.

Long-term perspectives for this work can also be mentioned:

- Developing a micromechanical model of the pulmonary microstructure and coupling it with the present organ scale model. Indeed, the alveolar scale is more adequate to model some phenomena, like the surfactant behavior as mentioned in a previous perspective. This requires to get data on the pulmonary microstructure with micro-tomography, but also mechanical data [Pallière et al., 2019; Richardson et al., 2019]. The upscaling strategy will then allow to investigate relations between microscopic parameters, characterizing the microstructure like the alveolar size or the alveolar wall thickness, and the macroscopic parameters, like the compliance. The organ response will be explained with features of the tissue. It would bring a more complete tool to investigate pulmonary fibrosis considering both scales, and not only the organ scale, as done in this work.

- Modeling the pulmonary fibrosis remodeling. Using longitudinal data, *i.e.,* data of one patient over time (about several months), we could investigate the time evolution of the disease and the correlation between its expansion and local stresses. The mechanisms of the disease remodeling could be modeled in an evolution law and the hypothesis of a mechanical vicious circle in place in pulmonary fibrosis [Hinz and Suki, 2016] could also be studied. This would lead to a better understanding of the time evolution of the disease and then to a better prognosis for patients. The same approach can be considered to study COVID-19 long-term evolution since it is assumed that the disease could evolve into a fibrosing interstitial pulmonary disease [George et al., 2020; Spagnolo et al., 2020]. A better understanding of this evolution could allow to predict it. Finally, another application of the use of longitudinal data is to evaluate the mechanical impact of drugs on these diseases.
- Coupling the poromechanical model with airflow. The present model of lung behavior focuses on solid mechanics. However, ventilation is another important aspect of the organ, closely related to its main vital function. Ventilation and solid mechanics are coupled and they impact each other. The addition of an airflow model would allow the study of other pathologies like asthma.
- Extending the two-phase poromechanical model to a three-phase one. Lung edema is a disease where the pulmonary alveoli are filled by water. In some cases, the COVID-19 can lead to such complications and, for the most serious cases, clinicians have difficulties to set the ventilation parameters. We could adapt our model, in particular the material behavior, to a three-phase mixture to understand the impact of water in lungs on the pulmonary compliance. We could then optimally tune the parameters of the ventilator to improve the patient lung compliance.

To conclude, this work aimed to tackle clinical issues raised by idiopathic pulmonary fibrosis with the use of poromechanical modeling. The lung model developed, at the breathing time scale and the organ spatial scale, brings a proof of concept that a virtual lung can be used to access information which is not measurable, namely the regional effective and absolute compliances. Such information will be useful to improve the diagnosis of the disease. It also paves the way for further work to consider other scales in the organ, the alveolar scale mainly, as well as other clinical applications, like a better understanding of the disease and improvements of both diagnosis and treatment. Similar methods could also be used to study other pulmonary pathologies or even other organs. This work takes part in a wider worldwide trend to bring numerical tools for clinical applications, especially for personalized medicine.

Bibliography

Chapelle, D. and Moireau, P. (2014). General coupling of porous flows and hyperelastic formulations—From thermodynamics principles to energy balance and compatible time schemes. *European Journal of Mechanics - B/Fluids*, 46:82–96.

Genet, M., Chuan Lee, L., Ge, L., Acevedo-Bolton, G., Jeung, N., Martin, A., Cambronero, N., Boyle, A., Yeghiazarians, Y., Kozerke, S., and Guccione, J. M. (2015). A Novel Method for Quantifying Smooth Regional Variations in Myocardial Contractility Within an Infarcted Human Left Ventricle Based on Delay-Enhanced Magnetic Resonance Imaging. *Journal of Biomechanical Engineering*, 137(8):081009.

George, P. M., Wells, A. U., and Jenkins, R. G. (2020). Pulmonary fibrosis and COVID-19:

The potential role for antifibrotic therapy. *The Lancet Respiratory Medicine*, 8(8):807–815.

Govindjee, S. and Mihalic, P. A. (1996). Computational methods for inverse finite elastostatics. *Computer Methods in Applied Mechanics and Engineering*, 136(1-2):47–57.

Hinz, B. and Suki, B. (2016). Does Breathing Amplify Fibrosis? *American Journal of Respiratory and Critical Care Medicine*, 194(1):9–11.

Pallière, T., Lanel, A., Bel-Brunon, A., Bruyère-Garnier, K., Biboulet, N., and Lubrecht, T. (2019). Experimental protocol to evaluate lung parenchyma properties under inflation. *Computer Methods in Biomechanics and Biomedical Engineering*, 22(sup1):S14–S16.

Richardson, S., Gamage, T. P. B., HajiRassouliha, A., Jackson, T., Hedges, K., Clark, A., Taberner, A., Tawhai, M. H., and Nielsen, P. M. F. (2019). Towards a Real-Time Full-Field Stereoscopic Imaging System for Tracking Lung Surface Deformation Under Pressure Controlled Ventilation. In Nielsen, P. M. F., Wittek, A., Miller, K., Doyle, B., Joldes, G. R., and Nash, M. P., editors, *Computational Biomechanics for Medicine*, pages 119–130. Springer International Publishing, Cham.

Spagnolo, P., Balestro, E., Aliberti, S., Cocconcelli, E., Biondini, D., Casa, G. D., Sverzellati, N., and Maher, T. M. (2020). Pulmonary fibrosis secondary to COVID-19: A call to arms? *The Lancet Respiratory Medicine*, 8(8):750–752.

ECOLE
DOCTORALE

Titre : Mécanique pulmonaire personnalisée: modélisation, estimation et application à la fibrose pulmonaire.

Mots clés : Biomécanique; Médecine numérique; Modélisation pulmonaire; Poromécanique; Estimation à partir d'images.

Résumé : Les poumons réalisent leur fonction vitale d'échanges gazeux grâce notamment à leur élasticité et leur porosité. La fibrose pulmonaire idiopathique (FPI), une maladie pulmonaire interstitielle, impacte fortement la mécanique pulmonaire, soulevant des problématiques cliniques. L'objectif de ce travail est d'améliorer la compréhension et le diagnostic de la FPI en s'appuyant sur une modélisation poromécanique du poumon, personnalisée grâce à des données d'imagerie médicale. Dans une première partie, une analyse bibliographique fait l'état de l'art de la physiologie pulmonaire en relation avec les modélisations mécaniques existantes, en insistant sur les caractères multiéchelle, multiphasique et multiphysique de l'organe. Nous proposons ensuite un modèle poromécanique du poumon à l'échelle spatiale de l'organe et à l'échelle temporelle de la respiration, dérivé d'une théorie générale de poromécanique récemment formulée dans l'équipe MΞDISIM. La loi de comportement proposée reproduit notamment le comportement pression-volume du poumon ainsi que la quasi-incompressiblité de la phase solide. Les conditions aux limites prennent en compte l'environnement du poumon (cage thoracique, diaphragme, plèvre) et distinguent les cas de la respiration libre vs ventilée. La configuration déchargée, non observée au cours d'un cycle respiratoire, est estimée, avec une attention particulière apportée pour contraindre la positivité de la porosité. Plusieurs éléments du modèle sont ensuite personnalisés à partir de données cliniques standards, *i.e.,* deux images 3DCT prises en début et en fin d'inspiration. Un problème inverse est notamment formulé pour estimer la compliance pulmonaire en zones saines et fibrosées, la formulation poromécanique permettant de distinguer l'effet de la porosité de celui de la compliance du tissu interstitiel. Appliqué sur trois patients atteints de FPI, le modèle personnalisé permet de retrouver les propriétés pressenties de la FPI, *i.e.,* la rigidification des zones malades. Des surcontraintes sont aussi observées en bordure de la région malade, corroborant ainsi l'hypothèse d'un cercle vicieux mécanique régissant l'évolution de la FPI, où la fibrose entraînerait des contraintes importantes, qui à leur tour favoriseraient la fibrose. Cet outil numérique pourrait servir par la suite au diagnostic objectif et quantitatif de la FPI et, avec des données longitudinales, à l'étude de son remodelage induit par la mécanique.

Title : Personalized pulmonary mechanics: modeling, estimation and application to pulmonary fibrosis.

Keywords : Biomechanics; In Silico medicine; Lung modeling; Poromechanics; Image-based estimation.

Abstract : Lungs perform their vital function of gas exchanges thanks to their elasticity and porosity. Idiopathic pulmonary fibrosis (IPF), an interstitial lung disease, strongly impacts lung mechanics, which raises clinical issues. The objective of this work is to improve the understanding and diagnosis of IPF based on poromechanical modeling of the lung, personalized with clinical imaging data. In a first part, a literature review analyzes the state of the art of pulmonary physiology in relation to the existing mechanical models, insisting on the multi-scale, multi-phase and multi-physics characteristics of the organ. We then propose a poromechanical model of the lung at the organ spatial scale and breathing time scale, derived from a general poromechanical theory formulated recently in the MΞDISIM team. The constitutive law proposed reproduces mainly the pressure-volume behaviour of the lung as well as the quasi-incompressiblity of the solid phase. The boundary conditions take into account the lung environment (thoracic cage, diaphragm, pleura) and distinguish between free and ventilated breathing. The unloaded configuration, non observed during a breathing cycle, is estimated, with a special attention given to maintain a positive porosity. Various elements of the model are then personalized with standard clinical data, *i.e.,* two 3DCT images acquired at end-exhalation and end-inhalation. In particular, an inverse problem is formulated to estimate the pulmonary compliance of the healthy and fibrotic regions, since the poromechanical formulation allows to distinguish the effect of the porosity from that of the absolute compliance of the interstitial tissue. Applied to three patients suffering from IPF, the personalized model allows to find the foreseen properties of IPF, *i.e.,* the stiffening of the diseased region. Stress concentrations are also observed at the diseased region interface, supporting the hypothesis of a mechanical vicious circle governing the IPF progress, where fibrosis induces large stresses, which in turn favors fibrosis. This numerical tool could later be used for objective and quantitative diagnosis of IPF and, with longitudinal data, to study the mechanics-induced remodeling.

Institut Polytechnique de Paris
91120 Palaiseau, France